THE UNIVERSITY OF
WARWICK

University of Warwick institutional repository: http://go.warwick.ac.uk/wrap

A Thesis Submitted for the Degree of PhD at the University of Warwick

http://go.warwick.ac.uk/wrap/68820

This thesis is made available online and is protected by original copyright.

Please scroll down to view the document itself.

Please refer to the repository record for this item for information to help you to cite it. Our policy information is available from the repository home page.

The Modification of Surfaces: From Fundamentals to Applications

Paul M. S. Kirkman

Thesis

Submitted to the University of Warwick

for the degree of

Doctor of Philosophy

Department of Chemistry

THE UNIVERSITY OF WARWICK

September 2014

To my parents, without whom
I would have never made it this far.

Table of Contents

Table of Contents i
List of Figures v
List of Tables xix
Acknowledgements xx
Declaration xxi
Abstract xxii
Abbreviations xxiv
Glossary of Symbols xxvii

Chapter One: Introduction 1
  1.1 Carbon Materials 2
    1.1.1 Graphene 3
      1.1.1.1 Structure 3
      1.1.1.2 Synthesis and Transfer 4
      1.1.1.3 Characterization 8
      1.1.1.4 Electronic Properties 11
    1.1.2 CNTs and Fullerenes 15
    1.1.3 Graphite 16
      1.1.3.1 HOPG as an Electrode Material 17
  1.2 Electrochemistry 20
    1.2.1 Dynamic Electrochemistry 20
      1.2.1.1 Potential Sweeping Techniques 23
      1.2.1.2 Irreversible Systems 25
      1.2.1.3 Adsorbed Species 26
  1.3 Routes to Covalent Surface Modification 27
    1.3.1 Aryl Diazonium Compounds 27
      1.3.1.1 Structure of the Grafted Layer 28
      1.3.1.2 The Site of Radical Attack 31
    1.3.2 Self-Assembled Monolayers (SAMs) 33
      1.3.2.1 SAM Structure and Organization 34
      1.3.2.2 SAM Formation 36

1.4 Non-Electrochemical Techniques 38
  1.4.1 QCM 38
  1.4.2 AFM 41
    1.4.2.1 Force Measurements 44
    1.4.2.2 Chemical Force Microscopy (CFM) 49
1.5 Aims of this Thesis 50
1.6 References 53

Chapter Two: Experimental Methods 68

2.1 Chemicals, Solutions and Synthesis 69
  2.1.1 Model Dispersant Synthesis 71
  2.1.2 Diazonium Compound Synthesis 75
2.2 Sample Preparation 76
  2.2.1 SAM Preparation 76
  2.2.2 HOPG Substrate Preparation 77
  2.2.3 Graphene Synthesis 77
  2.2.4 PMMA Supported Graphene Transfer 78
  2.2.5 Polymer-Free Graphene Transfer 80
  2.2.6 Graphene Annealing and Microstrip Fabrication 81
2.3 QCM-D Measurements 84
2.4 AFM Force Measurements 86
  2.4.1 Instrumentation 86
  2.4.2 Micromanipulation 86
2.5 Macroscopic Electrochemical Measurements 89
  2.5.1 HOPG Substrates 89
  2.5.2 SAM Coated Substrates 90
2.6 SECCM 91
  2.6.1 Tip Fabrication 91
  2.6.2 Instrumentation 92
  2.6.3 Imaging Procedure 93
2.7 Characterization Techniques 94
  2.7.1 Optical Microscopy 94
  2.7.2 AFM 95
  2.7.3 SEM 95

2.7.4 Raman Spectroscopy 95
2.7.5 STM 96
2.7.6 Contact Angle 96
2.8 References.. 97

Chapter Three: Quantifying Dispersant-Soot Interactions: A Combined QCM-D and AFM Study 98
3.1 Introduction.. 99
3.1.1 The Structure of Soot 101
3.2 Results and Discussion 104
3.2.1 Synthesis of Model Dispersant Compounds 104
3.2.2 Production of Acid-Terminated SAMs 104
3.2.3 Characterization of SAMs at QCM Surfaces 107
3.2.4 Adsorption of Hydroxyl Based Dispersants at Model Surfaces 110
3.2.5 Adsorption of Amine Based Dispersants at Model Surfaces........... 114
3.2.6 Adsorption at Surfaces Lacking Polar Functionality..................... 119
3.2.7 Adsorption of Aromatic Based Dispersants at Model Surfaces 119
3.2.8 CFM to Study Aromatic Dispersant Interactions 121
3.3 Conclusions.. 125
3.4 References.. 126

Chapter Four: Molecular Functionalization of Graphite Surfaces: Basal Plane versus Step Edge Electrochemical Activity 129
4.1 Introduction.. 131
4.2 Results and Discussion 136
4.2.1 Macroscale Adsorption Studies 136
4.2.2 Complementary Surface Analysis 137
4.2.3 Time-Resolved Microscopic Adsorption Studies 142
4.3 Conclusions.. 149
4.4 References.. 151

Chapter Five: Spatial and Temporal Control of the Diazonium Modification of sp^2 Carbon Surfaces 155
5.1 Introduction.. 156
5.2 Results and Discussion 160
5.2.1 Diazonium Grafting at HOPG Surfaces.................................. 160

    5.2.2 Diazonium Grafting using SECCM 160
    5.2.3 Diazonium Microspot Array Deposition 163
    5.2.4 Patterned Spot AFM Analysis 165
    5.2.5 Basal vs. Step Edge Modification 168
    5.2.6 Patterned Spot Raman Analysis 169
    5.2.7 Modeling the Grafting Efficiency 172
    5.2.8 Estimating Diazonium Film Density 177
  5.3 Conclusions 179
  5.4 References 180

Chapter Six: The Direct Electrochemical Writing of Integrated Graphene Circuitry 184
  6.1 Introduction 185
  6.2 Results and Discussion 189
    6.2.1 Graphene Characterization 189
    6.2.2 Graphene Device Fabrication and Characterization 194
    6.2.3 Graphene Oxidative Patterning 197
    6.2.4 Diazonium Modification of Graphene using SECCM 204
  6.3 Conclusions 206
  6.4 References 208

Chapter Seven: A Biphasic Approach for the Polymer-Free Transfer of CVD Graphene 212
  7.1 Introduction 213
  7.2 Results and Discussion 214
    7.2.1 Biphasic Transfer Protocol 214
    7.2.2 Transferred Graphene Characterization 215
  7.3 Conclusions 219
  7.4 References 220

Chapter Eight: Conclusions 222

List of Figures

Figure 1.1 Illustration of the commonly depicted graphitic forms of carbon, where graphene acts as a 2D starting point for the formation of other materials. The action of wrapping a graphene sheet results in 0D fullerene structures, rolling produces 1D nanotubes, and stacking multiple sheets results in 3D graphite materials. 3

Figure 1.2 (a) AFM image of a predominantly single-layer exfoliated graphene flake on an Si/SiO$_2$ substrate, and measuring only a few micrometers in size. (b) Electronic gating measurements on a GO flake with increasing degrees of reduction treatment, showing it to become more conductive with time. The inset shows an optical image of the device measured. (c) Side-view illustration of monolayer epitaxial graphene on SiC (0001), separated from the bulk substrate by a covalently bound carbon layer. (d) Atomic-resolution TEM image of CVD graphene showing a grain boundary consisting of pentagons (blue), heptagons (red) and distorted hexagons (green). (e) SEM image of an as produced, single-crystal monolayer graphene domain on Cu, measuring 2.3 mm in diameter. (f) SEM image of single-layer CVD graphene grown on a polycrystalline Cu foil and transferred to an Si/SiO$_2$ substrate. 5

Figure 1.3 (a) STM topographic images of SLG (top) displaying the classic honeycomb structure, and multilayer graphene (bottom) showing the characteristic ‘three-for-six’ pattern as a result of electronic influences from underlying layers. (b) AFM topography image of predominantly SLG, measuring 9 Å in height, and a folded bilayer region measuring 13 Å in height. The 4 Å difference matches that expected for a SLG step. (c) Graphene crystallites on 300 nm SiO$_2$ imaged with white light (left) and green light of 510 nm wavelength (right), allowing for the clear distinction of layer thicknesses. (d) Characteristic Raman spectra of mono-, bi- and tri-layer graphene. (e) Raman spectra showing the 2D-band evolution with number of graphene 10 layers.

Figure 1.4 (a) Illustration of graphene's low-energy bandstructure of two cones touching at the Dirac point, E_{Dirac} (left). Adjusting the position of the Fermi energy (E_{f}) by applying a gate voltage in a FET arrangement determines the nature of graphene doping and the transport carrier, with p-doping (center) and n-doping (right) illustrated. (b) The ambipolar electric field effect in SLG, indicating changes in the position of the Fermi energy, E_{f}, with changing gate voltage (V_{g}), as schematically represented in (a). (c) Schematic representation of the bandstructure changes in BLG induced by an applied perpendicular electric field. The dotted line represents the structure in the absence of a field, while the solid line shows it in the presence of a strong electric field. (d) Transfer characteristics for a 1.5 nm wide GNR at various V_{sd} values. Inset shows an AFM image of the measured device, with a scale bar denoting 100 nm. (e) I_{sd}-V_{g} curves recorded at $V_{\mathrm{sd}} = 0.1$ V for SLG FET devices after several consecutive diazonium grafting experiments, with the captions showing the total grafting time. 13

Figure 1.5 An illustration of the structure of HOPG, from macroscale (cm) to nanoscale (nm). 16

Figure 1.6 Schematic illustration of the possible steps in a typical dynamic electrochemistry process. Steps such as adsorption/desorption and reactions in solution are limited to certain cases, and do not occur in typical redox systems. 21

Figure 1.7 (a) The potential waveform applied during a traditional CV measurement, and typical resulting current responses for a reversible redox process at a macroelectrode (b), and at a UME (c). 24

Figure 1.8 (a) The generalized diazonium grafting process, where A is the diazonium counter ion, and R represents a variety of possible functional groups. (b) The diazonium electrografting process. (c) Possible molecular arrangements in disordered multilayer aryl films. 27

Figure 1.9 (a) Topographic *in-situ* LFM images of an HOPG surface 32 following 5 cycles between -0.1 and -0.9 V vs. Ag/AgCl in the presence of 0.5 mM 4-diazo-N,N-diethylaniline fluoroborate. (b) 6 × 6 nm STM image of an HOPG surface derivatized by the electrochemical reduction of 4-nitrobenzenediazonium salt. (c) 20 × 20 nm electrochemical-STM image of an HOPG surface modified with a redox-active diazonium compound. (d) Raman spectroscopy maps of a graphene flake, showing the area under the D peak changing with time upon exposure to a diazonium compound, with certain areas appearing to react faster. (e) Raman spatial map of D-band/G-band intensity ratio after diazonium functionalization. Heavily modified stripes correspond to areas directly above Si/SiO_2, with less reacted areas separated from the substrate by a silane monolayer.

Figure 1.10 (a) Schematic illustration of typical adsorbed SAM molecules, showing their three constituent parts. (b) A single-chain model of an adsorbed SAM molecule, showing its orientation parameters. 34

Figure 1.11 (a) The steps typically depicted to be occurring during the SAM formation process. (b) Examples of just some of the reasons for defects being present within a formed SAM. 37

Figure 1.12 (a) Photograph of a QCM crystal. (b) Schematic illustrating the oscillation of a QCM chip under application of an alternating voltage between the two metal electrodes. (c) Illustration of the effect on oscillation frequency of adding mass to a QCM chip surface. (d) Illustration of the effect on frequency dissipation of adding a rigid vs. elastic mass to a QCM-D chip surface. 39

Figure 1.13 (a) Schematic of AFM setup, demonstrating the optical technique used to monitor changes in tip position at the sample surface. (b) Optical image of a typical V-shaped Si_3N_4 cantilever assembly, along with an SEM micrograph of the attached tip, itself made from Si. 43

Figure 1.14 (a) Schematic representations of the six main steps associated with acquiring a force-distance curve. (b) Typical waveform applied to tip-sample for the recording of a single force-curve. (c) An 45 idealized force curve, with marked points corresponding to the tip position, as described in (a).

Figure 2.1 The grafting reaction of maleic anhydride with 2-methyl-1-undecene to form the batch starting material MA-MUD. 71

Figure 2.2 The grafting reaction of MA-MUD with a generic amine compound, resulting in a model dispersant. 72

Figure 2.3 An FT-IR spectrum of the batch synthesized MA-MUD starting material, prior to further amine attachment, displaying a prominent peak at 1786 cm^{-1}. 74

Figure 2.4 An FT-IR spectrum of a synthesized dispersant compound upon reaction completion, determined by introduced peaks at 1774 cm^{-1} and 1704 cm^{-1}, and a lack of the originally present 1786 cm^{-1} anhydride peak. 75

Figure 2.5 A schematic representation of the PMMA supported graphene transfer process. 80

Figure 2.6 A schematic representation of the introduced polymer-free graphene transfer process. 81

Figure 2.7 (a) A schematic diagram of the designed lithography mask employed to produce graphene microstrips, where white coloring represents transparent acetate areas, and black coloring shows opaque areas, which are transferred when used in combination with a positive photoresist e.g. S1818. (b) The corresponding evaporation mask, made out of Kapton film, for producing metal contacts to the photolithographically defined microstrips. 82

Figure 2.8 Optical images of exfoliated multilayer graphene flakes (a) before and (b) after plasma treatment (Ar$^+$, 5 minutes, 50 W, 4 × 10^{-1} mbar). Red arrows highlight a spot of contamination, still mostly present after ashing, confirming the same location, and the red dashed line in (b) shows the area the largest flake was initially present. Scale bars denote 20 μm. 83

Figure 2.9 Schematic representation of the entire graphene microstrip fabrication process, starting with a transferred graphene sheet on Si/SiO_2, and resulting in 30 individually accessible, electrically connected graphene microstrips. 84

Figure 2.10 (a) A labeled photograph of the QCM-D experimental setup. (b) Schematic diagrams of a QCM-D flow cell, and corresponding Au coated QCM chip. 85

Figure 2.11 Schematic representation of the micromanipulation rig used in this work. 87

Figure 2.12 A summary of the process used for the production of colloidal AFM probes. 88

Figure 2.13 Schematic representation of the setup used for macroscale electrochemical measurements at HOPG surfaces, with the electrolyte droplet confined using a fluorosilicone rubber O-ring. 90

Figure 2.14 (a) SEM micrograph of laser-pulled SECCM tip, with a tapered opening of ~ 1 μm in diameter, and a zoom-in of the same tip (b). Scale bars denote 25 μm and 1 μm for (a) and (b) respectively. 91

Figure 2.15 (a) A photograph of the SECCM setup for a typical experiment. (b) Illustration of the SECCM tip setup, with applied potentials and measured currents labeled, full details of which are given in the text. 92

Figure 2.16 (a) The three main steps of meniscus state during an approach to the surface with an SECCM tip, and the corresponding typically measured i_{DC} (b) and i_{AC} (c) values. During approach, only a DC conductance current is measured, owing to the applied bias between the QRCEs. Upon initial surface contact, the meniscus is compressed, causing a decrease in the DC conductance current, but generating a signal in the AC component. At full meniscus opening and contact, large increases in both the DC and AC conductance currents are observed. 94

Figure 3.1 (a) Representation of the mechanism of action of dispersant compounds, preventing soot agglomeration through the formation of a 100 hindering barrier. (b) Schematic representation of a PIBSA based engine oil dispersant compound, separated into its three distinct parts.

Figure 3.2 (a) TEM image of a soot agglomerate extracted from used engine oil, with a corresponding high-resolution image shown in (b), where the scale bar represents 5 nm. (c) Schematic of the many surface oxygen functionalities present in soot, with functionalities relevant to this work highlighted in red. 102

Figure 3.3 STM images of (a) a typical Au (111) on mica surface prior to thiol modification (200 mV bias, set-point = 125 pA) (b) the resulting surface post modification with 1 mM 11-MUA in ethanol displaying the formation of bilayer areas (200 mV bias, set-point = 150 pA) and (c) the resulting surface post modification with 1 mM 11-MUA + CF_3COOH using the methodology introduced by Wang *et al.* (200 mV bias, set-point = 125 pA). Scale bars denote 50 nm. (d) High resolution STM image of an 11-MUA modified Au (111) sample using the Wang *et al.* method. (Filtered by Fourier transformation, 800 mV bias, set-point = 40 pA) Scale bar denotes 1.5 nm. (e) Height profile measurements corresponding to the dashed lines in (d), confirming the presence of a densely packed monolayer. 106

Figure 3.4 (a) Typical AFM image of a polycrystalline Au surface on a QCM-D chip, prior to modification with a SAM. Scale bar denotes 200 nm. (b) Images captured during water contact angle measurements for QCM-D chip surfaces functionalized with 1-dodecanethiol, 11-MUD and 11-MUA. The contact angle quoted in the text is also marked, denoted as θ. (c) CVs at 100 mV s^{-1} for the reduction of 10 mM $K_3[Fe(CN)_6]$ in 0.1 M KCl on a QCM-D electrode surface, before and after modification with 11-MUD. (d) A zoom-in of the area marked in (c), highlighting the complete lack of a faradaic current response. 108

Figure 3.5 The headgroup structures of model dispersant compounds **I** and **II**. 111

Figure 3.6 Typical Δf vs. time plots for the adsorption of compound **I** from a 1 mM solution (90 % toluene/10 % hexane (v/v)) at (a) –COOH 111 and (b) –OH functionalized surfaces. Only data collected from f_3 is presented as negligible overtone splitting was observed.

Figure 3.7 Typical Δf and D vs. time plots for the adsorption of compound **II** from a 1 mM solution (90 % toluene/10 % hexane (v/v)) at (a) –COOH and (b) –OH functionalized surfaces. In (b), only data collected from f_3 is presented as negligible overtone splitting was observed. 112

Figure 3.8 Determined Γ values (post-rinse via the Sauerbrey equation) for the adsorption of compounds **I** and **II** at (a) –COOH and (b) –OH functionalized surfaces from 1 mM solutions (90 % toluene/10 % hexane (v/v)). Coverage values are determined from data obtained at f_3, and are presented in duplicate. 114

Figure 3.9 The headgroup structures of model dispersant compounds **III** and **IV**. 115

Figure 3.10 Typical Δf and D vs. time plots for the adsorption of compound **III** from a 1 mM solution (90 % toluene/10 % hexane (v/v)) at (a) –COOH and (b) –OH functionalized surfaces. Only data collected from f_3 is presented as negligible overtone splitting was observed. 115

Figure 3.11 Determined Γ values (post-rinse via the Sauerbrey equation) for the adsorption of compound **III** at –COOH and –OH functionalized surfaces from a 1 mM solution (90 % toluene/10 % hexane (v/v)). Coverage values are determined from data obtained at f_3, and are presented in duplicate. 117

Figure 3.12 Typical Δf and D vs. time plots for the adsorption of compound **IV** from a 1 mM solution (90 % toluene/10 % hexane (v/v)) at (a) –COOH and (b) –OH functionalized surfaces. 117

Figure 3.13 Typical Δf and D vs. time plots for the adsorption of compounds (a) **III** and (b) **IV** at –CH_3 SAM functionalized surfaces from a 1 mM solution (90 % toluene/10 % hexane (v/v)). Only data collected from f_3 is presented as negligible overtone splitting was observed. 119

Figure 3.14 The headgroup structures of model dispersant compounds **V, VI** and **VII**. 120

Figure 3.15 Determined Γ values (post-rinse via the Sauerbrey equation) for the adsorption of compounds **V**, **VI** and **VII** at –COOH and –OH functionalized surfaces from 1 mM solutions (90 % toluene/10 % hexane (v/v)). Coverage values are determined from data obtained at f_3, and are presented in duplicate. 120

Figure 3.16 (a) False color SEM image of a commercial AFM probe modified with a colloidal glass particle and coated in Au. Histograms showing normalized F_{ad} values for 200 repeat force-curve measurements between tip-surface combinations displaying (b) $–CH_3$, and (c) –COOH functionality. Force curve measurements were performed in ethanol. 122

Figure 3.17 Histograms showing normalized F_{ad} values for 300 (2 × 150) repeat force-curve measurements between an aromatic dispersant coated tip and (a) a –COOH functionalized surface (b) an –OH functionalized surface, and (c) freshly cleaved ZYA HOPG. Force curve measurements were performed in hexane. 124

Figure 4.1 The electrochemical redox process associated with AQDS. 133

Figure 4.2 (a) CVs for the reduction/oxidation of 10 μM AQDS in 0.1 M $HClO_4$ at 100 mV s^{-1} on four different grades of freshly cleaved HOPG. (b) A plot of | i_p | (reduction wave) vs. scan rate, ν, for the case of AM grade HOPG, showing a distinct linear dependence. 136

Figure 4.3 AFM images of freshly cleaved, unmodified HOPG surfaces of (a) AM, (b) ZYA, (c) SPI-1 and (d) SPI-3 grade, along with associated histograms showing the height of each step (in atomic layers) for 7 different areas of the same freshly cleaved surface. Scale bars denote 1 μm in all cases. 138

Figure 4.4 (a) The range of adsorbed surface coverage values for a solution of AQDS (10 μM) in 0.1 M $HClO_4$ as determined by cyclic voltammetry at 100 mV s^{-1}, at four different grades of freshly cleaved HOPG. Error bars represent 1 S.D. (N = 10) (b) The range of step edge 139 coverage values, as determined by AFM, for the four grades of HOPG investigated. The mean for each data set is marked with a red line (N = 7).

Figure 4.5 (a) *Ex-situ* AFM image of an AM HOPG surface, post adsorption of AQDS from a 10 μM in 0.1 M $HClO_4$ solution, and zoom-in of the area marked by a dotted box (b). Resulting CVs from a surface pre-treated with 10 μM AQDS in 0.1 M $HClO_4$ before performing voltammetry in 0.1 M $HClO_4$ (c) and 0.5 mM $FcTMA^{+/2+}$ in 0.1 M $HClO_4$ (d). 141

Figure 4.6 (a) Schematic representation of the FSCV setup, with corresponding diagram of how FSCV can be employed to monitor adsorption at an electrode surface. (b) An optical micrograph of a typical tip used in such studies, with the scale bar denoting 10 μm. (c) The waveform applied to the substrate upon meniscus contact, and corresponding timescales for both FSCV measurements and adsorption. Inset, typical i_{DC} vs. time plot, showing a jump at contact. 144

Figure 4.7 FSCVs for the reduction/oxidation of 1 μM AQDS in 50 mM $HClO_4$ at 100 V s^{-1} using the SECCM setup, with *inter-CV adsorption* hold times of (a) 250 ms and (b) 5000 ms. (c) Observed fractional surface coverage values determined from FSCV measurements at six different areas of the AM HOPG surface. (d) A typical FSCV for the reduction/oxidation of 1 μM AQDS in 50 mM $HClO_4$ at 100 V s^{-1} after a hold time of 10 s, with a ~ 16 μm diameter tip. 146

Figure 4.8 (a) AFM image of an AM HOPG surface after AQDS adsorption via FSCV (area marked by a white dotted line) and a zoom-in at a step edge site showing no preferential adsorption. Scale bars denote 2 μm and 500 nm respectively. (b) % of step edges within the six adsorption spots for which FSCV measurements were made with corresponding surface coverage vs. time. 148

Figure 5.1 Literature examples of current methods for the surface patterning of diazonium compounds. (a) A fully diazonium-modified pyrolyzed photoresist film surface, with patterned trenches of exposed 158 substrate introduced using an AFM tip. (b) SEM and Kelvin force microscopy images of a diazonium patterned HOPG surface produced using photolithography. (c) Patterned diazonium patches introduced using a PDMS microcontact printing method. (d) Diazonium patches introduced on an Au substrate using reduction at a positionable Pt SECM tip.

Figure 5.2 (a) Schematic of the diazonium modification reaction at an HOPG electrode surface, resulting in the production of an sp^3 carbon center in the uppermost HOPG layer. (b) Schematic representation of the formation of aryl multilayers at an HOPG surface. 160

Figure 5.3 (a) The SECCM setup. CVs for the reduction of 0.1 mM 4-CBD at an HOPG surface obtained using (b) the SECCM setup, with 25 mM H_2SO_4 aqueous electrolyte and a 1 μm diameter pipet, and (c) with a 3.2 mm diameter macro-disk electrode (droplet confined using rubber O-ring) in 100 mM H_2SO_4. Both CVs were obtained with a scan rate of 100 mV s^{-1} on a freshly cleaved HOPG surface. 162

Figure 5.4 (a) Three typical current-time transients obtained during the spot deposition, one for each deposition potential employed. (b) Electrochemical charge associated with each of the spot depositions as a function of hold time, for each of the three deposition potentials employed. 164

Figure 5.5 AFM topography images of typical deposition arrays created at potentials E_{max} (a), E_{mid} (b), and E_{min} (c), using various deposition times. (d) Heights of each deposit (determined by AFM) as a function of hold time, for the different potentials employed. 166

Figure 5.6 Macroscale CVs obtained for the diazonium reduction process at (a) high quality AM HOPG and (b) SPI-3 grade HOPG from 0.1 mM 4-CBD in 50 mM H_2SO_4. CVs were obtained at a scan rate of 100 mV s^{-1} with a working electrode area of 0.32 cm^2. 168

Figure 5.7 Representative Raman spectra for both bare HOPG (a) and diazonium modified HOPG (b), using the CV conditions also employed 169 in Figure 5.6. Spectra were acquired using 633 nm laser, with ~ 1 μm laser spot size.

Figure 5.8 Typical Raman maps plotted as D-band intensity over the surface of the arrays created at E_{max} (a) and E_{mid} (b) along with representative spectra for both modified and unmodified areas of the surface. 170

Figure 5.9 Normalized D-band intensity (with respect to maximum D-band intensity measured), plotted for each of the spots as a function of hold time, for the aforementioned maps at both E_{max} and E_{mid}. 171

Figure 5.10 Corresponding Raman maps of D / G-band intensity to those presented in Figure 5.8, for modification at E_{max} (a) and E_{mid} (b). 172

Figure 5.11 Schematic representation showing the generation of an aryl radical at an HOPG surface (R1), and possible radical reaction routes, with the surface (R2) and solution (R3). 173

Figure 5.12 (a) LSV between 0.9 and 0.45 V vs. Pd-H_2 for the reduction of 1 mM 4-CBD at an HOPG electrode (line) and corresponding experimental fit to the data (crosses). (b) Plot of $f((E^{0'})_{\mathrm{opt}}, k_{\mathrm{i}}, k_{\mathrm{b}})$ values as a function of k_{i} and k_{b}. (c) k_{i} and k_{b} data for the global canyon visible in (b), and the fitted function according to eq. 5.11. The global minimum contour corresponds to $f_{\mathrm{min}} = 1.502$. 177

Figure 5.13 (a) Plots of surface coverage (determined from electrochemical charge with $s = 0.92$) against hold time for each of the three deposition potentials investigated. (b) Plots of surface coverage against deposition height for each of the three deposition potentials. 178

Figure 6.1 Examples of current methods for entire graphene device fabrication. (a) A single-layer graphene strip, narrowed by two oxidized regions, created with an AFM tip. (b) A fluorinated graphene flake selectively reduced back to graphene using electron beam irradiation. (c) A GO film with a zig-zag rGO ribbon fabricated using an AFM tip. 187

Figure 6.2 Schematic representation of the unique patterning concept introduced herein. 189

Figure 6.3 AFM images of (a) graphene on Si/SiO_2 post PMMA transfer with no additional treatment, and post annealing at (b) 450 °C (c) 350 °C and (d) 300 °C for 15 minutes in an Ar/H_2 atmosphere. Scale bars represent 1 μm. 191

Figure 6.4 Representative Raman spectra of (a) graphene on Si/SiO_2 post PMMA transfer, and post-annealing at (b) 450 °C (c) 350 °C and (d) 300 °C for 15 minutes in an Ar/H_2 atmosphere. Shown on all spectra are the corresponding I_D/I_G values. Spectra were acquired using a 514 nm Ar^+ laser (20 s laser exposure time), with a spot diameter of ~ 2 μm. 193

Figure 6.5 (a) Schematic representation of a fully fabricated device. (b) Photograph, photomicrograph and SEM micrograph of various sections of a fabricated device. Scale bar represents 100 μm in photomicrograph, and 500 μm in SEM images. 195

Figure 6.6 *i-V* curves for the 24 microstrips on a fabricated device formed from (a) annealed and (b) as-transferred graphene samples. Measured resistance values (determined from *i-V* curves) of individual graphene strips on a fabricated device, for (c) a sample that underwent 350 °C annealing, and (d) a device fabricated from as-transferred graphene. The arrow in (c) shows a strip having anomalously high resistivity, due to a tear in the strip, significantly reducing its width. Raman spectra acquired on (e) the center, and (f) the edge of a graphene fabricated microstrip, using identical conditions to those in Figure 6.4. 196

Figure 6.7 (a) Schematic representation of how the SECCM probe was employed in microstrip modification/mapping, with an SEM micrograph of a typical probe. Scale bar denotes 500 nm. (b) The electrochemical activity map of a pristine graphene microstrip towards 1 mM $[Ru(NH_3)_6]^{3+}$ reduction in 50 mM KCl at E_{surf} = -0.3 V vs. Ag/AgCl, acquired using the SECCM setup. Corresponding SECCM i_{DC} (c), i_{AC} (d) and topography (e), maps to (b). Horizontal scale bars denote 10 μm. 198

Figure 6.8 Electrochemical activity (i_{surf}) map of a graphene microstrip towards 1 mM $[Ru(NH_3)_6]^{3+}$ in 50 mM KCl at E_{surf} = -0.3 V vs. 201

Ag/AgCl, before (a), and after (b), oxidative cutting along the region marked in grey on (a). Oxidative cutting was performed at E_{surf} = 3.3 V vs. Ag/AgCl and at a scan speed of 0.25 μm s^{-1}. (c) An illustration of the graphene microstrip post-oxidative cutting, resulting in part of the microstrip being electrically isolated from the rest. (d) CVs for the $[Ru(NH_3)_6]^{3+}$ reduction process acquired at the crosses marked in (b). Horizontal scale bars denote 10 μm. (e) Normalized (with respect to measured maximum) *i-V* curves of the graphene microstrip, prior to, and post, the oxidative cutting procedure. (f) A zoom of the post-oxidation *i-V* curve.

Figure 6.9 Electrochemical activity map of a graphene microstrip towards the reduction of 1 mM $Ru(NH_3)_6^{3+}$ in 50 mM KCl at E_{surf} = -0.3 V vs. Ag/AgCl, before (a), and after (b), oxidative patterning in the region marked on (a). (c) Corresponding i_{DC} map to (b), showing a more wetting region at the oxidized area, manifested as higher i_{DC} values in SECCM. (d) Electrochemical activity map of a graphene microstrip towards the reduction of 1 mM $Ru(NH_3)_6^{3+}$ in 50 mM KCl at E_{surf} = -0.3 V vs. Ag/AgCl after oxidative patterning to narrow the strip. Horizontal scale bars represent 10 μm. (e) *i-V* curves of the graphene microstrip, prior to, and post, the oxidative narrowing procedure. (f) High contrast optical micrograph of the narrowed microstrip, with an oxidized region marked with an arrow. Scale bar represents 10 μm. 203

Figure 6.10 (a) CVs showing the reduction of 0.1 mM 4-NBD in 25 mM H_2SO_4 at a graphene surface using the SECCM setup, recorded at 100 mV s^{-1} with a tip 450 nm in diameter. (b) Raman spectra of a large graphene patch after CV modification using the parameters described in (a), and of the same area before modification. Spectra were acquired using a 633 nm laser, with ~ 1 μm laser spot size. 205

Figure 7.1 A schematic representation of the biphasic polymer-free transfer method introduced herein. 215

Figure 7.2 Optical micrographs of graphene on Si/SiO_2 transferred via (a) the biphasic method introduced herein and (b) the traditional PMMA 216 supported route. Scale bars denote 10 μm.

Figure 7.3 (a) AFM and (b) SEM images of graphene transferred via the biphasic approach to an Si/SiO$_2$ substrate. Scale bar denotes 1 μm in both cases. SEM inset further highlights bilayer patches, with a scale bar denoting 500 nm. Representative Raman spectra for graphene on Si/SiO$_2$ transferred using: (c) the biphasic method introduced herein, and (d) the common PMMA supported transfer route. Both samples were grown in the CVD chamber at the same time. Spectra are normalized to 2D band intensity. 217

List of Tables

Table 2.1 Details of chemicals and materials used throughout this thesis. 69

Table 2.2 The range of starting amine compounds used in model dispersant synthesis. 73

Acknowledgments

First and foremost, I would like to thank my supervisors, Prof. Patrick Unwin and Prof. Julie Macpherson. The passion and enthusiasm you share for science is infectious, and it never failed to inspire me, even when things got tough. Not only were you both incredible sources of knowledge, you were always kind and supportive throughout my studies. Over the past 4 years you've helped me to develop both academically and as an individual, and for that I am most grateful. I would like to thank Lubrizol for their sponsorship, and my industrial supervisors Dr. Steve Cook and Joanne Jones for their constant support.

I give special thanks to Dr. Aleix Güell. You've been a mentor to me, and without you, a lot of this work would not have been possible. No matter what time of day it was, or how much you had to do, you were always willing to stand in front of that whiteboard and discuss things – often for hours. You were never afraid to tell me when things weren't good enough, and although I didn't always enjoy that part, the high standards you set made me a better scientist.

I'd like to thank Dr. Robert Lazenby, Dr. Neil Ebejer, and Dr. Thomas Miller, who were always around for a coffee and a chat. Sometimes it was science, and sometimes it was the latest gossip... either way, it was always useful. I hope you enjoyed the fun times as much as I did. I give further thanks to Guohui Zhang and Anatolii Cuharuc, who both contributed to work in this thesis, and who always did the very best job they could.

Finally, I would like to thank my parents, family, and friends for their support, understanding and encouragement. I also give loving thanks to Amy Davis, who has likely been the most understanding of all. Whether it was proof reading a paper, or waiting up for me at some ridiculous hour, you were always there for me. I'm sure I wouldn't have got through this without you, and that's why I love you.

Declaration

This thesis is submitted to the University of Warwick in support of my application for the degree of Doctor of Philosophy. It has been composed by myself and has not been submitted in any previous application for any degree. All work contained is entirely my own, except for the following contributions:

Experiments in Chapter 4 were performed in conjunction with Mr. Guohui Zhang and modeling in Chapter 5 was performed by Mr. Anatolii Cuharuc.

Parts of this thesis have been published, as detailed below:

Chapter 4
G. Zhang, P. M. Kirkman, A. N. Patel, A. S. Cuharuc, K. McKelvey, and P. R. Unwin, Molecular Functionalization of Graphite Surfaces: Basal Plane versus Step Edge Electrochemical Activity, *J. Am. Chem. Soc.* **2014**, *136*, 11444.

Chapter 5
P. M. Kirkman, A. G. Güell, A. S. Cuharuc, and P. R. Unwin, Spatial and Temporal Control of the Diazonium Modification of sp^2 Carbon Surfaces, *J. Am. Chem. Soc.* **2014**, *136*, 36.

Two further publications based on this thesis (Chapters 6 and 7) are currently in preparation.

Work to which I have contributed, but is not featured in this thesis, is detailed below:

S. C. S. Lai, R. A. Lazenby, P. M. Kirkman, and P. R. Unwin, Nucleation, aggregative growth and detachment of metal nanoparticles during electrodeposition at electrode surfaces, *Chem. Sci.* **2015**, *6*, 1126.

Abstract

You're surrounded by surfaces. Viewed from a macro perspective they might appear soft, brightly colored, or textured. Maybe you don't think anything of them at all. But what happens when we take a closer look? Here, down at the nanoscale, chemical reactions at surfaces play a hugely important role in the world in which we live. Whether it's preventing metal corrosion, or developing the latest fuel cell, the state of surface being investigated is crucial. Indeed, by intentionally modifying surfaces we can introduce desirable properties, all because we're controlling what goes on at the molecular level.

The first part of this thesis discusses the use of model surfaces to probe fundamental properties and processes. Firstly, model surfaces displaying well-defined chemical functionality are created using self-assembled monolayers (SAMs), and are subsequently used as a means to understand the primary interactions that occur between carbonaceous soot contaminants, and surfactant-like molecules in engine oils. The quartz-crystal microbalance (QCM) is employed as a means to determine minute levels of surface adsorption, and a structure-activity relationship for these molecules is suggested. Next, a new approach for profiling the activity of molecular adsorbates at carbon surfaces is introduced, which allows for the impact of individual surface features on resulting electrochemical activity to be determined. It is used to study the case of quinone adsorption at graphite electrodes, a currently debated topic, and it is revealed that current literature models regarding the activity of the basal surface need revision, with significant implications for carbon electrochemistry as a whole.

The second part of this thesis turns to understanding and controlling surface modification processes. Through a range of complementary techniques, the ability of scanning electrochemical cell microscopy (SECCM) to control the extent of the aryl diazonium grafting process at sp^2 carbon surfaces is demonstrated. Aryl diazonium chemistry as been identified as a route to band-gap generation in graphene electronics, and as such, controlled routes to localized surface modification are of great interest. Next, the versatility of SECCM for controlled surface modification is further demonstrated, where it is used as a method to draw intricate patterns of defined surface chemistry in graphene, with a strong focus on the production of integrated graphene circuits, a prospect often promised. Finally, a new methodology for the transfer of graphene synthesized via chemical vapor deposition (CVD) is introduced. Crucially, it yields graphene surfaces with distinctly low levels of contamination, an area that currently poses a problem in graphene research.

Abbreviations

11-MUA	11-mercaptoundecanoic acid
11-MUD	11-mercapto-1-undecanol
4-CBD	4-carboxybenzenediazonium tetrafluorborate
4-NBD	4-nitrobenzenediazonium tetrafluoroborate
AC	Alternating current
AFM	Atomic force microscopy
AQDS	Anthraquinone-2,6-disulfonate
BLG	Bilayer graphene
CFM	Chemical force microscopy
CNT	Carbon nanotube
CV	Cyclic voltammetry
CVD	Chemical vapor deposition
DC	Direct current
DOS	Density of states
ET	Electron transfer
FET	Field-effect transistor
FSCV	Fast scan cyclic voltammetry
FT-IR	Fourier transform infrared
FWHM	Full-width-half-maximum
GC	Glassy carbon
GNR	Graphene nanoribbons
GO	Graphene oxide
h-BN	Hexagonal boron nitride

HOPG	Highly ordered pyrolytic graphite
LFM	Lateral force microscopy
LSV	Linear sweep voltammetry
MA	Maleic anhydride
MUD	2-methyl-1-undecence
NMR	Nuclear magnetic resonance
pBDD	Polycrstalline boron doped diamond
PCB	Printed circuit board
PDMS	Polydimethylsiloxane
PIBSA	Poly(iso-butylene) succinimide ester
PMMA	Polymethylmethacrylate
QCM	Quartz crystal microbalance
QCM-D	Quartz crystal microbalance with dissipation monitoring
QRCE	Quasi reference counter electrode
RBS	Rutherford backscattering
rGO	Reduced graphene oxide
SAM	Self-assembled monolayer
SC	Semiconducting
SCCM	Standard cubic centimeters per minute
SECCM	Scanning electrochemical cell microscopy
SECM	Scanning electrochemical microscopy
SEM	Scanning electron microscope
SLG	Single-layer graphene
SPM	Scanning probe microscopy
STM	Scanning tunneling microscopy

STS	Scanning tunneling spectroscopy
TEM	Transmission electron microscopy
UME	Ultra-microelectrode
XPS	X-ray photoelectron spectroscopy

Glossary of Symbols

A	Area
C_0	Double-layer capacitance
C_x	Concentration of species x
$C_{\mathrm{x},0}$	Bulk concentration of species x
D	Diffusion coefficient (Electrochemistry)
D	Dissipation (QCM)
E	Young's modulus (QCM and AFM)
E	Potential (Electrochemistry)
$E^{0'}$	Formal electrode potential
E_surf	Surface potential in SECCM
F	Force (AFM)
F	Faraday's constant (Electrochemistry)
f	Frequency
f_n	n$^\mathrm{th}$ frequency overtone
F_ad	Adhesion force
i	Current
i_AC	AC component of SECCM barrel current
i_barrel	SECCM barrel current
i_DC	DC component of SECCM barrel current
i_surf	Surface current in SECCM
j	Current density
j_av	Average current density
k	Cantilever spring constant

k_0	Standard electron rate transfer constant
k_b	Backward reaction rate constant
k_f	Forward reaction rate constant
k_t	Mass transport rate constant
L	Cantilever length
Q	Charge
R	Molar gas constant
R_a	Roughness average
s	Sticking coefficient
t	Cantilever thickness
T	Temperature
w	Cantilever width
α	Charge transfer coefficient
Γ	Surface coverage
Γ_0	Maximum possible surface coverage
ΔE_p	Peak-to-peak separation
Δf	Frequency change
Δm	Mass change
Δz	Cantilever displacement
θ_{ads}	Fractional surface coverage
μ	Shear modulus
v	Scan rate
ρ	Density

Chapter One

Introduction

This thesis concerns modification and adsorption processes at surfaces, in numerous capacities, ranging from fundamental applications, to real-world problems, to advanced technological platforms. Firstly, this chapter provides an overview of the materials of specific interest herein, covering their synthesis, characterization, and intrinsic properties. Secondly, it summarizes the range of techniques and methodologies used throughout this work, from both experimental and theoretical perspectives.

1.1 Carbon Materials

To label carbon as a unique element is somewhat self-evident; indeed, by definition, all elements are unique. But carbon is perhaps different. Its capacity to form thermodynamically stable bonds with a wide range of elements (B, N, O, Si, Cl, to give but a few examples) defines the field of organic chemistry alone. But carbon's ability to form bonds with itself in pure carbon materials, leading to allotropes with an incredibly diverse range of properties, is central to carbon's uniqueness and is the focus of the studies in this thesis.

Separated into two categories, carbon materials of a graphitic nature such as fullerenes,[1] carbon nanotubes (CNTs),[2] graphene[3] and graphite[4] all have pure sp^2 structures, with differences only in the arrangement of their aromatic building blocks creating the substantial variation observed in their many properties. On the other hand, tetrahedral based building blocks, exclusively made of sp^3 carbon, are the basis of materials such a diamond.[5] The fact that both the world's best electrical conductor and the world's hardest natural material are contained within list allotropes only further demonstrates the versatility of carbon.[6]

Figure 1.1 illustrates the main aforementioned forms of graphitic carbon, and the following sections detail their characteristics, with emphasis on those relevant to this thesis.

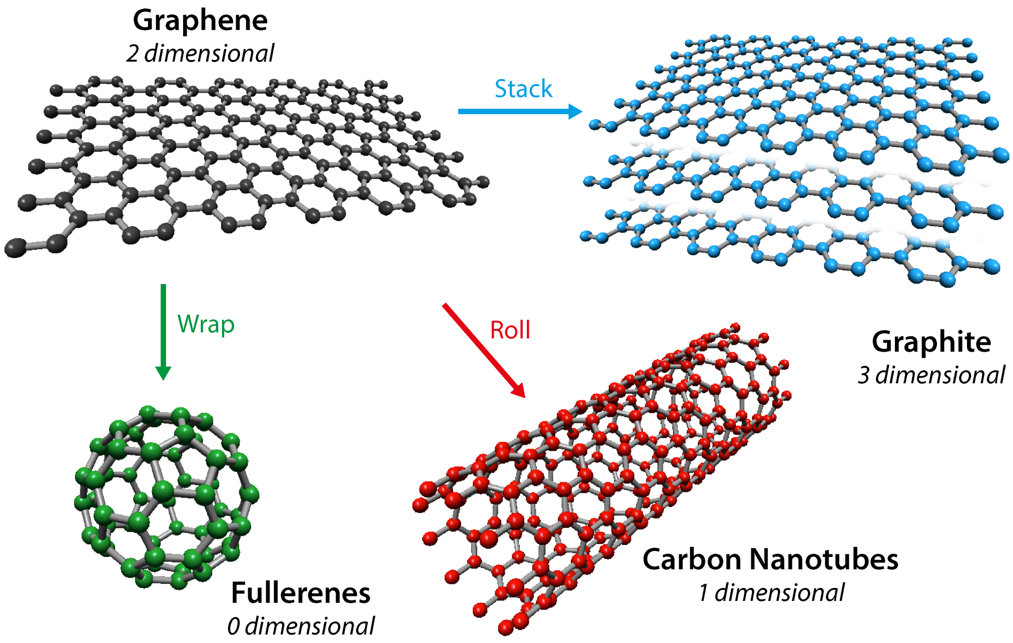

Figure 1.1 Illustration of the commonly depicted graphitic forms of carbon, where graphene acts as a 2D starting point for the formation of other materials. The action of wrapping a graphene sheet results in 0D fullerene structures, rolling produces 1D nanotubes, and stacking multiple sheets results in 3D graphite materials.

1.1.1 Graphene

1.1.1.1 Structure

For years, it was argued that strictly 2D materials could not exist, with Peierls[7] and Landau[8] suggesting that on such a small scale, thermal fluctuations (comparable to interatomic distances) should lead to the displacement of atoms, essentially resulting in melting of the material at thicknesses below dozens of atomic layers.[9] The experimental discovery of graphene in 2004 thus drew significant attention,[3] and continuous, high quality 2D crystals have now shown to be obtainable on top of non-crystalline substrates,[10,11] suspended in liquids,[12] and as supported membranes.[13] A single 2D sheet of graphene takes a regular hexagonal structure (Figure 1.1), no different than that of a single layer of graphite, with each carbon atom forming three σ bonds of length 1.42 Å, one to each of its nearest neighbors. This gives rise to a lattice that is impermeable to the smallest gas molecules (He),[14] has an associated Young's modulus of ~ 1 TPa,[15] and a thermal conductivity of ~ 4000 W mK^{-1}.[16] Additionally, and in contrast to diamond-like materials, carbon's fourth valence electron does not participate in covalent bonding in graphene, remaining in the $2p_z$ state oriented perpendicular to the 2D sheet, forming a π conduction band. The electronic properties of graphene, and CNTs for that matter, are a direct consequence of this (*vide infra*).[17] Graphene's unique structural characteristics mean it has already shown promise in areas such as composite materials,[12] whilst additional factors such as its enormous surface area-to-volume ratio[18] make it ideal for single-molecule sensing,[19] as a material for energy storage,[20] and for incorporation into batteries[21] and ultra-capacitors.[22]

1.1.1.2 Synthesis and Transfer

Mechanical exfoliation methods are, at present, the route of choice for the production of pristine graphene flakes on an insulating support, a route credited to Geim and Novoselov,[3] who noted that peeling away layers from a highly ordered pyrolytic graphite (HOPG) surface and rubbing them onto Si/SiO_2 substrates resulted in transferred graphene (Figure 1.2(a)). Samples produced in this way are of very high quality (low defect density), making them suitable for fundamental studies of the material, but this simple scotch-tape approach typically produces micron-sized flakes of various thicknesses that are scattered across the substrate. This is an unrealistic format when one considers the potential graphene demand for future applications.[23] Furthermore, the painstaking task of searching for transferred graphene flakes is far from ideal.[24] Recent attempts to improve the yields of exfoliation techniques have been reported, with Si pillars employed to effectively stamp graphene flakes,[25] and applied voltages shown to encourage exfoliation from bulk crystals.[26] The intercalation of solvent molecules into graphite layers has also been shown to promote exfoliation,[27-29] as have thermal methods[30] and sonication techniques,[31,32] but with small monolayer fragments the primary product, additional steps such as spray coating and drop casting are necessary for the formation of a continuous sheet.

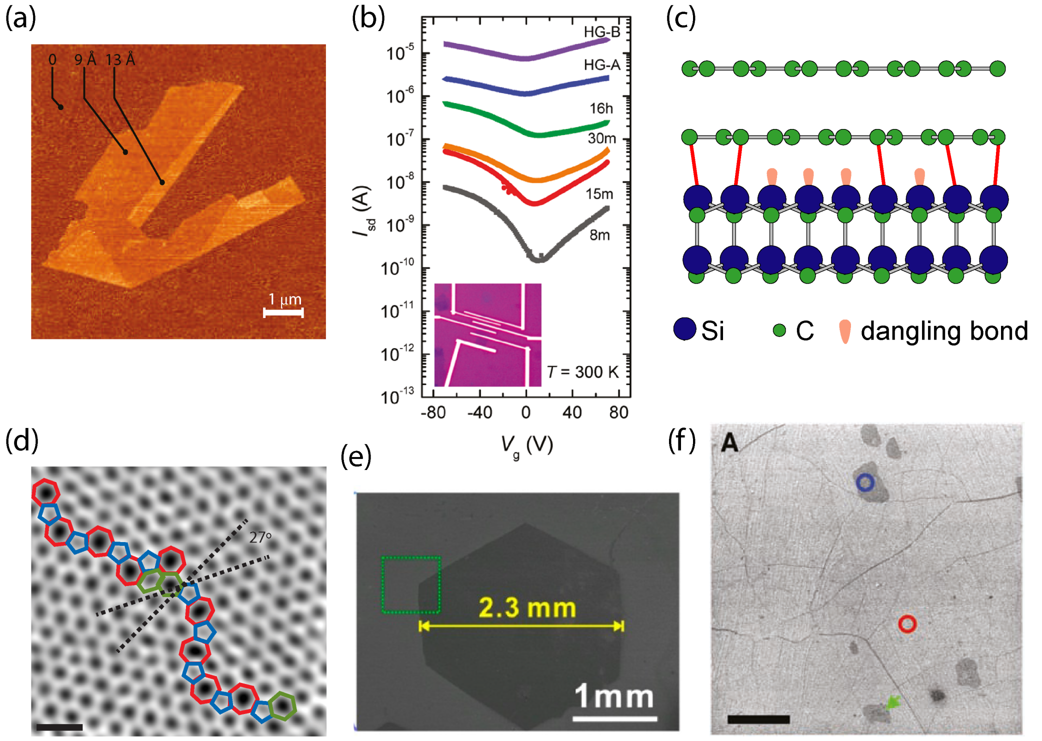

Figure 1.2 (a) AFM image of a predominantly single-layer exfoliated graphene flake on an Si/SiO$_2$ substrate, and measuring only a few micrometers in size.[33] (b) Electronic gating measurements on a GO flake with increasing degrees of reduction treatment, showing it to become more conductive with time. The inset shows an optical image of the device measured.[34] (c) Side-view illustration of monolayer epitaxial graphene on SiC (0001), separated from the bulk substrate by a covalently bound carbon layer.[35] (d) Atomic-resolution TEM image of CVD graphene showing a grain boundary consisting of pentagons (blue), heptagons (red) and distorted hexagons (green).[36] (e) SEM image of an as produced, single-crystal monolayer graphene domain on Cu, measuring 2.3 mm in diameter.[37] (f) SEM image of single-layer CVD graphene grown on a polycrystalline Cu foil and transferred to an Si/SiO$_2$ substrate.[38]

The production of graphene-like films via chemical means has a significant literature base and is an industrially attractive route, offering low costs and the potential for high throughput solution processing.[39,40] The most common methodology is through the production of graphite oxide – graphite that has been subjected to harsh oxidative chemical treatments, such as the Hummers[41] or Brodie[42] methods, producing a material of layered hydrophilic graphene oxide (GO) sheets.[43] Stirring or sonication in polar media produces exfoliated GO sheets dispersed in solution (dispersion further promoted by the action of intercalated water molecules),[44,45] which when coated on a surface can be subsequently reduced via chemical (e.g. hydrazine,[46,47] $NaBH_4$[48]) or physical (e.g. electrochemical,[49] thermal[50]) means to provide reduced GO (rGO). Such reduction is often a necessity, as GO is completely insulating due to its disrupted sp^2 bonding network,[34,51] but whilst electrical conductivity can be somewhat restored through such reduction (Figure 1.2(b)), rGO still displays oxygen functionality and significant defect concentrations, preventing it from matching the electrical properties of pristine graphene.[47,52]

A further approach to graphene production is its direct growth, via both epitaxial and chemical vapor deposition (CVD) methods. The thermal treatment of SiC or SiC coated surfaces[35,53] results in graphitization of the uppermost layer (through enhanced sublimation of Si), yielding wafer-scale graphene[54] on a semi-conducting substrate. Not only is this directly compatible with current industrial technology, Riedl *et al.* demonstrated precise *in-situ* monitoring of the number of graphene layers present during growth, further enhancing the attractiveness of this route.[55] Unfortunately, a covalently bound carbon interface layer that mediates the growth process and resides between the bulk SiC substrate and produced graphene (Figure 1.2(c)), results in intrinsically n-doped graphene, so long as it remains on the SiC surface.[35] Very recently, epitaxial growth on hexagonal boron nitride (h-BN) substrates has also been reported.[56] h-BN has also received significant attention in the graphene community recently due to its near identical lattice to graphene (lattice constant difference of only 2 %)[57] and lack of charged impurities when compared to Si/SiO_2, impurities that often introduce unwanted doping effects in supported graphene.[58]

Finally, CVD methods using catalytic substrates have emerged as a convenient route to obtain large, high-quality graphene sheets. Despite films often being labeled as continuous, the growth mechanism generally results in polycrystalline graphene, forming a patchwork-like structure of single graphene crystals, highlighted by Huang *et al.* and Tsen *et al.* who imaged crystals sewn together by 5 and 7 membered carbon rings (Figure 1.2(d))[36] and overlapped bilayer regions.[59] As recently reviewed by Tour *et al.*,[60] growth on single crystal structures alleviates this problem (Figure 1.2(e)),[37,61,62] but this may not be realistic in large-scale applications. Initial CVD studies used polycrystalline Ni surfaces as growth substrates,[63-65] producing graphene with a predominantly multilayer structure due to the dissolution-precipitation mechanism that operates at this surface. The subsequent use of Cu substrates by Ruoff *et al.* demonstrated the ability to produce predominantly single layer (SLG) graphene on the cm^2 scale (Figure 1.2(f))[38] owing to a self-limiting growth mechanism,[66] sparking additional interest in the CVD route, which is now the method of choice for many researchers. Indeed, the production of graphene sheets 30-inches across using Cu substrates has since been reported,[67] as has CVD growth on Pd[68] and Ru[69] surfaces.

A significant downside of the CVD growth process is that the resulting graphene resides on a conducting metal substrate, with only a few reported exceptions that demonstrate catalyzed growth directly onto Si/SiO_2.[70,71] The subsequent transfer of such films from their growth material to a substrate of interest (typically insulating) is thus necessary – far from easy given graphene's atomically thin nature. Polymer supported transfer routes have been developed by many groups, with polymethylmethracrylate (PMMA),[72,73] polydimethylsiloxane (PDMS)[63] and polycarbonate[74] layers (amongst others) all reported as suitable supports for graphene transfer to a range of substrates. Such layers act to hold the graphene layer steady whilst the underlying growth metal is etched away, providing a sturdy backbone for subsequent transfer to another surface before final dissolution of the polymer layer. However, even with widespread use and development of this method, strong polymer-graphene interactions[75] often result in transferred graphene surfaces being littered with stubborn polymer residue,[76] despite claims to the contrary,[72] detrimentally effecting graphene's intrinsic properties.[77,78] Recent reports of polymer-free graphene transfer may hold the key to this problem,[79,80] where the need for polymer supports was negated through the use of etchant solutions with low surface tension, which act to stabilize the graphene at the solution surface post-etch, rather than destroying it, as is observed in pure aqueous systems.

1.1.1.3 Characterization

Graphene has been studied through a range of modern characterization techniques and its signature responses are relatively well understood. Such characterization is a necessity for researchers in the field, who rely on numerous techniques as analytical tools to understand their system/sample, often employing them to confirm the existence of SLG.

Scanning tunneling microscopy (STM) allowed graphene's lattice to be studied (Figure 1.3(a)),[81] also making visible defects in its hexagonal structure, although the small scan sizes and need for an electrical contact to the sample somewhat limit the applicability of the technique on a larger scale, at least for exclusively topographical imaging. Scanning tunneling spectroscopy (STS) has also been employed to study graphene's electronic structure.[82]

Atomic force microscopy (AFM) characterization has been extensively reported in the literature, predominantly as a diagnostic tool to measure graphene flake thickness and size, although measurement artifacts complicate this approach. SLG should stand only 3.5 Å proud from a substrate, meaning effects that are usually of lesser importance in AFM begin to play a substantial role in distorting images (tapping amplitude set-point has a great effect, for example[83]). Indeed, SLG has been measured at various thicknesses, with Novoselov *et al.* reporting 1 – 1.6 nm[3] and Gupta *et al.* measuring 0.7 nm,[84] these differences most likely a result of differing tip interactions between the graphene and its substrate (Si/SiO_2) with adsorbed water molecules. Step measurements at folded regions on the graphene are thus considered to be the most accurate measurement route (Figure 1.3(b)),[10] often showing heights close to those expected, although the presence of such regions is of course down to luck, and is often unwanted.

Optical microscopy offers a surprisingly powerful route to graphene characterization, where even SLG flakes on an Si/SiO_2 substrate provide sufficient optical contrast to be seen by eye.[24] The contrast is heavily dependent on the oxide thickness (typically 300 nm in literature),[85-87] with 5 % thickness deviation having a significant effect[33] and a 200 nm oxide completely removing such contrast for flakes < 10 layers.[24] The use of green light further enhances this contrast (Figure 1.3(c)), and this has indeed been exploited to determine layer thickness.[88]

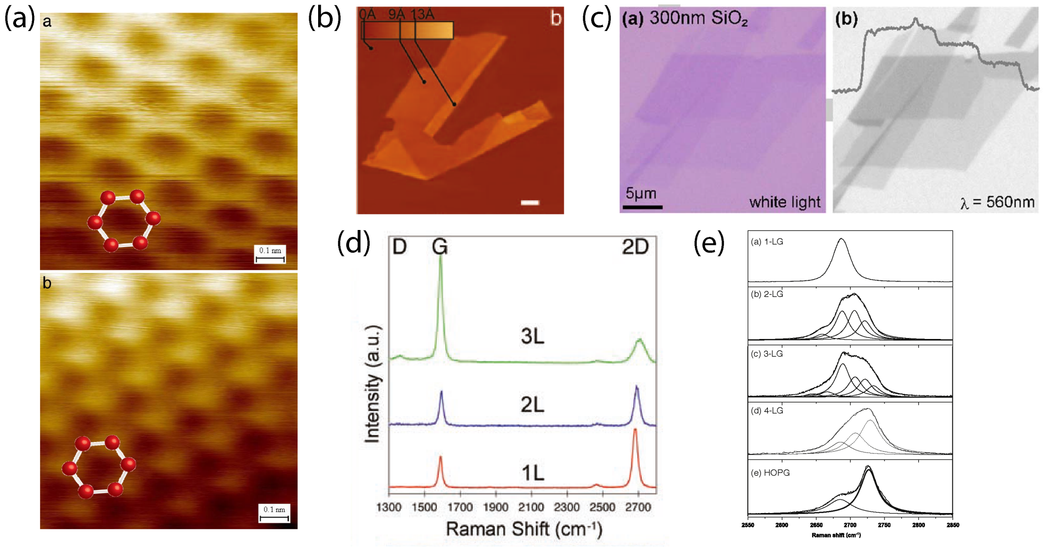

Figure 1.3 (a) STM topographic images of SLG (top) displaying the classic honeycomb structure, and multilayer graphene (bottom) showing the characteristic 'three-for-six' pattern as a result of electronic influences from underlying layers.[81] (b) AFM topography image of predominantly SLG, measuring 9 Å in height, and a folded bilayer region measuring 13 Å in height. The 4 Å difference matches that expected for a SLG step.[10] (c) Graphene crystallites on 300 nm SiO_2 imaged with white light (left) and green light of 510 nm wavelength (right), allowing for the clear distinction of layer thicknesses.[24] (d) Characteristic Raman spectra of mono-, bi- and tri-layer graphene.[38] (e) Raman spectra showing the 2D-band evolution with number of graphene layers.[89]

By far, the most integral graphene characterization technique is Raman spectroscopy,[89-92] thanks to its fast, high-resolution and non-destructive nature. The Raman spectrum of graphene displays distinct bands, namely the G (graphite), D (disorder) and 2D (or G') bands (Figure 1.3(d)), analogous to those observed for other sp^2 materials, such HOPG and CNTs. The only first-order Raman scattering process is the G-band, located at 1582 cm^{-1}, a result of in-plane vibrations from the sp^2 structure of graphene. Both the D (1350 cm^{-1}) and 2D (~ 2700 cm^{-1}) bands are second-order processes, the former being a result of disorder within the sp^2 lattice (i.e. the present of sp^3 carbon centers), and is thus not present in completely defect-free sp^2 materials, unless the edges are probed.

The ratio of the intensities of the D and G bands (I_D and I_G, respectively) thus informs of the level of defectiveness of an sp^2 material, and is commonly termed the degree of graphitization (I_D/I_G). The D and 2D bands also show dispersive behavior, with peak positions depending on the laser excitation wavelength used, shifting ~ 50 cm^{-1} and 100 cm^{-1} per eV, respectively.[89] A combined Raman/transmission electron microscopy (TEM) study by Ferrari *et al.*[90] investigated the dependence of the G- and 2D-bands with respect to the number of graphene layers, showing the 2D-band intensity and width to be strongly dependent upon thickness (Figure 1.3(e)), at least for the case of AB Bernal stacking between layers. For SLG, the 2D peak was shown to be a sharp single Lorentzian peak, roughly 4 times the height of the G peak, with a full-width-at-half-maximum (FWHM) of 24 cm^{-1}. For an increasing number of graphene layers, the 2D-band became upshifted and broader (Figure 1.3(e)), splitting into four components (each with FWHM of 24 cm^{-1}) in bilayer graphene (BLG), up to a point at which it differs little from that of bulk graphite (~ 5 layers).

1.1.1.4 Electronic Properties

In graphene, the π and π^* states, forming the valence and conduction bands respectively, generate a somewhat unique bandstructure, first predicted by Wallace in 1947.[93] These bands touch at six points, the so-called Dirac points, E_{Dirac}, and if one limits analysis to low energies, these bands have a linear dispersion and a bandstructure that can be viewed as two cones (Figure 1.4(a)).[94] Indeed, the fact that these bands touch at all means that graphene has zero band-gap, being labeled a zero-gap semiconductor or a semimetal as a result. This bandstructure leads to graphene displaying exceptional electronic transport properties in comparison to common semiconductors, exhibiting characteristics such as the ambipolar field effect[3] and phenomenally high charge carrier mobilities.[95] In a field-effect transistor (FET) configuration, carriers can be tuned between electrons and holes through the applied gate voltage (Figure 1.4(b)), with carrier densities of 10^{13} cm^{-2} induced through such gating, and ballistic transport exhibited over short distances, as is the case with metallic CNTs.[96] Carrier mobilities of 10,000 cm^2 V^{-1} s^{-1} and 15,000 cm^2 V^{-1} s^{-1} have been measured for exfoliated[3] and CVD graphene[97] samples on Si/SiO_2 respectively, but by removing substrate effects (e.g. charged impurities causing elastic scattering), suspended graphene has demonstrated mobility values of 200,000 cm^2 V^{-1} s^{-1}.[95] To add perspective, charge carriers in Si have values ~ 1400 cm^2 V^{-1} s^{-1}.

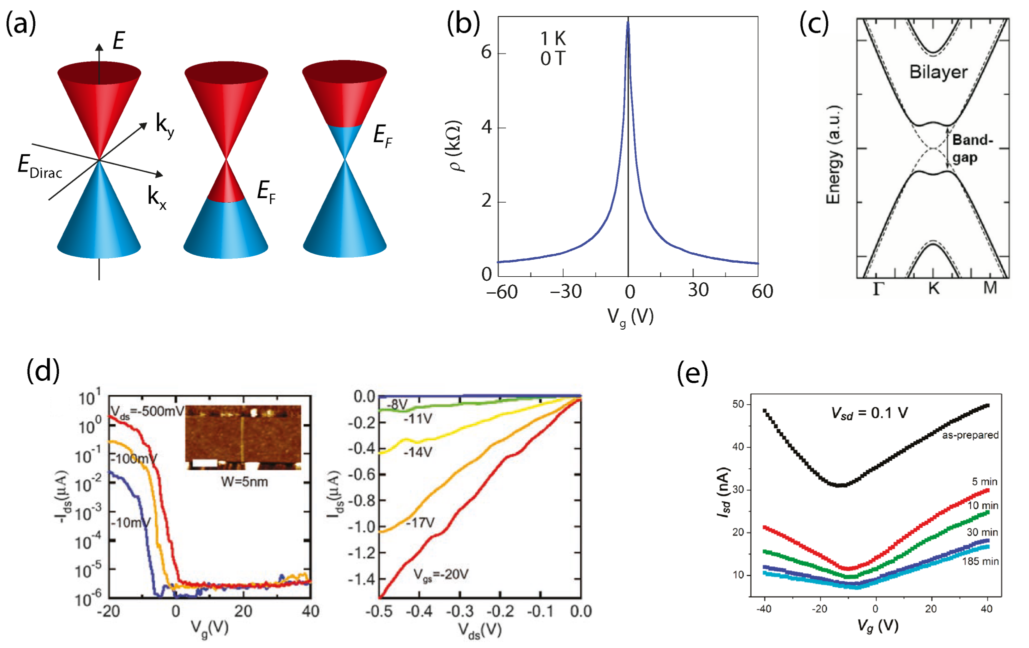

Figure 1.4 (a) Illustration of graphene's low-energy bandstructure of two cones touching at the Dirac point, E_{Dirac} (left). Adjusting the position of the Fermi energy (E_f) by applying a gate voltage in a FET arrangement determines the nature of graphene doping and the transport carrier, with p-doping (center) and n-doping (right) illustrated. (b) The ambipolar electric field effect in SLG, indicating changes in the position of the Fermi energy, E_f, with changing gate voltage (V_g), as schematically represented in (a).[33] (c) Schematic representation of the bandstructure changes in BLG induced by an applied perpendicular electric field. The dotted line represents the structure in the absence of a field, while the solid line shows it in the presence of a strong electric field.[94] (d) Transfer characteristics for a 1.5 nm wide GNR at various V_{sd} values. Inset shows an AFM image of the measured device, with a scale bar denoting 100 nm. (e) I_{sd}-V_g curves recorded at V_{sd} = 0.1 V for SLG FET devices after several consecutive diazonium grafting experiments, with the captions showing the total grafting time.[98]

Such impressive numbers mean graphene is a superb candidate for applications in high-speed electronics, however its aforementioned lack of an electronic band-gap makes direct incorporation into modern digital circuitry pointless.[94] Experimental graphene FETs often display ON / OFF ratios < 10,[99] and with conventional semiconductors and semiconducting (SC) nanotubes showing gate switching ratios of 10^4 – 10^7,[94] this is an enormous difference. The lack of a band-gap has not hampered graphene's use in analogue circuitry however, where it has also shown promise.[100]

Bernal stacked BLG displays an electronic structure that is somewhat different to that of SLG, instead consisting of two almost parallel conduction bands above two almost parallel valence bands (hyperbolic, not linear), the lowest and highest of which touch, respectively, again leading to zero band-gap (Figure 1.4(c)).[101] Interestingly, the application of a strong electric field perpendicular to the BLG plane induces asymmetry, resulting in the formation of a band-gap.[102,103] Significant gap opening has been further demonstrated through a dual-gating approach.[99,104]

The production of thin graphene strips, so-called graphene nanoribbons (GNRs) reduces the dimensionality of graphene to 1D. This also results in the strip having a band-gap, the size of which is inversely proportional to its width,[105] as proven experimentally through FET measurements (Figure 1.4(d)). However, the generation of a substantial band-gap (≥ 0.5 eV) requires the GNR to be 2 - 3 nm in width,[94] ruling out established lithographic methods[106,107] as a realistic option for production. CNT unzipping[108] and ribbon edge etching[109] have been demonstrated as routes to GNR formation. However, whilst ribbons 2 – 3 nm in width can be produced, the physical state of their edges is by no means pristine, having a significant effect at such small length scales.[110] Lastly, chemical modification methods have been shown to be a route to band-gap generation. The reaction of graphene's sp^2 lattice with hydrogen to produce graphane,[111] for example, has been demonstrated as a suitable method,[112] as has the reaction of graphene with oxygen,[113] fluorine[114] and diazonium compounds (Figure 1.4(e)).[115-118] As with GNRs, the size of the gap can be tuned simply by controlling the extent of the sp^2 to sp^3 rehybridization process, and with band-gap values up to 4.66 eV (i.e. completely insulating at ambient conditions) predicted for the hydrogenation route alone,[112] the attractiveness of this chemical route becomes obvious.

1.1.2 CNTs and Fullerenes

Whilst not studied directly in this thesis, a brief description of these materials is given for completeness. In its simplest form, a CNT can be considered as a rolled graphene sheet, forming a 1D cylinder with a diameter as small as 7 Å and a length on the micron scale,[119] although centimeter and longer lengths are possible.[120] The electronic properties of CNTs are determined by the manner in which the starting graphene sheet is rolled, with the curvature of the CNT disrupting the symmetry of the sheet, resulting in either metallic or SC properties, a crucial difference to their 2D counterpart.[121] Also synthesized through CVD techniques,[122] CNTs attracted vast amounts of attention from the research community in the 1990s and 2000s but have since been somewhat overshadowed by the rise of graphene.[6] Nevertheless, they are still considered a material with significant promise, and are already utilized in applications ranging from medicine[123] to transistors.[124]

Fullerenes are highly-strained graphitic spheres, with the most common, C_{60}, containing 20 hexagons and 12 pentagons, in contrast to a purely hexagonal graphene sheet.[125] Their ability to act as a superconductor when combined with alkali metals attracted significant attention upon discovery,[126] whilst their formation of a stable hexaanion in cyclic voltammetry (CV) measurements is somewhat unique.[127] Typically, low solubility has meant that surface derivitization reactions are somewhat common practice for fullerene applications, and has led to their use in solar cells for example.[128]

1.1.3 Graphite

Taking a lamellar like structure of stacked graphene sheets in an ABAB fashion, with interlayer spacing of 3.35 Å, graphite is graphene's 3D analogue.[4] As is the case with graphene, π orbitals make graphite conductive both parallel (*a*-axis) and perpendicular (*c*-axis) to its layers. HOPG, the most ordered form of graphite, demonstrates substantially higher conductivity within the layers, with values of 25,000 S cm^{-1} and 11 S cm^{-1} measured for the *a*-axis and *c*-axis respectively.[129,130] A small (~ 0.04 eV) overlap of the valence and conduction bands also makes HOPG a semi-metal.[131,132] Whilst strong (i.e. covalent) forces exist between atoms within a graphitic plane, individual planes are held together only by van der Waals attraction, allowing for layers to be removed by cleaving (often with scotch tape or using a razor blade) to reveal a pristine surface. HOPG is a focus of the work contained herein, and further discussion of graphite is thus centralized around this highly ordered variant.

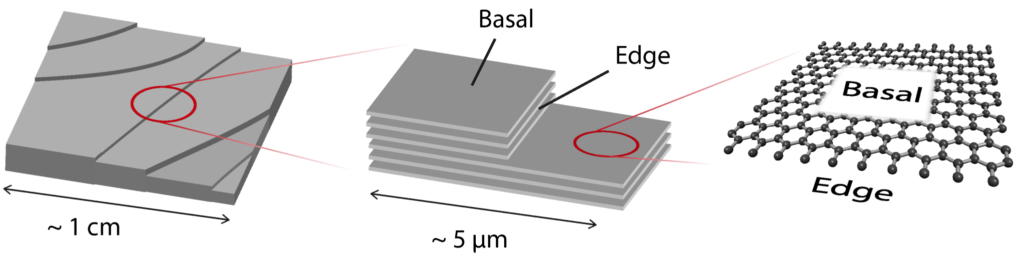

Figure 1.5 An illustration of the structure of HOPG, from macroscale (cm) to nanoscale (nm).

An HOPG surface displays a certain level of heterogeneity (Figure 1.5), consisting predominantly of basal areas of pure sp^2 carbon, completely unreactive to air unless at elevated temperatures,[4] and often atomically smooth over a scale of a few microns.[133] Intersecting step edges, the height and frequency of which depend heavily upon the quality of the HOPG material (*vide* *infra*) quickly react with oxygen and water under ambient conditions, forming various oxygen-containing functional groups along such edges as a result.[4,134]

As a material, HOPG has received much attention in the literature, not least due to its role in isolating graphene.[3] Its atomically flat nature makes it an ideal substrate for studying self-assembly processes using STM,[135-137] but another significant role is as an electrode material. Intense interest in this area has been driven primarily by a desire to understand electrochemical processes at CNTs and graphene,[138] which have attracted huge amounts of interest in electrochemically-related applications.[18,139-142] HOPG often serves as a model substrate for these materials,[143,144] due to its similar structural motif. Furthermore, it often provides a platform to study a range of fundamental processes, from (electro)catalysis[145] to metal nucleation,[146] and it has even been employed in the field of bio-sensing.[147]

1.1.3.1 HOPG as an Electrode Material

Despite its widespread use as an electrode material, and more importantly, as a model electrode, the electrochemical response of HOPG is still under significant scrutiny,[148] stemming primarily from its aforementioned surface heterogeneity. Work in the 1980s and early 1990s by McCreery *et al.* suggested that the overwhelming majority of electron transfer (ET) at graphite electrodes originates at step edge sites. They mainly studied the $Fe(CN)_6^{3-/4-}$ redox couple, typically measuring potential separations between the oxidation and reduction peaks (ΔE_p) of ~ 1 V, far from the 59 mV associated with reversible systems (see section 1.2.1). Laser damage to the same surfaces generated defect sites (i.e. exposed step areas) on the basal surface and subsequently yielded ΔE_p values close to reversible. They thus concluded that ET occured at such defected sites.[149,150] Subsequent studies used the $Fe(CN)_6^{3-/4-}$ redox couple as a 'validation method' to determine sample quality, with samples labeled as 'high-quality' (i.e. predominantly basal plane) if they showed ΔE_p values typically > 700 mV. Such validated samples were then exposed to a variety of other redox couples, and again demonstrated sluggish ET transfer behavior.[151,152] More recent work by Compton *et al.*[153,154] again showed sluggish behavior for the $Fe(CN)_6^{3-/4-}$ redox couple. However, only a single CV was presented and an attempt to fit the response to a model that assumed only step-edge areas to be active proved unsuccessful for the experimentally determined step density. Moreover, Compton worked with a rather defective grade of HOPG that should have shown quite fast kinetics under the McCreery model described above. Despite this, it was still concluded that basal areas are essentially inert to ET.

Results in complete contradiction to those above were published by Patel *et al.*, who not only showed completely reversible behavior for the $Fe(CN)_6^{3-/4-}$ redox couple across a range of HOPG surfaces of different quality,[148] but also showed the redox couple to gradually block the surface through complementary AFM measurements, offering up a potential explanation for the differences with previous literature. Indeed, the same group have since come to similar conclusions using other, more complex redox mediators.[133,147]

Recent advances in micro and nanoscale measurements have also allowed electrochemical measurements to be made on completely isolated basal areas of HOPG, ensuring the measured response originates only from such areas, rather than being a convolution of basal/step edge areas as is the case for macroscale experiments. Lai *et al*. used the recently developed scanning electrochemical cell microscopy (SECCM) technqiue[155,156] to perform highly localized electrochemical measurements on both basal and step edge sites of HOPG, with no significant differences in activity observed.[157] By covalently linking a redox mediator to the end of an AFM tip, Demaille *et al.* were able to obtain corresponding topography and electrochemical activity maps of an HOPG surface, concluding basal terraces showed significant activity towards ET,[158] whilst Frederix *et al.* obtained similar results by including an ultra-micro electrode (UME) within an AFM tip,[159] allowing localized measurements to be made. Some approaches also revealed apparent degradation of the surface activity with time, providing another possible explanation for results obtained at the macroscale.[157,159]

Quinone compounds have been shown to spontaneously adsorb at carbon surfaces, and those that also contain redox functionality have provided yet another route to study electrochemical activity. McCreery *et al.* proposed a correlation between step edge density and level of anthraquinone-2,6-disulphonate (AQDS) at HOPG surfaces, showing increased levels of adsorption (determined through voltammetry) at surfaces with increased step densities.

Such debate has now carried to CNTs, where a structural analogy is made between their sidewalls and basal areas of HOPG, and between CNT defects and HOPG step edges. Gooding *et al.* showed that shortened and open-ended vertically aligned CNTs displayed faster ET for $Fe(CN)_6^{3-/4-}$ (ΔE_p = 59 mV) vs. Au electrodes modified with randomly oriented CNTs of the same quality (ΔE_p = 99 mV), prompting the conclusion that such activity arose from the defected CNT ends.[160] Wildgoose *et al.* intentionally introduced defects into CNTs through acid-treatment, and showed that ET became slower after such defects were subsequently removed through annealing methods.[161] The ability of such annealing to remove defects is, however, debatable.

Localized SECCM studies of pristine CVD grown CNTs by Güell *et al.* have again shown their sidewalls to be fully active,[162-164] as have studies by Dekker *et al.*[165] and Amemiya *et al.*,[166] who also made electrochemical measurements confined to pristine sidewalls, ruling out significant influences from CNT defects/ends. Similar arguments have been applied to graphene electrodes.[88,143,167-169]

1.2 Electrochemistry

1.2.1 Dynamic Electrochemistry

Dynamic electrochemistry refers to the study of electrochemical processes and reactions in which the electrochemical system is perturbed in some way, often through the application of a potential, E, at a working electrode surface (with respect to a well-defined reference), whilst the resulting charge transfer at said electrode is monitored as a current, i. Measured currents originate from both faradaic (i_f) and non-faradaic (i_c) processes, with the former being charge passed across the electrode/electrolyte interface as a result of an electrochemical reaction, and latter associated with capacitive processes at the electrode surface, often termed as background currents. Numerous factors can influence the dynamics of the resulting faradaic charge transfer process, with the applied potential, the species under investigation, the state of the electrode surface (and any heterogeneities thereon), and mass-transport/adsorption being a few examples.[170] Figure 1.6 summarizes the general steps that take place during an electrochemical reaction.

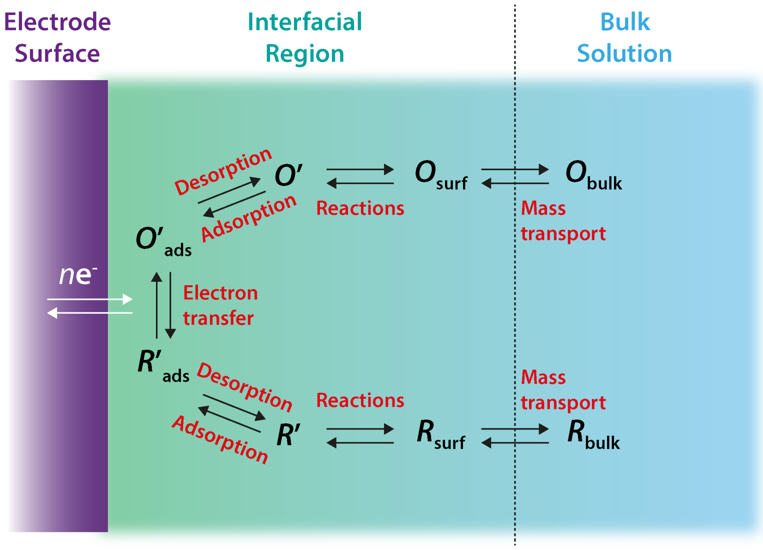
Electrode Surface
Interfacial Region
Bulk Solution
Desorption
Adsorption
O′
O′ads
Reactions
Osurf
Obulk
Mass transport
ne-
Electron transfer
R′ads
Desorption
Adsorption
R′
Reactions
Rsurf
Mass transport
Rbulk

Figure 1.6 Schematic illustration of the possible steps in a typical dynamic electrochemistry process. Steps such as adsorption/desorption and reactions in solution are limited to certain cases, and do not occur in typical redox systems.

Here, an oxidized species in solution, O, undergoes mass transport from bulk solution to the electrode surface, where it undergoes ET to form the corresponding reduced species, R, summarized by eq. 1.1

$$O + n\,e^{-} \rightleftharpoons R \tag{1.1}$$

Additional chemical reactions may also take place in solution, as may adsorption/desorption of species onto the electrode surface, although such steps are not always present. The rate of these steps determines the generated current at the electrode surface.

For a system at equilibrium, the concentration of O and R at the electrode surface can be related to the potential applied by the Nernst equation, eq. 1.2

$$E = E^{0\prime} + \frac{RT}{nF} \ln\left(\frac{[O]}{[R]}\right) \tag{1.2}$$

where E is the electrode potential, $E^{0'}$ is the formal electrode potential, R is the molar gas constant (8.314 J K^{-1} mol^{-1}), T is the temperature, n is the number of electrons transferred per redox event, F is the Faraday constant (96485 C mol^{-1}) and $[O]$ and $[R]$ are the concentrations of the oxidized and reduced forms of the redox mediator, respectively. For instances where the standard ET rate constant, k_0, is very large, and the mass transport rate (k_t) is thus the limiting step of the reaction, it is reasonable to assume Nernstian behavior at the electrode surface.

For systems that are not limited by mass transport, the kinetics of the ET step must be considered, with a relationship developed by Butler and Volmer widely used in this case,[170] described in eqs. 1.3 – 1.5

$$O + n\, e^- \underset{k_\mathrm{b}}{\overset{k_\mathrm{f}}{\rightleftharpoons}} R \tag{1.3}$$

$$k_\mathrm{f} = k_0 \exp\left(-\propto \frac{nF(E - E^{0\prime})}{RT}\right) \tag{1.4}$$

$$k_\mathrm{b} = k_0 \exp\left((1{-}\propto)\frac{nF(E - E^{0\prime})}{RT}\right) \tag{1.5}$$

where k_f and k_b are the forward and backward rate constants for the redox reaction, α is the charge transfer coefficient (typically taking a value of 0.5), and all other symbols take their usual/predefined meaning.

Three distinct processes, namely convection, diffusion, and migration, govern the mass transport rate of a species to an electrode surface.

Convection in a system is often driven by thermal gradients or agitation (e.g. stirring). Influences of convection are negligible for the majority of electrochemical experiments, as long as the setup is in an area of stable temperature and unnecessary movement of the system is avoided. Systems such as the rotating disc electrode make use of such convection to dramatically increase mass transport to the electrode surface.[171]

Diffusion is the natural movement of species in solution due to a concentration gradient, typically occurring as a result of the production or depletion of a species at a surface. Diffusion will always operate in electrochemical systems when the electrode potential is set such that a reaction is occurring, perturbing concentrations of species at the interface.

Finally, migration is the movement of charged species in solution as a result of an applied electric field, resulting in electrostatic attraction or repulsion of the species (ions) at the electrode/electrolyte interface. This is typically suppressed in electrochemical systems, where the presence of an inert supporting electrolyte in excess concentration of any charged analyte minimizes such effects.[172] This electrolyte also serves to significantly reduce the solution resistance, hence reducing ohmic drop (iR) effects.[173] In certain systems (e.g. SECCM) the effects of migration cannot be completely disregarded, requiring modeling to understand its contribution.[155]

1.2.1.1 Potential Sweeping Techniques

Potential sweeping techniques are often the method of choice in dynamic electrochemistry measurements, especially in preliminary experiments. A typical potential-time waveform applied to the working electrode in such sweep measurements is shown in Figure 1.7(a). Linear sweep voltammetry (LSV) involves the sweeping the potential, E, between E_1 and E_2 at a known, constant scan rate (ν) whilst the cell current, i, is measured as a function of potential (time). CV is a more widely used technique where upon reaching E_2 the potential sweep is reversed (typically at the same scan rate) to E_1, at which point the measurement is terminated or further cycling is initiated. The observed current response is governed by a number of factors, including electrode size/geometry, scan rate and the redox system under investigation.

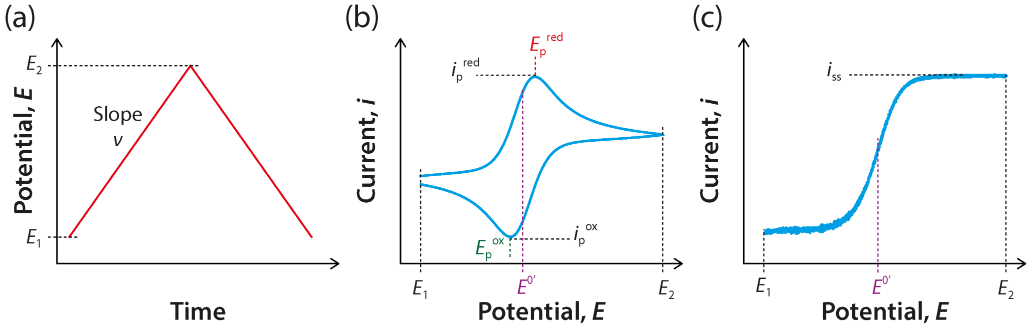

Figure 1.7 (a) The potential waveform applied during a traditional CV measurement, and typical resulting current responses for a reversible redox process at a macroelectrode (b), and at a UME (c).

Consider a simple reversible reaction of the type described by eq. 1.3 at an electrode large enough to display a linear diffusion profile. Starting at a potential, E_1, where no faradaic process occurs, the potential is swept towards E_2, resulting in reduction of O when the potential nears $E^{0'}$. Assuming the rate of electron transfer is rapid at the surface, the concentrations of O and R immediately (and continuously) adjust to the ratio described by the Nernst equation (section 1.2.1). As the potential is swept further, the concentration of O at the surface progressively decreases, increasing the steepness of the concentration gradient, and hence the flux toward the surface and the current measured. However, as the potential moves past $E^{0'}$, the surface concentration of

O nears zero, with mass transfer of O to the surface thus reaching a maximum rate, before subsequently declining as depletion effects set in. Such processes give rise to a peak shaped current response, located at potential E_p^{red} and current i_p^{red} (Figure 1.7(b)). Reversing the potential sweep results in a similar peak shaped response (potential E_p^{ox} and current i_p^{ox}), but of opposite sign, based on similar arguments to those for the forward sweep. Such reversible systems display numerous characteristic qualities, including an i_p that scales linearly vs. $\nu^{1/2}$, i_p values for the reduction and oxidation waves are of equal magnitude but opposite sign, $\Delta E_p = 59$ / n mV, and E_p values are independent of ν. At UMEs, the rate of mass-transport is significantly higher (due to a substantial radial component) resulting in potential sweeps that can produce a steady-state current response, i_{ss}, independent of ν (Figure 1.7(c)), depending on the magnitude of ν compared to the characteristic diffusion time of the UME.

1.2.1.2 Irreversible Systems

In the case of an irreversible electrode reaction, the rate of electron transfer is insufficient to maintain the Nernstian equilibrium (i.e. $k_t > k_0$), resulting in a CV shape different to that in the reversible case. Here, the CV becomes more drawn out with decreasing k_0 values (at a particular ν). For CVs performed with low values of ν, the rate of electron transfer is greater than that of mass-transfer, resulting in reversible CV behavior. The peak to peak separation gradually becomes more drawn out with increasing ν.[174] Strictly speaking, such systems may be termed quasi-reversible.

Irreversible ET systems have very large peak to peak separations. The lack of a peak on the reverse sweep may further signify a following chemical reaction after the initial ET step.

1.2.1.3 Adsorbed Species

The electrochemical response for the general electrode reaction in eq. 1.3 can be affected significantly by the adsorption of either O or R at the electrode surface. Consider a simple case where only adsorbed O is electroactive, i.e. ν is so large that O in solution cannot diffuse significantly to the electrode, or the reduction wave for adsorbed O is significantly shifted from O in solution and can be studied independently. Since there are no longer mass-transport limitations, the observed response differs significantly from that shown in section 1.2.2, typically appearing as a sharp symmetrical peak with $E_\mathrm{p} = E^{0'}$, so long as O and R show the same strength of adsorption. i_p now appears proportional to ν (as is the case for capacitive currents),[170] and the wave upon scan reversal appears as a mirror image, reflected through the potential axis. For an ideal Nernstian reaction, $E_\mathrm{p}^\mathrm{red} = E_\mathrm{p}^\mathrm{ox}$ with each wave having a FWHM of 90.6 / n mV.[175] Furthermore, the area under each voltammetric peak corresponds to the charge, Q, associated with the reduction (or oxidation) of the adsorbed layer, allowing for its surface coverage to be determined according to eq. 1.6

$$\Gamma = \left|\frac{Q}{nF}\right| \tag{1.6}$$

where Γ is the surface coverage, and n and F take their predefined meanings.

1.3 Routes to Covalent Surface Modification

1.3.1 Aryl Diazonium Compounds

Aryl diazonium compounds have long been considered particularly attractive for surface modification, owing to their flexibility.[176] Indeed, they have not only proven suitable for the modification of carbon materials (glassy carbon (GC),[177] HOPG,[178] CNTs,[179] and diamond[180]), but also metals,[181] semi-conductors,[182] and more recently, graphene.[46,183] A generalized grafting reaction mechanism is summarized in Figure 1.8(a), where **A** represents the diazonium counter ion (typically Cl^- or BF_4^-) and **R** any one of a variety of aryl substituents (e.g. halides, carboxylic acid, nitro, redox mediator) reported in the literature.[184]

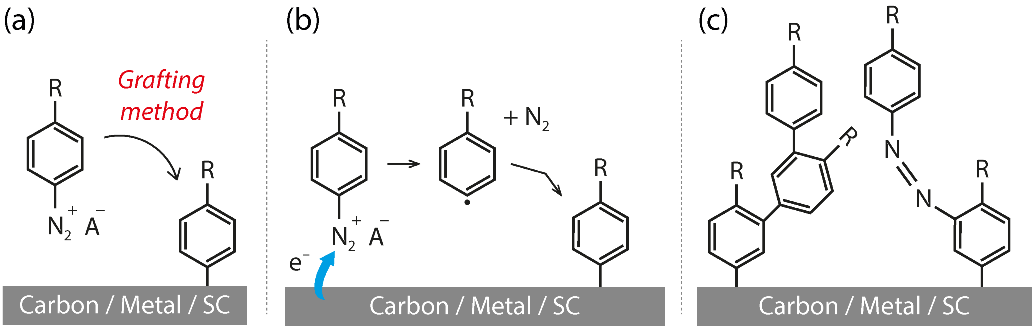

Figure 1.8 (a) The generalized diazonium grafting process, where A is the diazonium counter ion, and R represents a variety of possible functional groups. (b) The diazonium electrografting process. (c) Possible molecular arrangements in disordered multilayer aryl films.

Modification is performed in either aprotic (often acetonitrile) or acidic aqueous (diazonium salts are unstable at $pH > 3$)[185] media,[184] and can be driven by a number of grafting methods, including ultraviolet light,[186] ultra-sonication,[180] heating,[187] microwave radiation,[188] chemical reducing agents,[189] and even spontaneous reaction.[190] However, electrografting has arguably proven to be the most effective technique, whereby the potential of the surface to be grafted is adjusted in such a way that reduction of the diazonium species occurs at the surface, leading to the formation of an aryl radical (Ar$^\bullet$), which can, in turn, react with the surface (Figure 1.8(b)).[191] The electron-withdrawing nature of the diazonium functionality means that only mildly reducing potentials are required for this homolytic pathway to proceed (~ 0 V vs. saturated calomel reference electrode), avoiding the subsequent reduction of Ar$^\bullet$ to an aryl anion, often observed at more reducing potentials,[192] such as those required for the homolytic reduction of aryl halides.[193]

Diazonium electrografting at metal electrodes was first reported in 1980 by Parker *et al.*,[194] who observed a broad irreversible reduction wave during CV experiments in the presence of a diazonium salt. This wave quickly disappeared and was absent on subsequent CV cycles, leading to the conclusion that a deactivation mechanism occurred at the electrode surface. In 1992, Pinson and Savéant observed this same response in their pioneering work investigating diazonium compounds at carbon surfaces (GC and HOPG).[191] Such a response was determined to be as a result of Ar$^\bullet$ production and subsequent electrode grafting, causing blocking at the surface and preventing further diazonium reduction,[177] and this response is now considered a characteristic property of the diazonium electrografting process.

1.3.1.1 Structure of the Grafted Layer

The formation of a covalently bonded organic layer at grafted surfaces has been investigated through a broad range of techniques. X-ray photoelectron spectroscopy (XPS) at GC and HOPG electrodes by both Savéant *at al.*[177] and Bélanger *et al.*[195] showed the presence of NO_2 functionality at the surface post-electrografting with 4-nitrobenzenediazonium, and the lack of a detectable diazonium functional group suggested a C-C covalent linkage to the surface. Rutherford backscattering (RBS) has been employed to confirm the presence of larger atoms (Br and I) that were present in the starting diazonium compound structure at the R position.[182,196,197] Interestingly, the existence of covalent bonds has also been reported at metal surfaces.[197,198] Infrared spectroscopy has also shown the diazonium stretching vibration (~ 2300 cm^{-1}) present in isolated diazonium salts to disappear upon grafting,[176,180] in agreement with XPS data, again suggesting the presence of a covalent bond with the surface. STM imaging of electrografted HOPG surfaces by Liu *et al*. revealed the presence of a densely packed molecular surface layer, suggesting aryl groups oriented perpendicular to the surface,[199] and this was similarly observed at Si surfaces by Allongue *et al*.[200] Through Raman spectroscopy studies of basal/edge plane HOPG and GC diazonium electrografted surfaces, McCreery *et al*.[201,202] further confirmed the presence of a covalently bonded layer, using comparisons of the levels of sp^2 and sp^3 carbon prior to and post-modification. Finally, AFM studies, performed mainly by Downard *et al*. have allowed for the visual observation of surfaces after electrografting,[203,204] as well as layer depth profiling,[205] with images clearly showing the formation of a layer of variable height and roughness, both factors highly dependent on the grafting conditions.[206] Indeed, such variation in height highlights a distinctive feature of the diazonium grafting process: *the formation of multilayers*.

The surface concentration, Γ, of a closely packed monolayer of aryl (or *para*-substituted aryl) groups at a surface has been estimated as 1.35×10^{-9} mol cm^{-2},[176] and can be determined experimentally by numerous methods, including CV integration,[177] Raman spectroscopy,[177] and RBS.[177] Moreover, there is agreement amongst groups interested in diazonium modification that it is possible to tune the surface concentration of the grafted layer, through control of the extent of surface reaction, such as limiting the charge passed during electrografting (i.e. controlling electrolysis time and grafting potential).[176] At GC electrodes, Savéant *et al.* showed Γ to increase with electrolysis time (at 0.8 V more cathodic than E_p), limiting at $3 – 4 \times 10^{-9}$ mol cm^{-2} after 600 s,[177] not far from a closely-packed monolayer when one considers typical roughness factors of GC surfaces. Values of 1.8×10^{-9} mol cm^{-2} and 0.65×10^{-9} mol cm^{-2} were obtained by Bélanger[195] and McCreery[202] respectively, under similar grafting conditions. The basal plane of HOPG, a substrate known for minimal roughness has yielded values of $1.2 – 1.6 \times 10^{-9}$ mol cm^{-2},[177,202] again very close to that of a compact monolayer. Of course, it should be noted that such values could also correspond to layers thicker than a monolayer, each less compact than the theoretical maximum. Downard *et al.* compared Γ values measured through CV integration, with film thickness values determined by AFM for 4-nitrophenyl layers on atomically flat pyrolyzed carbon films.[203] A film with associated Γ value of 1.2×10^{-9} mol cm^{-2}, very close to that of a closely packed monolayer, actually had a thickness equivalent to roughly 4 aryl groups, giving the film a compactness of only 21 % with respect to a closely packed layer. Similar studies of 4-nitrophenyl at metal surfaces also demonstrated films to be 6 – 10 aryl layers in height.[197] The formation of aryl films of monolayer thickness has, however, been demonstrated at both carbon[205] and silicon surfaces,[200] as have layers over 1 μm thick,[207] all through careful control of the reaction conditions.

The structure of such multilayers is likely to be somewhat disordered, with multilayers formed through radical attack at already grafted aryl moieties, to form polymeric type structures. Podrovica *et al.* proposed such a mechanism based on a time-of-flight secondary ion mass spectroscopy study, in which they examined the structure of grafted poly-aryl films.[208] The use of sterically hindered diazonium compounds (bulky groups at the *ortho*- and *meta*- positions of the aryl ring) by Pinson *et al.* managed to halt such extended reactions, by preventing abstraction of the usually present hydrogen atom.[209] The presence of azo linkages (aryl-N=N-aryl) within grafted layers has also been proposed.[210,211] Such disordered multilayer structures are summarized in Figure 1.8(c).

1.3.1.2 The Site of Radical Attack

Whilst there is general acceptance that aryl radical attack at carbon surfaces results in a C-C covalent bond, the rate of such bond formation has been shown to vary with the structure of carbon materials. Indeed, the yield of the radical surface reaction is not unity, with a proportion of radicals generated being lost to reactions in solution.[177,212] In their original study, Pinson and Savéant analyzed electrografting CVs in acetonitrile, determining 84 % of 4-nitrophenyl radicals reacted at GC surfaces whilst the rest were lost to solution, but the same conditions at HOPG surfaces had an associated grafting efficiency of 56 %, leading them to conclude graphitic edge plane carbon (the major component of GC) reacts faster than basal plane.[177] A similar conclusion was drawn by McCreery *et al.*, who used spatially resolved Raman spectroscopy to determine the location and coverage of nitroazonbenzene moieties at GC and HOPG.[213] Even coverage was observed at GC electrodes, whereas HOPG showed modification to first occur at step edge sites, before subsequent attachment to the basal plane. Kariuki and McDermott used lateral force microscopy (LFM) to monitor 4-diethylaminophenyl radical attack at basal plane HOPG, tentatively suggesting that attachment only occurs at defect sites, leading to polyaryl chains on the surface, anchored only at these points (Figure 1.9(a)).[214] In contrast to these findings, STM has allowed for homogenous grafted HOPG surfaces to be visualized,[177] even with molecular resolution, revealing densely packed 4-nitrobenzene moieties at the basal plane (Figure 1.9(b)).[199] The reduction of an alkylferrocene derivative of benzene diazonium at HOPG also yielded densely packed modifiers on the surface, demonstrated by electrochemical-STM (Figure 1.9(c)).[215]

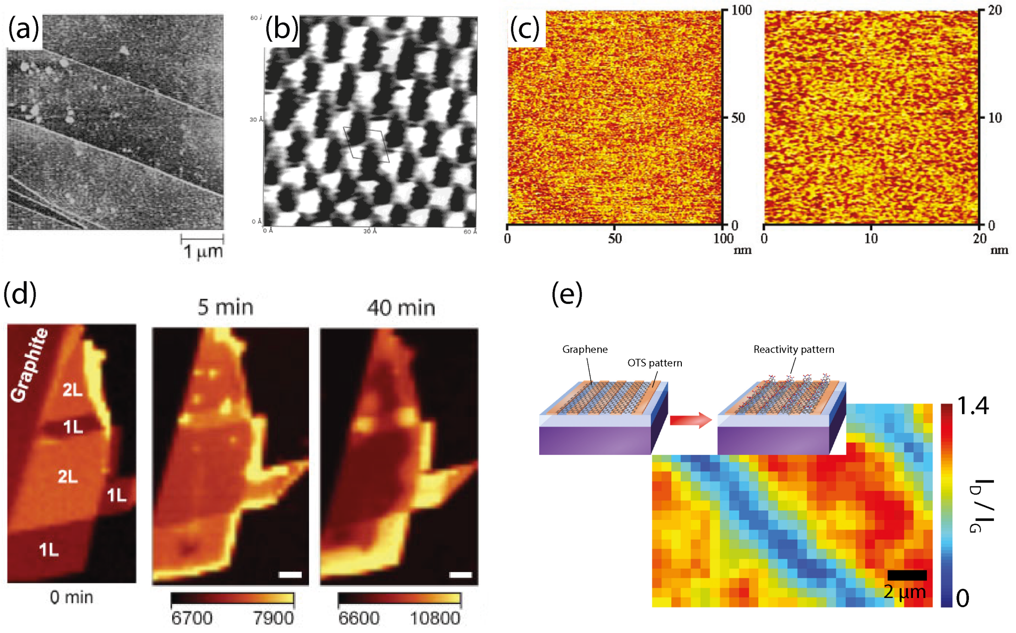

Figure 1.9 (a) Topographic *in-situ* LFM images of an HOPG surface following 5 cycles between -0.1 and -0.9 V vs. Ag/AgCl in the presence of 0.5 mM 4-diazo-N,N-diethylaniline fluoroborate.[214] (b) 6 × 6 nm STM image of an HOPG surface derivatized by the electrochemical reduction of 4-nitrobenzenediazonium salt.[199] (c) 20 × 20 nm electrochemical-STM image of an HOPG surface modified with a redox-active diazonium compound.[215] (d) Raman spectroscopy maps of a graphene flake, showing the area under the D peak changing with time upon exposure to a diazonium compound, with certain areas appearing to react faster.[190] (e) Raman spatial map of D-band/G-band intensity ratio after diazonium functionalization. Heavily modified stripes correspond to areas directly above Si/SiO_2, with less reacted areas separated from the substrate by a silane monolayer.[58]

Further insight into the rate of radical reaction may also be gained from studies of aryldiazonium reduction at graphene surfaces, where the diazonium reduction process has been thoroughly studied, as a consequence of its ability to generate an electronic band-gap within the intrinsic semi-metal.[116,216] Koehler *et al*. monitored the spontaneous aryl grafting process in water on areas of SLG and BLG with spatially resolved Raman spectroscopy (Figure 1.9(d)), revealing edge plane and SLG basal areas to react faster than bilayer by monitoring the intensity of the sp^3 induced D-band at the graphene surface.[190] They attributed such a difference to the ability of SLG to incorporate the rehybridization process (from sp^2 to sp^3) upon radical attack, with BLG unable to accommodate this so easily because of interactions with the underlying sheet. Such an argument was also used to explain why the edges displayed apparently higher reactivity. Strano *et al.* observed the same increased reactivity of SLG, using an explanation of charged impurities in the SiO_2 substrate resulting in localized electron and hole 'puddles', affecting the reactivity of SLG towards diazonium grafting, and further arguing that the underlying graphene layer in BLG screens such charges.[86] This justification has been further strengthened in a thorough study using graphene on different substrates (h-BN, Al_2O_3, etc.) where separation of the graphene from the SiO_2 substrate was achieved using a silane monolayer, resulting in significantly reduced reactivity (Figure 1.9(e)).[58]

1.3.2 Self-Assembled Monolayers (SAMs)

SAMs provide a somewhat more straightforward route to surface property tailoring. They can be readily applied to metals, metal oxides and SC materials,[217] again acting as an interface between a substrate and its surrounding environment, producing an interface with fully tunable physical and chemical characteristics. They have attracted attention in technological processes, including synthesis,[218] sensing[219] and cell-adhesion,[220] whist the invention of molecular electronics has seen SAMs employed to study the effects of insulating and conjugated bonds on the resulting molecular chain conductivity,[221,222] and the effect of surface bound redox species in electrochemical measurements.[223] Furthermore, the ability to pattern discrete areas of high-quality SAM on length scales from 10 nm to 10 cm has been demonstrated through techniques such a micro-contact printing,[224] energetic beam damage[225,226] and scanning probe microscopy,[227] providing further options for the use of SAMs.

1.3.2.1 SAM Structure and Organization

By far the most studied SAMs are those of *n*-alkanethiol molecules at noble and coinage metal surfaces,[228] with Au,[229,230] Ag,[231] Pd[232] and Hg[233] having received significant attention, owing to the high affinity of thiol compounds with these materials.[217] First reported in 1983 by Nuzzo and Allara,[234] *n*-alkanethiols at Au surfaces will be the focus of this section. Such SAMs are formed from either liquid or gas phase chemistry,[235] using molecules that typically consist of 3 constituent parts, shown in Figure 1.10(a).

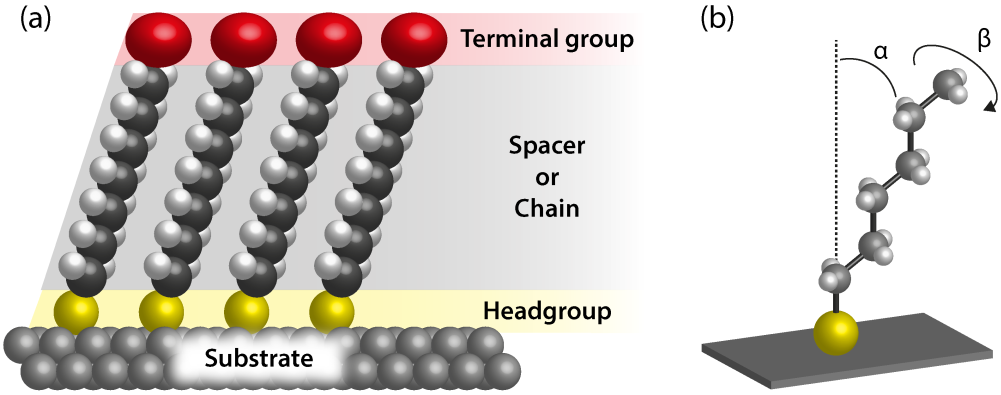

Figure 1.10 (a) Schematic illustration of typical adsorbed SAM molecules, showing their three constituent parts. (b) A single-chain model of an adsorbed SAM molecule, showing its orientation parameters.

With respect to a single molecule, the *headgroup* provides anchorage to the substrate surface, typically constituting of a moiety that has a high affinity for the surface in question (in this case a thiol group). The alkyl-chain *spacer* serves two purposes, not only offering a barrier between the surface and its environment, but also providing stability to the formed SAM through interactions between adjacent molecules (van der Waals attraction of ~ 1 – 2 kcal mol^{-1} per methylene unit).[236] Lastly, the *terminal group* determines the overall functionality that will be displayed at the resulting modified surface. For the case of *n*-alkanethiols at Au surfaces, the attachment of the thiol to the Au surface is believed to occur through an Au – S bonding mechanism, known to have a relatively high bond energy of ~ 48 kcal mol^{-1}. The presumed adsorption chemistry is shown in eq. 1.7, inferring an oxidative addition of the S - H bond to the Au surface.[237]

$$\mathrm{RS-H\ +Au_{(s)}\ \rightarrow\ RS-Au+\ 1/2\ H_2} \qquad (1.7)$$

Whist formed SAMs are often depicted as simple aligned molecules at a surface, their structure at a molecular level is far from random, with molecules adopting conformations that allow for high-levels of van der Waals interaction, thus minimizing the free energy of the organic layer.[238] A single-chain model (Figure 1.10(b)) is usually enough to describe the molecular orientation adopted by SAM molecules, highlighting the angle of molecule tilt from the surface normal, α, and the rotation angle about the long axis of the molecule, β. These parameters take values of $\alpha = 28°$ and $\beta = 53°$ for the case of *n*-alkanethiols at an Au (111) surface,[217,228] but can change dramatically for other cases, with $\alpha = 0°$ measured for *n*-alkanethiols on Hg for example,[217,233] where molecules stand perpendicular to the liquid metal surface.

1.3.2.2 SAM Formation

The most commonly employed procedure for SAM formation is a solution based route, whereby the substrate of interest is immersed in a dilute solution (typically 1 – 10 mM)[229] of the thiol precursor for a period of at least 12 hours. Despite the widespread use of this route, the solution environment can hamper mechanistic studies into the dynamics of the SAM formation process,[217] thus the most extensive studies of the formation process have taken place through vapor modification processes,[239] where distinct formation phases have been visualized.[240] Nonetheless, techniques such as electrochemistry[241] and the quartz-crystal microbalance (QCM)[242] have provided insight into the dynamics of the solution route, where it is accepted that SAM formation can be divided into two thermodynamically differing steps, the first being surface adsorption, followed by a surface rearrangement process.

The first step involves the movement of adsorbates from bulk solution to the surface by mass-transport, followed by a chemisorption process that leaves the molecules covalently bound to the surface (Figure 1.11(a-i)). The formation of a monolayer blocking the entire surface (Figure 1.11(a-ii)) is very quick, with coverage on the minute timescale often reported. Increased adsorbate concentrations can decrease this time yet further.[229]

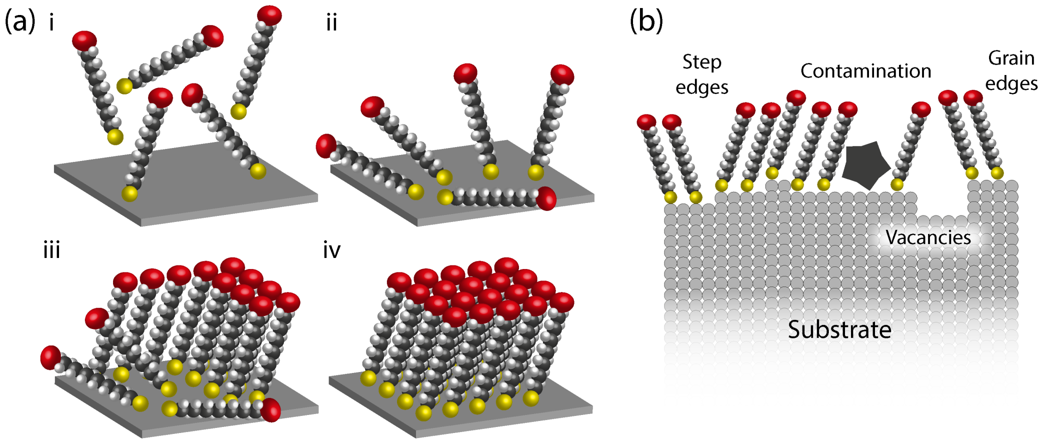

Figure 1.11 (a) The steps typically depicted to be occurring during the SAM formation process. (b) Examples of just some of the reasons for defects being present within a formed SAM.

The majority of the time required to form a SAM is associated with a rearrangement phase (Figure 1.11(a-iii)), whereby adsorbed molecules rearrange themselves to form a much denser monolayer, a process driven by interactions between the alkyl *spacer* groups, finally resulting in an ordered, crystalline structure (Figure 1.11(a-iv)), after many hours.[243] It is worth noting that the fate of the hydrogen from the S-H bond is still a topic of debate, despite the vast range of techniques employed for its study.[244] Studies in vacuum have demonstrated the release of atomic hydrogen,[245] whilst it has been proposed that the presence of oxygen in solution may subsequently lead to the formation of water.[217]

Furthermore, despite the well-ordered crystalline structure usually portrayed in SAM illustrations, in reality they are likely to be substantially more complex, with structures plagued by defects. Polycrystalline Au surfaces are the benchmark substrate for the majority of applied SAM experiments, and with these surfaces taking a complex grain structure, containing numerous boundaries and facets, the resulting SAM structure is far from perfect. Even at single crystal surfaces such as Au (111), a surface frequently used for fundamental SAM studies, the presence of atomic steps and vacancies generates disorder.[246] Additional complications such as solution or surface contamination can create trapped impurities and discontinuities within structure (Figure 1.11(b)). Most importantly, the fact that SAMs are dynamic systems should always be considered.

1.4 Non-Electrochemical Techniques

1.4.1 QCM

The QCM instrument[247,248] has become increasingly popular in recent years as a versatile tool to investigate the properties of solvated interfaces.[249-251] Based on the converse piezoelectric effect, discovered by the Curies in the late 1880s,[252,253] the technique utilizes a thin quartz layer (typically 300 μm) sandwiched between two metallic electrodes (Figure 1.12(a)). Being a piezoelectric material, the application of an alternating voltage across the electrodes results in an oscillatory motion of the quartz, the exact nature of which depends on the cut of the crystal relative to its crystallographic axes. AT-cut crystals, often used in QCM, oscillate in the thickness-shear mode, where the two crystals surfaces vibrate in an anti-parallel fashion, with the level of movement on the nm scale (Figure 1.12(b)).[254] The use of AT-cut crystals is further an advantage due to their low temperature coefficients.

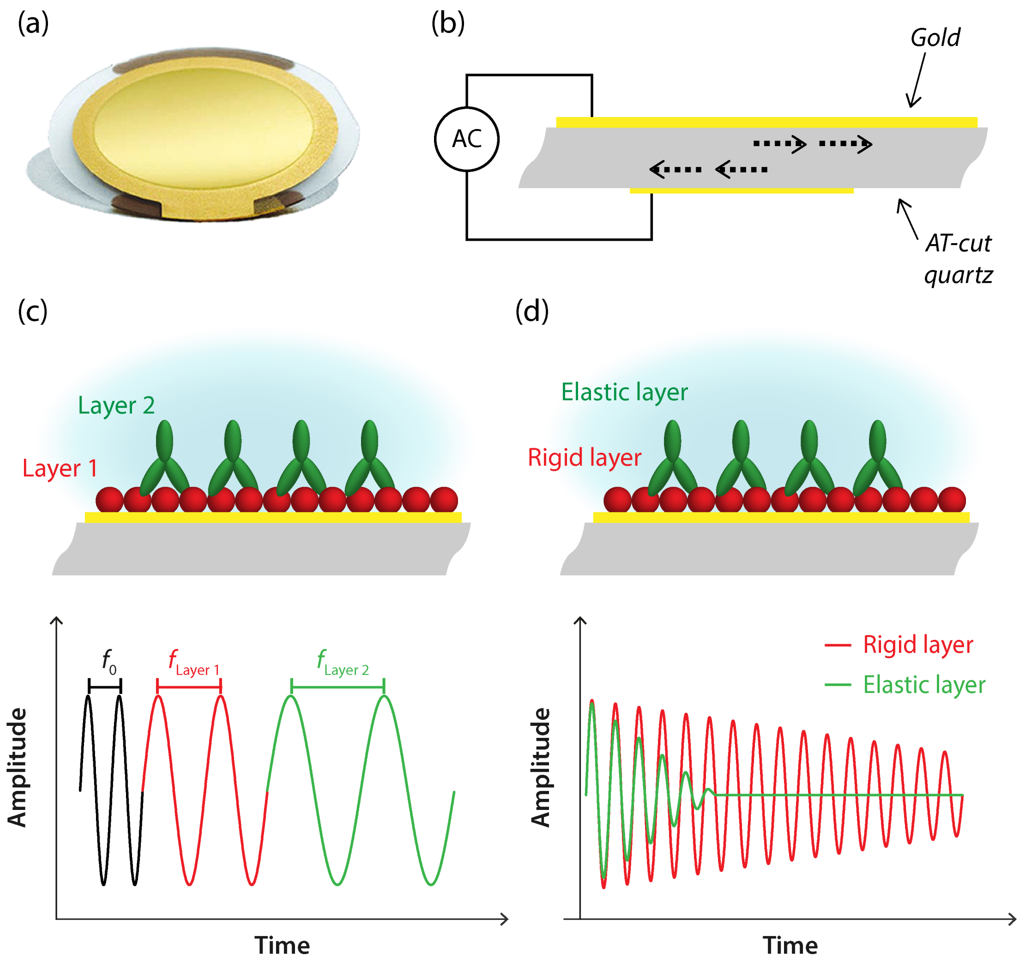
(a)
(b)
Gold
AC
AT-cut quartz
(c)
Layer 2
Layer 1
(d)
Elastic layer
Rigid layer
Amplitude
f_0
$f_{\mathrm{Layer\ 1}}$
$f_{\mathrm{Layer\ 2}}$
Time
Amplitude
Rigid layer
Elastic layer
Time

Figure 1.12 (a) Photograph of a QCM crystal. (b) Schematic illustrating the oscillation of a QCM chip under application of an alternating voltage between the two metal electrodes. (c) Illustration of the effect on oscillation frequency of adding mass to a QCM chip surface. (d) Illustration of the effect on frequency dissipation of adding a rigid vs. elastic mass to a QCM-D chip surface.

Upon the application of an the alternating voltage, a transverse acoustic wave propagates across the thickness of the crystal, reflecting back into the crystal at the surfaces. In resonance (i.e. when an AC voltage is applied with a frequency close to the resonance frequency, f_0, of the particular crystal), the crystal surfaces will be located at the antinodes of a standing wave, which decays rapidly in liquids, making the QCM technique incredibly interface specific. As such, when a uniform layer of foreign material is added to the crystal surface, it will act as an extension of the crystal surface, causing a fractional change in the thickness, resulting in a fractional (but measureable) change in the oscillation frequency, Δf (Figure 1.12(c)).[255] The true power of QCM lies in the fact that this frequency change can be related linearly to a mass change through the Sauerbrey equation,[256] eq. 1.8

$$\Delta f = \frac{-2\,\Delta m\,{f_0}^2}{A\left(\rho_q \mu_q\right)^{0.5}} \qquad (1.8)$$

where Δf is the frequency change, f_0 is the fundamental frequency of the crystal before mass change, Δm is the corresponding mass change, A is the piezoeletrically active area, ρ_q is the density of quartz (2.65 g cm^{-3}) and μ_q is the shear-modulus of quartz (2.95×10^{11} dyn cm^{-2}). Thus, for crystals with an f_0 of ~ 5 MHz (typically used in QCM), a mass sensitivity of 18 ng cm^{-2} Hz^{-1} exists.

There are several requirements for the viable application of the Sauerbrey equation, such as the level of adsorption must be continuous across the entire crystal surface, and that a homogenous layer exists, rather than discretely adsorbed particles. However, the most crucial requirement is that the adsorbed layer is rigid, displaying minimal elastic character, and thus essentially acting as an extension of the quartz crystal.[254] This condition makes the Sauerbrey relationship inappropriate when studying adsorbed layers with significant levels of solvent intercalation for example,[257] or when studying the adsorption of proteins[258] and cells,[259] for which QCM has a very large market.

However, more extensive data can be obtained in the QCM technique (aside from mass addition) through the use of a ‘ring-down’ scheme, first introduced by Rodahl *et al.* in 1995[260] and now commercialized by Q-Sense, and termed QCM with dissipation monitoring (QCM-D). In this approach, the alternating drive voltage is turned off intermittently, leaving the crystal oscillations to decay freely. The piezoelectric nature of quartz means that a measureable voltage is now generated (rather than applied) during these decaying oscillations, yielding a dimensionless parameter known as the dissipation, D, defined in eq. 1.9[261]

$$D = \frac{E_{Dissipated}}{2\pi \, E_{Stored}} \tag{1.9}$$

where $E_{\mathrm{Dissipated}}$ is the energy dissipated during an oscillatory cycle, and E_{Stored} is the energy stored during an oscillatory cycle.

When an adsorbed mass is viscous and soft, so that it does not follow the crystal oscillation well (i.e. it is not a rigid layer), friction within the layer leads to energy dissipation, evident in the measured D value, shown schematically in Figure 1.12(d).

The QCM-D approach thus allows for probing both f and D values at the millisecond timescale, with resolution typically on the order of ± 0.1 Hz and 10^{-7} respectively. The collection of data at multiple harmonics (overtones) permits the modeling of viscoelastic data (i.e. where the Sauerbrey is not applicable), allowing values such as film mass, density, thickness, and storage modulus to be accurately determined, making QCM-D more than just a microbalance.[261]

1.4.2 AFM

AFM traditionally offers itself as a high-resolution (sub nm) route to probing the structure and local properties of surfaces. Developed in the 1980s by Binnig, Quate and Gerber,[262] it was intended to fill the instrumental gap surrounding the imaging of non-conducting substrates, with their earlier introduced STM[263] being limited to conducting substrates.[264] By instead measuring sharply decaying interaction forces between probe and sample, rather than a tunneling current (as with STM), AFM allows for topographical imaging of almost any substrate, on the nm to μm length scale.[265,266] Furthermore, numerous developments in both AFM instrumentation and probe preparation methods have since extended the capabilities of the imaging technique in a myriad of ways, with a variety of localized complementary measurements now possible across a surface. Conducting AFM,[267,268] magnetic force microscopy,[269] and LFM,[270] are but a few examples, providing complementary high-resolution maps of localized electrical conductivity, magnetic fields, and surface friction properties, respectively, in addition to topography.

The general AFM measurement setup is shown in Figure 1.13(a). Briefly, a sharp probe (tip), with radius of curvature typically on the nm scale for maximized resolution, is mounted at the end of a flexible cantilever (Figure 1.13(b)). Cantilevers exist as both rectangular and V-shaped assemblies,[262] having an associated spring constant, k, reflecting the stiffness of the cantilever, determined by factors such as cantilever length, width, thickness, and material (*vide infra*).[271] Crucially, when tip and sample are in close proximity, interactions between the two result in minute changes (i.e. bending) of the cantilever. Such interactions are monitored by reflecting a laser beam from the cantilever's reverse (typically Au coated to maximize reflectivity), with small cantilever deflections thus leading to measurable shifts in the laser reflection (at a detector) over the path lengths used in AFM.

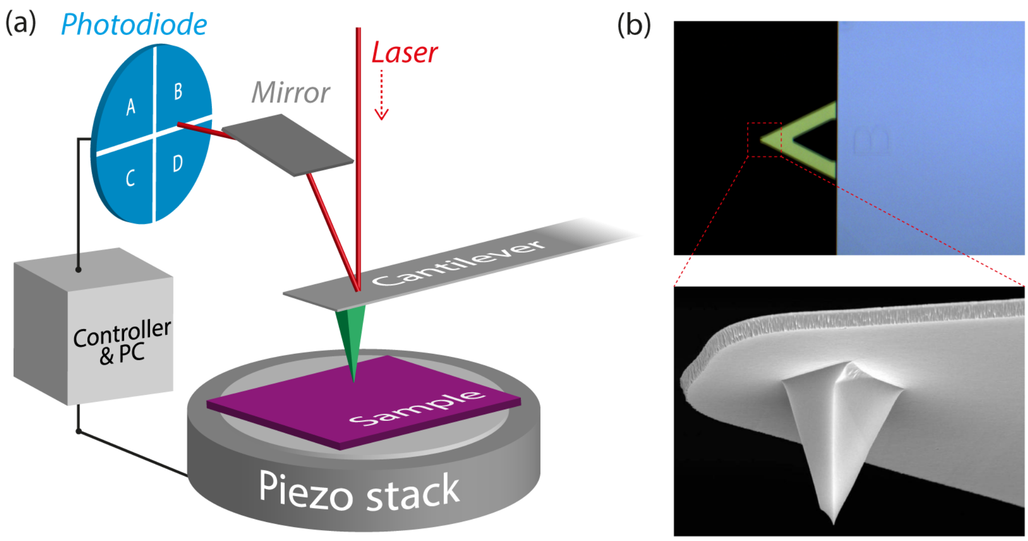

Figure 1.13 (a) Schematic of AFM setup, demonstrating the optical technique used to monitor changes in tip position at the sample surface. (b) Optical image of a typical V-shaped Si_3N_4 cantilever assembly, along with an SEM micrograph of the attached tip, itself made from Si.

A quadrant position-sensitive photodiode then allows for both normal (vertical motion) and torsional (lateral twisting) movements to be recorded, and with cantilever k values typically in the range of 0.01 – 100 N m^{-1}, instrumental sensitivities for normal deflection are ~ 0.01 nm.

Topographical imaging is achieved through contacting the tip with the surface of interest, before scanning it in an x-y raster fashion through the use of piezoelectric positioners. Upon contact, constant cantilever deflection (and thus tip-sample force) is maintained through a closed-loop feedback system via movement of the sample (or tip) in the z direction, producing a map of structural features on the surface. Unfortunately, a significant drawback of such direct contact is the sometimes excessive force applied to samples, resulting in their deformation or destruction, particularly relevant with soft materials and biological samples.[272] As such, non-contact mode (somewhat synonymous with tapping mode) AFM was introduced by Martin *et al.*,[273] which instead employed an oscillating cantilever. The flexible AFM cantilever is driven to oscillate at its resonant frequency in air (typically 100s of kHz) by a dedicated piezoelectric crystal, where it takes a distinct oscillation amplitude that is very sensitive to the surrounding environment. Close proximity of the tip with the sample surface dampens oscillation from the free value (in air) to a lower one, with more damping at closer proximity, and thus higher applied force. This oscillation amplitude provides an imaging set point, with a feedback loop again employed to ensure constant amplitude (measured at photodiode detector), also minimizing sample interaction by only making intermittent contact (i.e. tapping) with the surface. Moreover, the phase changes of the oscillation during a scan can be recorded, highlighting variations in adhesion, friction, and viscoelasticity.[274-276]

In addition to topographical imaging, however, AFM can also probe local nanomechanical and adhesive properties, by quantifying interactions occurring at tip-sample interface. The remainder of this introduction will focus on such measurements.

1.4.2.1 Force Measurements

One of the simplest, yet most valuable approaches to quantifying surface interaction forces is through the collection and analysis of a force-distance curve, often referred to simply as a force curve.[277] A complete force curve is a single approach-withdraw cycle (Figure 1.14(a)) whereby the sample is approached to the tip until contact is made, before retracting the sample. Experimentally, this is achieved through the application of a triangular wave voltage pattern to the *z*-axis scanner, causing expansion and subsequent contraction in the vertical direction, Figure 1.14(b).

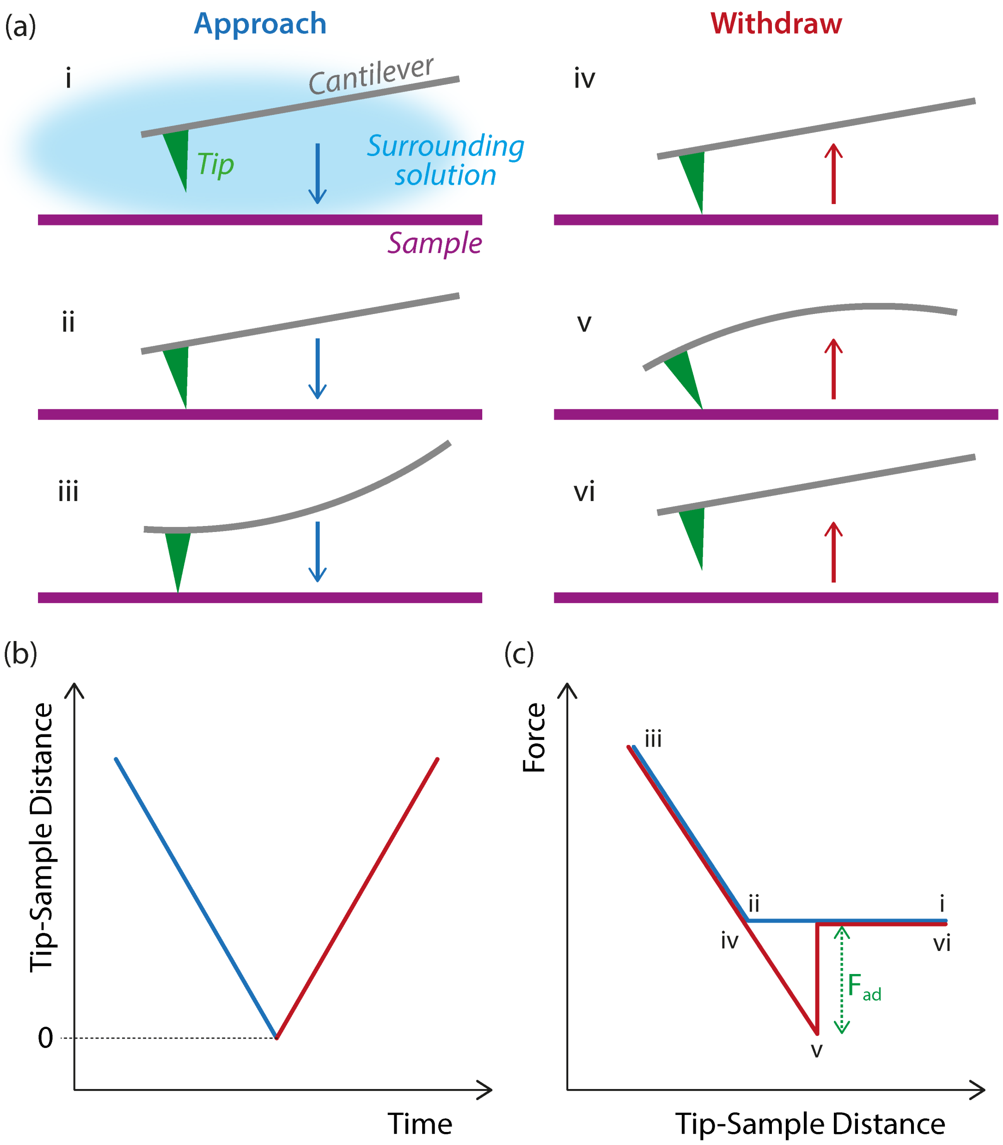
(a)
Approach
Withdraw
i
Cantilever
Tip
Surrounding solution
Sample
ii
iii
iv
v
vi
(b)
Tip-Sample Distance
0
Time
(c)
Force
iii
ii
i
iv
vi
F_{ad}
v
Tip-Sample Distance

Figure 1.14 (a) Schematic representations of the six main steps associated with acquiring a force-distance curve. (b) Typical waveform applied to tip-sample for the recording of a single force-curve. (c) An idealized force curve, with marked points corresponding to the tip position, as described in (a).

The force curve is obtained by plotting the vertical displacement of the cantilever from its resting position, monitored by the photodiode detector, as a function of separation distance between the tip and sample. Cantilever displacement, Δz, is then converted to force, F, according to the relationship shown in eq. 1.10

$$F = k\,\Delta z \tag{1.10}$$

where k is the cantilever spring constant. Typical instrumental sensitivities of 0.01 nm correspond to force limits of 10^{-13} – 10^{-8} N (dependent upon cantilever properties), and as such, interaction forces ranging from weak van der Waals (< 10^{-12} N) to strong covalent bonds (10^{-7} N)[278] can be measured, and quantified.

Figure 1.14(c) shows an idealized force curve, marked at several points corresponding to specific positions in the approach-withdraw cycle, as depicted in Figure 1.14(a). At position **i**, the beginning of the measurement, the tip is not in contact with the surface. Long-range repulsive (or attractive) forces may deflect the cantilever upward (or downward) if existent,[279] but these are negated in the example shown. Sample approach leads to position **ii**, at which point contact between the tip and sample is made, with a 'jump to contact' sometimes exhibited in the force curve, resulting from attractive forces (typically van der Waals) becoming significant at such short distances. Continued approach pushes the tip into the surface, deflecting the cantilever upwards (position **iii**), until the point at which a user-defined force is exerted, and withdrawal begins. This region is often termed 'constant compliance', where, for hard substrates, the distance the cantilever deflects is equal to the distance moved by the sample as they are pushed together. Of course, applying excessive force at this point can lead to tip/sample damage, introducing inaccuracy and variation.

Sample withdrawal introduces hysteresis to the force curve, where instead of losing contact with the surface at point **iv** (and reversing the contact made at point **ii**), adhesion forces formed between the tip and sample now cause downward bending of the cantilever. Continued withdrawal eventually overcomes these adhesion forces, leading to separation, marked at point **v**. The key measurement of an AFM force curve is the point at which this ‘snap off’ occurs, crucially providing the force associated with overcoming adhesion, labeled as F_{ad}.

Determining reliable values for F_{ad} of course relies on the piezoelectric scanner and the sensitivity of the photodiode detector being well calibrated, easily achieved through imaging calibration standards[280] and analysis of force curves on materials that do not deform.[281] However, determining an accurate value for k for the cantilever in use poses more of a challenge. For the case of rectangular cantilevers, knowledge of critical dimensions allows for an estimation of k, through eq. 1.11

$$k = \frac{Ewt^3}{4L^3} \qquad (1.11)$$

where E is the Young’s modulus of the cantilever material, and w, t, and L are the width, thickness, and length of cantilever, respectively.[282] Parallel bar approximations exist for V-shaped cantilevers,[283,284] however, in all cases, error in determining values for the above parameters (especially t and L) generates significant uncertainty in k, and factors such as reflective coatings add complexity. Furthermore, nominal values provided by manufacturers have been shown to differ greatly from actual values,[285] prompting the development of numerous other methods to determine k accurately.

Cleveland *et al.* introduced a non-destructive technique that required the addition of small masses to the cantilever (often μm sized metallic spheres), which resulted in changes in its resonant frequency, allowing k to be determined if repeated numerous times.[285] Sader *et al.* further commented on this approach, highlighting the potential for significant variation through effects of reflective coatings and positioning of the added mass.[286]

A method utilizing hydrodynamic drag was introduced by Maeda and Senden,[287] whilst an approach focused on nanoindentation apparatus was demonstrated by Holbery *et al.*[288] Numerous groups have also made use of reference cantilevers, which themselves have an accurately known k, allowing for a cantilever with unknown k to be calculated by pressing them together.[289-291]

Finally, Hutter *et al.* reported an elegant method to determine k for a cantilever by measuring its deflection in response to thermal noise. By simplifying the oscillating cantilever to a harmonic oscillator, the amplitude of oscillation was linked to the temperature of the system, thus allowing k to be determined.[292]

A final consideration in AFM force measurements is the size and shape of the tip radius, with both playing a major role in determining the area of the microcontact. Methods for visualizing tips include direct imaging through electron microscopy, as well as using the tip to image surfaces that display features with large contrast.[293,294] The reconstruction of tips has also been demonstrated, through imaging uniform latex spheres[295] and colloidal Au clusters,[296] for example. Hüttl *et al.* etched tips using oxygen plasma in an attempt to produce a consistent rounded shape;[297] in reality, however, tips often have a poorly defined geometry, making comparisons between obtained data sets and established models difficult.[298]

To overcome this problem, a somewhat universal solution is to replace the tip with a colloidal particle of well-defined spherical shape. This colloidal probe technique was developed by Ducker *et al.*[299,300] and Butt[301] in the early

1990s, and is now a well-established technique for measuring interaction forces. The measurement principle differs in no-way to that described previously, however the significantly larger contact area associated with colloidal spheres (typically 1 – 50 μm radii) means stiffer cantilevers are often needed to ensure particle detachment after contact. Attachment of colloidal particles is typically performed using micromanipulators under an optical microscope, with a tiny amount of glue first applied to the cantilever tip, before making contact with the colloidal particle.[300,302] Possible measurement contamination from glue has also been avoided by adhering polystyrene and glass particles using sintering methods instead.[303,304]

The colloidal probe technique has allowed for single particle-surface interactions to be studied and quantified under a wide range of conditions, and the effects of factors such as applied load and contact time,[305] humidity,[306] surface roughness,[307] and crucially, surface coatings (*vide infra*),[308] to be studied.

1.4.2.2 Chemical Force Microscopy (CFM)

A downfall of conventional colloidal force microscopy is its lack of chemical specificity, with chemical interactions determined purely by the sample of interest, and the material of which the colloidal probe consists of. This has been overcome through the process of chemically modifying AFM tips, making them sensitive to specific molecular interactions. Coating the tip (colloidal or not) with a well-defined molecular layer was pioneered by Lieber *et al.*,[309-311] who used SAM chemistry to introduce functionality at Au-coated tips, before studying adhesion and friction between combinations of methyl (–CH_3) and carboxyl (–COOH) functional groups. Specific interactions such as H-bonding lead to –COOH/–COOH interactions being larger than $–CH_3$/$–CH_3$. Forces between complementary DNA strands[312] and ligand-receptor pairs[313] have also been studied through CFM, as have discrete, single unfolding events in protein systems.[314]

Performing such detailed measurements under ambient conditions can make interpretation somewhat complex, with capillary forces associated with adsorbed water layers likely dominating the result.[278,315] As such, measurements under dry gas atmospheres have been performed,[316,317] although complete liquid immersion is most common,[318,319] also providing an additional advantage for biological systems[320] and those that display a dependency on factors such as pH and ionic strength.[301,321]

1.5 Aims of this Thesis

The aim of this thesis is to understand and exploit a number of surface modification processes, through approaches that combine results from complementary techniques, including electrochemistry, and that have implications at both the fundamental level and in real-life applications. Speaking broadly, two classes of processes will be investigated. Firstly, Chapters 3 and 4 monitor adsorption processes at surfaces that are chosen as simplistic models, with the aim of elucidating how specific surface features and chemistries impact the behavior observed at a wider level. Secondly, Chapters 5 and 6 examine modification processes that can be selectively driven, with an evident focus on understanding, controlling, and probing the extent of surface modification. Lastly, Chapter 7 builds on findings introduced in Chapter 6, examining a specific problem, and introducing a novel solution.

In Chapter 3, the adsorption of a range of surfactant like compounds is examined at model surfaces that are representative of carbonaceous soot, having direct relevance and application in the oil additives industry. A range of compounds are designed and synthesized that mimic those typically found in automotive lubricant oils, before their adsorption behavior is screened against model surfaces using the QCM technique, not only providing information on their favored sites of interaction, and thus allowing for intelligent future design, but also with the ultimate aim of being able to predict their ability to disperse carbonaceous soot in a real engine, without the extortionate costs associated with engine testing.

In Chapter 4, a new methodology based on SECCM is introduced that allows for the local delivery of, and subsequent monitoring of, molecular adsorbates at electrode surfaces. The specific case of quinone adsorption is monitored at a model sp^2 carbon surface, addressing the debated question of whether or not the adsorption, and associated electroactivity of these compounds is limited to step edge surface features. Crucially, the relatively small adsorption footprint of the introduced technique makes possible subsequent probing of the interrogated surface using complementary techniques, such as AFM, allowing for structure-activity relationships to be unambiguously drawn.

In Chapter 5, SECCM is investigated as a viable route to introduce highly-localized modification at surfaces. There is currently significant interest in the controlled diazonium modification of sp^2 carbon surfaces, interest that has arisen primarily through the ability of diazonium compounds to introduce an electronic band-gap in graphene. Thus, methods that exhibit control over both the location, and the extent of grafting could pave the way for entire graphene device fabrication. Electrochemical data is correlated with that obtained through AFM, Raman spectroscopy, and modeling, allowing conclusions to be drawn about the exact degree of surface modification.

In Chapter 6, the ability of SECCM to act as an intricate writing tool for patterned modification is explored, with respect to the production of graphene circuitry. Graphene devices are fabricated from well-characterized samples to demonstrate the effects of patterning, using complementary electronic measurements to corroborate that obtained through electrochemistry.

In Chapter 7, a process for the polymer-free transfer of single-layer, CVD graphene is explored. Direct comparisons are made to graphene samples transferred using a more traditional method, with SEM, Raman spectroscopy, and AFM data all used to draw conclusions.

1.6 References

(1) Kroto, H. W.; Heath, J. R.; Obrien, S. C.; Curl, R. F.; Smalley, R. E. *Nature* **1985**, *318*, 162.

(2) Iijima, S. *Nature* **1991**, *354*, 56.

(3) Novoselov, K. S.; Geim, A. K.; Morozov, S. V.; Jiang, D.; Zhang, Y.; Dubonos, S. V.; Grigorieva, I. V.; Firsov, A. A. *Science* **2004**, *306*, 666.

(4) McCreery, R. L. *Chem. Rev.* **2008**, *108*, 2646.

(5) May, P. W. *Philos. T. Roy. Soc. A* **2000**, *358*, 473.

(6) Savage, N. *Nature* **2012**, *483*, S30.

(7) Peierls, R. *Ann. Inst. Henri Poincaré* **1935**, *5*, 177.

(8) Landau, L. D. *Phys. Z. Sowjetunion* **1937**, *11*, 26.

(9) Evans, J. W.; Thiel, P. A.; Bartelt, M. C. *Surf. Sci. Rep.* **2006**, *61*, 1.

(10) Novoselov, K. S.; Jiang, D.; Schedin, F.; Booth, T. J.; Khotkevich, V. V.; Morozov, S. V.; Geim, A. K. *P. Natl. Acad. Sci. USA* **2005**, *102*, 10451.

(11) Zhang, Y. B.; Tan, Y. W.; Stormer, H. L.; Kim, P. *Nature* **2005**, *438*, 201.

(12) Stankovich, S.; Dikin, D. A.; Dommett, G. H. B.; Kohlhaas, K. M.; Zimney, E. J.; Stach, E. A.; Piner, R. D.; Nguyen, S. T.; Ruoff, R. S. *Nature* **2006**, *442*, 282.

(13) Meyer, J. C.; Geim, A. K.; Katsnelson, M. I.; Novoselov, K. S.; Booth, T. J.; Roth, S. *Nature* **2007**, *446*, 60.

(14) Bunch, J. S.; Verbridge, S. S.; Alden, J. S.; van der Zande, A. M.; Parpia, J. M.; Craighead, H. G.; McEuen, P. L. *Nano Lett.* **2008**, *8*, 2458.

(15) Lee, C.; Wei, X.; Kysar, J. W.; Hone, J. *Science* **2008**, *321*, 385.

(16) Balandin, A. A.; Ghosh, S.; Bao, W.; Calizo, I.; Teweldebrhan, D.; Miao, F.; Lau, C. N. *Nano Lett.* **2008**, *8*, 902.

(17) Avouris, P.; Chen, Z.; Perebeinos, V. *Nat. Nanotechnol.* **2007**, *2*, 605.

(18) Stoller, M. D.; Park, S.; Zhu, Y.; An, J.; Ruoff, R. S. *Nano Lett.* **2008**, *8*, 3498.

(19) Schedin, F.; Geim, A. K.; Morozov, S. V.; Hill, E. W.; Blake, P.; Katsnelson, M. I.; Novoselov, K. S. *Nat. Mater.* **2007**, *6*, 652.

(20) Pumera, M. *Energy Environ. Sci.* **2011**, *4*, 668.

(21) Yoo, E.; Kim, J.; Hosono, E.; Zhou, H.-s.; Kudo, T.; Honma, I. *Nano Lett.* **2008**, *8*, 2277.

(22) Zhu, Y.; Murali, S.; Stoller, M. D.; Ganesh, K. J.; Cai, W.; Ferreira, P. J.; Pirkle, A.; Wallace, R. M.; Cychosz, K. A.; Thommes, M.; Su, D.; Stach, E. A.; Ruoff, R. S. *Science* **2011**, *332*, 1537.

(23) Van Noorden, R. *Nature* **2012**, *483*, S32.

(24) Blake, P.; Hill, E. W.; Neto, A. H. C.; Novoselov, K. S.; Jiang, D.; Yang, R.; Booth, T. J.; Geim, A. K. *Appl. Phys. Lett.* **2007**, *91*, 063124.

(25) Liang, X.; Chang, A. S. P.; Zhang, Y.; Harteneck, B. D.; Choo, H.; Olynick, D. L.; Cabrini, S. *Nano Lett.* **2009**, *9*, 467.

(26) Sidorov, A. N.; Yazdanpanah, M. M.; Jalilian, R.; Ouseph, P. J.; Cohn, R. W.; Sumanasekera, G. U. *Nanotechnology* **2007**, *18,* 135301.

(27) Hernandez, Y.; Nicolosi, V.; Lotya, M.; Blighe, F. M.; Sun, Z.; De, S.; McGovern, I. T.; Holland, B.; Byrne, M.; Gun'ko, Y. K.; Boland, J. J.; Niraj, P.; Duesberg, G.; Krishnamurthy, S.; Goodhue, R.; Hutchison, J.; Scardaci, V.; Ferrari, A. C.; Coleman, J. N. *Nat. Nanotechnol.* **2008**, *3*, 563.

(28) Lotya, M.; Hernandez, Y.; King, P. J.; Smith, R. J.; Nicolosi, V.; Karlsson, L. S.; Blighe, F. M.; De, S.; Wang, Z.; McGovern, I. T.; Duesberg, G. S.; Coleman, J. N. *J. Am. Chem. Soc.* **2009**, *131*, 3611.

(29) Li, X.; Zhang, G.; Bai, X.; Sun, X.; Wang, X.; Wang, E.; Dai, H. *Nat. Nanotechnol.* **2008**, *3*, 538.

(30) Yu, A.; Ramesh, P.; Itkis, M. E.; Bekyarova, E.; Haddon, R. C. *J. Phys. Chem. C* **2007**, *111*, 7565.

(31) Bunch, J. S.; Yaish, Y.; Brink, M.; Bolotin, K.; McEuen, P. L. *Nano Lett.* **2005**, *5*, 287.

(32) Li, X. L.; Wang, X. R.; Zhang, L.; Lee, S. W.; Dai, H. J. *Science* **2008**, *319*, 1229.

(33) Geim, A. K.; Novoselov, K. S. *Nat. Mater.* **2007**, *6*, 183.

(34) Eda, G.; Mattevi, C.; Yamaguchi, H.; Kim, H.; Chhowalla, M. *J. Phys. Chem. C* **2009**, *113*, 15768.

(35) Riedl, C.; Coletti, C.; Starke, U. *J. Phys. D Appl. Phys.* **2010**, *43*, 374009.

(36) Huang, P. Y.; Ruiz-Vargas, C. S.; van der Zande, A. M.; Whitney, W. S.; Levendorf, M. P.; Kevek, J. W.; Garg, S.; Alden, J. S.; Hustedt, C. J.; Zhu, Y.; Park, J.; McEuen, P. L.; Muller, D. A. *Nature* **2011**, *469*, 389.

(37) Yan, Z.; Lin, J.; Peng, Z.; Sun, Z.; Zhu, Y.; Li, L.; Xiang, C.; Samuel, E. L.; Kittrell, C.; Tour, J. M. *ACS Nano* **2012**, *6*, 9110.

(38) Li, X.; Cai, W.; An, J.; Kim, S.; Nah, J.; Yang, D.; Piner, R.; Velamakanni, A.; Jung, I.; Tutuc, E.; Banerjee, S. K.; Colombo, L.; Ruoff, R. S. *Science* **2009**, *324*, 1312.

(39) Dreyer, D. R.; Park, S.; Bielawski, C. W.; Ruoff, R. S. *Chem. Soc. Rev.* **2010**, *39*, 228.

(40) Zhu, J. *Nat. Nanotechnol.* **2008**, *3*, 528.

(41) Hummers, W. S.; Offeman, R. E. *J. Am. Chem. Soc.* **1958**, *80*, 1339.

(42) Brodie, B. C. *Ann. Chim. Phys.* **1860**, *59*, 466.

(43) Buchsteiner, A.; Lerf, A.; Pieper, J. *J. Phys. Chem. B* **2006**, *110*, 22328.

(44) Paredes, J. I.; Villar-Rodil, S.; Martinez-Alonso, A.; Tascon, J. M. D. *Langmuir* **2008**, *24*, 10560.

(45) Park, S.; An, J. H.; Jung, I. W.; Piner, R. D.; An, S. J.; Li, X. S.; Velamakanni, A.; Ruoff, R. S. *Nano Lett.* **2009**, *9*, 1593.

(46) Lomeda, J. R.; Doyle, C. D.; Kosynkin, D. V.; Hwang, W.-F.; Tour, J. M. *J. Am. Chem. Soc.* **2008**, *130*, 16201.

(47) Stankovich, S.; Dikin, D. A.; Piner, R. D.; Kohlhaas, K. A.; Kleinhammes, A.; Jia, Y.; Wu, Y.; Nguyen, S. T.; Ruoff, R. S. *Carbon* **2007**, *45*, 1558.

(48) Si, Y.; Samulski, E. T. *Nano Lett.* **2008**, *8*, 1679.

(49) Zhou, M.; Wang, Y.; Zhai, Y.; Zhai, J.; Ren, W.; Wang, F.; Dong, S. *Chem. Eur. J.* **2009**, *15*, 6116.

(50) McAllister, M. J.; Li, J.-L.; Adamson, D. H.; Schniepp, H. C.; Abdala, A. A.; Liu, J.; Herrera-Alonso, M.; Milius, D. L.; Car, R.; Prud'homme, R. K.; Aksay, I. A. *Chem. Mater.* **2007**, *19*, 4396.

(51) Wei, Z.; Wang, D.; Kim, S.; Kim, S.-Y.; Hu, Y.; Yakes, M. K.; Laracuente, A. R.; Dai, Z.; Marder, S. R.; Berger, C.; King, W. P.; de Heer, W. A.; Sheehan, P. E.; Riedo, E. *Science* **2010**, *328*, 1373.

(52) Park, S.; Ruoff, R. S. *Nat. Nanotechnol.* **2009**, *4*, 217.

(53) Berger, C.; Song, Z.; Li, X.; Wu, X.; Brown, N.; Naud, C.; Mayou, D.; Li, T.; Hass, J.; Marchenkov, A. N.; Conrad, E. H.; First, P. N.; de Heer, W. A. *Science* **2006**, *312*, 1191.

(54) Emtsev, K. V.; Bostwick, A.; Horn, K.; Jobst, J.; Kellogg, G. L.; Ley, L.; McChesney, J. L.; Ohta, T.; Reshanov, S. A.; Roehrl, J.; Rotenberg, E.; Schmid, A. K.; Waldmann, D.; Weber, H. B.; Seyller, T. *Nat. Mater.* **2009**, *8*, 203.

(55) Riedl, C.; Zakharov, A. A.; Starke, U. *Appl. Phys. Lett.* **2008**, *93*, 033106.

(56) Yang, W.; Chen, G.; Shi, Z.; Liu, C.-C.; Zhang, L.; Xie, G.; Cheng, M.; Wang, D.; Yang, R.; Shi, D.; Watanabe, K.; Taniguchi, T.; Yao, Y.; Zhang, Y.; Zhang, G. *Nat. Mater.* **2013**, *12*, 792.

(57) Liu, Z.; Ma, L.; Shi, G.; Zhou, W.; Gong, Y.; Lei, S.; Yang, X.; Zhang, J.; Yu, J.; Hackenberg, K. P.; Babakhani, A.; Idrobo, J.-C.; Vajtai, R.; Lou, J.; Ajayan, P. M. *Nat. Nanotechnol.* **2013**, *8*, 119.

(58) Wang, Q. H.; Jin, Z.; Kim, K. K.; Hilmer, A. J.; Paulus, G. L. C.; Shih, C.-J.; Ham, M.-H.; Sanchez-Yamagishi, J. D.; Watanabe, K.; Taniguchi, T.; Kong, J.; Jarillo-Herrero, P.; Strano, M. S. *Nat. Chem.* **2012**, *4*, 724.

(59) Tsen, A. W.; Brown, L.; Levendorf, M. P.; Ghahari, F.; Huang, P. Y.; Havener, R. W.; Ruiz-Vargas, C. S.; Muller, D. A.; Kim, P.; Park, J. *Science* **2012**, *336*, 1143.

(60) Yan, Z.; Peng, Z.; Tour, J. M. *Accounts Chem. Res.* **2014**, *47*, 1327.

(61) Zhou, H.; Yu, W. J.; Liu, L.; Cheng, R.; Chen, Y.; Huang, X.; Liu, Y.; Wang, Y.; Huang, Y.; Duan, X. *Nat. Commun.* **2013**, *4*, 2096.

(62) Wu, T.; Ding, G.; Shen, H.; Wang, H.; Sun, L.; Jiang, D.; Xie, X.; Jiang, M. *Adv. Funct. Mater.* **2013**, *23*, 198.

(63) Kim, K. S.; Zhao, Y.; Jang, H.; Lee, S. Y.; Kim, J. M.; Kim, K. S.; Ahn, J.-H.; Kim, P.; Choi, J.-Y.; Hong, B. H. *Nature* **2009**, *457*, 706.

(64) Reina, A.; Jia, X.; Ho, J.; Nezich, D.; Son, H.; Bulovic, V.; Dresselhaus, M. S.; Kong, J. *Nano Lett.* **2009**, *9*, 30.

(65) Reina, A.; Thiele, S.; Jia, X.; Bhaviripudi, S.; Dresselhaus, M. S.; Schaefer, J. A.; Kong, J. *Nano Res.* **2009**, *2*, 509.

(66) Artyukhov, V. I.; Liu, Y.; Yakobson, B. I. *P. Natl. Acad. Sci. USA* **2012**, *109*, 15136.

(67) Bae, S.; Kim, H.; Lee, Y.; Xu, X.; Park, J.-S.; Zheng, Y.; Balakrishnan, J.; Lei, T.; Kim, H. R.; Song, Y. I.; Kim, Y.-J.; Kim, K. S.; Özyilmaz, B.; Ahn, J.-H.; Hong, B. H.; Iijima, S. *Nat. Nanotechnol.* **2010**, *5*, 574.

(68) Kwon, S.-Y.; Ciobanu, C. V.; Petrova, V.; Shenoy, V. B.; Bareno, J.; Gambin, V.; Petrov, I.; Kodambaka, S. *Nano Lett.* **2009**, *9*, 3985.

(69) Sutter, P. W.; Flege, J.-I.; Sutter, E. A. *Nat. Mater.* **2008**, *7*, 406.

(70) Shin, H.-J.; Choi, W. M.; Yoon, S.-M.; Han, G. H.; Woo, Y. S.; Kim, E. S.; Chae, S. J.; Li, X.-S.; Benayad, A.; Duong Dinh, L.; Gunes, F.; Lee, Y. H.; Choi, J.-Y. *Adv. Mater.* **2011**, *23*, 4392.

(71) Kim, H.; Song, I.; Park, C.; Son, M.; Hong, M.; Kim, Y.; Kim, J. S.; Shin, H.-J.; Baik, J.; Choi, H. C. *ACS Nano* **2013**, *7*, 6575.

(72) Li, X.; Zhu, Y.; Cai, W.; Borysiak, M.; Han, B.; Chen, D.; Piner, R. D.; Colombo, L.; Ruoff, R. S. *Nano Lett.* **2009**, *9*, 4359.

(73) Suk, J. W.; Kitt, A.; Magnuson, C. W.; Hao, Y.; Ahmed, S.; An, J.; Swan, A. K.; Goldberg, B. B.; Ruoff, R. S. *ACS Nano* **2011**, *5*, 6916.

(74) Park, H. J.; Meyer, J.; Roth, S.; Skakalova, V. *Carbon* **2010**, *48*, 1088.

(75) Lin, Y.-C.; Jin, C.; Lee, J.-C.; Jen, S.-F.; Suenaga, K.; Chiu, P.-W. *ACS Nano* **2011**, *5*, 2362.

(76) Lin, Y.-C.; Lu, C.-C.; Yeh, C.-H.; Jin, C.; Suenaga, K.; Chiu, P.-W. *Nano Lett.* **2012**, *12*, 414.

(77) Suk, J. W.; Lee, W. H.; Lee, J.; Chou, H.; Piner, R. D.; Hao, Y.; Akinwande, D.; Ruoff, R. S. *Nano Lett.* **2013**, *13*, 1462.

(78) Pirkle, A.; Chan, J.; Venugopal, A.; Hinojos, D.; Magnuson, C. W.; McDonnell, S.; Colombo, L.; Vogel, E. M.; Ruoff, R. S.; Wallace, R. M. *Appl. Phys. Lett.* **2011**, *99*, 122108.

(79) Lin, W.-H.; Chen, T.-H.; Chang, J.-K.; Taur, J.-I.; Lo, Y.-Y.; Lee, W.-L.; Chang, C.-S.; Su, W.-B.; Wu, C.-I. *ACS Nano* **2014**, *8*, 1784.

(80) Regan, W.; Alem, N.; Aleman, B.; Geng, B.; Girit, C.; Maserati, L.; Wang, F.; Crommie, M.; Zettl, A. *Appl. Phys. Lett.* **2010**, *96*, 113102.

(81) Stolyarova, E.; Rim, K. T.; Ryu, S.; Maultzsch, J.; Kim, P.; Brus, L. E.; Heinz, T. F.; Hybertsen, M. S.; Flynn, G. W. *P. Natl. Acad. Sci. USA* **2007**, *104*, 9209.

(82) Hossain, M. Z.; Walsh, M. A.; Hersam, M. C. *J. Am. Chem. Soc.* **2010**, *132*, 15399.

(83) Nemes-Incze, P.; Osvath, Z.; Kamaras, K.; Biro, L. P. *Carbon* **2008**, *46*, 1435.

(84) Gupta, A.; Chen, G.; Joshi, P.; Tadigadapa, S.; Eklund, P. C. *Nano Lett.* **2006**, *6*, 2667.

(85) Withers, F.; Bointon, T. H.; Dubois, M.; Russo, S.; Craciun, M. F. *Nano Lett.* **2011**, *11*, 3912.

(86) Sharma, R.; Baik, J. H.; Perera, C. J.; Strano, M. S. *Nano Lett.* **2010**, *10*, 398.

(87) Huang, P.; Zhu, H.; Jing, L.; Zhao, Y.; Gao, X. *ACS Nano* **2011**, *5*, 7945.

(88) Guell, A. G.; Ebejer, N.; Snowden, M. E.; Macpherson, J. V.; Unwin, P. R. *J. Am. Chem. Soc.* **2012**, *134*, 7258.

(89) Malard, L. M.; Pimenta, M. A.; Dresselhaus, G.; Dresselhaus, M. S. *Phys. Rep.* **2009**, *473*, 51.

(90) Ferrari, A. C.; Meyer, J. C.; Scardaci, V.; Casiraghi, C.; Lazzeri, M.; Mauri, F.; Piscanec, S.; Jiang, D.; Novoselov, K. S.; Roth, S.; Geim, A. K. *Phys. Rev. Lett.* **2006**, *97*, 187401.

(91) Graf, D.; Molitor, F.; Ensslin, K.; Stampfer, C.; Jungen, A.; Hierold, C.; Wirtz, L. *Nano Lett.* **2007**, *7*, 238.

(92) Ferrari, A. C.; Basko, D. M. *Nat. Nanotechnol.* **2013**, *8*, 235.

(93) Wallace, P. R. *Phys. Rev.* **1947**, *71*, 622.

(94) Avouris, P. *Nano Lett.* **2010**, *10*, 4285.

(95) Bolotin, K. I.; Sikes, K. J.; Jiang, Z.; Klima, M.; Fudenberg, G.; Hone, J.; Kim, P.; Stormer, H. L. *Solid State Commun.* **2008**, *146*, 351.

(96) Mann, D.; Javey, A.; Kong, J.; Wang, Q.; Dai, H. J. *Nano Lett.* **2003**, *3*, 1541.

(97) Li, X.; Magnuson, C. W.; Venugopal, A.; An, J.; Suk, J. W.; Han, B.; Borysiak, M.; Cai, W.; Velamakanni, A.; Zhu, Y.; Fu, L.; Vogel, E. M.; Voelkl, E.; Colombo, L.; Ruoff, R. S. *Nano Lett.* **2010**, *10*, 4328.

(98) Sinitskii, A.; Dimiev, A.; Corley, D. A.; Fursina, A. A.; Kosynkin, D. V.; Tour, J. M. *ACS Nano* **2010**, *4*, 1949.

(99) Xia, F.; Farmer, D. B.; Lin, Y.-m.; Avouris, P. *Nano Lett.* **2010**, *10*, 715.

(100) Bourzac, K. *Nature* **2012**, *483*, S34.

(101) Koshino, M. *Phys. Rev. B* **2010**, *81*, 125304.

(102) Ohta, T.; Bostwick, A.; Seyller, T.; Horn, K.; Rotenberg, E. *Science* **2006**, *313*, 951.

(103) McCann, E. *Phys. Rev. B* **2006**, *74*, 161403.

(104) Zhang, Y.; Tang, T.-T.; Girit, C.; Hao, Z.; Martin, M. C.; Zettl, A.; Crommie, M. F.; Shen, Y. R.; Wang, F. *Nature* **2009**, *459*, 820.

(105) Han, M. Y.; Öezyilmaz, B.; Zhang, Y.; Kim, P. *Phys. Rev. Lett.* **2007**, *98*, 206805.

(106) Chen, Z.; Lin, Y.-M.; Rooks, M. J.; Avouris, P. *Phys. E* **2007**, *40*, 228.

(107) Öezyilmaz, B.; Jarillo-Herrero, P.; Efetov, D.; Kim, P. *Appl. Phys. Lett.* **2007**, *91*, 192107.

(108) Jiao, L.; Zhang, L.; Wang, X.; Diankov, G.; Dai, H. *Nature* **2009**, *458*, 877.

(109) Wang, X.; Dai, H. *Nat. Chem.* **2010**, *2*, 661.

(110) Nakada, K.; Fujita, M.; Dresselhaus, G.; Dresselhaus, M. S. *Phys. Rev. B* **1996**, *54*, 17954.

(111) Elias, D. C.; Nair, R. R.; Mohiuddin, T. M. G.; Morozov, S. V.; Blake, P.; Halsall, M. P.; Ferrari, A. C.; Boukhvalov, D. W.; Katsnelson, M. I.; Geim, A. K.; Novoselov, K. S. *Science* **2009**, *323*, 610.

(112) Gao, H.; Wang, L.; Zhao, J.; Ding, F.; Lu, J. *J. Phys. Chem. C* **2011**, *115*, 3236.

(113) Nourbakhsh, A.; Cantoro, M.; Klekachev, A. V.; Pourtois, G.; Vosch, T.; Hofkens, J.; van der Veen, M. H.; Heyns, M. M.; De Gendt, S.; Sels, B. F. *J. Phys. Chem. C* **2011**, *115*, 16619.

(114) Cheng, S. H.; Zou, K.; Okino, F.; Gutierrez, H. R.; Gupta, A.; Shen, N.; Eklund, P. C.; Sofo, J. O.; Zhu, J. *Phys. Rev. B* **2010**, *81*, 205435.

(115) Bekyarova, E.; Sarkar, S.; Wang, F.; Itkis, M. E.; Kalinina, I.; Tian, X.; Haddon, R. C. *Accounts Chem. Res.* **2013**, *46*, 65.

(116) Niyogi, S.; Bekyarova, E.; Itkis, M. E.; Zhang, H.; Shepperd, K.; Hicks, J.; Sprinkle, M.; Berger, C.; Lau, C. N.; deHeer, W. A.; Conrad, E. H.; Haddon, R. C. *Nano Lett.* **2010**, *10*, 4061.

(117) Johns, J. E.; Hersam, M. C. *Accounts Chem. Res.* **2013**, *46*, 77.

(118) Park, J.; Yan, M. *Accounts Chem. Res.* **2013**, *46*, 181.

(119) Dai, H. J. *Surf. Sci.* **2002**, *500*, 218.

(120) Li, S. D.; Yu, Z.; Rutherglen, C.; Burke, P. J. *Nano Lett.* **2004**, *4*, 2003.

(121) Wildoer, J. W. G.; Venema, L. C.; Rinzler, A. G.; Smalley, R. E.; Dekker, C. *Nature* **1998**, *391*, 59.

(122) Edgeworth, J. P.; Wilson, N. R.; Macpherson, J. V. *Small* **2007**, *3*, 860.

(123) Heister, E.; Brunner, E. W.; Dieckmann, G. R.; Jurewicz, I.; Dalton, A. B. *ACS Appl. Mater. Interfaces* **2013**, *5*, 1870.

(124) Tans, S. J.; Verschueren, A. R. M.; Dekker, C. *Nature* **1998**, *393*, 49.

(125) Prato, M. *J. Mater. Chem.* **1997**, *7*, 1097.

(126) Hebard, A. F.; Rosseinsky, M. J.; Haddon, R. C.; Murphy, D. W.; Glarum, S. H.; Palstra, T. T. M.; Ramirez, A. P.; Kortan, A. R. *Nature* **1991**, *350*, 600.

(127) Xie, Q. S.; Perezcordero, E.; Echegoyen, L. *J. Am. Chem. Soc.* **1992**, *114*, 3978.

(128) Scharber, M. C.; Wuhlbacher, D.; Koppe, M.; Denk, P.; Waldauf, C.; Heeger, A. J.; Brabec, C. L. *Adv. Mater.* **2006**, *18*, 789.

(129) Chung, D. D. L. *J. Mater. Sci.* **2002**, *37*, 1475.

(130) Celzard, A.; Mareche, J. F.; Furdin, G.; Puricelli, S. *J. Phy. D Appl. Phys.* **2000**, *33*, 3094.

(131) Banerjee, S.; Sardar, M.; Gayathri, N.; Tyagi, A. K.; Raj, B. *Phys. Rev. B* **2005**, *72*, 075418.

(132) Cooper, J. D.; Woore, J.; Young, D. A. *Nature* **1970**, *225*, 721.

(133) Patel, A. N.; Tan, S.-Y.; Unwin, P. R. *Chem. Commun.* **2013**, *49*, 8776.

(134) Langley, L. A.; Villanueva, D. E.; Fairbrother, D. H. *Chem. Mater.* **2006**, *18*, 169.

(135) De Feyter, S.; De Schryver, F. C. *Chem. Soc. Rev.* **2003**, *32*, 139.

(136) Grimsdale, A. C.; Mullen, K. *Angew. Chem. Int. Ed.* **2005**, *44*, 5592.

(137) Theobald, J. A.; Oxtoby, N. S.; Phillips, M. A.; Champness, N. R.; Beton, P. H. *Nature* **2003**, *424*, 1029.

(138) Pumera, M. *Chem. Soc. Rev.* **2010**, *39*, 4146.

(139) Xiao, J.; Mei, D.; Li, X.; Xu, W.; Wang, D.; Graff, G. L.; Bennett, W. D.; Nie, Z.; Saraf, L. V.; Aksay, I. A.; Liu, J.; Zhang, J.-G. *Nano Lett.* **2011**, *11*, 5071.

(140) Simon, P.; Gogotsi, Y. *Nat. Mater.* **2008**, *7*, 845.

(141) Li, Y.; Zhou, W.; Wang, H.; Xie, L.; Liang, Y.; Wei, F.; Idrobo, J.-C.; Pennycook, S. J.; Dai, H. *Nat. Nanotechnol.* **2012**, *7*, 394.

(142) Wang, J. *Electroanal.* **2005**, *17*, 7.

(143) Li, W.; Tan, C.; Lowe, M. A.; Abruna, H. D.; Ralph, D. C. *ACS Nano* **2011**, *5*, 2264.

(144) Ritzert, N. L.; Rodriguez-Lopez, J.; Tan, C.; Abruna, H. D. *Langmuir* **2013**, *29*, 1683.

(145) Patten, H. V.; Ventosa, E.; Colina, A.; Ruiz, V.; Lopez-Palacios, J.; Wain, A. J.; Lai, S. C. S.; Macpherson, J. V.; Unwin, P. R. *J. Solid State Electr.* **2011**, *15*, 2331.

(146) Zach, M. P.; Inazu, K.; Ng, K. H.; Hemminger, J. C.; Penner, R. M. *Chem. Mater.* **2002**, *14*, 3206.

(147) Patel, A. N.; Tan, S.-y.; Miller, T. S.; Macpherson, J. V.; Unwin, P. R. *Anal. Chem.* **2013**, *85*, 11755.

(148) Patel, A. N.; Collignon, M. G.; O'Connell, M. A.; Hung, W. O. Y.; McKelvey, K.; Macpherson, J. V.; Unwin, P. R. *J. Am. Chem. Soc.* **2012**, *134*, 20117.

(149) Rice, R. J.; McCreery, R. L. *Anal. Chem.* **1989**, *61*, 1637.

(150) Bowling, R. J.; Packard, R. T.; McCreery, R. L. *J. Am. Chem. Soc.* **1989**, *111*, 1217.

(151) Cline, K. K.; McDermott, M. T.; McCreery, R. L. *J. Phys. Chem.* **1994**, *98*, 5314.

(152) Kneten, K. R.; McCreery, R. L. *Anal. Chem.* **1992**, *64*, 2518.

(153) Ji, X.; Banks, C. E.; Xi, W.; Wilkins, S. J.; Compton, R. G. *J. Phys. Chem. B* **2006**, *110*, 22306.

(154) Davies, T. J.; Moore, R. R.; Banks, C. E.; Compton, R. G. *J. Electroanal. Chem.* **2004**, *574*, 123.

(155) Snowden, M. E.; Guell, A. G.; Lai, S. C. S.; McKelvey, K.; Ebejer, N.; O'Connell, M. A.; Colburn, A. W.; Unwin, P. R. *Anal. Chem.* **2012**, *84*, 2483.

(156) Ebejer, N.; Schnippering, M.; Colburn, A. W.; Edwards, M. A.; Unwin, P. R. *Anal. Chem.* **2010**, *82*, 9141.

(157) Lai, S. C. S.; Patel, A. N.; McKelvey, K.; Unwin, P. R. *Angew. Chem. Int. Ed.* **2012**, *51*, 5405.

(158) Anne, A.; Cambril, E.; Chovin, A.; Demaille, C.; Goyer, C. *ACS Nano* **2009**, *3*, 2927.

(159) Frederix, P. L. T. M.; Bosshart, P. D.; Akiyama, T.; Chami, M.; Gullo, M. R.; Blackstock, J. J.; Dooleweerdt, K.; de Rooij, N. F.; Staufer, U.; Engel, A. *Nanotechnology* **2008**, *19*, 384004.

(160) Liu, J. Q.; Chou, A.; Rahmat, W.; Paddon-Row, M. N.; Gooding, J. J. *Electroanal.* **2005**, *17*, 38.

(161) Holloway, A. F.; Wildgoose, G. G.; Compton, R. G.; Shao, L.; Green, M. L. H. *J. Solid State Electr.* **2008**, *12*, 1337.

(162) Guell, A. G.; Ebejer, N.; Snowden, M. E.; McKelvey, K.; Macpherson, J. V.; Unwin, P. R. *P. Natl. Acad. Sci. USA* **2012**, *109*, 11487.

(163) Guell, A. G.; Meadows, K. E.; Dudin, P. V.; Ebejer, N.; Macpherson, J. V.; Unwin, P. R. *Nano Lett.* **2014**, *14*, 220.

(164) Byers, J. C.; Guell, A. G.; Unwin, P. R. *J. Am. Chem. Soc.* **2014**, *136*, 11252.

(165) Heller, I.; Kong, J.; Heering, H. A.; Williams, K. A.; Lemay, S. G.; Dekker, C. *Nano Lett.* **2005**, *5*, 137.

(166) Kim, J.; Xiong, H.; Hofmann, M.; Kong, J.; Amemiya, S. *Anal. Chem.* **2010**, *82*, 1605.

(167) Valota, A. T.; Kinloch, I. A.; Novoselov, K. S.; Casiraghi, C.; Eckmann, A.; Hill, E. W.; Dryfe, R. A. W. *ACS Nano* **2011**, *5*, 8809.

(168) Ambrosi, A.; Pumera, M. *J. Phys. Chem. C* **2013**, *117*, 2053.

(169) Brownson, D. A. C.; Banks, C. E. *Phys. Chem. Chem. Phys.* **2011**, *13*, 15825.

(170) Bard, A. J.; Faulkner, L. R. *Electrochemical Methods: Fundamentals and Applications*; Wiley, 2001.

(171) Unwin, P. R.; Compton, R. G. *J. Electroanal. Chem.* **1988**, *245*, 287.

(172) Dickinson, E. J. F.; Limon-Petersen, J. G.; Rees, N. V.; Compton, R. G. *J. Phys. Chem. C* **2009**, *113*, 11157.

(173) Ciszkowska, M.; Stojek, Z. *J. Electroanal. Chem.* **1999**, *466*, 129.

(174) Shain, I.; Nicholson, R. S. *CC/Phys. Chem. Earth* **1981**, 18.

(175) Greef, R.; Peat, R.; Peter, L. M.; Pletcher, D.; Robinson, J. *Instrumental Methods in Electrochemistry*; Ellis Horwood Limited, 1985.

(176) Pinson, J.; Podvorica, F. *Chem. Soc. Rev.* **2005**, *34*, 429.

(177) Allongue, P.; Delamar, M.; Desbat, B.; Fagebaume, O.; Hitmi, R.; Pinson, J.; Saveant, J. M. *J. Am. Chem. Soc.* **1997**, *119*, 201.

(178) Bradbury, C. R.; Kuster, L.; Fermin, D. J. *J. Electroanal. Chem.* **2010**, *646*, 114.

(179) Bahr, J. L.; Yang, J. P.; Kosynkin, D. V.; Bronikowski, M. J.; Smalley, R. E.; Tour, J. M. *J. Am. Chem. Soc.* **2001**, *123*, 6536.

(180) Mangeney, C.; Qin, Z.; Dahoumane, S. A.; Adenier, A.; Herbst, F.; Boudou, J. P.; Pinson, J.; Chehimi, M. M. *Diam. Relat. Mater.* **2008**, *17*, 1881.

(181) Munteanu, S.; Garraud, N.; Roger, J. P.; Amiot, F.; Shi, J.; Chen, Y.; Combellas, C.; Kanoufi, F. *Anal. Chem.* **2013**, *85*, 1965.

(182) deVilleneuve, C. H.; Pinson, J.; Bernard, M. C.; Allongue, P. *J. Phys. Chem. B* **1997**, *101*, 2415.

(183) Paulus, G. L. C.; Wang, Q. H.; Strano, M. S. *Accounts Chem. Res.* **2013**, *46*, 160.

(184) Mahouche-Chergui, S.; Gam-Derouich, S.; Mangeney, C.; Chehimi, M. M. *Chem. Soc. Rev.* **2011**, *40*, 4143.

(185) Pazo-Llorente, R.; Bravo-Diaz, C.; Gonzalez-Romero, E. *Eur. J. Org. Chem.* **2004**, 2004, 3221.

(186) Kosynkin, D.; Bockman, T. M.; Kochi, J. K. *J. Am. Chem. Soc.* **1997**, *119*, 4846.

(187) Bahr, J. L.; Tour, J. M. *Chem. Mater.* **2001**, *13*, 3823.

(188) Brunetti, F. G.; Herrero, M. A.; Munoz, J. d. M.; Diaz-Ortiz, A.; Alfonsi, J.; Meneghetti, M.; Prato, M.; Vazquez, E. *J. Am. Chem. Soc.* **2008**, *130*, 8094.

(189) Masheter, A. T.; Wildgoose, G. G.; Crossley, A.; Jones, J. H.; Compton, R. G. *J. Mater. Chem.* **2007**, *17*, 3008.

(190) Koehler, F. M.; Jacobsen, A.; Ensslin, K.; Stampfer, C.; Stark, W. J. *Small* **2010**, *6*, 1125.

(191) Delamar, M.; Hitmi, R.; Pinson, J.; Saveant, J. M. *J. Am. Chem. Soc.* **1992**, *114*, 5883.

(192) Gooding, J. J. *Electroanal.* **2008**, *20*, 573.

(193) Chan, C. K.; Beechem, T. E.; Ohta, T.; Brumbach, M. T.; Wheeler, D. R.; Stevenson, K. J. *J. Phys. Chem. C* **2013**, *117*, 12038.

(194) Ahlberg, E.; Helgee, B.; Parker, V. D. *Acta Chem. Scand. B* **1980**, *34*, 181.

(195) Saby, C.; Ortiz, B.; Champagne, G. Y.; Belanger, D. *Langmuir* **1997**, *13*, 6805.

(196) Adenier, A.; Bernard, M. C.; Chehimi, M. M.; Cabet-Deliry, E.; Desbat, B.; Fagebaume, O.; Pinson, J.; Podvorica, F. *J. Am. Chem. Soc.* **2001**, *123*, 4541.

(197) Bernard, M. C.; Chausse, A.; Cabet-Deliry, E.; Chehimi, M. M.; Pinson, J.; Podvorica, F.; Vautrin-Ul, C. *Chem. Mater.* **2003**, *15*, 3450.

(198) Laforgue, A.; Addou, T.; Belanger, D. *Langmuir* **2005**, *21*, 6855.

(199) Liu, S. Q.; Tang, Z. Y.; Shi, Z.; Niu, L.; Wang, E. K.; Dong, S. J. *Langmuir* **1999**, *15*, 7268.

(200) Allongue, P.; de Villeneuve, C. H.; Cherouvrier, G.; Cortes, R.; Bernard, M. C. *J. Electroanal. Chem.* **2003**, *550*, 161.

(201) Itoh, T.; McCreery, R. L. *J. Am. Chem. Soc.* **2002**, *124*, 10894.

(202) Liu, Y. C.; McCreery, R. L. *J. Am. Chem. Soc.* **1995**, *117*, 11254.

(203) Brooksby, P. A.; Downard, A. J. *Langmuir* **2004**, *20*, 5038.

(204) Brooksby, P. A.; Downard, A. J. *J. Phys. Chem. B* **2005**, *109*, 8791.

(205) Anariba, F.; DuVall, S. H.; McCreery, R. L. *Anal. Chem.* **2003**, *75*, 3837.

(206) Downard, A. J. *Langmuir* **2000**, *16*, 9680.

(207) Ceccato, M.; Bousquet, A.; Hinge, M.; Pedersen, S. U.; Daasbjerg, K. *Chem. Mater.* **2011**, *23*, 1551.

(208) Combellas, C.; Kanoufi, F.; Pinson, J.; Podvorica, F. I. *Langmuir* **2005**, *21*, 280.

(209) Combellas, C.; Kanoufi, F.; Pinson, J.; Podvorica, F. I. *J. Am. Chem. Soc.* **2008**, *130*, 8576.

(210) Shewchuk, D. M.; McDermott, M. T. *Langmuir* **2009**, *25*, 4556.

(211) Doppelt, P.; Hallais, G.; Pinson, J.; Podvorica, F.; Verneyre, S. *Chem. Mater.* **2007**, *19*, 4570.

(212) Bhugun, I.; Saveant, J. M. *J. Electroanal. Chem.* **1995**, *395*, 127.

(213) Ray, K.; McCreery, R. L. *Anal. Chem.* **1997**, *69*, 4680.

(214) Kariuki, J. K.; McDermott, M. T. *Langmuir* **1999**, *15*, 6534.

(215) Tanaka, M.; Sawaguchi, T.; Sato, Y.; Yoshioka, K.; Niwa, O. *Langmuir* **2011**, *27*, 170.

(216) Zhang, H.; Bekyarova, E.; Huang, J.-W.; Zhao, Z.; Bao, W.; Wang, F.; Haddon, R. C.; Lau, C. N. *Nano Lett.* **2011**, *11*, 4047.

(217) Love, J. C.; Estroff, L. A.; Kriebel, J. K.; Nuzzo, R. G.; Whitesides, G. M. *Chem. Rev.* **2005**, *105*, 1103.

(218) Daniel, M. C.; Astruc, D. *Chem. Rev.* **2004**, *104*, 293.

(219) Frisk, M. L.; Tepp, W. H.; Johnson, E. A.; Beebe, D. J. *Anal. Chem.* **2009**, *81*, 2760.

(220) Hudalla, G. A.; Murphy, W. L. *Langmuir* **2009**, *25*, 5737.

(221) Bumm, L. A.; Arnold, J. J.; Cygan, M. T.; Dunbar, T. D.; Burgin, T. P.; Jones, L.; Allara, D. L.; Tour, J. M.; Weiss, P. S. *Science* **1996**, *271*, 1705.

(222) Li, X. L.; He, J.; Hihath, J.; Xu, B. Q.; Lindsay, S. M.; Tao, N. J. *J. Am. Chem. Soc.* **2006**, *128*, 2135.

(223) Chidsey, C. E. D. *Science* **1991**, *251*, 919.

(224) Wilbur, J. L.; Kumar, A.; Kim, E.; Whitesides, G. M. *Adv. Mater.* **1994**, *6*, 600.

(225) Berggren, K. K.; Bard, A.; Wilbur, J. L.; Gillaspy, J. D.; Helg, A. G.; McClelland, J. J.; Rolston, S. L.; Phillips, W. D.; Prentiss, M.; Whitesides, G. M. *Science* **1995**, *269*, 1255.

(226) Golzhauser, A.; Eck, W.; Geyer, W.; Stadler, V.; Weimann, T.; Hinze, P.; Grunze, M. *Adv. Mater.* **2001**, *13*, 806.

(227) Liu, G. Y.; Xu, S.; Qian, Y. L. *Accounts Chem. Res.* **2000**, *33*, 457.

(228) Laibinis, P. E.; Whitesides, G. M.; Allara, D. L.; Tao, Y. T.; Parikh, A. N.; Nuzzo, R. G. *J. Am. Chem. Soc.* **1991**, *113*, 7152.

(229) Bain, C. D.; Troughton, E. B.; Tao, Y. T.; Evall, J.; Whitesides, G. M.; Nuzzo, R. G. *J. Am. Chem. Soc.* **1989**, *111*, 321.

(230) Bain, C. D.; Evall, J.; Whitesides, G. M. *J. Am. Chem. Soc.* **1989**, *111*, 7155.

(231) Schoenfisch, M. H.; Pemberton, J. E. *J. Am. Chem. Soc.* **1998**, *120*, 4502.

(232) Love, J. C.; Wolfe, D. B.; Haasch, R.; Chabinyc, M. L.; Paul, K. E.; Whitesides, G. M.; Nuzzo, R. G. *J. Am. Chem. Soc.* **2003**, *125*, 2597.

(233) Magnussen, O. M.; Ocko, B. M.; Deutsch, M.; Regan, M. J.; Pershan, P. S.; Abernathy, D.; Grubel, G.; Legrand, J. F. *Nature* **1996**, *384*, 250.

(234) Nuzzo, R. G.; Allara, D. L. *J. Am. Chem. Soc.* **1983**, *105*, 4481.

(235) Chailapakul, O.; Sun, L.; Xu, C. J.; Crooks, R. M. *J. Am. Chem. Soc.* **1993**, *115*, 12459.

(236) Ulman, A. *Chem. Rev.* **1996**, *96*, 1533.

(237) O'Dwyer, C.; Gay, G.; de Lesegno, B. V.; Weiner, J. *Langmuir* **2004**, *20*, 8172.

(238) Bareman, J. P.; Klein, M. L. *J. Phys. Chem.* **1990**, *94*, 5202.

(239) Schreiber, F. *Prog. Surf. Sci.* **2000**, *65*, 151.

(240) Poirier, G. E. *Chem. Rev.* **1997**, *97*, 1117.

(241) Henderson, A. P.; Seetohul, L. N.; Dean, A. K.; Russell, P.; Pruneanu, S.; Ali, Z. *Langmuir* **2009**, *25*, 931.

(242) Kim, H. J.; Kwak, S.; Kim, Y. S.; Seo, B. I.; Kim, E. R.; Lee, H. *Thin Solid Films* **1998**, *327*, 191.

(243) Yang, G. H.; Liu, G. Y. *J. Phys. Chem. B* **2003**, *107*, 8746.

(244) Hasan, M.; Bethell, D.; Brust, M. *J. Am. Chem. Soc.* **2002**, *124*, 1132.

(245) Kankate, L.; Turchanin, A.; Goelzhaeuser, A. *Langmuir* **2009**, *25*, 10435.

(246) Sun, L.; Crooks, R. M. *Langmuir* **1993**, *9*, 1951.

(247) Johannsmann, D. *Phys. Chem. Chem. Phys.* **2008**, *10*, 4516.

(248) Ward, M. D.; Buttry, D. A. *Science* **1990**, *249*, 1000.

(249) Cho, N.-J.; Frank, C. W.; Kasemo, B.; Hook, F. *Nat. Protoc.* **2010**, *5*, 1096.

(250) Harms, H. A.; Tetreault, N.; Gusak, V.; Kasemo, B.; Graetzel, M. *Phys. Chem. Chem. Phys.* **2012**, *14*, 9037.

(251) Richter, R. P.; Hock, K. K.; Burkhartsmeyer, J.; Boehm, H.; Bingen, P.; Wang, G.; Steinmetz, N. F.; Evans, D. J.; Spatz, J. P. *J. Am. Chem. Soc.* **2007**, *129*, 5306.

(252) Curie, P.; Curie, J. *C. R. Acad. Sci. Paris* **1880**, *91*, 294.

(253) Curie, P.; Curie, J. *C. R. Acad. Sci. Paris* **1881**, *93*, 1137.

(254) Buttry, D. A.; Ward, M. D. *Chem. Rev.* **1992**, *92*, 1355.

(255) Reviakine, I.; Johannsmann, D.; Richter, R. P. *Anal. Chem.* **2011**, *83*, 8838.

(256) Sauerbrey, G. *Z. Phys.* **1959**, *155*, 206.

(257) Bittrich, E.; Rodenhausen, K. B.; Eichhorn, K.-J.; Hofmann, T.; Schubert, M.; Stamm, M.; Uhlmann, P. *Biointerphases* **2010**, *5*, 159.

(258) Dobrzanska, D. A.; Cooper, A. L.; Dowson, C. G.; Evans, S. D.; Fox, D. J.; Johnson, B. R.; Biggs, C. I.; Randev, R. K.; Stec, H. M.; Taylor, P. C.; Marsh, A. *Langmuir* **2013**, *29*, 2961.

(259) Fredriksson, C.; Kihlman, S.; Rodahl, M.; Kasemo, B. *Langmuir* **1998**, *14*, 248.

(260) Rodahl, M.; Hook, F.; Krozer, A.; Brzezinski, P.; Kasemo, B. *Rev. Sci. Instrum.* **1995**, *66*, 3924.

(261) Dixon, M. C. *J. Biomol. Tech.* **2008**, *19*, 151.

(262) Binnig, G.; Quate, C. F.; Gerber, C. *Phys. Rev. Lett.* **1986**, *56*, 930.

(263) Binnig, G.; Rohrer, H.; Gerber, C.; Weibel, E. *Phys. Rev. Lett.* **1982**, *49*, 57.

(264) Binnig, G.; Rohrer, H.; Gerber, C.; Weibel, E. *Appl. Phys. Lett.* **1982**, *40*, 178.

(265) Albrecht, T. R.; Quate, C. F. *J. Appl. Phys.* **1987**, *62*, 2599.

(266) Marti, O.; Drake, B.; Hansma, P. K. *Appl. Phys. Lett.* **1987**, *51*, 484.

(267) Macpherson, J. V. *Nat. Nanotechnol.* **2011**, *6*, 84.

(268) Xu, D. G.; Watt, G. D.; Harb, J. N.; Davis, R. C. *Nano Lett.* **2005**, *5*, 571.

(269) Konings, S.; Miguel, J.; Goedkoop, J.; Camarero, J.; Vogel, J. *J. Appl. Phys.* **2006**, *100*, 033904.

(270) Marti, A.; Hahner, G.; Spencer, N. D. *Langmuir* **1995**, *11*, 4632.

(271) Albrecht, T. R.; Akamine, S.; Carver, T. E.; Quate, C. F. *J. Vac. Sci. Technol. A* **1990**, *8*, 3386.

(272) Weisenhorn, A. L.; Khorsandi, M.; Kasas, S.; Gotzos, V.; Butt, H.-J. *Nanotechnology* **1993**, *4*, 106.

(273) Martin, Y.; Williams, C. C.; Wickramasinghe, H. K. *J. Appl. Phys.* **1987**, *61*, 4723.

(274) Finot, M. O.; McDermott, M. T. *J. Am. Chem. Soc.* **1997**, *119*, 8564.

(275) Whangbo, M. H.; Bar, G.; Brandsch, R. *Surf. Sci.* **1998**, *411*, L794.

(276) Magonov, S. N.; Elings, V.; Whangbo, M. H. *Surf. Sci.* **1997**, *375*, L385.

(277) Cappella, B.; Dietler, G. *Surf. Sci. Rep.* **1999**, *34*, 1.

(278) Israelachvili, J. N. *Intermolecular and Surface Forces*; Academic Press, 2011.

(279) Butt, H. J. *Biophys. J.* **1991**, *60*, 777.

(280) Colton, R. J.; Ebeling, W.; Frommer, J. E.; Gaub, H. E.; Gewirth, A. A.; Guckenberger, R.; Rabe, J.; Heckl, W. M.; Parkinson, B. *Procedures in Scanning Probe Microscopies*; Wiley, 1998.

(281) Takano, H.; Kenseth, J. R.; Wong, S. S.; O'Brien, J. C.; Porter, M. D. *Chem. Rev.* **1999**, *99*, 2845.

(282) Luthi, R.; Meyer, E.; Haefke, H.; Howald, L.; Gutmannsbauer, W.; Guggisberg, M.; Bammerlin, M.; Guntherodt, H. J. *Surf. Sci.* **1995**, *338*, 247.

(283) Neumeister, J. M.; Ducker, W. A. *Rev. Sci. Instrum.* **1994**, *65*, 2527.

(284) Daeinabi, K.; Korayem, M. H.; Yarijani, S. A. *Micro & Nano Lett.* **2011**, *6*, 1007.

(285) Cleveland, J. P.; Manne, S.; Bocek, D.; Hansma, P. K. *Rev. Sci. Instrum.* **1993**, *64*, 403.

(286) Sader, J. E.; Larson, I.; Mulvaney, P.; White, L. R. *Rev. Sci. Instrum.* **1995**, *66*, 3789.

(287) Maeda, N.; Senden, T. J. *Langmuir* **2000**, *16*, 9282.

(288) Holbery, J. D.; Eden, V. L.; Sarikaya, M.; Fisher, R. M. *Rev. Sci. Instrum.* **2000**, *71*, 3769.

(289) Rabinovich, Y. I.; Yoon, R. H. *Langmuir* **1994**, *10*, 1903.

(290) Gibson, C. T.; Watson, G. S.; Myhra, S. *Nanotechnology* **1996**, *7*, 259.

(291) Scholl, D.; Everson, M. P.; Jaklevic, R. C. *Rev. Sci. Instrum.* **1994**, *65*, 2255.

(292) Hutter, J. L.; Bechhoefer, J. *Rev. Sci. Instrum.* **1993**, *64*, 1868.

(293) Atamny, F.; Baiker, A. *Surf. Sci.* **1995**, *323*, L314.

(294) Griffith, J. E.; Grigg, D. A.; Vasile, M. J.; Russell, P. E.; Fitzgerald, E. A. *J. Vac. Sci. Technol. A* **1992**, *10*, 674.

(295) Odin, C.; Aime, J. P.; Elkaakour, Z.; Bouhacina, T. *Surf. Sci.* **1994**, *317*, 321.

(296) Vesenka, J.; Miller, R.; Henderson, E. *Rev. Sci. Instrum.* **1994**, *65*, 2249.

(297) Huttl, G.; Beyer, D.; Muller, E. *Surf. Interface Anal.* **1997**, *25*, 543.

(298) Kappl, M.; Butt, H. J. *Part. Part. Sys. Charact.* **2002**, *19*, 129.

(299) Ducker, W. A.; Senden, T. J.; Pashley, R. M. *Nature* **1991**, *353*, 239.

(300) Ducker, W. A.; Senden, T. J.; Pashley, R. M. *Langmuir* **1992**, *8*, 1831.

(301) Butt, H. J. *Biophys. J.* **1991**, *60*, 1438.

(302) Raiteri, R.; Preuss, M.; Grattarola, M.; Butt, H. J. *Colloid Surface A* **1998**, *136*, 191.

(303) Schaefer, D. M.; Carpenter, M.; Reifenberger, R.; Demejo, L. P.; Rimai, D. S. *J. Adhes. Sci. Technol.* **1994**, *8*, 197.

(304) Bonaccurso, E.; Kappl, M.; Butt, H. J. *Phys. Rev. Lett.* **2002**, *88*, 076103.

(305) Biggs, S.; Spinks, G. *J. Adhes. Sci. Technol.* **1998**, *12*, 461.

(306) Fuji, M.; Machida, K.; Takei, T.; Watanabe, T.; Chikazawa, M. *J. Phys. Chem. B* **1998**, *102*, 8782.

(307) Bowen, W. R.; Doneva, T. A. *J. Colloid Interf. Sci.* **2000**, *229*, 544.

(308) Giesbers, M.; Kleijn, J. M.; Fleer, G. J.; Stuart, M. A. C. *Colloid Surface A* **1998**, *142*, 343.

(309) Noy, A.; Frisbie, C. D.; Rozsnyai, L. F.; Wrighton, M. S.; Lieber, C. M. *J. Am. Chem. Soc.* **1995**, *117*, 7943.

(310) Frisbie, C. D.; Rozsnyai, L. F.; Noy, A.; Wrighton, M. S.; Lieber, C. M. *Science* **1994**, *265*, 2071.

(311) Vezenov, D. V.; Noy, A.; Rozsnyai, L. F.; Lieber, C. M. *J. Am. Chem. Soc.* **1997**, *119*, 2006.

(312) Lee, G. U.; Chrisey, L. A.; Colton, R. J. *Science* **1994**, *266*, 771.

(313) Florin, E. L.; Moy, V. T.; Gaub, H. E. *Science* **1994**, *264*, 415.

(314) Rief, M.; Gautel, M.; Oesterhelt, F.; Fernandez, J. M.; Gaub, H. E. *Science* **1997**, *276*, 1109.

(315) Grigg, D. A.; Russell, P. E.; Griffith, J. E. *J. Vac. Sci. Technol. A* **1992**, *10*, 680.

(316) Thomas, R. C.; Houston, J. E.; Crooks, R. M.; Kim, T.; Michalske, T. A. *J. Am. Chem. Soc.* **1995**, *117*, 3830.

(317) Green, J. B. D.; McDermott, M. T.; Porter, M. D.; Siperko, L. M. *J. Phys. Chem.* **1995**, *99*, 10960.

(318) Weisenhorn, A. L.; Hansma, P. K.; Albrecht, T. R.; Quate, C. F. *Appl. Phys. Lett.* **1989**, *54*, 2651.

(319) Drake, B.; Prater, C. B.; Weisenhorn, A. L.; Gould, S. A. C.; Albrecht, T. R.; Quate, C. F.; Cannell, D. S.; Hansma, H. G.; Hansma, P. K. *Science* **1989**, *243*, 1586.

(320) Vesenka, J.; Mosher, C.; Schaus, S.; Ambrosio, L.; Henderson, E. *Biotechniques* **1995**, *19*, 240.

(321) Weisenhorn, A. L.; Maivald, P.; Butt, H. J.; Hansma, P. K. *Phys. Rev. B* **1992**, *45*, 11226.

Chapter Two

Experimental Methods

In this chapter, the methodologies, experimental procedures and instrumentation used throughout this thesis are detailed.

2.1 Chemicals, Solutions and Synthesis

All aqueous solutions were prepared with 18.2 MΩ cm (at 25 °C) Milli-Q reagent water (Millipore Corp.). All chemicals were used as received and were weighed using a 4 decimal place analytical balance. Details of chemicals and materials used in this thesis are given in Table 2.1.

Material	**Details & Supplier**
Chemicals	-
1-Dodecanethiol	≥ 98 %, Sigma Aldrich
11-Mercaptoundecanoic acid	95 %, Sigma Aldrich
11-Mercapto-1-undecanol	97 %, Sigma Aldrich
Ammonium hydroxide solution	30 wt. %, *A.C.S. Reagent*, Sigma Aldrich
Anthraquionone-2,6-disulphonic acid	95 %, Acros Organics
4-Aminobenzoic acid	≥ 99 %, Sigma Aldrich
4-Nitroaniline	≥ 99 %, Sigma Aldrich
Ammonium persulphate	≥ 98 %, Sigma Aldrich
Fluoroboric acid	50 wt. %, Acros Organics
Trifluoroacetic acid	*ReagentPlus*, 99 %, Sigma Aldrich
Potassium chloride	*ReagentPlus*, 99 %, Sigma Aldrich
Sodium nitrite	*A.C.S. Reagent*, > 97 %, Sigma Aldrich
Hydrogen peroxide	30 wt %, *A.C.S. Reagent*, Sigma Aldrich
Sulphuric acid (piranha cleaning)	*Analytical Reagent*, > 95 %, Sigma Aldrich
Sulphuric acid (electrolyte)	99.999 %, Sigma Aldrich
Perchloric acid	70 %, Acros Organics
Potassium (III) ferricyanide ($K_3Fe(CN)_6$)	99 %, Sigma Aldrich
Ruthenium (III) hexamine ($Ru(NH_3)_6Cl_3$)	98 %, Sigma Aldrich
$(FcTMA)PF_6$	Prepared through in-house metathesis

Dichlorodimethylsilane	> 99 %, Sigma Aldrich
Polymethyl methacrylate	M_w ~ 996,000, Sigma Aldrich
Solvents	-
Acetone	*AnalaR NORMAPUR*, VWR
Diethyl ether	*GPR RECTAPUR*, VWR
Ethanol	*AnalaR NORMAPUR*, VWR
Hexane	*AnalaR NORMAPUR*, VWR
Propan-2-ol	*Analytical Reagent*, Fisher
Toluene	*Analytical Reagent*, VWR
Materials	-
Silver wire (QRCE)	0.25 mm diameter, 99.9 %, MaTecK GmbH
Palladium wire (QRCE)	0.25 mm diameter, > 99.95 %, MaTecK GmbH
Platinum / Iridium (80 / 20) wire (STM tips)	Goodfellow Cambridge Ltd.
Copper foil	0.025 mm thick, 99.8 %, Alfa Aesar
Chromium coated tungsten bar	99.9 %, Goodfellow Cambridge Ltd.
Gold (Evaporation)	99.995 %, MaTecK GmbH
Oxidized silicon wafer	4-inch diameter, 525 µm thick, 1-10 Ω cm resistivity, n-type, single side polished, 300 nm thermal oxide layer, IDB Technologies Ltd.
Gold (111) on mica	George Albert PVD, Germany
SPI-1 grade HOPG	SPI Supplies, USA
SPI-3 grade HOPG	SPI Supplies, USA
ZYA grade HOPG	SPI Supplies, USA
AM grade HOPG	Courtesy of Prof. Richard L. McCreery, University of Alberta, Canada
Gases	-
Argon	99.9995 %, BOC gases
Hydrogen	99.95 %, BOC gases
Methane	99.995 %, BOC gases

Table 2.1 Details of chemicals and materials used throughout this thesis.

2.1.1 Model Dispersant Synthesis

Model dispersant compounds for QCM studies were synthesized in collaboration with Joanne Jones at Lubrizol Corporation, Hazelwood, UK, using specialty in-house chemicals. The hydrophobic tail selected for model dispersant compounds was 2-methyl-1-undecene, denoted as MUD from herein. In order to render it polar and suitable for further synthesis, it was first functionalized by grafting maleic anhydride (MA) at high temperature to form MA-MUD, a reaction summarized in Figure 2.1 below.

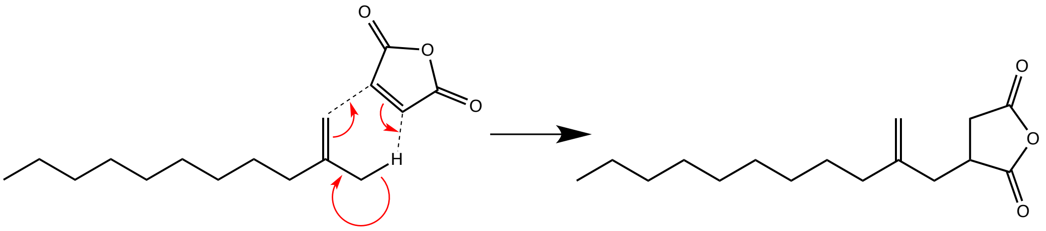

Figure 2.1 The grafting reaction of maleic anhydride with 2-methyl-1-undecene to form the batch starting material MA-MUD.

MUD (99.1 g, 0.589 mols, 1 eq.) was added to a three-neck round bottom flask with stirrer bar, before the slow addition of MA (57.8 g, 0.589 mols, 1 eq.) and the attachment of water-cooled reflux condenser apparatus. The reaction was heated to 190 °C under a gentle flow of nitrogen with constant stirring, before reducing the reaction temperature to 175 °C and leaving overnight. After ~ 20 hours of reaction, thin layer chromatography showed no starting compounds to be present in the reaction mixture, confirming complete conversion to MA-MUD. The resulting dark brown mixture was purified using column chromatography, with the column matrix consisting of packed diatomaceous earth and ethyl acetate the eluent, resulting in 60 g of purified MA-MUD.

Post-purification, the synthesized MA-MUD starting material was suitable for grafting with selected amine molecules, to produce the desired model dispersant compounds. The addition of amine compounds was carried out according to standard procedure provided by Lubrizol Corporation, and is summarized below in Figure 2.2. Ring opening of the MA-MUD compound occurs due to nucleophilic attack of the selected primary amine on the electron deficient carbonyl carbon. Performing the reaction at high-temperature facilitates the removal of water and hence ring closure, to obtain the corresponding succinimide. This procedure allowed for the synthesis of several model dispersant compounds, each varying in headgroup, R’, as determined by the amine compound employed during this synthesis step.

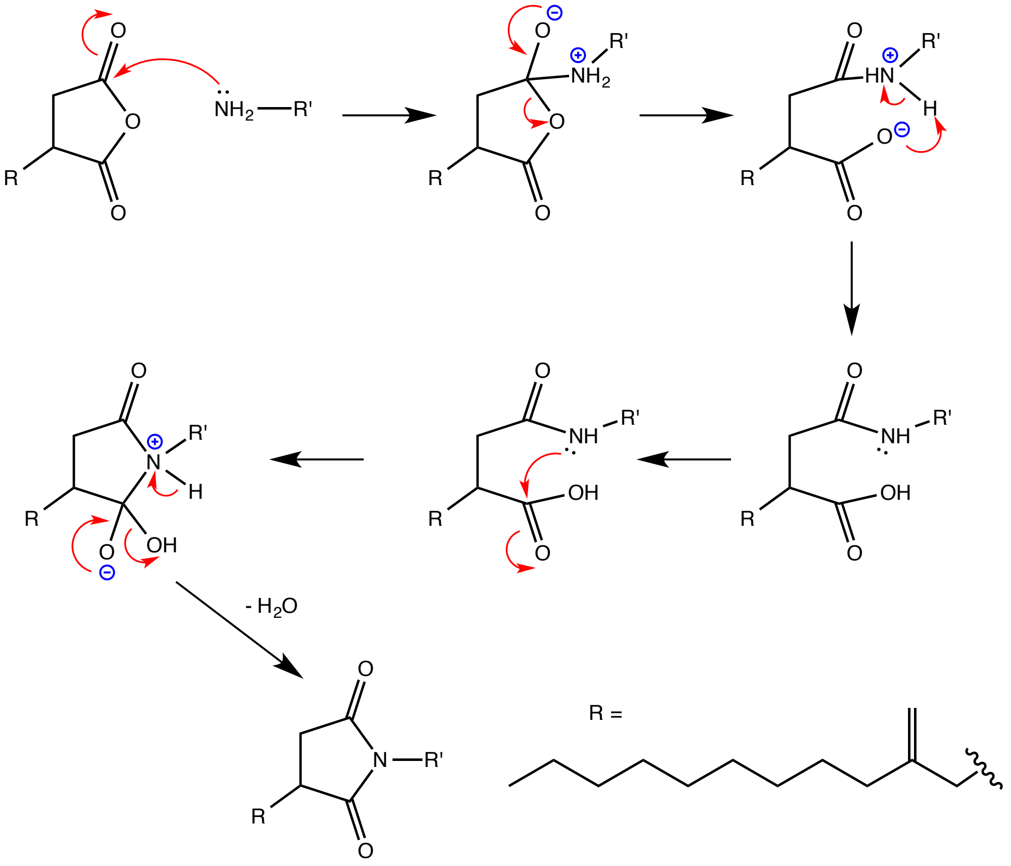

Figure 2.2 The grafting reaction of MA-MUD with a generic amine compound, resulting in a model dispersant.

Subsequent modification with amine compounds was typically performed by heating a small amount (~ 1 g) of MA-MUD to 100 °C in a round bottom flask with constant stirring, before the dropwise addition of the selected amine, typically in a 1:1 molar ratio with respect to MA-MUD. The reaction was left stirring at 100 °C for between 4 and 20 hours, depending on the amine compound used. Fourier transform infrared (FT-IR) spectroscopy on small aliquots was used to monitor the progress of the reaction and confirm completion (*vide infra*). Table 2.2 lists the range of amine compounds used for dispersant synthesis and highlights any compounds that differed from the 1:1 reaction ratio typically employed during the reaction.

Tail	Amine	Amine structure	Ratio
MA-MUD	Dimethylaminopropylamine	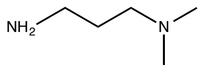	1:1
MA-MUD	Triethylenetetramine	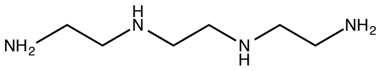	1:1
MA-MUD	Aniline	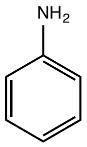	1:1
MA-MUD	Benzylamine	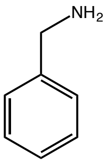	1:1
MA-MUD	Aminodiphenylamine	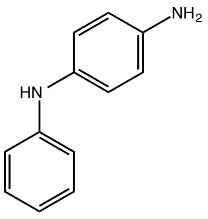	1:1
MA-MUD	Ethanolamine	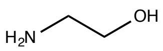	1:1
MA-MUD	Ethylene glycol	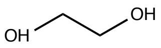	2:1

Table 2.2 The range of starting amine compounds used in model dispersant synthesis.

Synthesized model dispersant compounds were fully characterized prior to use, since structural variation is likely to affect their adsorption properties. Characterization was performed using both FT-IR and nuclear magnetic resonance (NMR) spectroscopy. FT-IR was predominantly used throughout the synthesis stage to ensure reaction completion (based on functional group assignment) whilst NMR was employed post synthesis to ensure negligible impurities. The FT-IR spectrum of the batch starting material (MA-MUD) is shown below in Figure 2.3 where it displays a prominent adsorption peak at 1786 cm^{-1}, owing to its anhydride functionality.

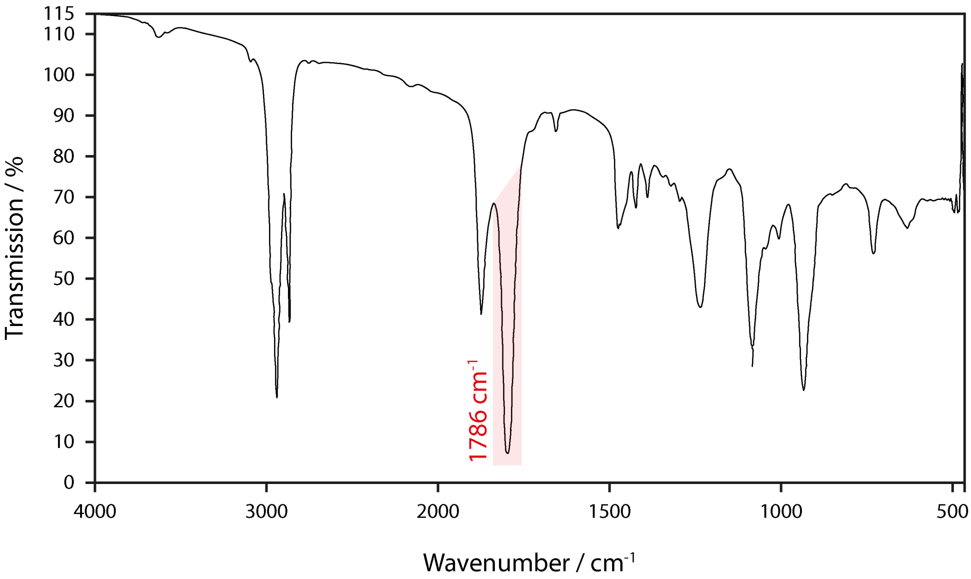

Figure 2.3 An FT-IR spectrum of the batch synthesized MA-MUD starting material, prior to further amine attachment, displaying a prominent peak at 1786 cm^{-1}.

Upon the addition of an amine compound, new peaks arise in the spectrum as a result of the previously described grafting mechanism. Loss of the anhydride functionality results in the gradual decrease of the peak at 1786 cm^{-1}, and this was thus used to determine reaction completion, whilst the occurrence of peaks at 1774 cm^{-1} and 1704 cm^{-1} confirmed its replacement with the introduced imide functionality. Figure 2.4 shows a typical FT-IR spectrum of a fully synthesized model dispersant compound after 20 hours of reaction.

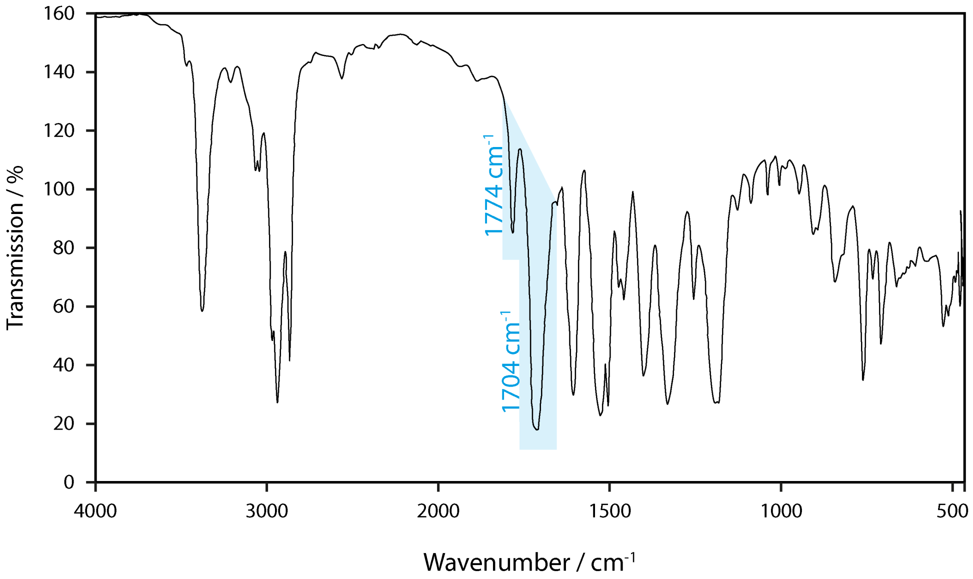

Figure 2.4 An FT-IR spectrum of a synthesized dispersant compound upon reaction completion, determined by introduced peaks at 1774 cm^{-1} and 1704 cm^{-1}, and a lack of the originally present 1786 cm^{-1} anhydride peak.

2.1.2 Diazonium Compound Synthesis

4-carboxynitrobenzenediazonium tetrafluroborate (4-CBD) and 4-nitrobenzenediazonium tetrafluroborate (4-NBD) were synthesized in-house according to a previously published method.[1] The below synthetic method describes the synthesis of 4-CBD, but is identical to that used for 4-NBD synthesis, apart from the starting material (*vide infra*). 4-aminobenzoic acid (0.75 g, 5.46 mmol) was added to 5 mL of water and cooled to -2 °C under constant stirring. 3 mL ice-cold HBF_4 (48 wt. %) was added dropwise to the cold solution, causing immediate dissolution of the starting material. After stirring for 30 minutes at -2 °C, 2 mL of ice-cold water containing $NaNO_2$ (0.40 g, 5.80 mmol) was added dropwise, producing a white precipitate. This precipitate was immediately filtered off using vacuum filtration, and washed with 5 mL ice-cold water and 5 mL ice-cold diethyl ether. It was then dried in a desiccator for 48 hours before analysis. After drying, FT-IR spectroscopy showed a strong adsorption peak at 2308 cm^{-1} (not present in the starting material), assigned to the diazonium functional group.[2] ^{1}H NMR (CD_3CN) showed two doublets in the spectrum, at 8.42-8.48 ppm and 8.60-8.65 ppm, as observed in the literature for this compound.[1] 4-NBD synthesis used 4-nitroaniline as the starting material.

2.2 Sample Preparation

2.2.1 SAM Preparation

SAMs were formed on two types of Au substrates. Firstly, Au on mica (200 nm thickness, George Albert PVD, Germany) displaying predominantly the (111) crystal face, and secondly on polycrystalline Au-coated QCM-D chips (4.95 MHz, AT-cut, Q-Sense, Sweden). Prior to SAM formation, QCM-D chips were cleaned by immersion in piranha solution for 10 minutes, as recommended by the manufacturer. Piranha solution consists of a 3:1 ratio (by volume) of concentrated sulphuric acid and hydrogen peroxide (30 %). **CAUTION:** This highly corrosive solution reacts aggressively with any organic material, and must be treated with extreme care. Upon careful mixing, the solution began to spontaneously boil, at which point QCM-D chips to be cleaned were added and left to stand for 10 minutes, before careful removal and rinsing with copious amounts of deionized water. They were then dried under a gentle stream of purified N_2. Gold on mica substrates were stored under N_2 in a clean room, and did not undergo any cleaning procedure prior to functionalization.

Immediately before immersion into solutions containing the thiol of interest, both types of gold substrate were rinsed with ethanol. Modification solutions consisted of 1 mM of either 1-dodecanethiol ($HS(CH_2)_{11}CH_3$), 11-mercaptoundecanoic acid (11-MUA) ($HS(CH_2)_{10}COOH$) or 11-mercapto-1-undecanol (11-MUD) ($HS(CH_2)_{11}OH$) in ethanol. Samples were left immersed in thiol solutions in the dark for 24 hours, at which point they were removed and rinsed with copious amounts of ethanol, before drying under a gentle stream of purified N_2. SAM functionalized samples were used immediately after removal, or stored in pure ethanol if this was not practical, for a maximum of 12 hours. The preparation method for 11-MUA SAMs was adapted slightly, as described in Chapter 3.

2.2.2 HOPG Substrate Preparation

Commercially available grades of HOPG (SPI-1, SPI-3, and ZYA) were obtained from SPI-supplies and a high-quality but ungraded sample of HOPG, herein referred to as AM grade, was kindly provided by Prof. R. L. McCreery (University of Alberta, Canada), which originated from Dr. A Moore, Union carbide, now GE Advanced ceramics. In order to obtain freshly exposed surfaces of reproducible quality, single side scotch tape was gently pressed onto the HOPG surface and peeled back to removed the top layers. Once cleaved using this technique, samples were used as quickly as possible, to minimize atmospheric surface contamination.

2.2.3 Graphene Synthesis

Graphene was synthesized in a commercial low-pressure CVD system (NanoCVD 8G, Moorefield Associates, UK). Cu foils were cut to 1 cm × 1 cm squares from a larger foil (0.025 mm thickness, 99.8 %, Alfa Aesar) and sonicated in acetone and propan-2-ol for 5 minutes each, before being rinsed with propan-2-ol and dried under a flow of purified N_2. Once dry, the foils were submerged in a 20 % HCl solution (v/v) at 50 °C for 30 seconds (to remove surface oxides) before rinsing with water and drying with purified N_2. To flatten the foils they were placed between two glass slides (themselves cleaned with acetone and isopropan-2-ol) and clamped in a vice.

Cu foils were placed into the growth chamber and a purge regime was performed, pumping the system to vacuum and back filling with Ar, five times. Post-purge, the sample was heated to 900 °C as quickly as possible, under a flow of 190 standard cubic centimeters per minute (sccm) Ar and 10 sccm H_2, before maintaining 900 °C for 2 minutes. The temperature was then increased to 1000 °C as quickly as possible under the same gas flow conditions. The pressure regime of the system was then changed, being set to maintain a chamber pressure of 10 Torr, and left to stabilize for 30 seconds, before 5 % (of total gas flow) CH_4 was introduced to the system for 100 seconds, promoting graphene growth. Post-growth, all gas flow was halted (whilst the temperature was still maintained at 1000 °C) and the pressure was allowed to return to its base value, quickly removing carbon-containing gas. Finally, the chamber was again set to maintain a pressure of 10 Torr, and a 90 % Ar and 10 % H_2 mixture was introduced for 2 minutes, still at 1000 °C, before allowing the system to cool to 200 °C under a flow of 190 sccm Ar and 10 sccm H_2, at which point samples were removed.

2.2.4 PMMA Supported Graphene Transfer

PMMA supported graphene transfer to insulating Si/SiO_2 substrates was based on an already developed procedure,[3] adapted with reference to other reports.[4] The Cu foil was stuck (Gel-Pak, CA, USA) graphene side facing up to a square of glass and PMMA (460 mg, M_w ~ 996,000, Sigma Aldrich) in chlorobenzene (10 mL) was spin-coated onto the surface (2000 RPM, 45 seconds). The sample was dried under vacuum in a desiccator for 1 hour, before the underside of the sample (i.e. not coated with PMMA) was gently polished with sand paper (Struers waterproof silicon carbide paper #4000) to remove unwanted graphitic coverage. The sample was then floated on a 0.1 M ammonium phosphate ($(NH_4)_2S_2O_8$) solution, PMMA side up, and left overnight, dissolving the copper, and leaving the graphene/PMMA floating on the solution. The graphene/PMMA was cleaned by repeatedly introducing fresh water using a syringe. The floating sample was then removed from pure water using an Si/SiO_2 square, previously cleaned with acetone and propan-2-ol, cut slightly bigger than the graphene/PMMA. The sample was left to dry at room temperature in air, before heating to 180 °C for 1 hour, flattening the graphene/PMMA, and then allowed to cool. Finally, PMMA was dissolved in acetone at 50 °C. Figure 2.5 summarizes the graphene transfer process.

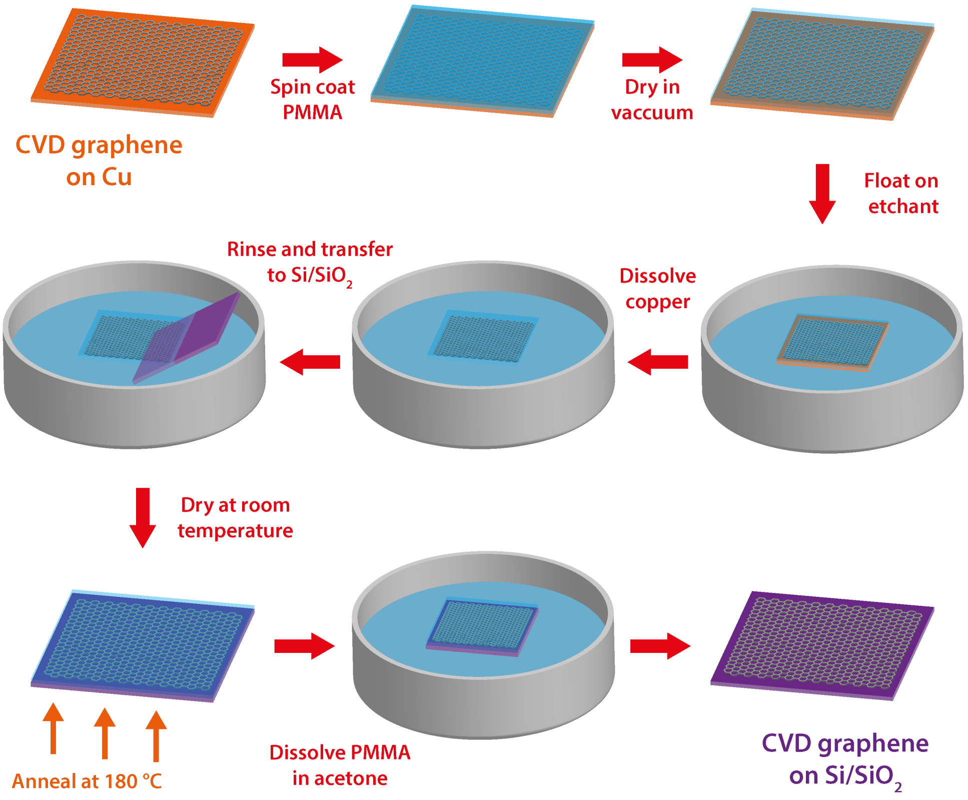
CVD graphene
on Cu
Spin coat
PMMA
Dry in
vaccuum
Float on
etchant
Dissolve
copper
Rinse and transfer
to Si/SiO2
Dry at room
temperature
Anneal at 180 °C
Dissolve PMMA
in acetone
CVD graphene
on Si/SiO2

Figure 2.5 A schematic representation of the PMMA supported graphene transfer process.

2.2.5 Polymer-Free Graphene Transfer

The use of samples completely free from PMMA transfer residue was sometimes necessary, and as such, a polymer-free transfer method was developed (Chapter 7). This biphasic transfer approach is shown schematically in Figure 2.6. As-grown monolayer graphene on Cu samples were first floated (graphene side up) atop a 0.1 M $(NH_4)_2S_2O_8$ etchant solution, before a crucial hexane layer was gently introduced to the solution using a syringe, which, when done carefully, trapped the graphene/Cu substrate at the formed organic/aqueous biphasic interface, with the hydrophobic graphene in contact only with the hexane, and the Cu foil contacting the etchant solution. After Cu etching, the synthesized graphene sheet is left trapped in the same position at the interface, stabilized by the hexane layer, preventing the surface tension of the water pulling the sheet apart, as would be the case if the non-polar layer were not present.[5] The etchant solution was then replaced with pure water by syringe pumping, at which point it was crucial to minimize any disturbance to the delicate graphene layer. Finally, the free standing graphene is removed from the interface using a pre-cleaned Si/SiO_2 substrate in a single swift motion, before being left to dry at room temperature, revealing polymer-free transfer graphene on the Si/SiO_2 substrate.

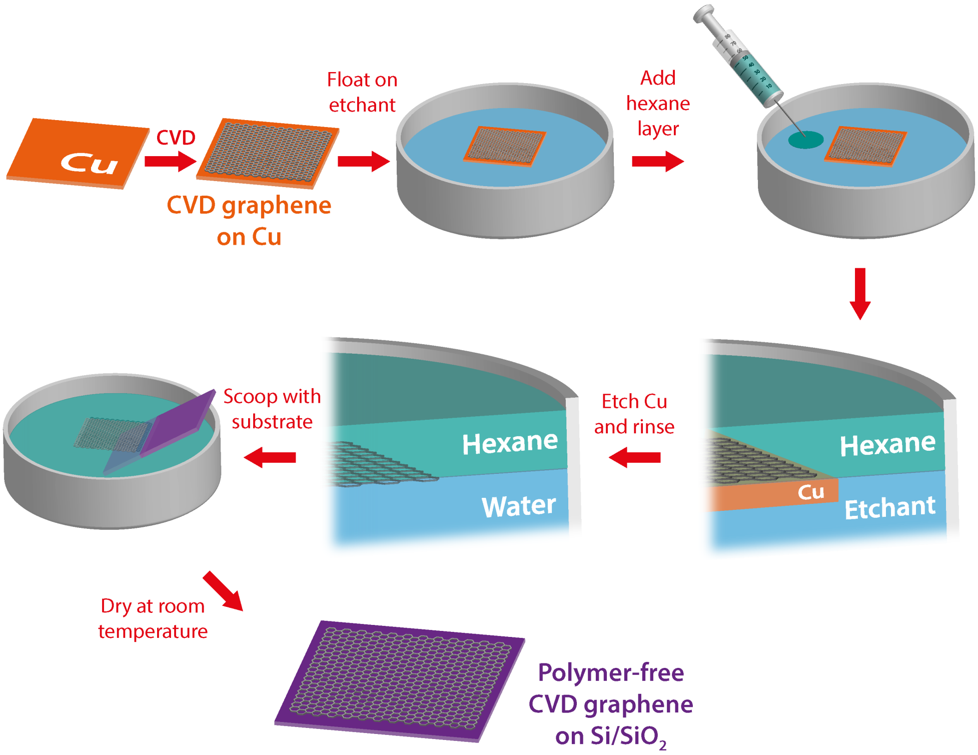
Cu
CVD
CVD graphene on Cu
Float on etchant
Add hexane layer
Scoop with substrate
Hexane
Water
Etch Cu and rinse
Hexane
Cu
Etchant
Dry at room temperature
Polymer-free CVD graphene on Si/SiO2

Figure 2.6 A schematic representation of the introduced polymer-free graphene transfer process.

2.2.6 Graphene Annealing and Microstrip Fabrication

Post PMMA transfer, graphene samples were annealed in a quartz-tube furnace (Lindberg/Blue M, Thermo/Fisher Scienctific) under a flow of 150 sccm H_2 and 1.5 standard litres per minute Ar to remove unwanted PMMA residue. Samples were placed into the chamber, and purged under the gas flow conditions above, before heating to the desired temperature (between 300 °C and 450 °C) as quickly as possible. Samples were annealed for 15 minutes before cooling to 50 °C, always under continuous gas flow, and then removed. Annealed graphene samples were next fabricated into micro-strip devices through a number of steps. Firstly, graphene was spin-coated (3000 RPM, 45 seconds) with a layer of S1818 (Rohm and Haas, USA) positive photoresist and baked at 115 °C for 60 seconds. Photolithography was performed using a mask-aligner (MJB4 SÜSS MircoTec, Germany), exposing the sample to UV light under a specifically designed mask (Figure 2.7(a)), before developing in MF-319 developer solution (Shipley Europe Limited, UK), to leave thin photoresist strips measuring 20 μm × 100 μm across the sample.

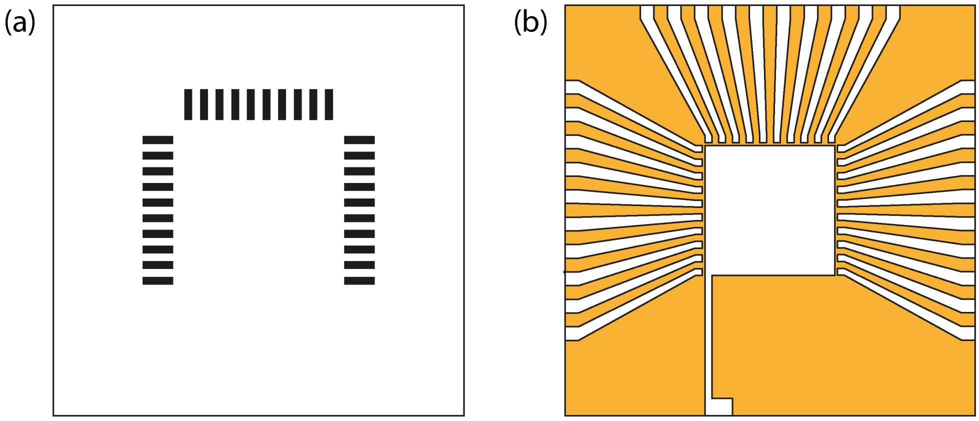

Figure 2.7 (a) A schematic diagram of the designed lithography mask employed to produce graphene microstrips, where white coloring represents transparent acetate areas, and black coloring shows opaque areas, which are transferred when used in combination with a positive photoresist e.g. S1818. (b) The corresponding evaporation mask, made out of Kapton film, for producing metal contacts to the photolithographically defined microstrips.

The entire sample was then exposed to Ar^+ plasma[6] for 5 minutes in a plasma asher (50 W, 4×10^{-1} mbar Ar pressure), conditions determined to be sufficient to completely remove even multilayer areas of graphene to leave a clean surface

(Figure 2.8), unless covered by photoresist strips, which are themselves unaffected by the plasma using the conditions employed.

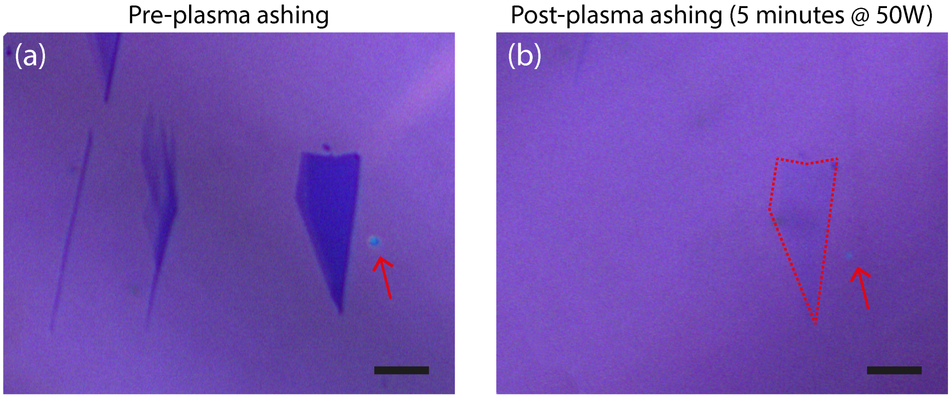

Figure 2.8 Optical images of exfoliated multilayer graphene flakes (a) before and (b) after plasma treatment (Ar^+, 5 minutes, 50 W, 4×10^{-1} mbar). Red arrows highlight a spot of contamination, still mostly present after ashing, confirming the same location, and the red dashed line in (b) shows the area the largest flake was initially present. Scale bars denote 20 μm.

Photoresist strips were subsequently removed by immersion in acetone for 15 minutes. Metallic electrode contacts were made to the individual resulting graphene strips by physical masking with a laser-cut Kapton (Dupont, USA), mask (Figure 2.7(b)) the dimensions of which corresponded to those of the photolithography mask, ensuring perfect electrode alignment with the graphene strips. A thin film of Cr (adhesion layer, 3 nm) followed by Au (60 nm) (Moorfields MiniLab 060, Moorfield associates, Cheshire, UK) was then thermally evaporated onto the sample. Finally, to allow contacting to each of the graphene micro-strips, the sample was mounted on a specifically designed printed circuit board (PCB), to which the individual Au electrodes were connected using wire bonding. The entire device fabrication process (post-anneal, if relevant) is summarized in Figure 2.9.

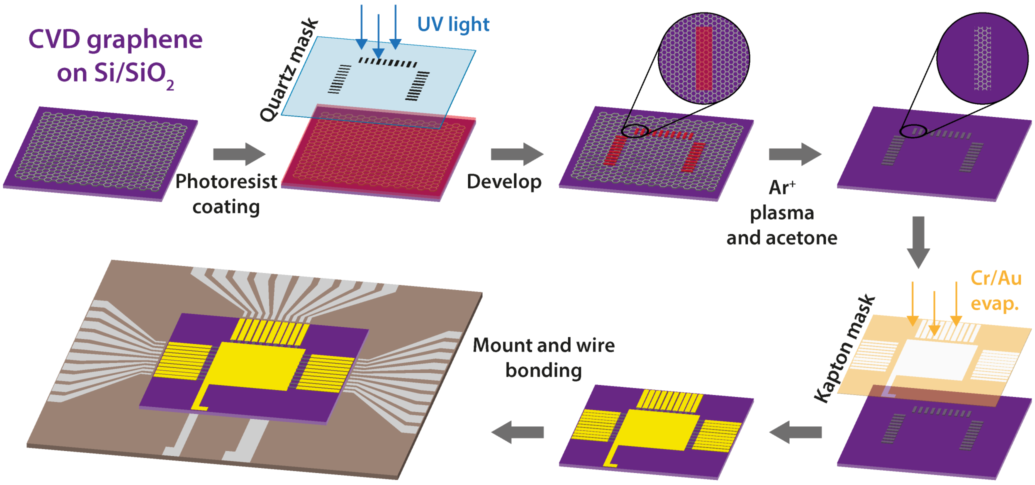
CVD graphene on Si/SiO2
Quartz mask
UV light
Photoresist coating
Develop
Ar+ plasma and acetone
Cr/Au evap.
Kapton mask
Mount and wire bonding

Figure 2.9 Schematic representation of the entire graphene microstrip fabrication process, starting with a transferred graphene sheet on Si/SiO_2, and resulting in 30 individually accessible, electrically connected graphene microstrips.

2.3 QCM-D Measurements

QCM-D binding studies were performed using the Q-Sense E4 system (Q-Sense, Sweden) equipped with a peristaltic pump (IPC-N, Ismatec, Germany) utilizing Kalrez perfluoroelastomer tubing for solvent resistance. Figure 2.10(a) is a photograph of the experimental setup. Post chip functionalization (if relevant), the QCM chip (Figure 2.10(b)) was sealed in the QCM-D flow module (Figure 2.10(b)), before flowing the relevant carrier solvent to be used at 350 μL min^{-1} (previously determined to be the optimal flow rate to avoid excessive pump noise). When solvent could be seen in the outlet tubing, gentle tapping of the flow cell was employed to remove trapped air bubbles, before sealing the cell in the temperature controlled system, set at 25 °C, and leaving the system to equilibrate for a minimum of 30 minutes.

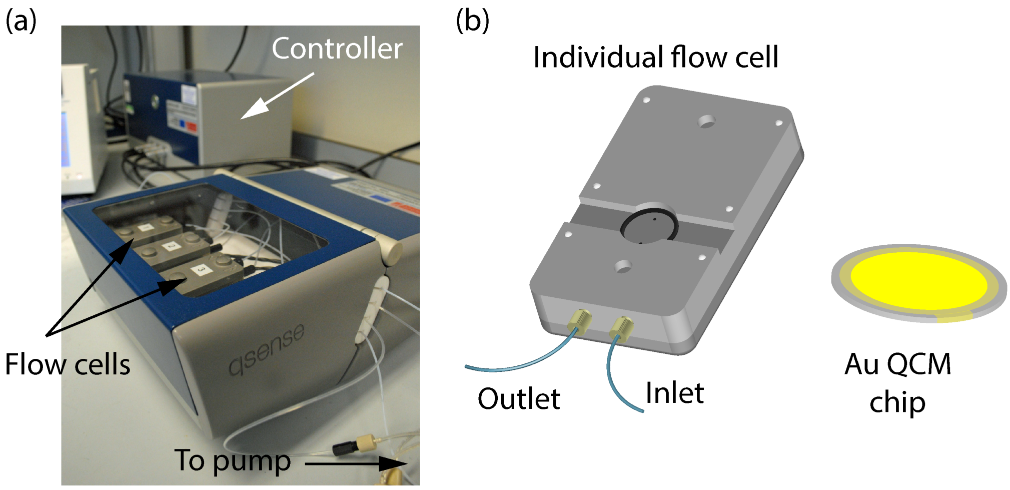

Figure 2.10 (a) A labeled photograph of the QCM-D experimental setup. (b) Schematic diagrams of a QCM-D flow cell, and corresponding Au coated QCM chip.

Post equilibration, the chip was tuned, with the fundamental frequency, f, and overtones $f_3 - f_9$ recorded during the tuning process, along with absolute dissipation, D, values for each tuned frequency. QCM-D chips themselves are reusable if treated carefully, although they have a limited lifetime, with faulty chips highlighting themselves at this tuning stage. Chips that displayed a D value outside the manufacturer's specification ($150 - 250 \times 10^{-6}$ for f_3) were discarded. Post-tuning, pure solvent flow was continued, and it was confirmed that a stable baseline was still present after 10 minutes (< 0.5 Hz drift). Assuming a stable baseline, the pump unit was halted, the solution of interest introduced, and pumping was resumed at 350 μL min^{-1}. Frequency and dissipation changes were recorded for all tuned overtones, until the changes observed had stabilized, indicating no further surface processes occurring. Finally, at this point a pure solvent rinse step was performed. All solutions were sonicated for 5 minutes prior to introduction to the QCM-D system.

2.4 AFM Force Measurements

2.4.1 Instrumentation

Sprint constant determination and force-curve measurements were both performed using a Multimode V AFM with Nanoscope V controller and PicoForce control unit. The probes used had standard Si_3N_4 cantilevers (SNL-10, Bruker Probes, USA), with nominal beam lengths of 200 μm and widths of either 25 μm or 40 μm. Each cantilever had an Si tip with height 2.5 μm – 8.0 μm, notably smaller than the diameter of the colloidal spheres to be attached.

All measurements were performed in a sealed glass fluid cell, filled with the solution of interest, preventing the formation of an atmospheric water contamination layer on surfaces, which would likely dominate any adhesion measurements as a result of capillary forces. After set-up, the system was left for a minimum of 30 minutes for temperature equilibration.

2.4.2 Micromanipulation

A micromanipulation rig was constructed in-house. It consisted of two *xyz* positioning devices (New Focus Inc., USA) mounted on aluminum blocks. Each positioning device had a long metal arm attached, with rigid copper wire securely fastened at the opposite end. Attached to the copper wire was a single eyelash, acting as a sharp probe for micro positioning. The two positioning devices were placed either side of a light microscope (Olympus BH2-UMA), with the eyelash probes visible under the lens. The entire setup was created on a vibration isolation table, and is shown schematically in Figure 2.11.

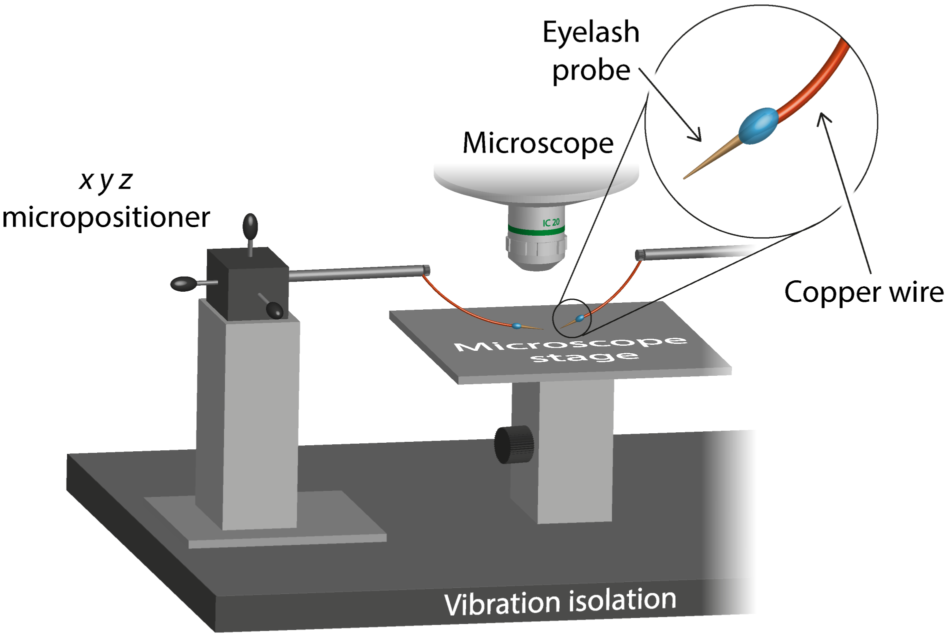

Figure 2.11 Schematic representation of the micromanipulation rig used in this work.

Traditionally, the micromanipulation of colloidal spheres onto AFM tips is performed using rigid tungsten wire, itself etched to a sharp point, allowing for the pickup of small objects. However, initial experiments conducted showed the rigidity of the wire often caused breaking of the delicate AFM cantilevers during manipulation, and a more flexible 'wire' was thus needed. Eyelashes were chosen based on their more flexible nature, and the fact they already provide a sharp point. Eyelashes (previously cleaned by sonication in ethanol, acetone and IPA) were attached to a short length of copper wire (~ 10 cm) with araldite (Bostik Ltd, Leicester). The copper wire was chosen as it could be easily attached to the metal arms of the setup and could be bent into shape easily to allow positioning of the eyelash directly below the microscope objective lens.

Probe modification was performed by placing a single AFM chip and small pile of colloidal particles (14.5 μm diameter, Duke Scientific Corp.) on a glass slide below the microscope objective lens. A droplet of chemically resistant glue (RX771C/NC, Robnor Resins, Wiltshire, UK), smaller than the diameter of the glass spheres, was placed on onto the end of the commercial V-shaped Si_3N_4 cantilever assembly (Figure 2.12(a)) using an eyelash probe, before using the second eyelash probe to place a single colloidal particle (picked up from the pile using capillary forces) onto the drop of glue, securing it to the end of the cantilever. Modified probes were left to dry for 48 hours before further handling.

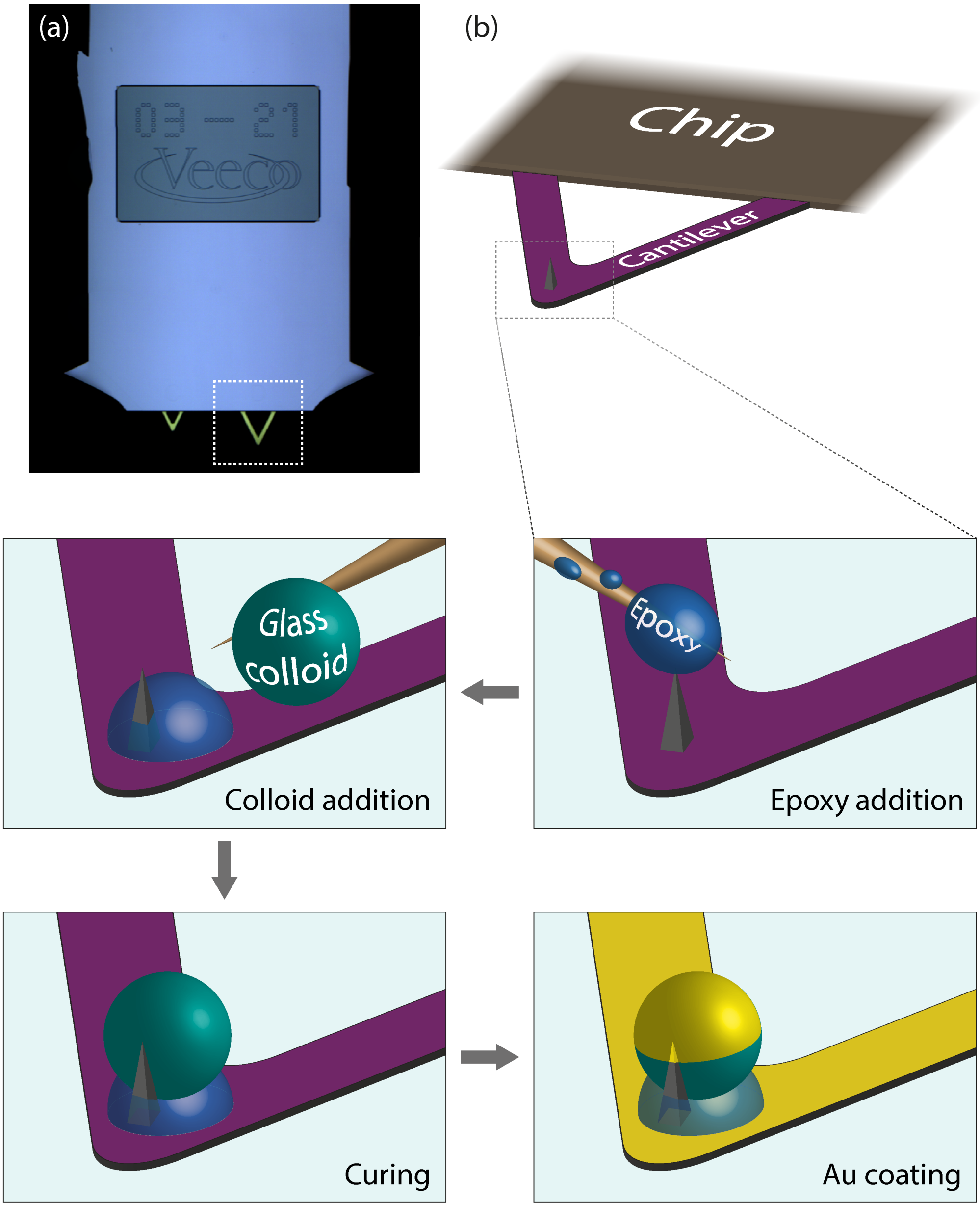
(a)
Veeco
(b)
Chip
Cantilever
Glass colloid
Epoxy
Colloid addition
Epoxy addition
Curing
Au coating

Figure 2.12 A summary of the process used for the production of colloidal AFM probes.

After drying, modified probes were coated with a thin film of Cr (adhesion layer, 3 nm) followed by Au (40 nm) using a thermal evaporator. Au evaporation was performed at a slow rate of 1 Å s^{-1} to avoid excessive heating of the cantilever assembly. The entire probe modification process is summarized in Figure 2.12(b).

2.5 Macroscopic Electrochemical Measurements

All macroscale electrochemical measurements were performed inside a home-built a Faraday cage, housed in an air-conditioned laboratory maintained at 25 °C. Solutions were not deaerated prior to use.

2.5.1 HOPG Substrates

HOPG samples were mounted on top of Cr/Au (2.5 nm / 50 nm) coated Si/SiO_2 wafers using Ag epoxy (RS components), providing electrical contact and a rigid support for the substrate. Macroscopic electrochemical measurements were performed on these HOPG surfaces, by confining the area of the electrolyte droplet using a fluorosilicone rubber O-ring (6.2 mm diameter, Bruker, USA), gently sat on top of the freshly cleaved HOPG surface, before filling with the solution of interest. Electrochemical measurements were performed using a 3-electrode setup, with the required reference (determined by the electrolyte system, typically Ag/AgCl or Pd-H_2) and counter (coiled Pt wire) electrodes placed into the droplet, and contact to the HOPG made via the Au layer using a metal pin. Measurements were subsequently controlled using a bipotentiostat (various models, CH Instruments, Texas, USA). The general setup employed is shown schematically in Figure 2.13, below.

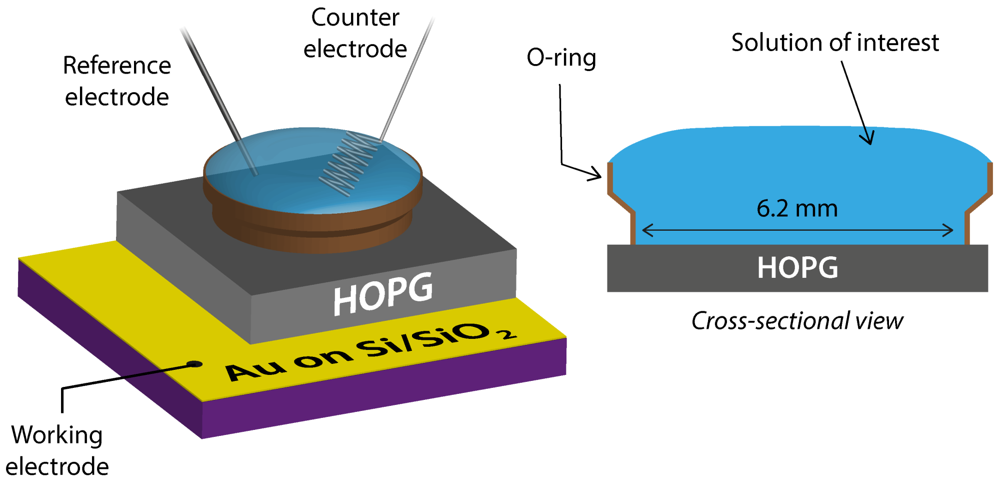
Reference electrode
Counter electrode
HOPG
Au on Si/SiO₂
Working electrode
O-ring
Solution of interest
6.2 mm
HOPG
Cross-sectional view

Figure 2.13 Schematic representation of the setup used for macroscale electrochemical measurements at HOPG surfaces, with the electrolyte droplet confined using a fluorosilicone rubber O-ring.

2.5.2 SAM Coated Substrates

The electrochemical characterization of SAMs required a more constricted electrode area, with the O-ring setup unable to confine the solution of interest on hydrophilic SAMs. Confinement was achieved using a square of Kapton tape (Dupont, USA), ~ 15 mm × 15 mm, with a laser cut hole in the center, exactly 1 mm in diameter. This was stuck over a functionalized QCM-D surface, leaving the gold/SAM exposed through the laser cut hole, with an exposed area of 0.79 mm^2. Electrochemical measurements were performed using the same 3-electrode setup described above, with the exposed area of the QCM-D chip acting as the working electrode (contacted directly through a sharp metal pin).

2.6 SECCM

2.6.1 Tip Fabrication

SECCM tips were pulled from borosilicate theta capillaries (TG 150-10, Harvard Apparatus, UK) using a CO_2 laser puller (Model P-2000, Sutter Instruments, USA) producing tapered pipets with a selectable opening size (ranging from 400 nm to 15 μm in this work). Tapered pipets were silanized by submerging the tip opening in dimethyldichlorosilane whilst flowing Ar through at high pressure (~ 6 bar), resulting in a hydrophobic outer-wall of the pipet. Each barrel was then filled with the solution of interest (*vide infra*), and a relevant quasi-reference counter electrode (QRCE) inserted into each barrel. Capillary laser pulling resulted in two identically sized tapered tips, only one of which was used for SECCM imaging, with the other kept for accurate size measurement using SEM. A typical tapered tip (~ 1 μm in diameter) is shown in Figure 2.14(a), with a zoom-in of the opening in Figure 2.14(b).

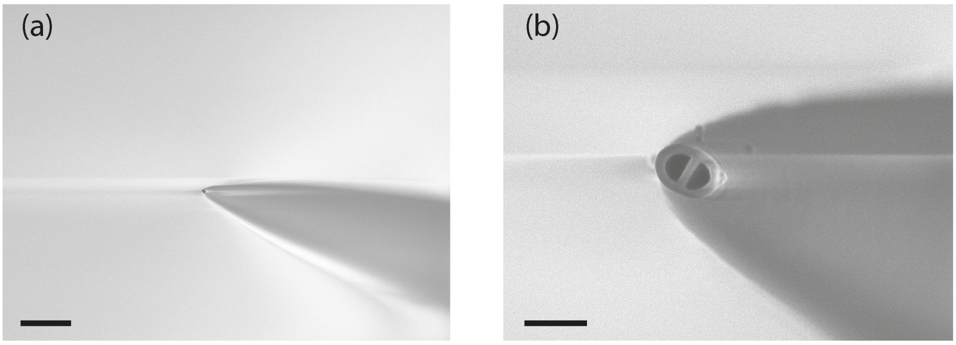

Figure 2.14 (a) SEM micrograph of laser-pulled SECCM tip, with a tapered opening of ~ 1 μm in diameter, and a zoom-in of the same tip (b). Scale bars denote 25 μm and 1 μm for (a) and (b) respectively.

2.6.2 Instrumentation

The home-built SECCM setup[7-9] (Figure 2.15(a)) was controlled using software written in-house, and was contained within a Faraday cage, housed in an air-conditioned laboratory maintained at 25 °C. Solutions were not deaerated prior to use.

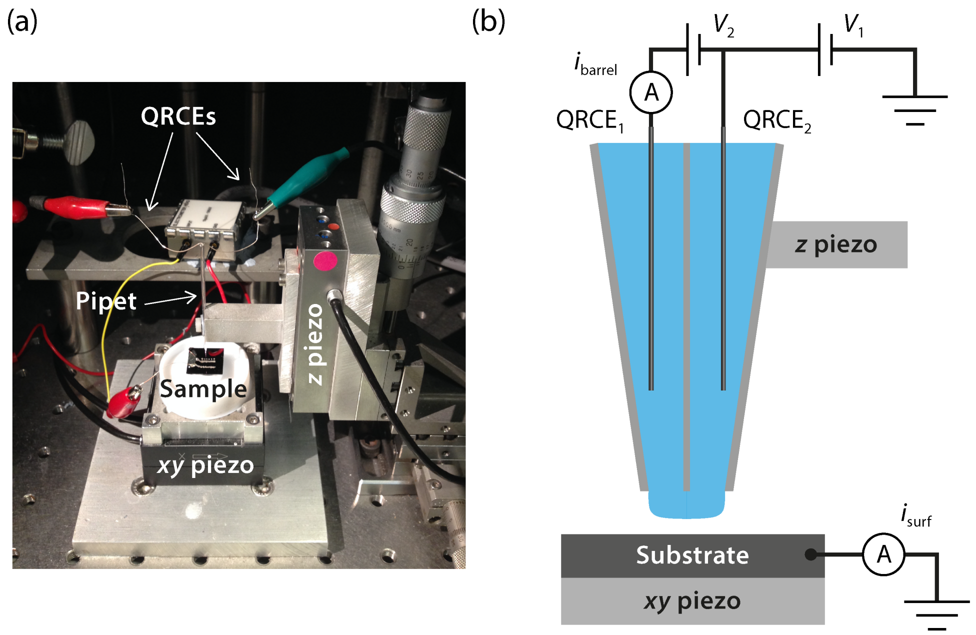

Figure 2.15 (a) A photograph of the SECCM setup for a typical experiment. (b) Illustration of the SECCM tip setup, with applied potentials and measured currents labeled, full details of which are given in the text.

Figure 2.15(b) illustrates the experimental setup schematically. SECCM probes were mounted onto a one-axis *z*-piezoelectric positioner (P-753.3CD, Physik Instrumente, Germany) and oscillated normal to the surface in a sinusoidal fashion, at a pre-determined frequency and amplitude (δ_{osc}) by a means of an alternating current (AC) signal generated by a lock-in amplifier (SR380, Stanford Research Systems, USA). The sample of interest was mounted with a 'moat' of saturated KCl (to reduce evaporation from the meniscus), on a two-axis *xy* piezoelectric stage (P-622.1CD, Physik Instrumente, Germany). Application of a potential bias between the two QCREs (V_2) induced an ion conductance current across the meniscus (i_{barrel}). Application of a second potential to the entire tip (V_1) allowed the potential of the substrate (E_{surf}), itself held at ground, to be controlled, such that $E_{\mathrm{surf}} = -(V_1 + V_2 / 2)$ vs. the chosen QRCE. Any resulting electrochemical current was thus measured as i_{surf}. Both i_{barrel} and i_{surf} were measured using high-sensitivity current to voltage converters, built in-house by Dr. Alex Colburn (Department of Chemistry, University of Warwick).

2.6.3 Imaging Procedure

Post-experimental setup, the tip was manually positioned above the substrate using micro positioners to a distance of ~ 20 μm. The tip was then controllably approached toward the surface (Figure 2.16(a)) at a rate of 50 nm s^{-1}, whilst constantly monitoring both the direct current (DC) (Figure 2.16(b)) and AC (Figure 2.16(c)) components of i_{barrel}. Upon initial contact, compression of the meniscus significantly increased the meniscus resistance, causing a drop in the DC component of i_{barrel} (i_{DC}), and a corresponding increase in the AC component (i_{AC}) due to the periodic deformation of the meniscus with the tip oscillation.[10] Continued approach toward the surface led to the meniscus opening and wetting of the surface, resulting in a sharp increase in both i_{DC} and i_{AC}, the latter of which is highly dependent upon the tip-sample separation, and hence the meniscus contact area. This sensitive parameter was thus used as a feedback set point for imaging and spot deposition, to ensure constant distance between the end of the tip and the substrate. Scanning in the *xy* direction (if applicable) was commenced after a few seconds of meniscus contact, at rates between 0.25 and 1 μm s^{-1}, using i_{AC} set points of 60 pA to 80 pA typically.

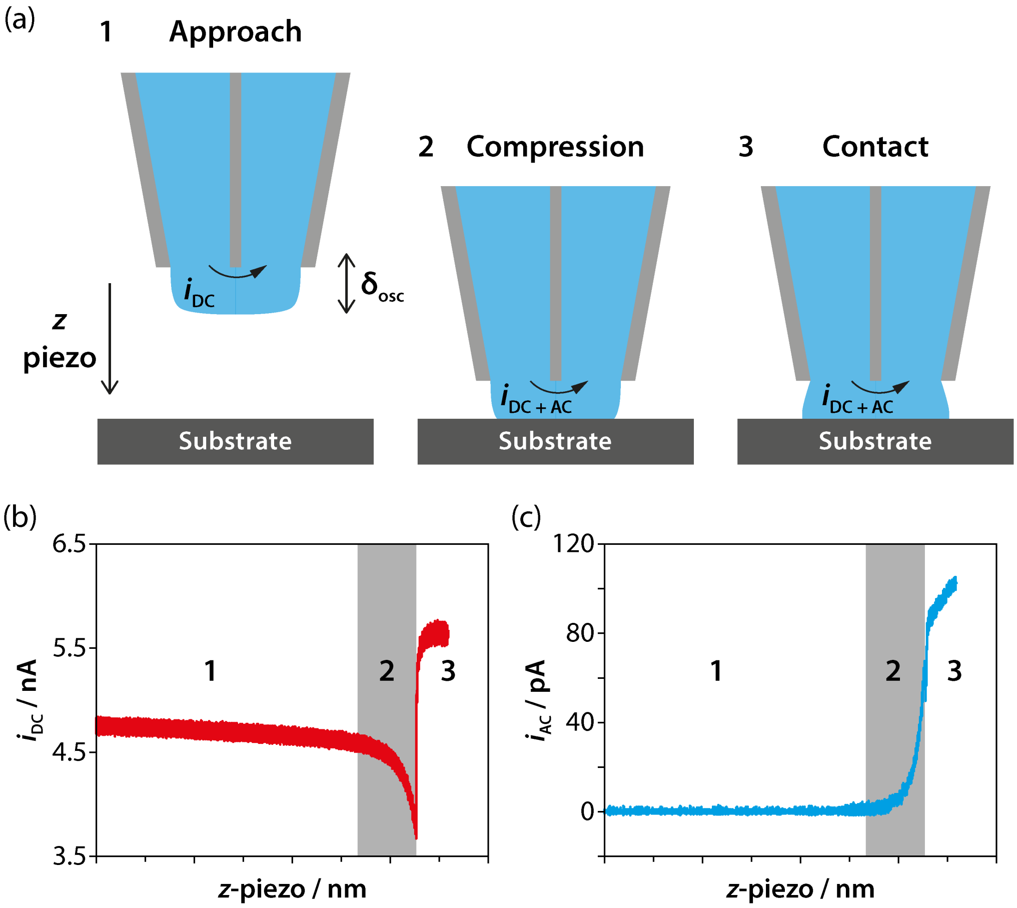

Figure 2.16 (a) The three main steps of meniscus state during an approach to the surface with an SECCM tip, and the corresponding typically measured i_{DC} (b) and i_{AC} (c) values. During approach, only a DC conductance current is measured, owing to the applied bias between the QRCEs. Upon initial surface contact, the meniscus is compressed, causing a decrease in the DC conductance current, but generating a signal in the AC component. At full meniscus opening and contact, large increases in both the DC and AC conductance currents are observed.

Data acquisition was performed at a rate of 1000 Hz using an FPGA card (PCIe-7852R, National Instruments) and a LabVIEW interface.

2.7 Characterization Techniques

2.7.1 Optical Microscopy

Optical microscopy was performed using an Olympus BH2 optical microscope fitted with lenses ranging from 50 × to 1000 × magnification.

2.7.2 AFM

AFM images were recorded using a Bruker-Nano Enviroscope with Nanoscope IV controller under ambient conditions. Images were acquired using standard silicon tapping mode tips (RFESP type, Bruker Probes). Scan sizes are stated in each individual image, whilst scan parameters were adjusted to give the best image obtainable.

2.7.3 SEM

SEM images were acquired using a Zeiss SUPRA 55 VP FE-SEM, typically using a 5 kV accelerating voltage. For colloidal AFM probes, images were acquired post use, preventing contamination of the probe surface. To minimize the extent of charging when imaging borosilicate glass SECCM tips, the majority of the tip was coated with silver epoxy, leaving the very end untouched.

2.7.4 Raman Spectroscopy

Raman spectroscopy was crucial to monitor both the level of diazonium modification at HOPG surfaces, and to investigate the structural integrity and number of layers of graphene (and the subsequent effects of annealing) employed in graphene microstrip device patterning.

Spectra were acquired using Renishaw inVia Raman microscope (coupled to a Leica microscope) fitted with a CCD detector and either a HeNe 633 nm or Ar^+ 514 nm (10 mW power) laser. Spectra were typically acquired using a 50 × magnification lens, resulting in a laser spot with diameter ~ 1 μm.

Prior to acquisition, the spectrometer was calibrated using an Si sample, which displays a prominent peak at 521 cm^{-1}.

Raman mapping measurements were performed using an automated *xy* stage, with a step size of 500 nm, giving some spectral overlap with laser spot size present.

2.7.5 STM

STM tips were mechanically cut from 250 µm diameter Pt/Ir (80/20) wire (Goodfellow Cambridge Limited, UK) using a pair of wire cutters. Tips were cut at roughly a 45 ° angle, with a pulling motion in an attempt to draw out the end to an atomically sharp point. HOPG was imaged to verify tip imaging capabilities at the atomic level. Tips unable to provide atomic resolution on HOPG were re-cut and re-validated. The STM equipment was an ambient system, originally an AFM (Multimode, Veeco, USA) converted for STM use, controlled by a Nanoscope E Controller (Veeco, USA). It was operated in constant-current mode, with selected imaging parameters detailed alongside any obtained data.

2.7.6 Contact Angle

Contact angle measurements were made using a KRÜSS DSA100 drop shape analyzer. Prior to measurements, the water used was sonicated for ~ 20 minutes to remove air bubbles. Droplets were analyzed using specialist KRÜSS software, using a conic section method, and quoted values are an average of 3 individual measurements, taken at both the left and right hand sides of the image (i.e. 6 values in total).

2.8 References

(1) Saby, C.; Ortiz, B.; Champagne, G. Y.; Belanger, D. *Langmuir* **1997**, *13*, 6805.

(2) Williams, D. H.; Fleming, I. *Spectroscopic Methods in Organic Chemistry*; McGraw-Hill, 1995.

(3) Li, X.; Zhu, Y.; Cai, W.; Borysiak, M.; Han, B.; Chen, D.; Piner, R. D.; Colombo, L.; Ruoff, R. S. *Nano Lett.* **2009**, *9*, 4359.

(4) Kang, J.; Shin, D.; Bae, S.; Hong, B. H. *Nanoscale* **2012**, *4*, 5527.

(5) Lin, W.-H.; Chen, T.-H.; Chang, J.-K.; Taur, J.-I.; Lo, Y.-Y.; Lee, W.-L.; Chang, C.-S.; Su, W.-B.; Wu, C.-I. *ACS Nano* **2014**, *8*, 1784.

(6) Ryu, S.; Maultzsch, J.; Han, M. Y.; Kim, P.; Brus, L. E. *ACS Nano* **2011**, *5*, 4123.

(7) Ebejer, N.; Schnippering, M.; Colburn, A. W.; Edwards, M. A.; Unwin, P. R. *Anal. Chem.* **2010**, *82*, 9141.

(8) Güell, A. G.; Ebejer, N.; Snowden, M. E.; McKelvey, K.; Macpherson, J. V.; Unwin, P. R. *P. Natl. Acad. Sci. USA* **2012**, *109*, 11487.

(9) Güell, A. G.; Ebejer, N.; Snowden, M. E.; Macpherson, J. V.; Unwin, P. R. *J. Am. Chem. Soc.* **2012**, *134*, 7258.

(10) Snowden, M. E.; Güell, A. G.; Lai, S. C. S.; McKelvey, K.; Ebejer, N.; O'Connell, M. A.; Colburn, A. W.; Unwin, P. R. *Anal. Chem.* **2012**, *84*, 2483.

Chapter Three

Quantifying Dispersant-Soot Interactions: A Combined QCM-D and AFM Approach

In this chapter, well-characterized model systems are employed as a means to understand the dispersion of carbonaceous soot, a material that displays complex surface chemistry. A systematic study is performed, in which a number of model soot dispersant compounds are designed and synthesized to contain a range of discrete functionalities. Using QCM-D the adsorption of these compounds is screened against model soot surfaces displaying defined functionalities that are typically associated with soot. This approach not only provides an insight into the possible mechanisms of action of dispersant compounds, but also highlights specific chemistries that display a high affinity for the model surfaces, and that may prove effective in soot dispersion as a result. Obtained data corroborates with current literature theory on the sites of interaction of dispersant compounds, and furthermore, CFM is briefly used to highlight the likely site of interaction of the next generation of dispersant compounds.

3.1 Introduction

The popularity of diesel combustion engines has increased significantly in recent years,[1] a trend driven primarily by their more economical operation and reduced greenhouse gas emissions (with respect to petrol engines).[1-3] However, despite their advantages, diesel engines suffer from their own specific drawbacks, emitting high levels of NO_x gases (oxides of nitrogen)[4,5] and generating carbonaceous soot through incomplete diesel fuel pyrolysis within the engine cylinder.[6] Once formed, these highly-acidic, carbon rich colloidal particles are either expelled into the atmosphere through the engine exhaust (exhaust soot), or retained within the engine oil lubricant (engine soot), which they pass to by adsorbing into the thin oil film that coats the cylinder liner.[7] Unfortunately, both of these removal routes pose problems.

The former case makes soot particulate matter one of the main pollutant emissions of exhaust systems,[1,8] the effects of which are linked to respiratory disease[9,10] and global warming.[11] In fact, up to 0.5 % of the fuel mass consumed by diesel engines is emitted as particulate matter,[1] potentially overshadowing the aforementioned advantages of the diesel engine.

Over time, soot retention in engine lubricants also introduces its own complications, the effects of which are the focus of this chapter. Collected particles can agglomerate into μm sized structures (*vide infra*), drastically thickening the oil and increasing its effective viscosity,[12] thus raising greenhouse gas emissions, reducing fuel economy, and increasing levels of engine wear.[4,5,13,14] To this end, packages of hydrocarbon-soluble additives are commonly incorporated into engine lubricants to improve engine combustion and running properties, with one example of such additives being dispersant compounds.[15,16] These widely used surfactants adsorb to the surface of carbonaceous contaminants, keeping them dispersed within the surrounding non-polar media (Figure 3.1(a)), and minimizing their aforementioned undesirable effects.

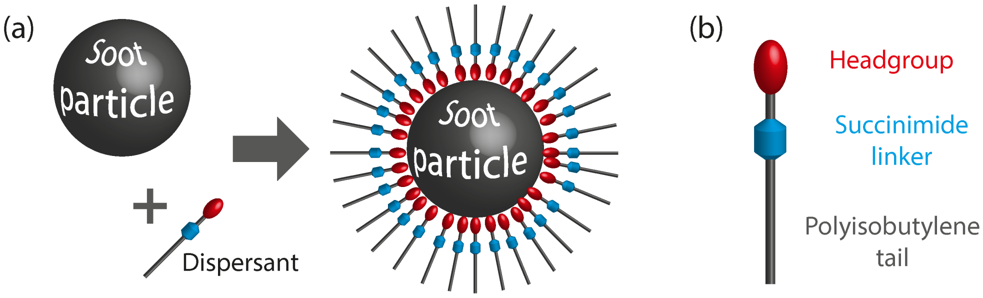

Figure 3.1 (a) Representation of the mechanism of action of dispersant compounds, preventing soot agglomeration through the formation of a hindering barrier. (b) Schematic representation of a PIBSA based engine oil dispersant compound, separated into its three distinct parts.

The most widely studied dispersant structures for automotive use are of the poly(iso-butylene) succinimide ester (PIBSA) class, typically consisting of a polar headgroup, often polyamine based,[14,17] and a non-polar polymer tail, which solubilizes both the molecule and the resulting micelle structure (Figure 3.1(b)). Interactions between dispersant headgroups and soot are mediated through polar atoms or polar oxygen-containing groups, present on the soot surface, effectively serving as binding locations for dispersants.[12] Previous studies have shown that adsorption characteristics can be heavily influenced by changing both the dispersant headgroup and the soot surface.[18] For example, the degree of soot graphitization has been shown to drastically effect its reactivity toward dispersant compounds,[19] with 'unreactive' soot often being more graphitized, likely having a lower surface oxygen content due to a reduced number of edge sites.[20] A study employing carbon black (a common model for automotive soot)[7] demonstrated that increasing the number of amine groups in the PIBSA headgroup increased adsorbed dispersant levels,[21] whilst dispersants of increased basicity were also shown to better handle oil viscosity increases in real engine tests.[22,23] Indeed, such findings suggest that soot-dispersant reactions are similar to acid base reactions.

Upon interaction, the stability of the resulting colloidal dispersion is of course dependent upon the interparticle forces of repulsion being greater than those of attraction, however, the exact nature of the repulsive forces in PIBSA stabilized particles is still unclear. Zeta potential measurements have suggested that PIBSA dispersants can have two effects on soot particles, not only introducing a steric barrier around them (Figure 3.1(a)), but also promoting charge exchange between the soot and dispersant compounds in solution, leaving an associated charge on the particle surface.[24,25] The role of charge stabilization in inorganic media is still poorly understood however,[14] and surface force apparatus experiments between two similarly coated PIBSA surfaces have suggested a pure steric repulsion mechanism, with the obtained results being consistent with models that predict electrostatics not to play a role.[26] The formation of multilayer polyamine dispersant coatings has also been observed through AFM and neutron scattering experiments, adding substance to the argument of steric effects.[21]

3.1.1 The Structure of Soot

The exact makeup of soot is somewhat complex, depending heavily on its synthesis conditions, with factors such as engine temperature, combustion time, and fuel identity all shown to have an effect on its intricate nanostrcture.[19] The literature contains numerous extensive studies investigating soot structure, with techniques such as TEM, Raman spectroscopy, and XPS all commonly used.[6,27-30] Figure 3.2(a) shows a TEM image of a ~ micron sized soot agglomerate, consisting of numerous joined primary soot particles, each ~ 50 nm in diameter, highly representative of that produced in diesel engines, and the ultimate cause of lubricant thickening. Analysis of a single primary particle (Figure 3.2(b)) shows the presence of graphitic domains within it, ordered in a turbostratic fashion. The edges of these domains display a range of oxygen-containing functionalities (i.e. sites for dispersant interaction), with the most common shown in Figure 3.2(c).[27] Functionalities of specific interest to this chapter are marked in red.

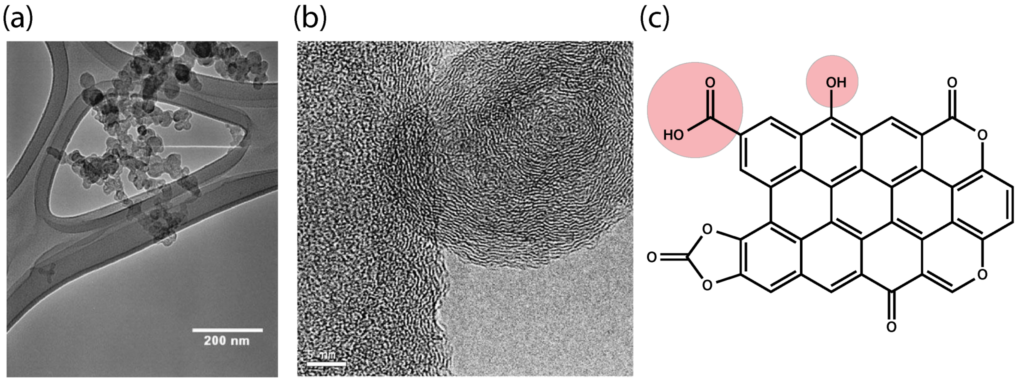

Figure 3.2 (a) TEM image of a soot agglomerate extracted from used engine oil, with a corresponding high-resolution image shown in (b), where the scale bar represents 5 nm.[27] (c) Schematic of the many surface oxygen functionalities present in soot, with functionalities relevant to this work highlighted in red.

Literature exists studying the structure-activity relationships of dispersant compounds, often using carbon black as a model for soot.[17] However, whilst it is a reasonable representation, differences do exist in both the levels of surface functionality and the structure when compared to real soot.[7] Indeed, short of performing costly engine tests for each new molecule synthesized, studying the effectiveness of dispersant compounds is not easy. Moreover, the aforementioned sensitivity of soot structure and surface chemistry to engine design and running conditions means that no two engines will produce identical soot,[22,23,31] with dispersants thus proving more effective in some engines compared to others, and vice versa.

This work provides a detailed, systematic study investigating the effects of changing dispersant headgroup chemistry on the resulting adsorption properties, providing insight into the key interactions occurring at the dispersant-soot interface. Well-defined model soot surfaces are produced using SAM chemistry at Au surfaces, crucially allowing for only a single oxygen-containing functionality (–COOH or –OH) to be displayed to the surrounding environment. The adsorption of 8 model dispersant compounds, which also exhibit a range of discrete headgroup functionalities (amine, carboxylic, hydroxyl, benzyl), is then probed at the model surfaces using QCM-D, a technique renowned for its ability to track minute mass changes at a surface. This approach not only highlights differences in headgroup chemistry on resulting binding affinities at the model surfaces, it provides knowledge at the fundamental level concerning the functionalities that dispersant compounds target, ultimately allowing for future chemistries to be tailored to specific soot chemistries. Furthermore, the real-time *in-situ* nature of QCM-D provides insight to the structural properties of adsorbed layers, not just the total mass adsorbed, providing additional insight into the mechanism of layer deposition. Finally, chemically functionalized AFM probes are developed and briefly used to study the interactions of new generation dispersant chemistries with model carbon surfaces, which are not currently compatible with QCM-D.

3.2 Results and Discussion

3.2.1 Synthesis of Model Dispersant Compounds

8 model PIBSA dispersant compounds were synthesized (details in section 2.1.1), covering a wide range of dispersant headgroup chemistries, whilst maintaining a consistent linker and non-polar tail (Figure 3.1(b)), ensuring that measured differences in binding affinity arise purely from headgroup effects. To aid their solubilization in short-chained non-polar media (model solvent for engine oil), and to simplify their structures generally, the poly(iso-butylene) chain used commercially was simplified to a 12-carbon aliphatic chain. In this thesis, the model dispersant compounds will primarily be compared through their headgroup chemistries, and will thus be drawn to reflect this.

3.2.2 Production of Acid-Terminated SAMs

The ability of 11-MUA and 11-MUD to form –COOH and –OH terminated SAMs and act model soot surfaces was first investigated, using a range of characterization techniques. Indeed, chemistries contained within the model dispersant compounds are known to interact directly at metal surfaces,[16,32] making it somewhat vital that full SAM coverage was achieved.

The formation of –COOH terminated SAMs from 11-MUA was first probed at Au coated mica surfaces, which typically display the Au (111) crystal face over extended areas (*vide infra*), making them suitable for high-resolution imaging studies. Despite the literature being in general agreement that long (i.e. > 6 -CH_2- spacer groups, section 1.3.2) methyl terminated alkanethiols form densely packed monolayers at Au surfaces in dilute ethanolic solutions,[33,34] a clear understanding on the preparation conditions required to obtain similar highly-ordered acid-terminated monolayers is somewhat more lacking. Both Nuzzo *et al.*[35] and Gorman *et al.*[36] have shown that densely packed structures can indeed be formed from acid-terminated alkanethiols in pure ethanol. However, numerous other studies have demonstrated a significant degree of disorder using this simple preparation method,[37,38] instead suggesting that the inclusion of acetic acid in the solution improves the quality of SAM structures. Furthermore, Willey *et al.*[39] showed that including a KOH rinse step in the preparation procedure improved alignment of the acid group, and Wang *et al.*[40] suggested the addition of CF_3COOH to the ethanolic thiol solution prevented the formation of bilayer structures at the surface.

Figure 3.3(a) shows a typical STM image of a bare Au on mica substrate, prior to SAM modification (STM details in section 2.7.5). Clearly visible are triangularly shaped, atomically flat domains, with lateral dimensions of 60 - 200 nm. Such features are typical of those observed for Au films on mica, and previous x-ray diffraction studies on similar terraces have shown them to consist predominantly of Au (111) crystallites,[41] whilst high-resolution STM studies have also revealed the characteristic $23 \times \sqrt{3}$ reconstruction associated with the Au (111) surface at such terraces.[42]

Figure 3.3(b) shows a typical STM image of an identical substrate after immersion in a 1 mM 11-MUA ethanolic solution for 24 hours, conditions typical of those used in the literature for the formation of SAMs at Au substrates.[34] The resultant surface appears littered with ‘particulate’ matter, despite rinsing in ethanol. Such features are near identical to those observed by Wang *et al.*,[40] who attributed them to non-chemisorbed thiol molecules forming bilayer type structures through cyclic H-bonding interactions with already bound acid moieties. Continual degradation in image resolution also suggested STM tip contamination over time, consistent with loosely bound matter at the surface.

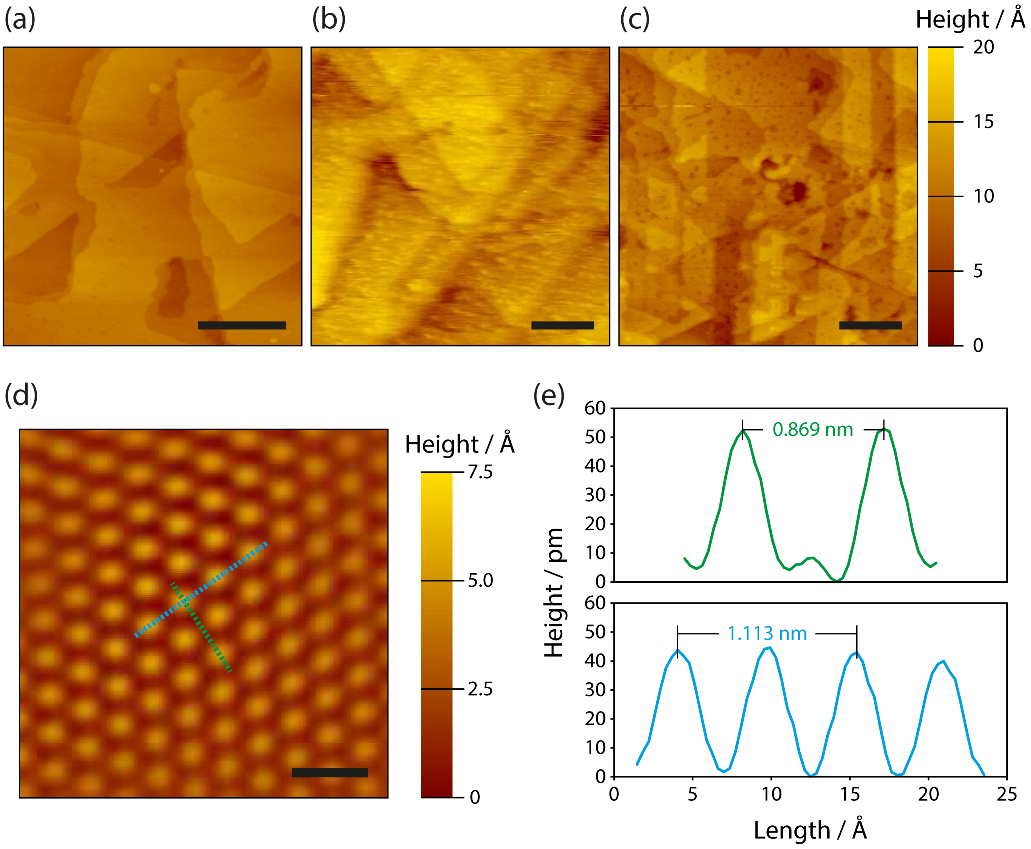

Figure 3.3 STM images of (a) a typical Au (111) on mica surface prior to thiol modification (200 mV bias, set-point = 125 pA) (b) the resulting surface post modification with 1 mM 11-MUA in ethanol displaying the formation of bilayer areas (200 mV bias, set-point = 150 pA) and (c) the resulting surface post modification with 1 mM 11-MUA + CF_3COOH using the methodology introduced by Wang *et al.* (200 mV bias, set-point = 125 pA). Scale bars denote 50 nm. (d) High resolution STM image of an 11-MUA modified Au (111) sample using the Wang *et al.* method. (Filtered by Fourier transformation, 800 mV bias, set-point = 40 pA) Scale bar denotes 1.5 nm. (e) Height profile measurements corresponding to the dashed lines in (d), confirming the presence of a densely packed monolayer.

A modified preparation procedure was thus adopted with the aim of preventing the formation of such bilayer structures. As introduced by Wang *et al.*,[40] this involved immersing the Au sample in a 1 mM 11-MUA ethanolic solution with 2% (v/v) CF_3COOH, for 24 hours, before thorough rinsing using 10% (v/v) NH_4OH and pure ethanol. Figure 3.3(c) shows an STM image of an Au (111) surface modified using this new procedure. Now, imaging typically revealed ordered domains of 11-MUA separated by domain boundaries, Au (111) step edges and a large number of newly introduced depressions, or so called ‘etch-pits’. Poirier[43] and Liu[44] investigated the origin of such pits, which are considered indicative of a surface modified by alkanethiol molecules and are generated as a result of an Au surface reconstruction upon thiol binding. It should be noted that such pits still contain SAM modified Au, but are depressed by a single Au atomic layer. Interestingly, similar pits were not visible in Figure 3.3(b), likely as a result of the low image quality obtainable. High-resolution imaging on individual terraces of this surface further revealed a densely packed SAM of 11-MUA molecules, with Figure 3.3(d) showing its well-ordered nature at molecular resolution. Colored dashed lines show height profile measurements, displayed in Figure 3.3(e), and profile measurements of 0.869 nm and 1.113 nm (theoretical 0.867 nm and 1.00 nm, respectively) are in agreement with the $(3 \times 2\sqrt{3})$ primitive unit cell for SAM structures made up from *n*-alkanethiols.[45]

Analysis of surfaces modified using 1 mM ethanolic solutions of 11-MUD and also 1-dodecanethiol ($-CH_3$ terminated) revealed similarly densely packed layers, with packing densities identical to that of 11-MUA. Indeed, identical packing densities between the SAM functionalities used herein is crucial to such a systematic study; ensuring any differences in observed adsorption behavior are due to the SAM head group chemistry, rather than variation in the number of available surface binding sites.

3.2.3 Characterization of SAMs at QCM Surfaces

Whilst the information gained from STM studies at model Au (111) surfaces provides high-resolution information on SAM formation and packing, in reality, it is the case that polycrystalline Au substrates are the benchmark for much of the published work in the QCM-D field, owing to the ease with which they can be commercially prepared. Sputtered polycrystalline surfaces have however been demonstrated to consist predominantly of the Au (111) crystal face, with O'Dwyer *et al.* performing x-ray diffraction on sputtered Au films (with a Cr adhesion layer) to demonstrate this.[46] Figure 3.4(a) shows a 1 µm × 1 µm AFM image of a typical clean QCM-D chip surface this used in this study, with many discrete crystallites now visible, leading to an associated roughness average, R_a, of 1.03 nm (as determined by AFM image analysis), significantly higher than that observed for Au on mica surfaces (Figure 3.3(a)).

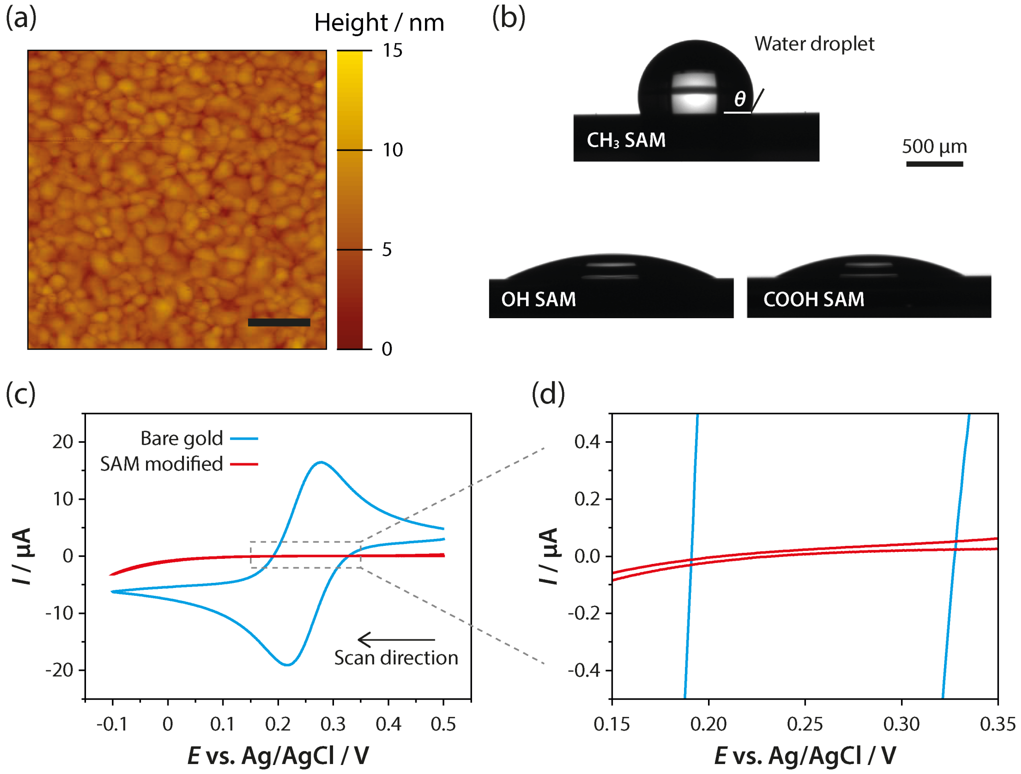

Figure 3.4 (a) Typical AFM image of a polycrystalline Au surface on a QCM-D chip, prior to modification with a SAM. Scale bar denotes 200 nm. (b) Images captured during water contact angle measurements for QCM-D chip surfaces functionalized with 1-dodecanethiol, 11-MUD and 11-MUA. The contact angle quoted in the text is also marked, denoted as *θ*. (c) CVs at 100 mV s^{-1} for the reduction of 10 mM $K_3[Fe(CN)_6]$ in 0.1 M KCl on a QCM-D electrode surface, before and after modification with 11-MUD. (d) A zoom-in of the area marked in (c), highlighting the complete lack of a faradaic current response.

The ability of the selected alkanethiol molecules to form densely packed SAMs at these polycrystalline Au surfaces was investigated through contact angle measurements (details in section 2.7.6). Figure 3.4(b) shows the wettability of surfaces modified using 1-dodecanthiol (–CH_3 terminated), 11-MUD (–OH terminated), and 11-MUA (–COOH terminated), with the latter prepared using the modified procedure method described above. Contact angle values (± 1 S.D.) of 109.2 ± 0.9 °, 26.2 ± 0.9 ° and 25.5 ± 0.7 ° were measured for –CH_3, –OH and –COOH terminations respectively (N=3), in very close agreement with values commonly found in the literature,[33] and indicative of well modified surfaces.

Further characterization of the SAM interface was performed using a CV method, in which the SAM coated QCM-D chip acted as the working electrode in an electrochemical measurement (details in section 2.5.2). A circular area measuring 0.79 mm^2 was defined on the QCM-D chip surface post modification, allowing for the confined addition of a solution containing the redox mediator $K_3[Fe(CN)_6]$ (10 mM in 0.1 M KCl). Figure 3.4(c) shows the CV response of this mediator at an 11-MUD modified electrode surface, along with a comparison for an identical surface that had not undergone SAM modification. Firstly, the bare electrode shows the expected response for the reduction of $K_3[Fe(CN)_6]$ at a macro-sized disk electrode, with a measured peak current, i_p, of 18.5 μA, in close agreement with that predicted by the Randles-Sevcik equation[47] of 17.9 μA (assuming a diffusion coefficient, D, of 7.20×10^{-6} cm^2 s^{-1}).[48] In comparison, the modified surface displays a completely diminished current response, with no evidence of a measurable faradaic process occurring, and significantly reduced background currents (Figure 3.4(d)). If present, exposed pinholes within the SAM layer would act as an array of recessed Au nanoelectrodes,[49] manifested as a reduced steady-state response around $E^{0'}$ in the CV.[50] Near identical CV responses, to that shown in Figure 3.6 (red line) were obtained for SAMs created from 11-MUA and 1-dodecanethiol, also suggesting the observed blocking is not attributed to electrostatic effects between the SAM head group and redox mediator.[51]

3.2.4 Adsorption of Hydroxyl Based Dispersants at Model Surfaces

With the ability of the selected thiol compounds to effectively form model soot surfaces confirmed, the adsorption of synthesized model dispersant compounds at modified QCM-D chip surfaces was investigated. Briefly, in a typical QCM-D adsorption experiment, pure solvent was passed over the modified chip surface until a stable baseline was observed, before the model dispersant compound of interest (dissolved in the same solvent) was introduced to the flow module, at a matching flow rate (350 μL min^{-1} herein). After adsorption had equilibrated (if applicable), flow was reverted back to pure solvent for a rinse process, removing loosely bound material from the surface and eliminating any effects associated with differences in the viscosity/density of the solutions used.[52,53] This methodology is common practice in the literature.[54] Frequency changes (Δf) were monitored for all available overtones (up to f_{13}), as was the absolute dissipation value, D. Full experimental details of QCM-D operation is described in section 2.3, and an overview of its principles of operation is provided in section 1.3.1. For all adsorption experiments discussed, measurements were made from a 1 mM model dispersant concentration in a 90 % toluene/10 % hexane (v/v) mix, conditions commonly used by Lubrizol as representative of commercial engine oil.

The adsorption of hydroxyl-based dispersant compounds **I** and **II** (Figure 3.5) was first monitored at –COOH and –OH SAM modified surfaces.

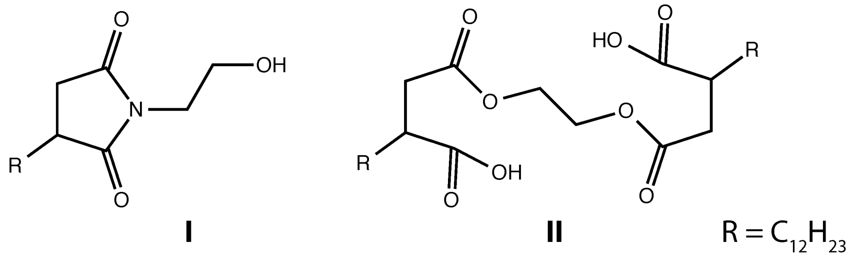

Figure 3.5 The headgroup structures of model dispersant compounds **I** and **II**.

Typical Δ*f* vs. time plots for the adsorption of compound **I** at –COOH and –OH surfaces are shown in Figures 3.6(a) and 3.6(b), respectively. Negligible overtone splitting was observed during adsorption, thus data from only the third overtone, f_3, is presented. Data recorded at the fundamental frequency is typically discarded in QCM experiments due to the high noise levels often observed within it, resulting from the overwhelming sensitivity of this overtone to factors such as O-ring seating/placement in the flow module.

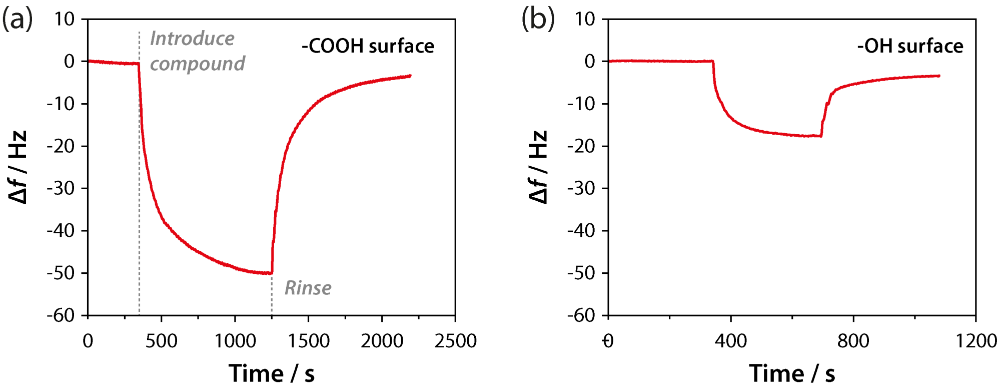

Figure 3.6 Typical Δ*f* vs. time plots for the adsorption of compound **I** from a 1 mM solution (90 % toluene/10 % hexane (v/v)) at (a) –COOH and (b) –OH functionalized surfaces. Only data collected from f_3 is presented as negligible overtone splitting was observed.

Obtained plots appear qualitatively similar at both functionalized surfaces, with the only apparent difference being in the magnitude of the measured frequency changes. Both show mass addition at the surface (i.e. negative Δf changes), with the adsorption processes equilibrating at ~ -50 Hz and ~ -18 Hz, suggestive of significantly more bound material at the –COOH surface. Upon rinsing, almost complete reversibility is observed, with the vast majority of compound **I** removed in both cases and a return to the baseline value evident, indicating that any attached material was loosely bound. This suggests compound **I** to have a low affinity for both the surfaces investigated, as may be expected due to its lack of basicity and current literature models. Such data is in good agreement with that observed by Lubrizol, who typically use compounds with headgroups similar to compound **I** as 'poor-reference tests'.

Figures 3.7(a) and 3.7(b) show typical QCM-D plots for the adsorption of compound **II** at –COOH and –OH surfaces, respectively.

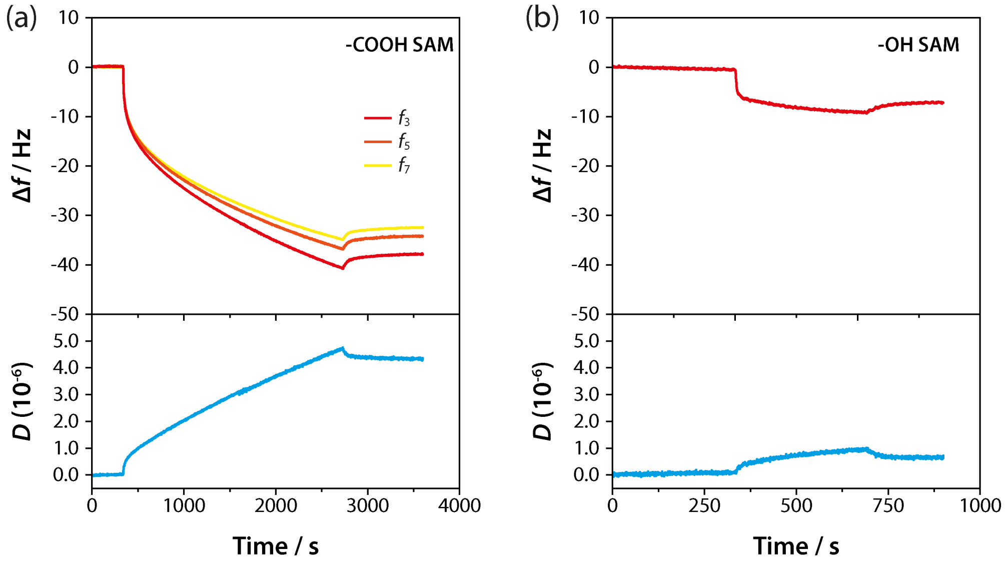

Figure 3.7 Typical Δf and D vs. time plots for the adsorption of compound **II** from a 1 mM solution (90 % toluene/10 % hexane (v/v)) at (a) –COOH and (b) –OH functionalized surfaces. In (b), only data collected from f_3 is presented as negligible overtone splitting was observed.

In stark contrast to that observed for **I**, the adsorption of **II** appears to be highly dependent on the surface functionality present. Focusing on the –COOH functionalized surface, an initially rapid adsorption process is observed, followed by one of a linear nature, which did not reach equilibrium even after 45 minutes. The initial process is likely due to binding at the bare –COOH surface, slowing after a change of ~ -18 Hz, at which point apparent multilayer adsorption begins at a constant rate. Overtones $f_3 - f_7$ are presented, showing a small amount of splitting in the linear adsorption step, suggesting the multilayer film displays increasing viscoelastic character, which is also evident in the measured D values, where a continual increase with time is seen. Adsorbed material appears irreversibly bound, with minimal mass loss occurring upon rinse, also ruling out solvent intercalation/swelling as the sole reason for the linear increase (since rinsing would likely encourage further solvent uptake). In comparison, adsorption at the –OH surface occurs to a much lesser extent, suggesting the proposed multilayer formation relies on an already present adsorbed layer, found only at the –COOH surface, likely as a result of hydrogen bonding to the –COOH groups present in the dispersant.

Quantitative surface coverage values, Γ, were determined for compounds **I** and **II** (post-rinse) using the Sauerbrey approximation (eq 1.8) and data obtained at f_3.[55] As described in section 1.3.1, the approximation is only valid for systems of a rigid nature, making its applicability to extended multilayer systems somewhat questionable. No long-standing rule exists on the exact point as which the Sauerbrey relationship breaks down, however Reviakine *et al.*[56] proposed that when $D/-\Delta f < 4 \times 10^{-7}$ Hz^{-1}, its application is still valid, and this rule is satisfied for the systems above. Figure 3.8 presents calculated Γ values for compounds **I** and **II** at –COOH and –OH functionalized surfaces, using the known molecular weights for each of the compounds.

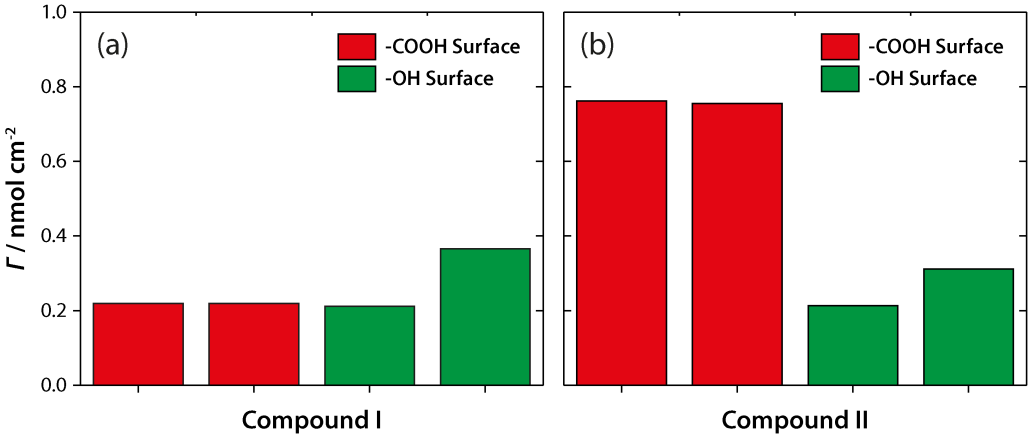

Figure 3.8 Determined Γ values (post-rinse via the Sauerbrey equation) for the adsorption of compounds **I** and **II** at (a) –COOH and (b) –OH functionalized surfaces from 1 mM solutions (90 % toluene/10 % hexane (v/v)). Coverage values are determined from data obtained at f_3, and are presented in duplicate.

In combination with the QCM-D plot analysis above, it is clear that compound **II** shows significantly higher levels of adsorption at –COOH surfaces, where multilayer structures likely appear, and that the layers formed in all other cases are only weakly bound. H-bonding interactions between the dispersant headgroup and model surface may drive this affinity. Investigations into compounds of similar structure to **I** and **II** are rare in the literature, although the data shown here suggests the extended multilayers formed may prove effective at preventing soot agglomeration. However, their acidic character may limit use in commercial applications, where it is desirable to keep additive acidity to a minimum.

3.2.5 Adsorption of Amine Based Dispersants at Model Surfaces

The adsorption of amine-based dispersant compounds **III** and **IV** (Figure 3.9) was next monitored at –COOH and –OH SAM modified surfaces.

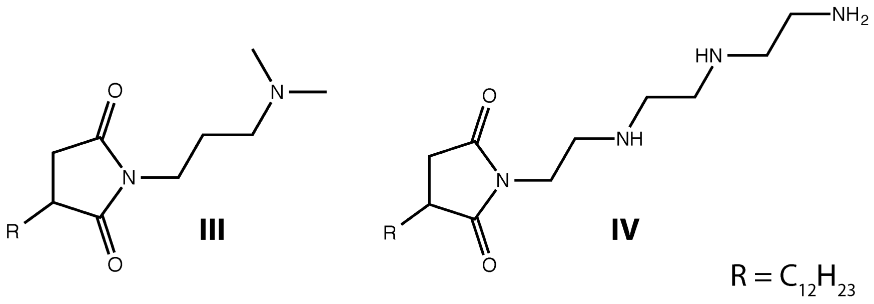

Figure 3.9 The headgroup structures of model dispersant compounds **III** and **IV**.

Typical Δf vs. time plots for the adsorption of compound **III** at –COOH and –OH surfaces are shown in Figures 3.10(a) and 3.10(b), respectively. Negligible overtone splitting was observed during adsorption, thus data from only the third overtone, f_3, is presented.

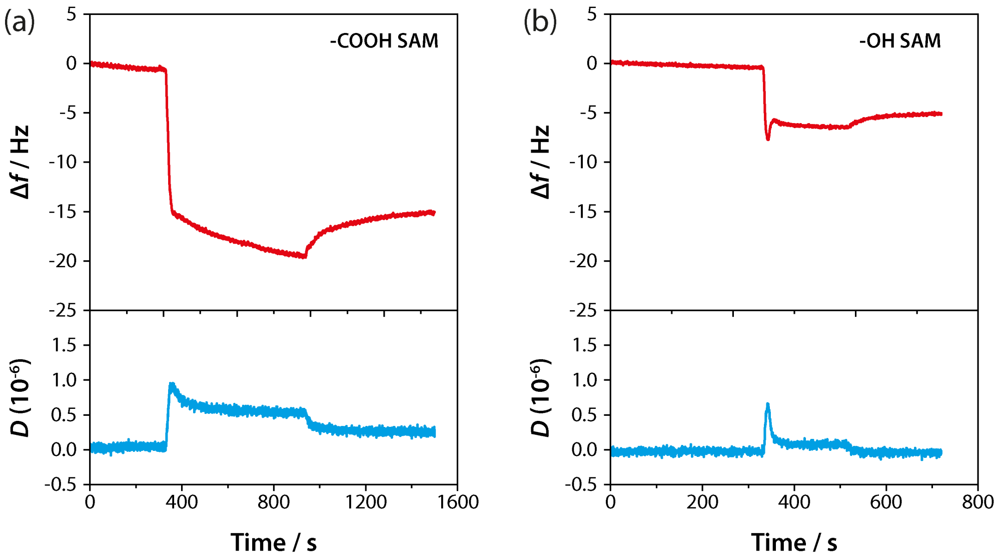

Figure 3.10 Typical Δf and D vs. time plots for the adsorption of compound **III** from a 1 mM solution (90 % toluene/10 % hexane (v/v)) at (a) –COOH and (b) –OH functionalized surfaces. Only data collected from f_3 is presented as negligible overtone splitting was observed.

As was the case for compound **I** (*vide supra*), obtained plots for the adsorption of compound **III** at both modified surfaces appear to be qualitatively similar, although some interesting additional features are also observed. Both plots appear to show two discrete processes occurring, with an initial fast process immediately upon dispersant introduction, followed by a much slower process. Inspection of the complementary D values also appears to show a unique feature, whereby the mass initially introduced at the surface (fast process) actually increases in rigidity after initial adsorption. Whilst unusual, almost identical responses have been observed in biological systems when studying vesicle adsorption process. Using various complementary analysis techniques, Richter *et al.*[57] attributed this initial fast process to the adsorption of vesicles at the QCM-D surface, with the slower process and subsequent reduction in *D* caused by vesicle spreading, to produce a thin, tightly bound film. The Δf vs. time plot for adsorption at the –OH surface further supports this idea, where an apparent reduction in mass occurs soon after initial adsorption, likely attributed to solvent associated with discrete particles also being trapped at the surface, before being released upon particle spreading/rupturing. The polar nature of the tertiary amine in compound **III** will likely encourage the formation of micelle type structures in aliphatic media (as used herein), and when investigating the adsorption of amine based dispersants at activated carbon surfaces Cox *et al.*[58] suggested that they adsorbed in an aggregated form. In addition, Kozak *et al.*[17] highlighted the possibility of hemi-micelle structures being present at surfaces when investigating dispersant adsorption. Figure 3.11 shows Γ values estimated using the Sauerbrey equation for the adsorption of compound **III** at model soot surfaces. Despite the somewhat unique adsorption behavior observed, an affinity difference is evident for the surfaces investigated. Post-rinse, compound **III** shows significantly more bound material at the –COOH surface ($\Gamma = 0.75$ nmol cm^{-2}), likely a result of acid-base interactions driven by the tertiary amine. In comparison, adsorption at –OH surfaces appears to be ~ 30 % of that at –COOH, with $\Gamma = 0.25$ nmol cm^{-2}.

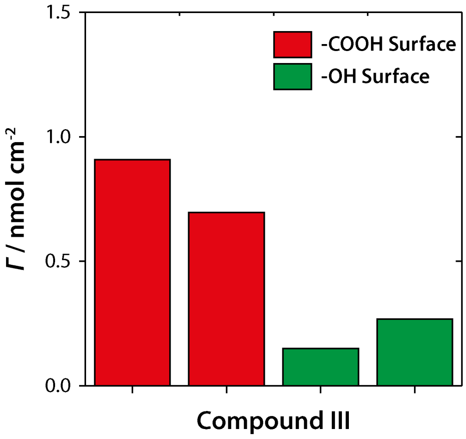

Figure 3.11 Determined *Γ* values (post-rinse via the Sauerbrey equation) for the adsorption of compound **III** at –COOH and –OH functionalized surfaces from a 1 mM solution (90 % toluene/10 % hexane (v/v)). Coverage values are determined from data obtained at f_3, and are presented in duplicate.

Finally, Figure 3.12 presents typical Δ*f* vs. time plots for the adsorption of compound **IV** at –COOH (Figure 3.12(a)) and –OH (Figure 3.12(b)) surfaces.

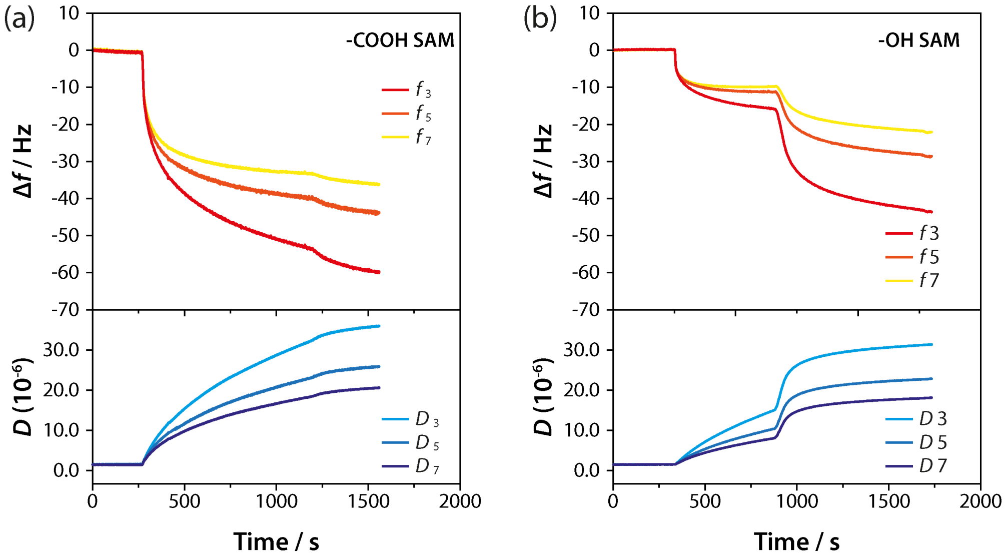

Figure 3.12 Typical Δ*f* and *D* vs. time plots for the adsorption of compound **IV** from a 1 mM solution (90 % toluene/10 % hexane (v/v)) at (a) –COOH and (b) –OH functionalized surfaces.

Δ*f* vs. time plots for compound **IV** show distinctly different behavior to that observed for all other model dispersants investigated. Indeed, such a fact is interesting in itself, since compound **IV**'s linear polyamine chain makes it by far the closest match to commercially used dispersant compounds. Focusing on the –COOH terminated surface, an initial, fast adsorption process is observed, which quickly slows to a second process, occurring over a longer timescale, and that doesn't appear to equilibrate, at least on the timescale investigated herein. Large associated values of *D* (in comparison with those observed previously) are also evident, suggesting the film to be of a viscoelastic nature, likely ascribed to multilayer formation, or possible solvent inclusion (*vide infra*). Such large values of *D* also rule out the possibility of estimating the mass adsorbed via the Sauerbrey equation, however, a qualitative view can still be obtained.

Unusually, a further slight increase in mass (i.e. decrease in frequency) is apparent upon rinsing. Firstly, this suggests the layer to be firmly attached, since no apparent mass loss is observed, likely as a result of the significant interactions between the –COOH surface and primary amine containing model dispersant. Secondly, the small change suggests a level of solvent intercalation/swelling to be occurring, further backed by the associated increase in *D* also observed during rinsing, indicating an increase in the fluid like properties of the formed film. Of course, such solvent incorporation during rinsing may also suggest significant levels of solvent to be contained within film during the formation step, but de-convoluting such effects is difficult.

Behavior at the –OH modified surface appears qualitatively similar, with the adsorption process resulting in 25 % of the change compared to the –COOH surface, likely as a result of preferential binding to –COOH sites. Similar values of *D* are also observed during binding, again suggesting a viscoelastic film. Strikingly, significant further mass addition is observed during the solvent rinse step, accompanied by a huge change in *D*. This again suggests solvent intercalation/swelling of the film, to a much more significant extent than observed at the –COOH surface.

3.2.6 Adsorption at Surfaces Lacking Polar Functionality

With both amine compounds displaying adsorption behavior highly dependent upon surface functionality, adsorption was next monitored at $–CH_3$ modified SAM surfaces. Figure 3.13 shows Δf vs. time plots (only f_3 presented due to negligible overtone splitting) for the adsorption of compounds **III** (Figure 3.13(a)) and **IV** (Figure 3.13(b)) at $–CH_3$ modified surfaces.

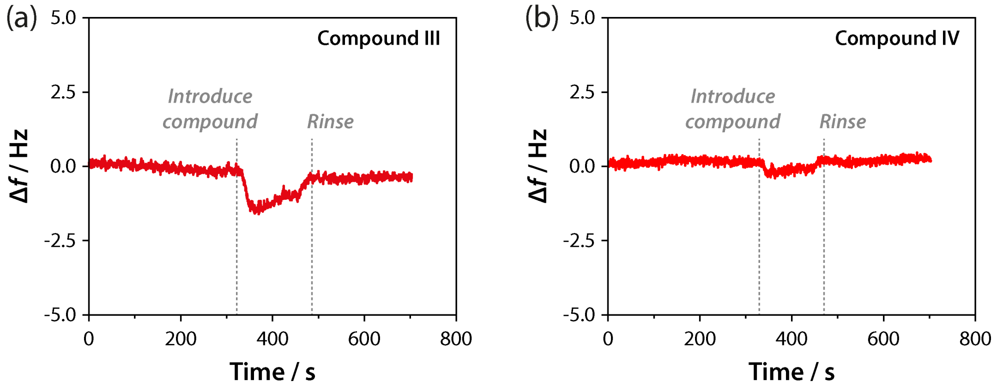

Figure 3.13 Typical Δf and D vs. time plots for the adsorption of compounds (a) **III** and (b) **IV** at $–CH_3$ SAM functionalized surfaces from a 1 mM solution (90 % toluene/10 % hexane (v/v)). Only data collected from f_3 is presented as negligible overtone splitting was observed.

Clearly evident in both cases, is a distinct lack of adsorption, suggesting the compounds have negligible surface affinity for the $–CH_3$ terminal groups displayed. This provides a good baseline reference for the data obtained above, reiterating the fact that binding is driven by interactions with oxygen containing functional groups at the surface of soot, in complete agreement with that proposed in the literature.[12]

3.2.7 Adsorption of Aromatic Based Dispersants at Model Surfaces

Finally, adsorption experiments of model dispersant compounds displaying aromatic functionality (Figure 3.14) were investigated. As can be seen from their structures, these compounds generally lack the amine or basic functionality traditionally associated with dispersant compounds. Despite this, in-house measurements at Lubrizol have highlighted such compounds as performing extremely well in testing, and they are somewhat representative of the latest generation of dispersant compounds.

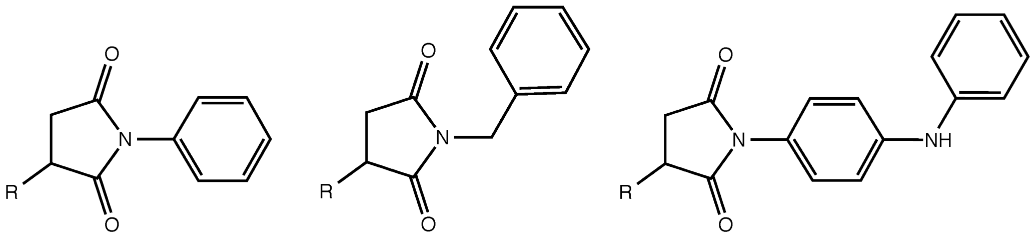

V **VI** **VII**

R = $C_{12}H_{23}$

Figure 3.14 The headgroup structures of model dispersant compounds **V, VI** and **VII**.

Figures 3.15(a), 3.15(b) and 3.15(c) summarize the levels of adsorption at oxygen-containing model soot surfaces, presenting calculated *Γ* values determined post-rinse using the Sauerbrey equation, for the adsorption of compounds **V**, **VI**, and **VII** respectively.

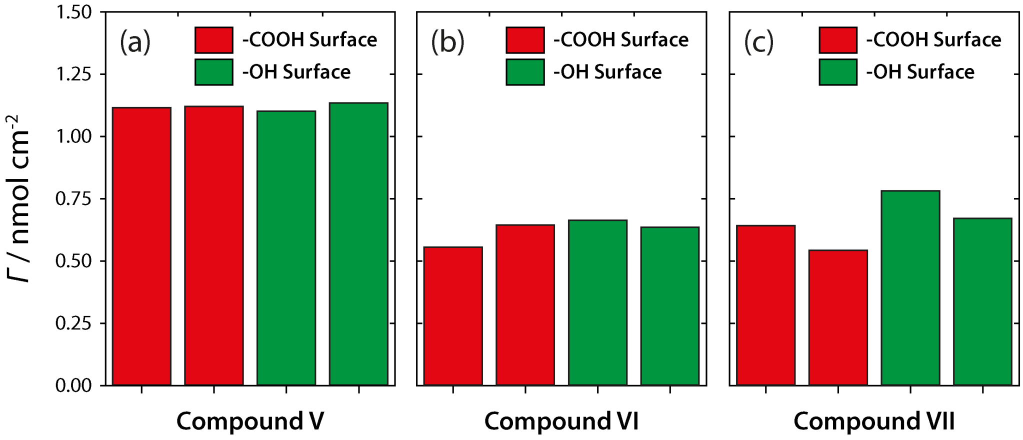

Figure 3.15 Determined *Γ* values (post-rinse via the Sauerbrey equation) for the adsorption of compounds **V**, **VI** and **VII** at –COOH and –OH functionalized surfaces from 1 mM solutions (90 % toluene/10 % hexane (v/v)). Coverage values are determined from data obtained at f_3, and are presented in duplicate.

It is clear is that none of the aromatic compounds show a distinct preference towards either functionalized surface, in agreement with the notion that basic functionality is often required for surface adsorption. Interestingly, significant levels of adsorption were seen overall, albeit independent of surface functionality. Additional QCM-D experiments at $-CH_3$ functionalized surfaces also showed high levels of adsorption, suggesting the observed response to be completely independent of surface functionality, and potentially related to the solubility of the compounds in solution.

3.2.8 CFM to Study Aromatic Dispersant Interactions

To gain further insight into the nature of the interactions between aromatic dispersant compounds and soot surfaces, quantitative force measurements were made using AFM apparatus, in the technique known as CFM (see section 1.4.2.1). A significant advantage of the CFM approach over QCM is the wide range of surfaces at which adhesion forces can be studied, including carbon substrates (*vide infra*).

Commercial AFM probes were first modified with colloidal glass particles measuring ~ 15 μm in diameter using a micromanipulation method, described in detail in section 2.4.2. Once modified, probes were coated with a thin Au layer (40 nm), to allow for their subsequent modification using SAM chemistry. Figure 3.16(a) shows a false color SEM image of a probe modified with a colloidal particle before being Au coated.

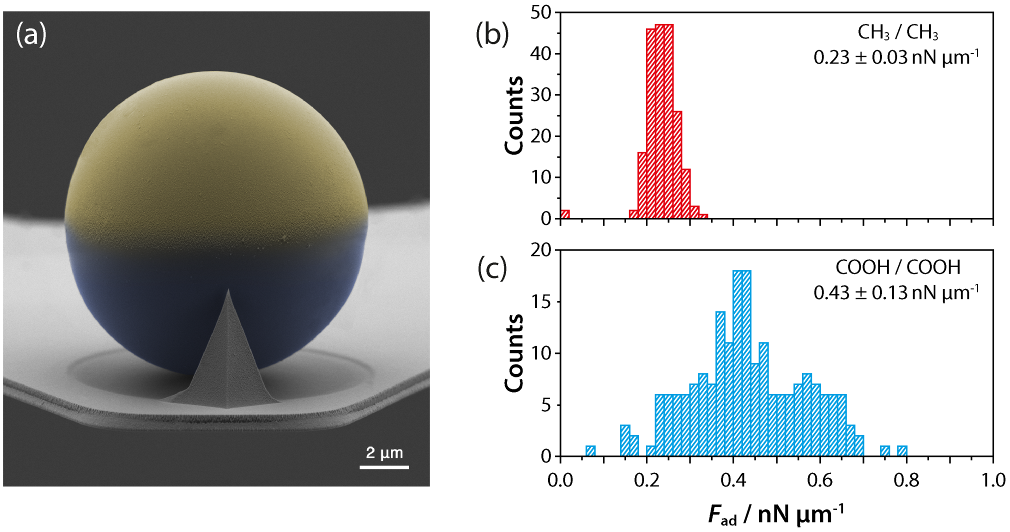

Figure 3.16 (a) False color SEM image of a commercial AFM probe modified with a colloidal glass particle and coated in Au. Histograms showing normalized F_{ad} values for 200 repeat force-curve measurements between tip-surface combinations displaying (b) $-CH_3$, and (c) –COOH functionality. Force curve measurements were performed in ethanol.

The validity of this tip modification procedure was verified by measuring adhesion forces between a functionalized tip and substrate for a previously well-characterized system. Au coated colloidal probes were modified with both $-CH_3$ and –COOH functionality using the SAM formation procedures described above, and Au coated Si/SiO_2 substrates (coated during AFM tip modification) were similarly modified to display $-CH_3$ and –COOH chemistries. Force-curve measurements were subsequently performed between–CH_3 modified tips and surfaces, and–COOH tips and surfaces, in a surrounding ethanol environment, which prevented the effects of capillary forces acting on the tip (full experimental details provided in section 2.4.1). Figures 3.16(b) and 3.16(c) show histograms of the measured adhesion forces, F_{ad}, for 200 repeat force-curve measurements using the $-CH_3$ functionalized tip-surface combination and the –COOH tip-surface combination, respectively. Determined forces are normalized by the radius of the colloidal sphere used in each case (accurately determined by SEM after force-curve measurements) to account for differences in contact area.

In the case of $–CH_3$ measurements, an average value (± 1 S.D.) of 0.23 ± 0.03 nN μm^{-1} was obtained for F_{ad}, almost half of that measured at –COOH terminated surfaces, where $F_{ad} = 0.43 \pm 0.13$ nN μm^{-1}. This difference can be explained by the presence of H-bonds between –COOH groups, increasing the measured interaction forces vs. $–CH_3$ groups, where van der Waals forces likely dominate adhesion. The differences observed agree closely with those in the literature for the same SAM combinations,[59,60] confirming this as a valid route for CFM probe preparation, and for measuring specific interaction forces.

To exploit this approach in measuring aromatic dispersant interactions, a variation on compound **VI** was synthesized by Lubrizol that contained a thiol moiety at the end of the non-polar chain (i.e. terminating the chain), allowing for the formation of SAMs that displayed aromatic headgroup character. Colloidal AFM probes were thus immersed in a 1 mM ethanolic solution of this thiol compound for 24 hours, resulting in their modification and thus the production of 'dispersant coated tips'. These tips were subsequently used to perform force-curve measurements at three different surfaces. Force-curve measurements were first performed between the aromatic dispersant tip and SAM coated surfaces that displayed –COOH and –OH functionality (prepared using identical method to QCM-D chips) - a concept analogous to that in QCM-D experiments, except the dispersant chemistry is now surface bound at the colloidal tip. Measurements were performed in a hexane environment, since issues related to solubility were no longer relevant, and curves were acquired 150 times, at two different surface locations, on both surfaces. Figures 3.17(a) and 3.17(b) are histograms showing the resulting F_{ad} values measured at both the –COOH and –OH surfaces, respectively.

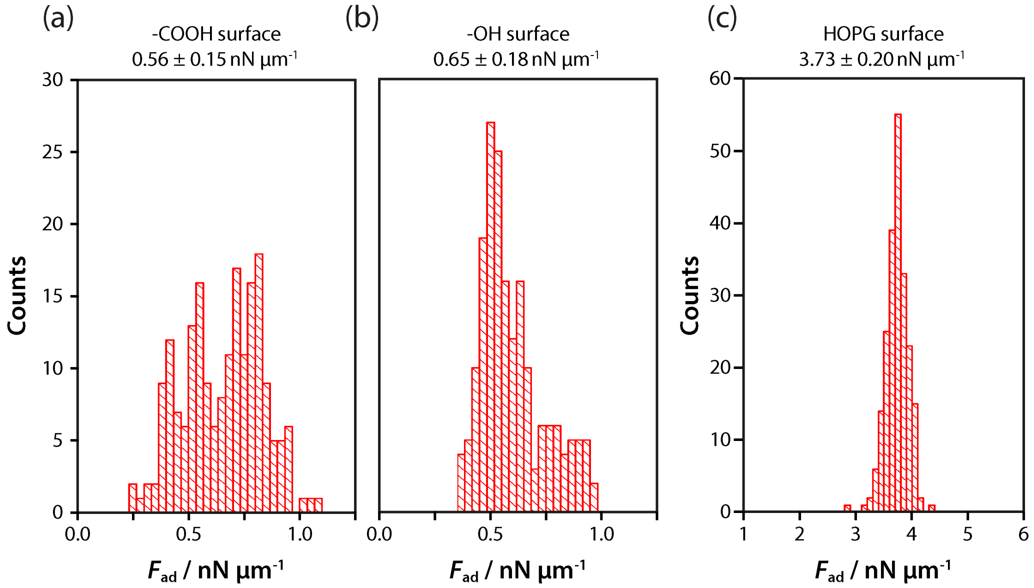

Figure 3.17 Histograms showing normalized F_{ad} values for 300 (2 × 150) repeat force-curve measurements between an aromatic dispersant coated tip and (a) a –COOH functionalized surface (b) an –OH functionalized surface, and (c) freshly cleaved ZYA HOPG. Force curve measurements were performed in hexane.

Average values (± 1 S.D.) of 0.56 ± 0.15 nN μm^{-1} and 0.65 ± 0.18 nN μm^{-1} were recorded for F_{ad} at the –COOH and –OH surfaces, which, within error, corroborates the QCM-D data that suggested aromatic dispersants had no preferential affinity for either of the oxygen containing functionalities. Secondly, force-curve measurements were performed at a pristine sp^2 carbon surface, namely freshly cleaved ZYA HOPG, chosen to be representative of graphitic domains of soot, where little oxygen functionality is present. Identical measurements to those above demonstrated a significant increase in average F_{ad}, now measured at 3.73 ± 0.20 nN μm^{-1}. This stark difference when compared to that measured at oxygen containing polar surfaces provides an insight into the likely interaction site for aromatic dispersant compounds, suggesting that such compounds target the graphitic nature of soot, rather than the polar groups that litter its surface, likely making such compounds good at dispersing soot that would otherwise be considered ‘unreactive’.

3.3 Conclusions

To conclude, the adsorption characteristics of a range of model dispersant compounds with varying headgroup chemistries were screened against model soot surfaces using the QCM-D technique. The adsorption of amine-based compounds was shown to heavily depend on the presence of polar, oxygen containing functionality at the surface, in agreement with the literature that such sites act as locations for dispersant binding. Surface sites that were acidic in nature (–COOH) heavily encouraged dispersant binding, primarily through acid-base interactions, also in agreement with the literature that such interactions are crucial in soot dispersion. Polyamine compounds were shown to form strongly bound, swollen multilayers, providing a possible explanation for their long proven ability to effectively disperse soot. Interestingly, dispersants containing acid functionality displayed similar features, however their acidic nature may limit their commercial value. Dispersant compounds that displayed aromatic character, and that have proven effective at dispersing soot (despite lacking basicity) were shown to adsorb at surfaces, but with little preference for specific functionality. Additional CFM measurements further investigated this, suggesting their likely site of interaction to be graphitic domains on soot, rather than polar functional groups, making them potential candidates for dispersing soot that may traditionally be considered unreactive.

3.4 References

(1) Xi, J.; Zhong, B. J. *Chem. Eng. Technol.* **2006**, *29*, 665.

(2) Daido, S.; Kodama, Y.; Inohara, T.; Ohyama, N.; Sugiyama, T. *JSAE Rev.* **2000**, *21*, 303.

(3) Maricq, M. M. *J. Aerosol Sci.* **2007**, *38*, 1079.

(4) George, S.; Balla, S.; Gautam, V.; Gautam, M. *Tribol. Int.* **2007**, *40*, 809.

(5) George, S.; Balla, S.; Gautam, M. *Wear* **2007**, *262*, 1113.

(6) Sadezky, A.; Muckenhuber, H.; Grothe, H.; Niessner, R.; Poschl, U. *Carbon* **2005**, *43*, 1731.

(7) Clague, A. D. H.; Donnet, J.; Wang, T. K.; Peng, J. C. M. *Carbon* **1999**, *37*, 1553.

(8) Pickett, L. M.; Siebers, D. L. *Combust. Flame* **2004**, *138*, 114.

(9) Stanmore, B. R.; Brilhac, J. F.; Gilot, P. *Carbon* **2001**, *39*, 2247.

(10) Miller, F. J.; Gardner, D. E.; Graham, J. A.; Lee, R. E.; Wilson, W. E.; Bachmann, J. D. *J. Air Pollut. Control Assoc.* **1979**, *29*, 610.

(11) Pueschel, R. F.; Kinne, S. A. *Sci. Total Environ.* **1995**, *160-61*, 811.

(12) Esangbedo, C.; Boehman, A. L.; Perez, J. M. *Tribol. Int.* **2012**, *47*, 194.

(13) La Rocca, A.; Di Liberto, G.; Shayler, P. J.; Parmenter, C. D. J.; Fay, M. W. *Tribol. Int.* **2014**, *70*, 142.

(14) Won, Y. Y.; Meeker, S. P.; Trappe, V.; Weitz, D. A.; Diggs, N. Z.; Emert, J. I. *Langmuir* **2005**, *21*, 924.

(15) Mortier, R. M.; Fox, M. F.; Orszulik, S. T. *Chemistry and Technology of Lubricants*; Springer, 2010.

(16) Kozak, D.; Davies, M.; Moreton, D.; Vincent, B. *J. Disper. Sci. Technol.* **2009**, *30*, 782.

(17) Kozak, D.; Moreton, D.; Vincent, B. *Colloid Surf. A* **2009**, *347*, 245.

(18) Aleman-Vazquez, L. O.; Villagomez-Ibarra, J. R. *Fuel* **2001**, *80*, 965.

(19) Wal, R. L. V.; Tomasek, A. J. *Combust. Flame* **2003**, *134*, 1.

(20) Boehm, H. P. *Carbon* **1994**, *32*, 759.

(21) Dubois-Clochard, M. C.; Durand, J. P.; Delfort, B.; Gateau, P.; Barre, L.; Blanchard, I.; Chevalier, Y.; Gallo, R. *Langmuir* **2001**, *17*, 5901.

(22) Covitch, M.; Humphrey, B.; Ripple, D. *SAE Technical Paper* **1985**, 852126.

(23) Bardasz, E.; Carrick, V.; George, H.; Graf, M.; Kornbrekke, R.; Pocinki, S. *SAE Technical Paper* **1997**, 971693.

(24) Pugh, R. J.; Matsunaga, T.; Fowkes, F. M. *Colloid Surface* **1983**, *7*, 183.

(25) Pugh, R. J.; Fowkes, F. M. *Colloid Surface* **1984**, *9*, 33.

(26) Georges, E.; Georges, J. M.; Hollinger, S. *Langmuir* **1997**, *13*, 3454.

(27) Patel, M.; Ricardo, C. L. A.; Scardi, P.; Aswath, P. B. *Tribol. Int.* **2012**, *52*, 29.

(28) Braun, A.; Shah, N.; Huggins, F. E.; Kelly, K. E.; Sarofim, A.; Jacobsen, C.; Wirick, S.; Francis, H.; Ilavsky, J.; Thomas, G. E.; Huffman, G. P. *Carbon* **2005**, *43*, 2588.

(29) Chen, Y. Z.; Shah, N.; Braun, A.; Huggins, F. E.; Huffman, G. P. *Energy Fuels* **2005**, *19*, 1644.

(30) Muller, J. O.; Su, D. S.; Jentoft, R. E.; Wild, U.; Schlogl, R. *Environ. Sci. Technol.* **2006**, *40*, 1231.

(31) *Internal Lubrizol documentation.*

(32) Chen, F.; Li, X.; Hihath, J.; Huang, Z.; Tao, N. *J. Am. Chem. Soc.* **2006**, *128*, 15874.

(33) Bain, C. D.; Troughton, E. B.; Tao, Y. T.; Evall, J.; Whitesides, G. M.; Nuzzo, R. G. *J. Am. Chem. Soc.* **1989**, *111*, 321.

(34) Ulman, A. *Chem. Rev.* **1996**, *96*, 1533.

(35) Nuzzo, R. G.; Dubois, L. H.; Allara, D. L. *J. Am. Chem. Soc.* **1990**, *112*, 558.

(36) Gorman, C. B.; He, Y. F.; Carroll, R. L. *Langmuir* **2001**, *17*, 5324.

(37) Arnold, R.; Azzam, W.; Terfort, A.; Woll, C. *Langmuir* **2002**, *18*, 3980.

(38) Dannenberger, O.; Weiss, K.; Himmel, H. J.; Jager, B.; Buck, M.; Woll, C. *Thin Solid Films* **1997**, *307*, 183.

(39) Willey, T. M.; Vance, A. L.; van Buuren, T.; Bostedt, C.; Nelson, A. J.; Terminello, L. J.; Fadley, C. S. *Langmuir* **2004**, *20*, 2746.

(40) Wang, H.; Chen, S. F.; Li, L. Y.; Jiang, S. Y. *Langmuir* **2005**, *21*, 2633.

(41) Chidsey, C. E. D.; Loiacono, D. N.; Sleator, T.; Nakahara, S. *Surf. Sci.* **1988**, *200*, 45.

(42) Barth, J. V.; Brune, H.; Ertl, G.; Behm, R. J. *Phys. Rev. B* **1990**, *42*, 9307.

(43) Poirier, G. E. *Langmuir* **1997**, *13*, 2019.

(44) Yang, G. H.; Liu, G. Y. *J. Phys. Chem. B* **2003**, *107*, 8746.

(45) Poirier, G. E.; Tarlov, M. J. *Langmuir* **1994**, *10*, 2853.

(46) O'Dwyer, C.; Gay, G.; de Lesegno, B. V.; Weiner, J. *Langmuir* **2004**, *20*, 8172.

(47) Bard, A. J.; Faulkner, L. R. *Electrochemical Methods: Fundamentals and Applications*; Wiley, 2001.

(48) Konopka, S. J.; McDuffie, B. *Anal. Chem.* **1970**, *42*, 1741.

(49) Finklea, H. O.; Snider, D. A.; Fedyk, J.; Sabatani, E.; Gafni, Y.; Rubinstein, I. *Langmuir* **1993**, *9*, 3660.

(50) Sheffer, M.; Vivier, V.; Mandler, D. *Electrochem. Commun.* **2007**, *9*, 2827.

(51) Malem, F.; Mandler, D. *Anal. Chem.* **1993**, *65*, 37.

(52) Parlak, Z.; Biet, C.; Zauscher, S. *Meas. Sci. Technol.* **2013**, *24*, 085301.

(53) Wang, D. X.; Mousavi, P.; Hauser, P. J.; Oxenham, W.; Grant, C. S. *Colloids Surf. A* **2005**, *268*, 30.

(54) Dobrzanska, D. A.; Cooper, A. L.; Dowson, C. G.; Evans, S. D.; Fox, D. J.; Johnson, B. R.; Biggs, C. I.; Randev, R. K.; Stec, H. M.; Taylor, P. C.; Marsh, A. *Langmuir* **2013**, *29*, 2961.

(55) Sauerbrey, G. *Z. Phys.* **1959**, *155*, 206.

(56) Reviakine, I.; Johannsmann, D.; Richter, R. P. *Anal. Chem.* **2011**, *83*, 8838.

(57) Richter, R. P.; Brisson, A. R. *Biophys. J.* **2005**, *88*, 3422.

(58) Cox, A. R.; Mogford, R.; Vincent, B.; Harley, S. *Colloids Surf. A* **2001**, *181*, 205.

(59) Noy, A.; Frisbie, C. D.; Rozsnyai, L. F.; Wrighton, M. S.; Lieber, C. M. *J. Am. Chem. Soc.* **1995**, *117*, 7943.

(60) Frisbie, C. D.; Rozsnyai, L. F.; Noy, A.; Wrighton, M. S.; Lieber, C. M. *Science* **1994**, *265*, 2071.

Chapter Four

Molecular Functionalization of Graphite Surfaces: Basal Plane versus Step Edge Electrochemical Activity

In this chapter, the adsorption and electrochemistry of AQDS is studied on HOPG as a model sp^2 *surface. A major focus is to elucidate whether adsorbed electroactive AQDS can be used as a marker of step edges, which have generally been regarded as the main electroactive sites on graphite electrode surfaces. First, the macroscopic electro-chemistry of AQDS is studied on a range of surfaces differing in step edge density by more than 2 orders of magnitude, complemented with ex situ tapping mode AFM data. These measurements show that step edges have little effect on the extent of adsorbed electroactive AQDS. Second, a new fast scan cyclic voltammetry protocol carried out with SECCM enables the evolution of AQDS adsorption to be followed locally on a rapid time scale. Subsequent AFM imaging of the areas probed by SECCM allows a direct correlation of the electroactive adsorption coverage and the actual step edge density of the entire working area. The amount of adsorbed electroactive AQDS and the electron transfer kinetics are independent of the step edge coverage. This work provides new methodology to monitor adsorption processes at surfaces and shows unambiguously that there is no correlation between the step edge density* *of graphite surfaces and the observed coverage of electroactive AQDS. The electroactivity is dominated by the basal surface, and studies that have used AQDS as a marker of steps need to be revised.*

4.1 Introduction

Since Sir Humphrey Davy's historic use of graphitic rods in his 1800s arc lamp, carbon has become somewhat synonymous with electrode materials.[1] From an electrochemical perspective, traditional materials such as GC, graphite and doped diamond have largely dominated, especially in (electro)analytical[2-6] and (electro)catalytic[7] applications, although recent emphasis on CNTs[8-11] and graphene[8,12-16] has generated interest in their use as well. The outstanding electrical properties and high surface area to mass ratios associated with these advanced scaffolds also make them highly desirable in technological applications, such as energy storage[17] and sensing.[18]

It is carbon's numerous cited advantages that have given it such a solid grounding, with its low cost,[1] low background currents,[19] wide potential window,[20] chemical inertness,[21] and biocompatibility[22] often making it more attractive as an electrode material than common metals. However, despite having such well-defined bulk properties, the surface chemistry of carbon materials is undoubtedly more complex than that of its metal counterparts,[1] somewhat as a result of differences in the underlying microstructure of its numerous forms, but primarily through the wide variety of surface bonds and functionalities that can be bestowed upon it.[23] Indeed, in electrochemical applications, functionalities present at the electrode/electrolyte interface are yet to be fully understood.[1]

Such rich surface chemistry offers up numerous routes for electrode surface modification,[24] allowing for carbon's already impressive intrinsic properties to be further tailored to specific applications. This has been exploited in areas such as sensing[25,26] and (electro)catalysis,[27] where the modification of GC and CNT electrodes has been demonstrated as a route to catalyze the oxygen reduction reaction for example,[28,29] and similar modification routes have proven essential in the detection of blood glucose levels.[30] Unquestionably, carbon electrodes are often extremely sensitive to small changes in their surface state.

Unfortunately, such sensitivity toward surface state can also introduce undesirable traits. This is particularly true of graphite, where the literature highlights substantial variation in electrochemical performance depending on pre-treatment procedures employed to the electrode,[20] even for the response of so-called simple redox meditators.[31,32] Such disparities have led to significant uncertainty regarding the inherent electrochemical activity of graphite materials, with heavy focus surrounding HOPG in particular, a material whose local electrochemical properties have recently undergone considerable revision.[33,34] Numerous reports exist suggesting redox reactions at HOPG are catalyzed solely by step edges at the electrode surface, with the basal plane thus regarded as largely inactive or completely inert,[31,32,35-40] while more recent reports suggest such findings are essentially a result of complex surface effects (ageing, fouling etc.) that serve to alter its behavior, demonstrating freshly cleaved basal surfaces to have significant ET activity.[33,34,41,42] Indeed, such claims about HOPG have also led to speculation about the sites of ET at CNTs[43,44] and graphene,[12] for which HOPG often serves as a model substrate.[45,46] Methodologies employed to probe the electroactivity of HOPG electrode surfaces range from macroscopic[34] to microscopic, and recently nanoscopic,[33] and cover both inner- and outer-sphere redox mediators. Surface modification has also been proposed as a route to understand the activity of HOPG surfaces, with the adsorption of redox active quinone compounds in particular often being used as a measure of the percentage of electrochemically active sites at HOPG.[35] Quinone compounds spontaneously adsorb to a range of surfaces,[47,48] and under acidic aqueous conditions can further undergo electrochemical reduction via a single 2e$^-$, 2H$^+$ process, an example of which is shown below for the case of AQDS, Figure 4.1.

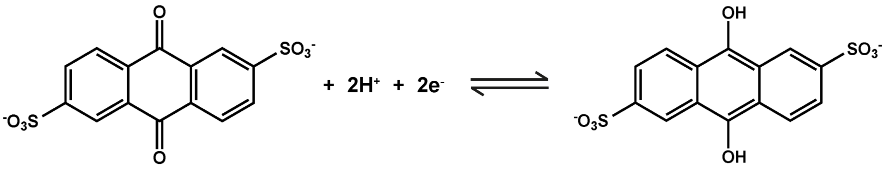

Figure 4.1 The electrochemical redox process associated with AQDS.

Faulkner *et al.* studied the adsorption of AQDS through voltammetry at Hg electrodes,[47] determining adsorbed surface coverage to be a little less than a completely packed monolayer, hardly surprising given the known ability of other molecules (e.g. alkanethiols) to form densely packed SAMs at such electrodes.[49] Soriaga and Hubbard[48] demonstrated similar close packing behavior at Pt electrode surfaces. Focusing on carbon, an early study by McCreery *et al.* used numerous basal plane HOPG surfaces, predetermined to vary in fractional step edge density, to study AQDS adsorption.[50] At high-quality, freshly cleaved HOPG surfaces (i.e. those containing low step edge densities) they observed no adsorption behavior, with a CV response dominated by a kinetically slow, diffusion controlled process. In retrospect, this is not surprising given the relatively high concentration and slow scan speed used, where the electrochemical response is biased towards solution diffusion processes. Samples showing increased step edge density (i.e. low quality) began to show a redox couple typical of that for an adsorbed species, and it was thus concluded that *AQDS adsorption only occurs at step edge sites.* A later study attempted to correlate step edge density on the basal plane of freshly-cleaved HOPG with numerous electrochemical measurements in aqueous solution, specifically the double-layer capacitance (C_0), heterogeneous ET rate constant, k_0, for the $Fe(CN)_6^{3-/4-}$ redox couple, and level of AQDS adsorption, Γ.[35] Again, it was concluded that surfaces with greater step edge density displayed higher Γ for AQDS adsorption, and in-turn, these surfaces displayed higher k_0 values for $Fe(CN)_6^{3-/4-}$ and increased C_0. Hence, these easily measurable parameters have become indirect proxies for determining the number of step edge defects at an HOPG surface, despite the $Fe(CN)_6^{3-/4-}$ redox couple being shown to be problematic at the basal surface of graphite[33] and other surfaces.[51] A reported direct correlation between measured HOPG step edge density (determined by STM) and corresponding Γ for AQDS (determined by voltammetry) further supported this indirect measurement route, although it is important to highlight the very small range of defect densities investigated (0.7 to 1.6 %).[52] Studies at GC surfaces were considered to be further supportive, where high edge plane concentrations yielded values of Γ for AQDS roughly 50 times greater than at basal rich graphite surfaces. However, the level of adsorption at HOPG exceeded what would have been expected had only step edges been responsible for adsorption by a factor of 30, with the authors proposing that a pronounced electronic disturbance extending ~ 5 nm from step edges (on the upper terrace of the step) must exist, and that ET occurred over this extended range, with the rest of the basal surface remaining inert.[35] Subsequent *in-situ* scanning force microscopy by McDermott *et al.* showed ~ 90 % coverage over HOPG surfaces, despite a voltammetric response indicating ~ 17 %, leading to the conclusion that *adsorption takes place indiscriminately on basal and step edge sites, but only adsorbed material at step edges was active.*[53] To this end, such findings have led to the consensus that AQDS adsorption is a valid method for determining the step edge density at HOPG electrodes.

Numerous recent studies have shown that models that consider the basal plane to be inert should be reconsidered,[34] revealing the basal plane of HOPG to actually have considerable ET activity to a wide range of redox processes.[33,42,54,55] In addition, STS studies have shown the density of states (DOS) to be more or less consistent over the entire HOPG surface, only being slightly enhanced over ~ 1 nm at zig-zag step edge sites,[56,57] and not at all at armchair sites, which dominate at step edges on graphite.[57]

In light of such studies, this work reports detailed investigations into the adsorption of AQDS at HOPG surfaces, with the ultimate goal of elucidating whether or not it is an appropriate measure for determining the number of step edge sites. By studying adsorption at a range of HOPG surfaces, with step edge densities covering a range of more than 2 orders of magnitude, we are able to precisely elucidate the effect of step edge density on AQDS Γ. We find that no correlation exists. These results are further confirmed through the introduction of a new, innovative fast-scan cyclic voltammetry (FSCV) technique, allowing for the evolution of adsorbed material to be tracked in real-time, in confined microscopic regions, with subsequent AFM analysis allowing exact determination of the step edge density in the probed region. The amount of adsorbed electroactive AQDS is orders of magnitude higher than would be expected if activity were confined only to edge sites. These studies show that the electrochemical response of adsorbed AQDS cannot be used as a route to measure step edge densities on graphitic surfaces, and add to increasing evidence of the intrinsic electroactivity of the graphitic basal surface.

4.2 Results and Discussion

4.2.1 Macroscale Adsorption Studies

AQDS adsorption was first probed at the macroscale for a range of different HOPG surfaces, using an O-ring confined droplet arrangement (details in section 2.5.1). Figure 4.2(a) shows representative overlaid CV responses of a 10 μM AQDS in 0.1 M $HClO_4$ solution at four freshly cleaved HOPG surfaces (AM, ZYA, SPI-1 and SPI-3), which vary greatly in surface quality, specifically in terms of step edge density, in which they differ by orders of magnitude (*vide infra*).[42] CVs were recorded as quickly as reasonably possible after solution was introduced to the surface, which in reality was ~ 15 seconds. Leaving the solution in contact with the surface for 60 minutes before recording the response led to no observable changes in the voltammetry, suggesting the adsorption limit is reached within this short time period (15 s).

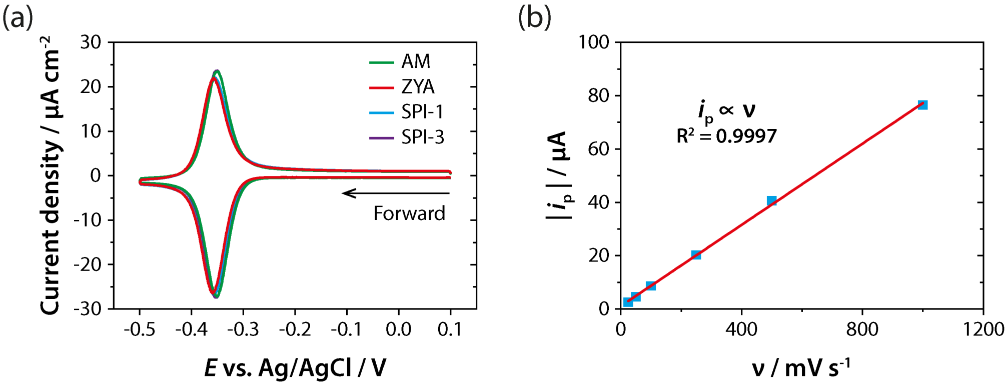

Figure 4.2 (a) CVs for the reduction/oxidation of 10 μM AQDS in 0.1 M $HClO_4$ at 100 mV s^{-1} on four different grades of freshly cleaved HOPG. (b) A plot of | i_p | (reduction wave) vs. scan rate, v, for the case of AM grade HOPG, showing a distinct linear dependence.

The resulting voltammetric response on each of the HOPG surfaces shows a signal representative of a fast (reversible) surface bound redox species, with waves centered at - 0.37 V vs. Ag/AgCl having an associated ΔE_p close to 0 mV, and exhibiting FWHM values of ~ 50 mV, in close-agreement with that predicted for a 2 e^- surface bound redox process of (90.6 / n) mV, where n is the number of electrons transferred per redox event.[58] Clearly evident is the similarity of the CV response over all grades of HOPG investigated, despite their extreme differences in step edge density. Such similarity suggests the equilibrium concentration of surface bound species to be the same in each case, at least when adsorption occurs from a 10 μM concentration solution, as used herein. A plot of i_p vs. ν for the case of AM grade HOPG (Figure 4.2(b)) shows a distinct linear correlation, as would be expected for a reversible surface bound redox process, confirming the lack of any response owing to a diffusional process at this low concentration.

4.2.2 Complementary Surface Analysis

If AQDS adsorption or electrochemical activity were to be limited to step edge sites,[35,52,53] the response would likely differ significantly at surfaces displaying higher levels of such defects, making a correlation between surface structure and electrochemical response crucial. Figures 4.3(a)-(d) show typical AFM images for each of the freshly cleaved HOPG surfaces at which adsorption CVs were recorded (Figure 4.2). It is clear that the number of step edge sites within the same size area varies significantly across the four grades, with SPI-3 and SPI-1 containing significantly more steps than ZYA and AM grades. The average height of such steps also increases drastically in the same way, with AM and ZYA grades display predominantly monolayer and bilayer steps, whereas SPI-1 and SPI-3 were typically found to show steps several layers high, as has been previously reported for these materials.[34] Also included in Figures 4.3(a)-(d) are corresponding histograms showing the measured heights of every step found through 7 AFM images of each HOPG surface.

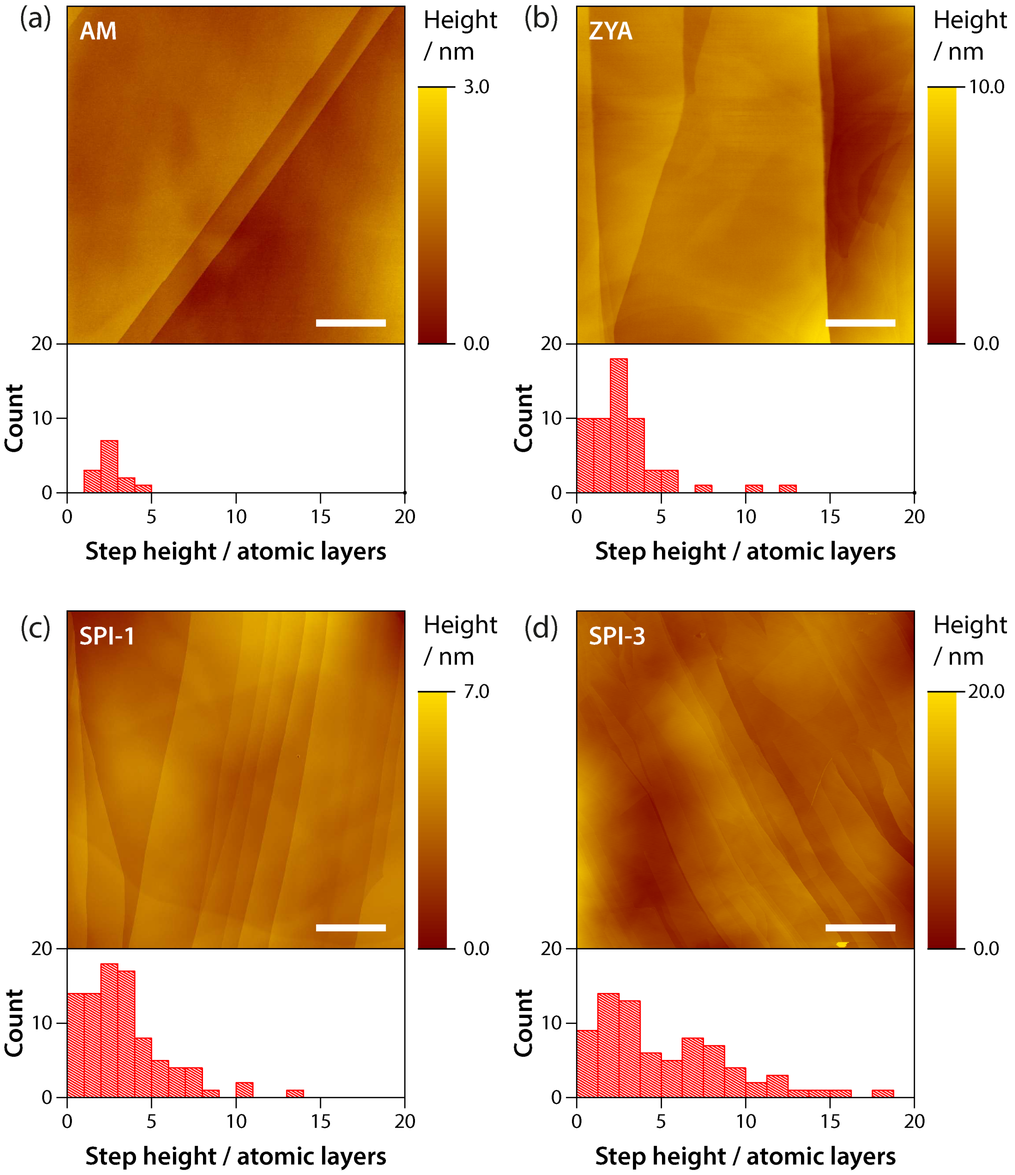

Figure 4.3 AFM images of freshly cleaved, unmodified HOPG surfaces of (a) AM, (b) ZYA, (c) SPI-1 and (d) SPI-3 grade, along with associated histograms showing the height of each step (in atomic layers) for 7 different areas of the same freshly cleaved surface. Scale bars denote 1 μm in all cases.

The associated AQDS fractional surface coverage (Θ_{ads}), defined as Γ/Γ_0, where Γ_0 is the maximum possible surface coverage (132 pmol cm^{-2} using a flat molecular orientation of 126 Å^2),[53] was calculated at each grade of HOPG using the charge associated with the CV reduction wave, as performed previously.[52,53,59] Across 10 repeat measurements on each HOPG grade, each at a freshly cleaved surface, the following mean Θ_{ads} values were obtained (± 1 S.D.):

29.7 ± 1.6 % for AM grade, 29.6 ± 2.4 % for ZYA grade, 27.5 ± 1.4 % for SPI-1 grade, and 28.0 ± 0.6 % for SPI-3 grade, as presented in Figure 4.4(a). It is clear that all four grades of HOPG show nearly identical Θ_{ads} values, which are in very close agreement with previous studies that employed high-quality AM grade HOPG.[52] AFM images (Figure 4.3) of the four grades were further analyzed to determine % step densities (quoted as defect area for a given image divided by total projected area of the image). In general agreement with the qualitative analysis provided above, it was found that AM HOPG provides the most pristine surface, with step edge coverage ranging between 0.006 and 0.48 % (mean 0.09 %), followed by ZYA (range of 0.03-1 %, mean 0.3 %) and SPI-1 (range of 0.5-3.4 %, mean 1.8 %), with SPI-3 showing the highest percentage coverage (range of 10-78 %, mean 31 %), summarized in Figure 4.4(b).

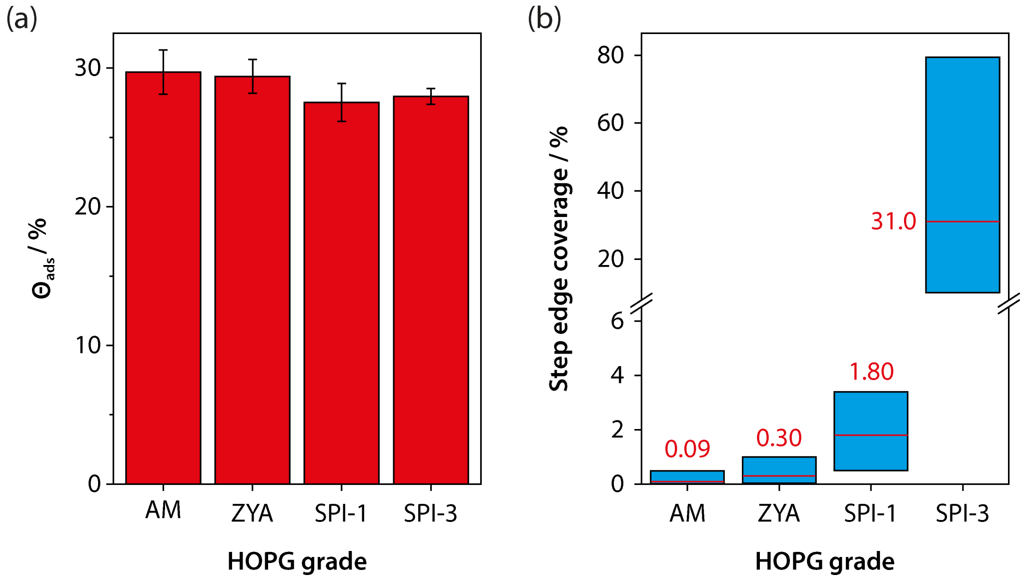

Figure 4.4 (a) The range of adsorbed surface coverage values for a solution of AQDS (10 μM) in 0.1 M $HClO_4$ as determined by cyclic voltammetry at 100 mV s^{-1}, at four different grades of freshly cleaved HOPG. Error bars represent 1 S.D. (N = 10) (b) The range of step edge coverage values, as determined by AFM, for the four grades of HOPG investigated. The mean for each data set is marked with a red line (N = 7).

Based on current literature,[35,52,53] which suggests that adsorption, or at least the electroactive response of adsorbed AQDS, is confined to only the step edges, the resulting surface coverage values should show a massive difference among the samples investigated. Instead, the results indicate that Θ_{ads} is strongly independent of step edge density, and is actually dominated by the basal surface. Thus, the electrochemistry of adsorbed AQDS at HOPG is analogous to that seen recently for other reactions, it is dominated by the basal surface. It is likely that obtained coverage values, around 30 % with respect to that of a completely packed surface, is as a result of non-ideal packing, reasonable given the short timescale over which equilibrium adsorption occurs (< 15 seconds), with Crooks *et al*. also commenting that a 'quiet time' of 5 seconds was enough to establish adsorption equilibrium at Hg electrodes.[47]

Ex-situ AFM imaging of an AM grade surface that had undergone AQDS adsorption, before having the solution removed, but without rinsing, allowed the underlying HOPG surfaces features to be observed (Figures 4.5(a) and (b)), and appeared to show the surface covered with a thin film. Adsorption appeared uniform across the entire surface, with no evidence of preferential adsorption on or around step edge sites. Small regions of particulate matter appear present, likely representing areas at which multilayer adsorption occurred, with similar features also observed by McDermott *et al.* when performing *in-situ* imaging, although significantly higher AQDS concentrations were used in that case.[53] This observation is again consistent with a model suggesting that adsorption occurs over the entire HOPG surface. Interestingly, *ex-situ* imaging performed by McDermott *et al.* claimed to only show adsorbed material at step edge sites, although no images were shown for comparison to those contained herein.[53]

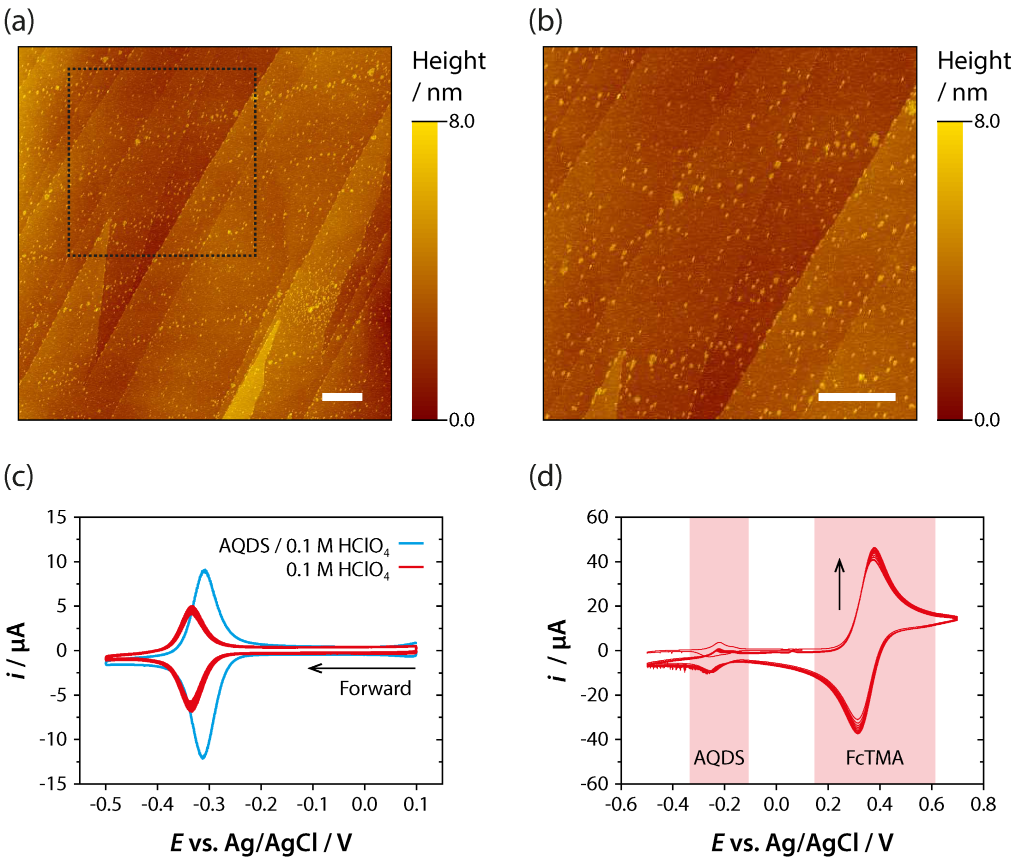

Figure 4.5 (a) *Ex-situ* AFM image of an AM HOPG surface, post adsorption of AQDS from a 10 µM in 0.1 M HClO$_4$ solution, and zoom-in of the area marked by a dotted box (b). Resulting CVs from a surface pre-treated with 10 µM AQDS in 0.1 M HClO$_4$ before performing voltammetry in 0.1 M HClO$_4$ (c) and 0.5 mM FcTMA$^{+/2+}$ in 0.1 M HClO$_4$ (d).

The stability of adsorbed AQDS at HOPG surfaces also was investigated by first 'pre-treating' the HOPG surface with 10 µM AQDS in 0.1 M HClO$_4$ for 60 seconds, during which time equilibrium adsorption would occur (*vide supra*), before gently removing the solution and replacing with either 0.1 M HClO$_4$ (i.e. pure solvent) or a 0.5 mM solution of the outer-sphere redox mediator (Ferrocenyl-methyl) trimethylammonium hexafluorophosphate (FcTMA$^{+/2+}$) in 0.1 M HClO$_4$, before subsequently performing voltammetry, shown in Figures 4.5(c) and 4.5(d), respectively. Potential cycling in 0.1 M HClO$_4$ showed a reduction in i_p of the AQDS redox process by ~ 50 %, suggesting desorption from the surface into bulk solution. The majority of desorption occurred within the 15 seconds required to start measurements after introducing new solution, although continual cycling showed a further slight decrease, before halting after 10 cycles. It should be noted that the possibility of disturbing the adsorbed film during solution replacement cannot be ruled out. The potential range employed for the latter case allowed for both the AQDS and the $\mathrm{FcTMA}^{+/2+}$ redox couples to be observed. The current associated with adsorbed AQDS again reduced in size with repetitive potential cycling (note different scale to Figure 4.5(c)), whilst the i_p associated with the $\mathrm{FcTMA}^{+/2+}$ process (centered around 0.35 V vs. Ag/AgCl) increased with cycling, halting at a value of 46.6 μA, in close agreement with the value of 48.0 μA for a freshly cleaved HOPG surface, and also to that predicted by the Randles-Sevcik equation (49.7 μA),[58] assuming a value of D of $6.0 \times 10\ \mathrm{cm}^2\ \mathrm{s}^{-1}$.[60] Furthermore, the observed ΔE_p of 65 mV for the reversible $\mathrm{FcTMA}^{+/2+}$ redox process is consistent with that of an unblocked electrode surface. Overall, such findings suggest desorption of the film takes place, although complete desorption was never observed, despite the fact the i_p measured for the $\mathrm{FcTMA}^{+/2+}$ redox process matched that of an unmodified surface, suggesting either a highly porous film, or one consisting of numerous pinholes, leading to diffusional overlap of the outer-sphere redox process,[61] and hence a response similar to that of a freshly cleaved surface.

4.2.3 Time-Resolved Microscopic Adsorption Studies

FSCV[62] was employed as a route to further study the AQDS adsorption process at HOPG electrode surfaces. Originally developed by Millar *et al.*,[63] FSCV applies the triangular waveform associated with traditional CV measurements, but over a very short timescale, through scan rates typically in excess of 100 V s^{-1}, although rates well into the 1000's of V s^{-1} are now readily reported thanks to modern high-speed electronics.[64] The resulting sub-second (millisecond or even lower) measurement technique has seen numerous applications, primarily in biological situations for the detection of dopamine[65] and adenosine,[66] for example.

Measured currents are inevitably a lot higher than those observed at traditional scan rates, owing to the steep diffusion gradient created at the electrode interface, leading to possible *iR* drop within the system. Furthermore, the measured background capacitance currents, i_c, are typically very large, scaling linearly with ν, with the desired faradaic current, i_f, only scaling with $\nu^{1/2}$ (for a diffusion controlled process at least). Such problems are usually overcome through the use of UMEs, where small electrode areas minimize the generated current, thus reducing *iR* effects and maximizing i_f / i_c. Unfortunately, this in turn rules out the use of certain electrode materials, where UME fabrication is not always practical, generally limiting measurements to metallic[67] or carbon fiber electrodes.[64] In this respect, SECCM[68] offers itself as a powerful platform to perform FSCV measurements. By instead confining the electrochemical cell to the micron scale through the use of a tapered glass pipet, rather than using a micron sized substrate, a whole new range of materials become available for study. Furthermore, the unique feedback system operating in SECCM allows for the moment the electrochemical cell contacts the surface to be determined precisely,[69] and for measurements to be made almost immediately upon contact. The fact that a conductance current is measured allows the impact of *iR* drop to be measured and quantified.[70]

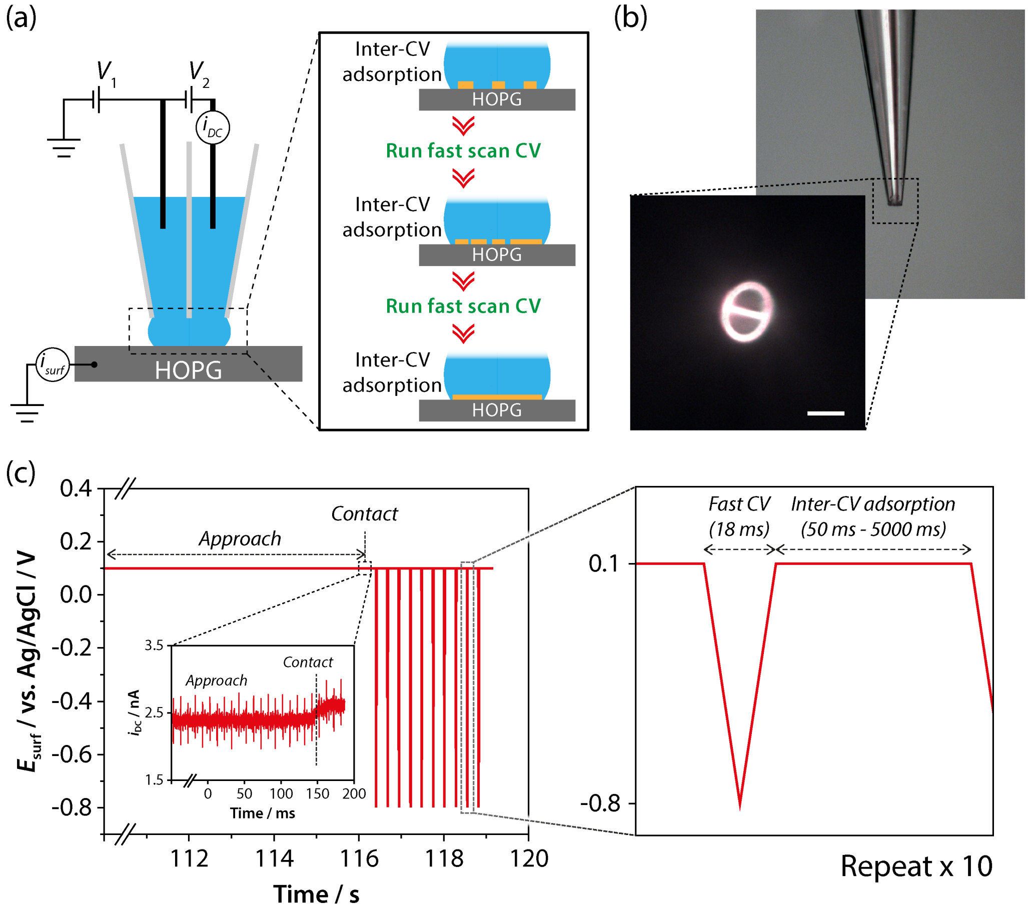
(a)
V_1
V_2
i_{DC}
i_{surf}
HOPG
Inter-CV adsorption
HOPG
Run fast scan CV
Inter-CV adsorption
HOPG
Run fast scan CV
Inter-CV adsorption
HOPG
(b)
(c)
E_{surf} / vs. Ag/AgCl / V
0.4
0.2
0.0
-0.2
-0.4
-0.6
-0.8
Approach
Contact
112
114
116
118
120
Time / s
3.5
2.5
1.5
i_{DC} / nA
Approach
Contact
0
50
100
150
200
Time / ms
Fast CV (18 ms)
Inter-CV adsorption (50 ms - 5000 ms)
0.1
-0.8
Repeat x 10

Figure 4.6 (a) Schematic representation of the FSCV setup, with corresponding diagram of how FSCV can be employed to monitor adsorption at an electrode surface. (b) An optical micrograph of a typical tip used in such studies, with the scale bar denoting 10 μm. (c) The waveform applied to the substrate upon meniscus contact, and corresponding timescales for both FSCV measurements and adsorption. Inset, typical i_{DC} vs. time plot, showing a jump at contact.

Figure 4.6(a) shows a schematic of the FSCV-SECCM configuration employed herein to monitor the rate of accumulation of AQDS at an HOPG surface. Briefly, the SECCM tip was filled with a solution of 1 μM AQDS in 50 mM $HClO_4$ and then approached toward a freshly-cleaved AM grade HOPG surface, whilst the surface potential, E_{surf}, was held at a potential where AQDS reduction would not occur (*vide supra*), through adjustment of V_1 (full SECCM details in section 2.6). Immediately upon meniscus contact, a pre-determined '*inter-CV adsorption*' hold time was begun, during which initial adsorption from the confined AQDS solution occurred. An FSCV was recorded at 100 V s^{-1} to quantify the level of adsorption at that point, before a second hold time was employed, and then a second FSCV initiated for further quantification. This process was continued 10 times, for a set hold time (Figure 4.6(b)), providing information on the level of AQDS adsorption with time at a small, localized area of the surface. Furthermore, this was repeated for hold times of 50 ms, 100 ms, 250 ms, 500 ms, 1000 ms and 5000 ms, each at a fresh area of the HOPG surface. The use of a high scan rate during FSCV meant that the analysis time (18 ms, defined by the potential range investigated) was almost negligible in the comparison to the hold times investigated, although it is included in the evaluations made below.

The effects of migration of AQDS toward the surface were minimized by adjustment of V_2, which was set at 50 mV, versus the 400 mV typically employed in SECCM.[12] In addition, the tip was not oscillated during measurements; instead the jump in i_{DC} was used to indicate surface contact. To allow for subsequent probing of the surface post-adsorption, the pipet was pulled to a relatively large opening ~ 18 μm in diameter (Figure 4.6(c)). Despite the need to move to a fresh area of HOPG and re-approach for each of the six hold times investigated, the nature of SECCM allowed for multiple measurements to be performed over a short period,[71] minimizing any effects of surface contamination over the 20 minute period required here.

Figure 4.7(a) shows a typical FSCV voltammogram obtained for a hold time of 250 ms, during which, 10 FSCVs were recorded in total at a single position on the surface. As was observed in the macroscale studies (Figure 2(a)), well-defined surface waves are evident in the voltammetry, indicating AQDS adsorption at the surface. The i_p values associated with both the reduction and oxidation waves of adsorbed AQDS increase with subsequent scan numbers, and since the typical time taken for the meniscus to fully wet the surface in SECCM measurements is on the order of < 1 ms,[69] such a response is attributed to continually increasing levels of adsorption at the surface, as would be expected over the short timescales investigated. When investigated with a 5000 ms hold time, it is evident that equilibrium adsorption is reached after the first two FSCVs (i.e. 10 s, Figure 4.7(b)), as would be expected based on the macroscale studies, which showed equilibrium adsorption had occurred after 15 s.

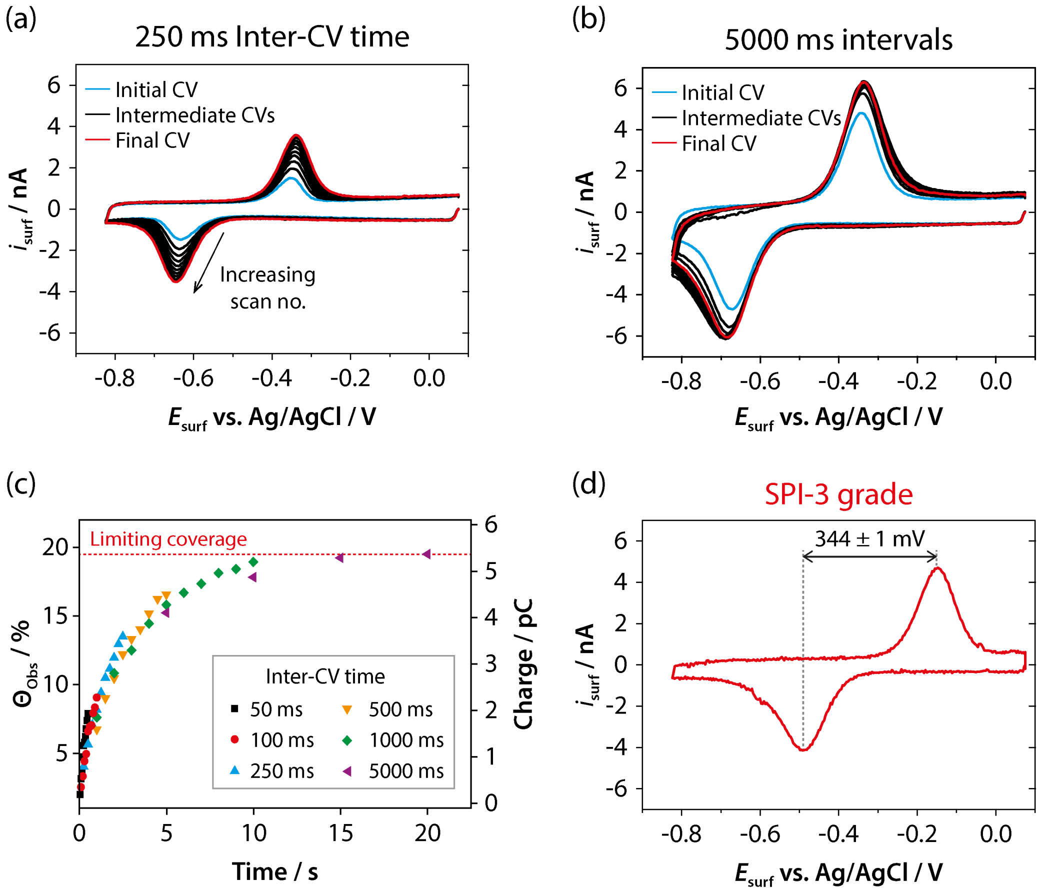

Figure 4.7 FSCVs for the reduction/oxidation of 1 µM AQDS in 50 mM $HClO_4$ at 100 V s^{-1} using the SECCM setup, with *inter-CV adsorption* hold times of (a) 250 ms and (b) 5000 ms. (c) Observed fractional surface coverage values determined from FSCV measurements at six different areas of the AM HOPG surface. (d) A typical FSCV for the reduction/oxidation of 1 µM AQDS in 50 mM $HClO_4$ at 100 V s^{-1} after a hold time of 10 s, with a ~ 16 µm diameter tip.

Interestingly, and in contrast to the macroscale studies, the much high scan rate employed in FSCV-SECCM leads to a large peak-to-peak separation of the potentials of the redox processes, indicating some kinetic influence. Whilst this does not effect evaluation of the surface coverage through integration of the peaks, it may open possibilities for investigating the impact of step density on kinetics, which is briefly commented upon below.

As was done in the macroscale studies, analysis of the charge associated with each of the individual cycles (again for the reduction process) was performed, allowing a plot of charge vs. time, and hence, Θ_{ads} vs. time to be created, shown in Figure 4.7(c). Clearly visible is a distinct adsorption trend of Θ_{ads} increasing sharply with time over the first 6 s, before slowing and plateauing after ~ 10 s. Agreement between the data performed at all six different *inter-CV adsorption* times, a total of 60 FSCVs, highlights the reproducibility of the technique, and its applicability for studying adsorption processes over these short timescales.

For comparison with the AM sample, further measurements of the adsorption of AQDS at an SPI-3 surface were performed. These yielded a fractional coverage of ~ 19 % at equilibrium adsorption, in close agreement with that measured at the AM surface, and matching conclusions from the macroscale studies. The measured ΔE_p values were 344 ± 1 mV (N = 5) and 341 ± 1 mV (N = 5) for SPI-3 and AM grade samples respectively, and since these two substrates differ in step edge density by more than 2 orders of magnitude, this clearly suggests that step edges do not influence reaction kinetics. Furthermore, since the overall DOS on SPI-3 grade HOPG would be reasonably expected to be higher than AM grade, this also suggests that the electroreduction of adsorbed AQDS at HOPG is likely in the adiabatic regime.

Finally, AFM imaging of each of *the entire adsorption sites* was carried out in order to make a direct correlation between Θ_{ads} and the actual step edge density of the probed area. Whilst previous studies have attempted such direct correlations, they have always been based on small representative AFM images of the surface, rather than exact correlations of electrochemistry and structure in the same area of the surface. Figure 4.8(a) shows a typical AFM image of an adsorption site after AQDS adsorption through FSCV, where the total adsorption time was 10 s (1000 ms x 10 FCSVs) and the Θ_{ads} calculated to be ~ 19.5 %. The AFM image shows adsorption to have occurred across > 90 % of the working area, with the step edge density ca. 0.02 % at the surface. If the step edges were to be the only site of electroactivity, and assuming such activity is limited to within 5 nm of the step edge as suggested by McCreery,[72] the predicted charge associated with the AQDS redox process would be 31 fC (assuming dense monolayer packing), orders of magnitude different from the value of 5.3 pC actually observed.

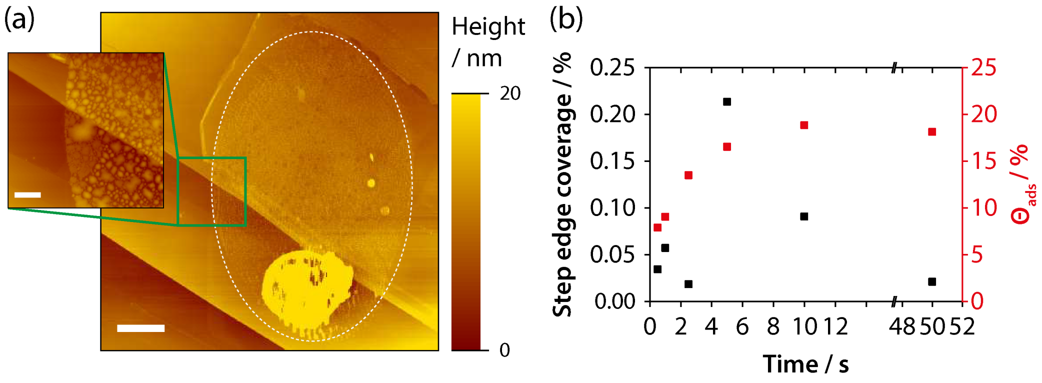

Figure 4.8 (a) AFM image of an AM HOPG surface after AQDS adsorption via FSCV (area marked by a white dotted line) and a zoom-in at a step edge site showing no preferential adsorption. Scale bars denote 2 μm and 500 nm respectively. (b) % of step edges within the six adsorption spots for which FSCV measurements were made with corresponding surface coverage vs. time.

Similar analysis of all spot deposition sites is shown in Figure 4.8(b), where the level of adsorption after the final FSCV at that spot is plotted with corresponding step edge density for the area covered by the spot. Such a direct correlation, never achieved previously, conclusively shows that no relationship exists between the step edge density of a sample, and the corresponding level of AQDS adsorption at that same sample, highlighting the activity of the basal plane of HOPG towards ET, and showing that AQDS adsorption is not a reliable marker of active sites/step edge density at electrode surfaces.

4.3 Conclusions

To conclude, a new approach for functionalizing and probing the activity of electrode surfaces has been developed, making use of the high spatial resolution offered through SECCM, and the possibility to monitor fast processes using FSCV. This approach allowed for the adsorption of AQDS at HOPG surfaces to be tracked in real time and compared at surfaces that differ in step density for more than 2 orders of magnitude. The localized nature of the adsorption experiments allowed for the *entire working area* to be further characterized, unambiguously showing that the level of AQDS adsorption at HOPG surfaces is independent of step edge density. The observed coverage of AQDS was found to be orders of magnitude higher than would be expected if only step edge sites were responsible for the measured response, suggesting adsorption is completely dominated by the basal plane.

Overall, the data presented herein indicates that AQDS cannot be used to determine the step edge density of an HOPG surface, and, that there is no correlation between the adsorbed electroactive AQDS and step edge density, which has been a long standing and widely held view.[53] This conclusion was drawn through a combination of macroscale and microscale measurements, with high consistency between them.

The electroactivity of HOPG has recently undergone considerable revision. Previously considered largely inert, a combination of nanoscale[33,34,41,42] to macroscale[34,41,42] studies have now shown the basal plane of HOPG to support relatively fast ET processes, for a range of reactions. The studies herein expand this revision, extending the range of systems that undergo facile ET at the basal surface of HOPG, and proving that AQDS adsorption is not a reliable methodology for characterizing step edge density.

4.4 References

(1) McCreery, R. L. *Chem. Rev.* **2008**, *108*, 2646.

(2) Hutton, L. A.; O'Neil, G. D.; Read, T. L.; Ayres, Z. J.; Newton, M. E.; Macpherson, J. V. *Anal. Chem.* **2014**, *86*, 4566.

(3) Sansuk, S.; Bitziou, E.; Joseph, M. B.; Covington, J. A.; Boutelle, M. G.; Unwin, P. R.; Macpherson, J. V. *Anal. Chem.* **2013**, *85*, 163.

(4) Channon, R. B.; Newland, J. C.; Bristow, A. W. T.; Ray, A. D.; Macpherson, J. V. *Electroanal.* **2013**, *25*, 2613.

(5) Fowler, J. D.; Allen, M. J.; Tung, V. C.; Yang, Y.; Kaner, R. B.; Weiller, B. H. *ACS Nano* **2009**, *3*, 301.

(6) Dan, Y.; Lu, Y.; Kybert, N. J.; Luo, Z.; Johnson, A. T. C. *Nano Lett.* **2009**, *9*, 1472.

(7) Sherigara, B. S.; Kutner, W.; D'Souza, F. *Electroanal.* **2003**, *15*, 753.

(8) Yang, W.; Ratinac, K. R.; Ringer, S. P.; Thordarson, P.; Gooding, J. J.; Braet, F. *Angew. Chem. Int. Ed.* **2010**, *49*, 2114.

(9) Wang, J. *Electroanal.* **2005**, *17*, 7.

(10) Li, Y.; Zhou, W.; Wang, H.; Xie, L.; Liang, Y.; Wei, F.; Idrobo, J.-C.; Pennycook, S. J.; Dai, H. *Nat. Nanotechnol.* **2012**, *7*, 394.

(11) Byers, J. C.; Güell, A. G.; Unwin, P. R. *J. Am. Chem. Soc.* **2014**, *136*, 11252.

(12) Güell, A. G.; Ebejer, N.; Snowden, M. E.; Macpherson, J. V.; Unwin, P. R. *J. Am. Chem. Soc.* **2012**, *134*, 7258.

(13) Li, W.; Tan, C.; Lowe, M. A.; Abruna, H. D.; Ralph, D. C. *ACS Nano* **2011**, *5*, 2264.

(14) Chen, D.; Tang, L.; Li, J. *Chem. Soc. Rev.* **2010**, *39*, 3157.

(15) Keeley, G. P.; McEvoy, N.; Nolan, H.; Holzinger, M.; Cosnier, S.; Duesberg, G. S. *Chem. Mater.* **2014**, *26*, 1807.

(16) Ambrosi, A.; Chua, C. K.; Bonanni, A.; Pumera, M. *Chem. Rev.* **2014**, *114*, 7150.

(17) Simon, P.; Gogotsi, Y. *Nat. Mater.* **2008**, *7*, 845.

(18) Balasubramanian, K.; Kern, K. *Adv. Mater.* **2014**, *26*, 1154.

(19) Güell, A. G.; Meadows, K. E.; Unwin, P. R.; Macpherson, J. V. *Phys. Chem. Chem. Phys.* **2010**, *12*, 10108.

(20) Hutton, L. A.; Iacobini, J. G.; Bitziou, E.; Channon, R. B.; Newton, M. E.; Macpherson, J. V. *Anal. Chem.* **2013**, *85*, 7230.

(21) Swain, G. M. *Adv. Mater.* **1994**, *6*, 388.

(22) Cohen-Karni, T.; Qing, Q.; Li, Q.; Fang, Y.; Lieber, C. M. *Nano Lett.* **2010**, *10*, 1098.

(23) Balasubramanian, K.; Burghard, M. *Small* **2005**, *1*, 180.

(24) Sundaram, R. S.; Gomez-Navarro, C.; Balasubramanian, K.; Burghard, M.; Kern, K. *Adv. Mater.* **2008**, *20*, 3050.

(25) Hutton, L.; Newton, M. E.; Unwin, P. R.; Macpherson, J. V. *Anal. Chem.* **2009**, *81*, 1023.

(26) Bahr, J. L.; Yang, J. P.; Kosynkin, D. V.; Bronikowski, M. J.; Smalley, R. E.; Tour, J. M. *J. Am. Chem. Soc.* **2001**, *123*, 6536.

(27) Baleizao, C.; Gigante, B.; Garcia, H.; Corma, A. *J. Catal.* **2004**, *221*, 77.

(28) Yang, H. H.; McCreery, R. L. *J. Electrochem. Soc.* **2000**, *147*, 3420.

(29) Miller, T. S.; Macpherson, J. V.; Unwin, P. R. *Phys. Chem. Chem. Phys.* **2014**, *16*, 9966.

(30) Mao, F.; Mano, N.; Heller, A. *J. Am. Chem. Soc.* **2003**, *125*, 4951.

(31) Kneten, K. R.; McCreery, R. L. *Anal. Chem.* **1992**, *64*, 2518.

(32) Rice, R. J.; McCreery, R. L. *Anal. Chem.* **1989**, *61*, 1637.

(33) Lai, S. C. S.; Patel, A. N.; McKelvey, K.; Unwin, P. R. *Angew. Chem. Int. Ed.* **2012**, *51*, 5405.

(34) Patel, A. N.; Collignon, M. G.; O'Connell, M. A.; Hung, W. O. Y.; McKelvey, K.; Macpherson, J. V.; Unwin, P. R. *J. Am. Chem. Soc.* **2012**, *134*, 20117.

(35) McDermott, M. T.; Kneten, K.; McCreery, R. L. *J. Phys. Chem.* **1992**, *96*, 3124.

(36) Bowling, R. J.; Packard, R. T.; McCreery, R. L. *J. Am. Chem. Soc.* **1989**, *111*, 1217.

(37) Ji, X.; Banks, C. E.; Crossley, A.; Compton, R. G. *ChemPhysChem* **2006**, *7*, 1337.

(38) Davies, T. J.; Moore, R. R.; Banks, C. E.; Compton, R. G. *J. Electroanal. Chem.* **2004**, *574*, 123.

(39) Cline, K. K.; McDermott, M. T.; McCreery, R. L. *J. Phys. Chem.* **1994**, *98*, 5314.

(40) Ji, X.; Banks, C. E.; Xi, W.; Wilkins, S. J.; Compton, R. G. *J. Phys. Chem. B* **2006**, *110*, 22306.

(41) Patel, A. N.; Tan, S.-y.; Miller, T. S.; Macpherson, J. V.; Unwin, P. R. *Anal. Chem.* **2013**, *85*, 11755.

(42) Patel, A. N.; Tan, S.-Y.; Unwin, P. R. *Chem. Commun.* **2013**, *49*, 8776.

(43) Güell, A. G.; Meadows, K. E.; Dudin, P. V.; Ebejer, N.; Macpherson, J. V.; Unwin, P. R. *Nano Lett.* **2014**, *14*, 220.

(44) Güell, A. G.; Ebejer, N.; Snowden, M. E.; McKelvey, K.; Macpherson, J. V.; Unwin, P. R. *Proc. Natl. Acad. Sci. U.S.A.* **2012**, *109*, 11487.

(45) Koehler, F. M.; Luechinger, N. A.; Ziegler, D.; Athanassiou, E. K.; Grass, R. N.; Rossi, A.; Hierold, C.; Stemmer, A.; Stark, W. J. *Angew. Chem. Int. Ed.* **2009**, *48*, 224.

(46) Ritzert, N. L.; Rodriguez-Lopez, J.; Tan, C.; Abruna, H. D. *Langmuir* **2013**, *29*, 1683.

(47) He, P. X.; Crooks, R. M.; Faulkner, L. R. *J. Phys. Chem.* **1990**, *94*, 1135.

(48) Soriaga, M. P.; Hubbard, A. T. *J. Am. Chem. Soc.* **1982**, *104*, 2735.

(49) Rampi, M. A.; Schueller, O. J. A.; Whitesides, G. M. *Appl. Phys. Lett.* **1998**, *72*, 1781.

(50) Robinson, R. S.; Sternitzke, K.; McDermott, M. T.; McCreery, R. L. *J. Electrochem. Soc.* **1991**, *138*, 2412.

(51) Pharr, C. M.; Griffiths, P. R. *Anal. Chem.* **1997**, *69*, 4673.

(52) McDermott, M. T.; McCreery, R. L. *Langmuir* **1994**, *10*, 4307.

(53) Ta, T. C.; Kanda, V.; McDermott, M. T. *J. Phys. Chem. B* **1999**, *103*, 1295.

(54) Patel, A. N.; McKelvey, K.; Unwin, P. R. *J. Am. Chem. Soc.* **2012**, *134*, 20246.

(55) Anne, A.; Cambril, E.; Chovin, A.; Demaille, C.; Goyer, C. *ACS Nano* **2009**, *3*, 2927.

(56) Niimi, Y.; Matsui, T.; Kambara, H.; Tagami, K.; Tsukada, M.; Fukuyama, H. *Phys. Rev. B* **2006**, *73*.

(57) Kobayashi, Y.; Fukui, K.; Enoki, T.; Kusakabe, K. *Phys. Rev. B* **2006**, *73*, 125415.

(58) Bard, A. J.; Faulkner, L. R. *Electrochemical Methods: Fundamentals and Applications*; Wiley, 2001.

(59) Forster, R. J. *Langmuir* **1995**, *11*, 2247.

(60) Patten, H. V.; Meadows, K. E.; Hutton, L. A.; Iacobini, J. G.; Battistel, D.; McKelvey, K.; Colburn, A. W.; Newton, M. E.; Macpherson, J. V.; Unwin, P. R. *Angew. Chem. Int. Ed.* **2012**, *51*, 7002.

(61) Amatore, C.; Saveant, J. M.; Tessier, D. *J. Electroanal. Chem.* **1983**, *147*, 39.

(62) Baur, J. E.; Kristensen, E. W.; May, L. J.; Wiedemann, D. J.; Wightman, R. M. *Anal. Chem.* **1988**, *60*, 1268.

(63) Millar, J.; Armstrongjames, M.; Kruk, Z. L. *Brain Res.* **1981**, *205*, 419.

(64) Bath, B. D.; Michael, D. J.; Trafton, B. J.; Joseph, J. D.; Runnels, P. L.; Wightman, R. M. *Anal. Chem.* **2000**, *72*, 5994.

(65) Bath, B. D.; Martin, H. B.; Wightman, R. M.; Anderson, M. R. *Langmuir* **2001**, *17*, 7032.

(66) Swamy, B. E. K.; Venton, B. J. *Anal. Chem.* **2007**, *79*, 744.

(67) Feeney, R.; Kounaves, S. P. *Electrochem. Commun.* **1999**, *1*, 453.

(68) Snowden, M. E.; Güell, A. G.; Lai, S. C. S.; McKelvey, K.; Ebejer, N.; O'Connell, M. A.; Colburn, A. W.; Unwin, P. R. *Anal. Chem.* **2012**, *84*, 2483.

(69) Kinnear, S. L.; McKelvey, K.; Snowden, M. E.; Peruffo, M.; Colburn, A. W.; Unwin, P. R. *Langmuir* **2013**, *29*, 15565.

(70) Aaronson, B. D. B.; Lai, S. C. S.; Uwnin, P. R. *Langmuir* **2014**, *30*, 1915.

(71) Kirkman, P. M.; Güell, A. G.; Cuharuc, A. S.; Unwin, P. R. *J. Am. Chem. Soc.* **2014**, *136*, 36.

(72) McCreery, R. L.; Cline, K. K.; McDermott, C. A.; McDermott, M. T. *Colloid Surface A* **1994**, *93*, 211.

Chapter Five

Spatial and Temporal Control of the Diazonium Modification of sp^2 Carbon Surfaces

In this chapter, the local diazonium modification of pristine sp^2 carbon surfaces is demonstrated, with high control, down at the micron scale through the use of SECCM. Interest in the controlled chemical functionalization of sp^2 carbon materials using diazonium compounds has been recently reignited, particularly as a means to generating a band-gap in graphene. Electrochemically-driven diazonium patterning is investigated at a range of driving forces, coupled with surface analysis using AFM and Raman spectroscopy. It is highlighted how the film density, level of sp^2/sp^3 rehybridization and the extent of multilayer formation can be controlled, paving the way for the use of localized electrochemistry as a route to controlled diazonium modification.

5.1 Introduction

Diazonium chemistry is widely recognized as a powerful approach to modifying the surface characteristics of numerous materials. Reactions at noble metal substrates[1-4] have been performed, with applications in molecular electronics,[5] for example, whilst coinage and industrial metal coatings have also been investigated,[4,6,7] with an evident focus on corrosion prevention.[8] The grafting of semiconducting materials has similarly been reported, where the modification of silicon surfaces[9] was shown to prevent the formation of an oxide layer.[10,11] However, the true versatility of diazonium compounds becomes particularly evident when one turns to carbon substrates, where, the modification of diamond,[12] CNTs,[13,14] GC[15-19] and graphite[15,20-23] have all been thoroughly investigated. The modification of graphene[24] has also become a hot topic in the diazonium field recently,[25-27] where its potential to generate an electronic band-gap in the material has sparked significant interest.[28,29]

Numerous approaches exist for driving the solution based modification process, with reducing agents,[30] ultrasonication,[31] heat,[32] and photochemistry[33] among the published methodologies for the formation of aryl radicals from their diazonium salt starting materials. However, the simplicity of such approaches puts them under the umbrella of bulk modification methods, whereby radicals are generated throughout the entire reaction solution, with only a certain proportion going on to react with the intended surface. Naturally, these routes are thus difficult to control, with factors such as surface coverage and degree of multilayer formation only determinable post modification.

In contrast, methods such as electrochemistry[10,15,34,35] and reducing substrates[36,37] may offer a more controllable alternative, with radicals only being generated at the surface of interest; a situation highly favorable for controlled modification. Indeed, numerous studies exist that focus on controlling the extent of surface modification through electrochemistry,[16,38,39] predominantly at carbon surfaces, where it often appears as the method of choice.

Overall, intense interest into diazonium surface modification has left the field relatively well equipped when it comes to performing large-scale surface modification, and as such, diazonium research interests have begun to shift recently, with surface patterning of the molecular layers now drawing attention. Indeed, such patterning will likely be an important step toward the application of diazonium chemistry into useful devices, and with previous research efforts into the patterning of comparable molecular layers (e.g. SAMs on noble metals[40] and silanes on oxide surfaces[41]), it is hardly surprising that localized diazonium modification is now desirable.

Already, numerous techniques have been demonstrated as potential routes to patterning, via both electrochemical and non-electrochemical means, taking both bottom-up and top-down approaches, with examples shown in Figure 5.1.

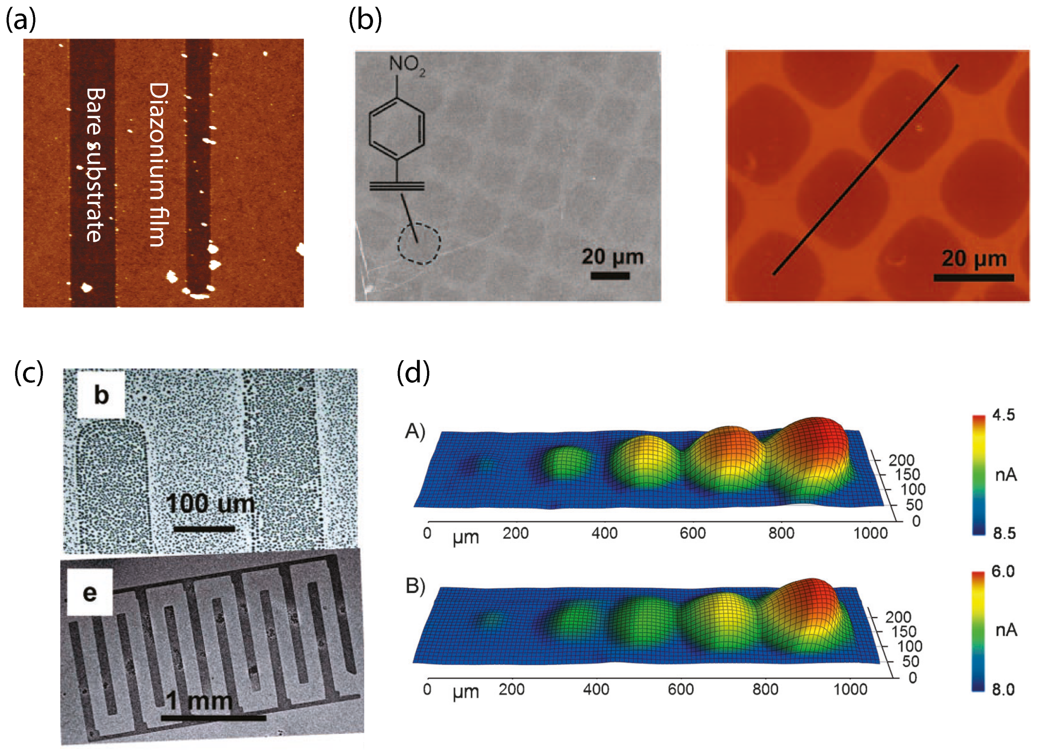

Figure 5.1 Literature examples of current methods for the surface patterning of diazonium compounds. (a) A fully diazonium-modified pyrolyzed photoresist film surface, with patterned trenches of exposed substrate introduced using an AFM tip.[42] (b) SEM and Kelvin force microscopy images of a diazonium patterned HOPG surface produced using photolithography.[23] (c) Patterned diazonium patches introduced using a PDMS microcontact printing method.[43] (d) Diazonium patches introduced on an Au substrate using reduction at a positionable Pt SECM tip.[44]

Patterning via complete surface modification, and subsequent film removal via scanning probe microscopy (SPM) 'nanoshaving' has been explored, utilizing both AFM[42] (Figure 5.1(a)) and STM[45] as tools to remove surface reacted material from desired regions. However, the slowness of the process limits its realistic application, and intricate details are somewhat difficult to produce. Lithographic techniques that partially block the surface prior to modification have also been demonstrated (Figure 5.1(b)),[23,46,47] although subsequent resist processing and removal likely introduces surface contamination to the grafted layer. As with alkanethiol SAMs, microcontact printing has been shown as effective for diazonium compound patterning (Figure 5.1(c)),[43] with both the length scale and possibility of intricate designs making it an attractive prospect, however, the reported surface contamination is highly undesirable.[48] In addition, the above routes require a consistent level of modification across the entire surface, ruling out the possibility of tuned grafting levels at different locations. Interestingly, scanning electrochemical microscopy (SECM) offers a route to both controlled and localized patterning, whereby aryl radicals generated at a metallic microelectrode above the surface of interest diffuse down to the surface and react (Figure 5.1(d)).[44] Of course, the diffusion element may introduce poor spatial resolution and the entire substrate is immersed in solution, allowing for unwanted spontaneous radical production at the substrate.[49] Such spontaneous reduction has since been avoided, through a one-pot reaction setup,[50] but poor patterning resolution still persists.

In this study, the localized diazonium modification of sp^2 carbon surfaces is demonstrated, under full electrochemical control, and is further coupled with detailed surface analysis to elucidate the extent of the grafting process. The focus is on HOPG, a substrate previously employed in diazonium modification, and one that has acted as a model substrate for the diazonium modification of graphene,[23] and graphene electrochemistry generally.[51] By confining the modification reaction to the micrometer scale, the surface can be controllably patterned with excellent precision and, furthermore, the influence of specific surface features on the grafting process can be investigated.

5.2 Results and Discussion

5.2.1 Diazonium Grafting at HOPG Surfaces

Herein, the diazonium grafting process proceeds via the electrochemical reduction of an aryl diazonium cation, producing an aryl radical following the release of a molecule of N_2. The highly reactive radical can bind with the sp^2 carbon surface to form a covalent bond, resulting in rehybridization of the surface atom to sp^3. This process is summarized in Figure 5.2(a).

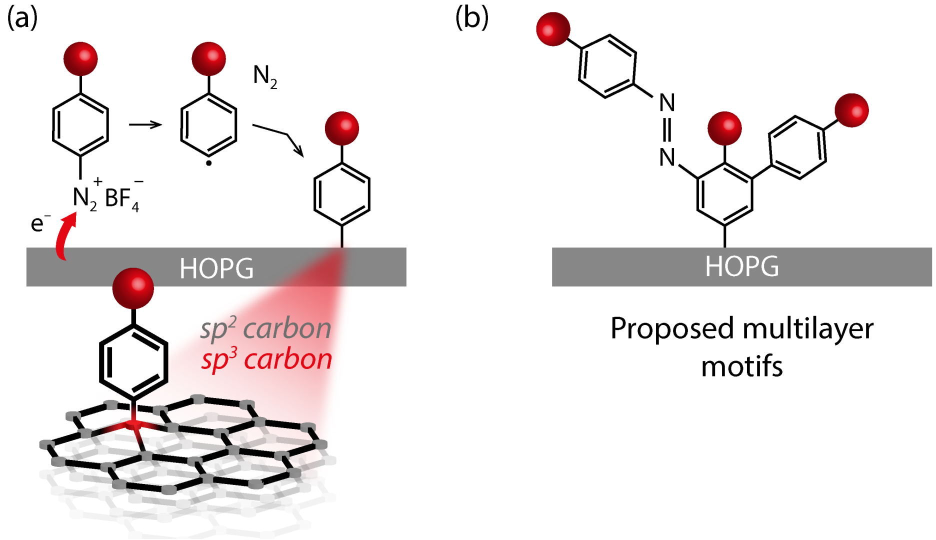

Figure 5.2 (a) Schematic of the diazonium modification reaction at an HOPG electrode surface, resulting in the production of an sp^3 carbon center in the uppermost HOPG layer. (b) Schematic representation of the formation of aryl multilayers at an HOPG surface.

The highly reactive radical produced also makes the formation of disordered multilayer structures a likely prospect (*vide infra*), with such structures likely consisting of a number of different bonding motifs (Figure 5.2(b)).[52]

5.2.2 Diazonium Grafting using SECCM

The diazonium grafting process was confined to the micron scale through the use of SECCM.[53,54] Briefly, SECCM employs a dual-channel borosilicate glass pipet, pulled to a sharp taper, with the solution of interest contained in each channel. By mounting the pipet on *xyz* piezoelectric positioners, a movable, confined-meniscus electrochemical cell is created when in contact with the surface (Figure 5.3(a)), which can be accurately positioned on the substrate of interest for an electrochemical measurement, before being withdrawn and moved to another location for further measurements. Application of a potential bias between the two QRCEs (200 mV in these experiments) induces an ion conductance current across the meniscus, i_{barrel}. By modulating the pipet position normal to the surface, an alternating component of the conductance current develops upon meniscus contact with the surface, enabling precise positioning without the probe itself ever making contact with the surface.[53,55] Such an approach completely avoids sample contamination in un-patterned areas, as may be introduced through patterning methods requiring complete physical contact with the surface, or sample immersion. During modification measurements, the potential of the surface, E_{surf}, is varied by the adjustment of V_1, (detailed fully in section 2.6), with the resulting electrochemical current measured as i_{surf}.

Figure 5.3(b) shows a typical CV recorded on HOPG using the SECCM setup, with the aqueous solution in the pipet channels comprising of 4-CBD and supporting electrolyte (25 mM aqueous H_2SO_4).

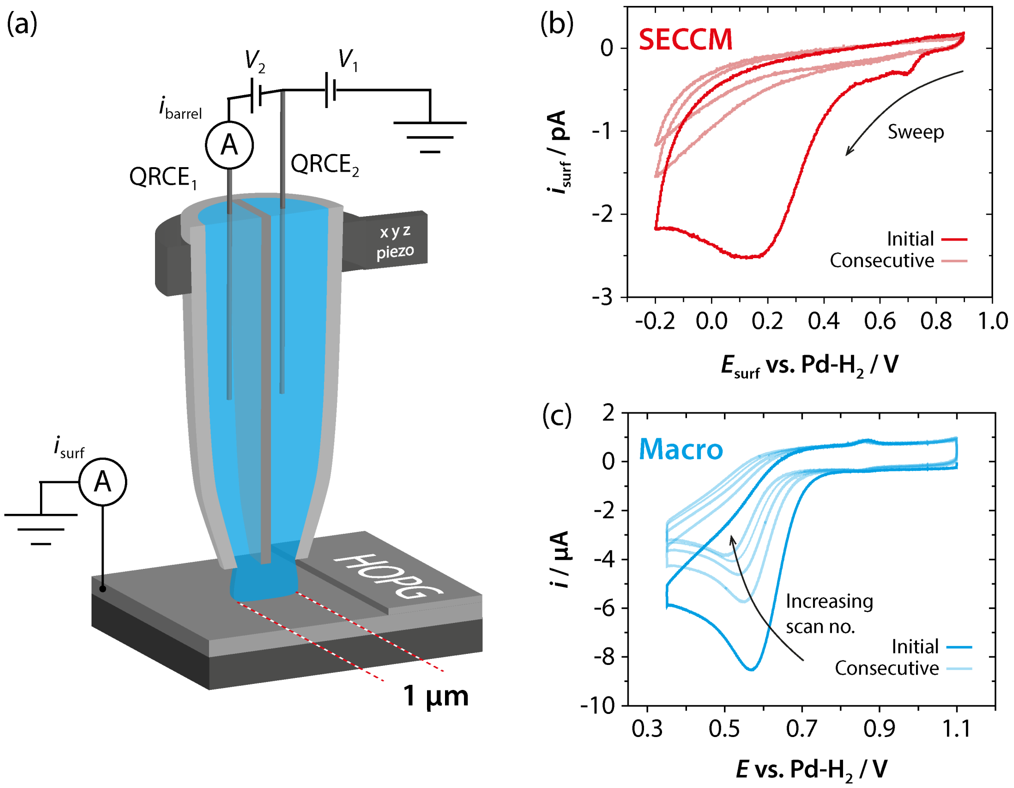

Figure 5.3 (a) The SECCM setup. CVs for the reduction of 0.1 mM 4-CBD at an HOPG surface obtained using (b) the SECCM setup, with 25 mM H_2SO_4 aqueous electrolyte and a 1 µm diameter pipet, and (c) with a 3.2 mm diameter macro-disk electrode (droplet confined using rubber O-ring) in 100 mM H_2SO_4. Both CVs were obtained with a scan rate of 100 mV s^{-1} on a freshly cleaved HOPG surface.

A broad irreversible reduction wave is observed on the initial potential sweep (peak potential, E_p = 0.15 V vs. Pd-H$_2$) assigned to the electrochemical reduction of the diazonium molecule. Consecutive scans display a diminished current magnitude since the aryl radicals produced covalently attach to the electrode surface, partly blocking it and inhibiting further electron transfer. This voltammetric behavior is similar to that observed during the macroscale modification process at the same concentration (Figure 5.3(c)), giving confidence that the microscale SECCM measurements mimic the macroscale process. Interestingly, the reduction wave of the macroscopic CV appears sharper and at a less driving potential to that of the SECCM measurement. The increased mass-transport rate associated with SECCM leads to enhanced surface modification rates, thus blocking of the HOPG surface occurs faster, shifting the position of the peak to a more reducing potential since modification becomes increasingly more kinetically hindered. Such an effect is also evident in subsequent CV cycles, which show essentially zero current in SECCM modification (since the surface is already extensively blocked), but still clearly show further modification using the macroscale setup. Furthermore, peak potentials for subsequent scans in the macroscale voltammetry are also gradually shifted to more reducing potentials, as the surface becomes blocked.

5.2.3 Diazonium Microspot Array Deposition

Aryl grafting using the CV technique has proven to be an effective route to surface modification,[15] however the sensitivity of the grafting process to factors such as diazonium concentration, potential range, and scan rate makes reproducible grafting somewhat difficult; hence, grafting at a constant reducing potential is now commonly employed for surface modification. The effect of variables such as diazonium concentration,[15] applied potential,[16] and electrolysis time,[38] on the resulting film thickness and surface coverage has been investigated, with all shown to have a significant effect. Intuitively, modification at low driving potentials, using solutions of low concentration would provide the highest level of grafting control, predominantly by slowing the grafting process down, extending the range of grafting time available, and hence levels of achievable surface modification.

To demonstrate the localized modification possible using SECCM, and to investigate the effects of substrate grafting potential and modification time on the resulting diazonium film structure, an array of diazonium-modified spots was created on the HOPG surface. For each individual modification, the potential V_1 was set to achieve a desired value of E_{surf}, before the pipet was approached to the surface until meniscus contact (determined by a sharp jump in the AC component of the barrel conductance current), at which point movement stopped and the pipet was held in place for a defined hold time. The pipet was then withdrawn, breaking the electrochemical circuit (meniscus contact), and immediately halting the modification reaction. The process was repeated at fresh areas of the HOPG surface for a range of hold times, typically between 0.5 seconds and 8.5 seconds, with a 0.5 second increment time. This created an array of 17 diazonium-patterned spots. In addition, deposition arrays were created at three different E_{surf} values, denoted E_{max}, E_{mid} and E_{min}, where $E_{\mathrm{max}} = E_{\mathrm{p}}$, $E_{\mathrm{mid}} = E_{\mathrm{p}} + 150$ mV and $E_{\mathrm{min}} = E_{\mathrm{p}} + 250$ mV, a sequence corresponding to less driving potentials, thereby providing lower rates of aryl radical production.

An insight into the grafting process can be obtained through examination of the current-time transients for the spot depositions at each of the three potentials, with an example of each shown in Figure 5.4(a).

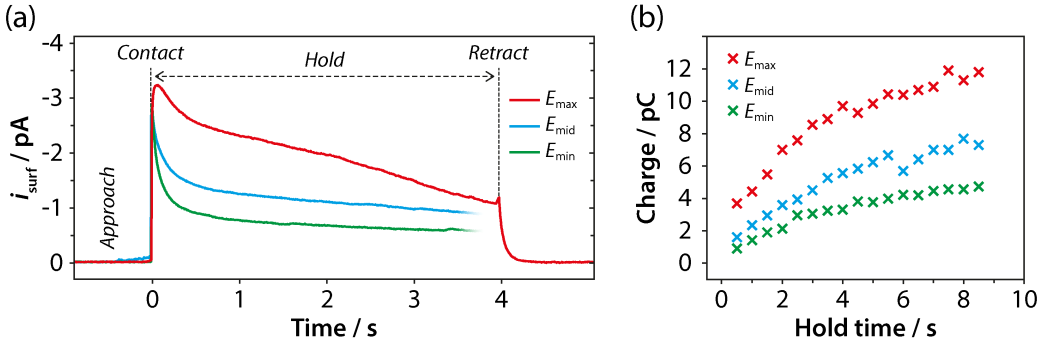

Figure 5.4 (a) Three typical current-time transients obtained during the spot deposition, one for each deposition potential employed. (b) Electrochemical charge associated with each of the spot depositions as a function of hold time, for each of the three deposition potentials employed.

The typical transients each show zero current during the approach of the meniscus to the surface, an immediate jump upon meniscus contact (owing to the diazonium reduction process), followed by a current decay during the hold step, and a final jump back to zero upon retraction of the pipet. Considering the first transient at E_{max}, the initial current decay (< 2 seconds), much longer than the characteristic diffusion time constant of SECCM (~ 5 milliseconds),[53] is mainly due to transient radical generation, starting at the bare/unreacted sp^2 carbon surface, coupled with some effective blocking of the HOPG surface by the electrogenerated radicals. There is a superimposed longer duration decay resulting from the increasingly thick, insulating diazonium layer that is formed, reducing the reactant flux to the electrode surface, thus hindering electron transfer. Potentials E_{mid} and E_{min} show somewhat simpler behavior, with the current decay occurring on a longer timescale. The electrochemical charge associated with each of the deposition spots (Figure 5.4(b)) is seen to increase monotonically with time, suggesting that radical production still occurred, even at the longest hold time of 8.5 seconds.

5.2.4 Patterned Spot AFM Analysis

AFM images of the spots produced at each of the three deposition potentials were acquired in order to provide additional information on the levels of surface modification, and degree of multilayer extension, over the range of deposition times investigated. Figures 5.5(a), (b) and (c) show TM-AFM images of the deposition spots at potentials E_{max}, E_{mid} and E_{min}, respectively.

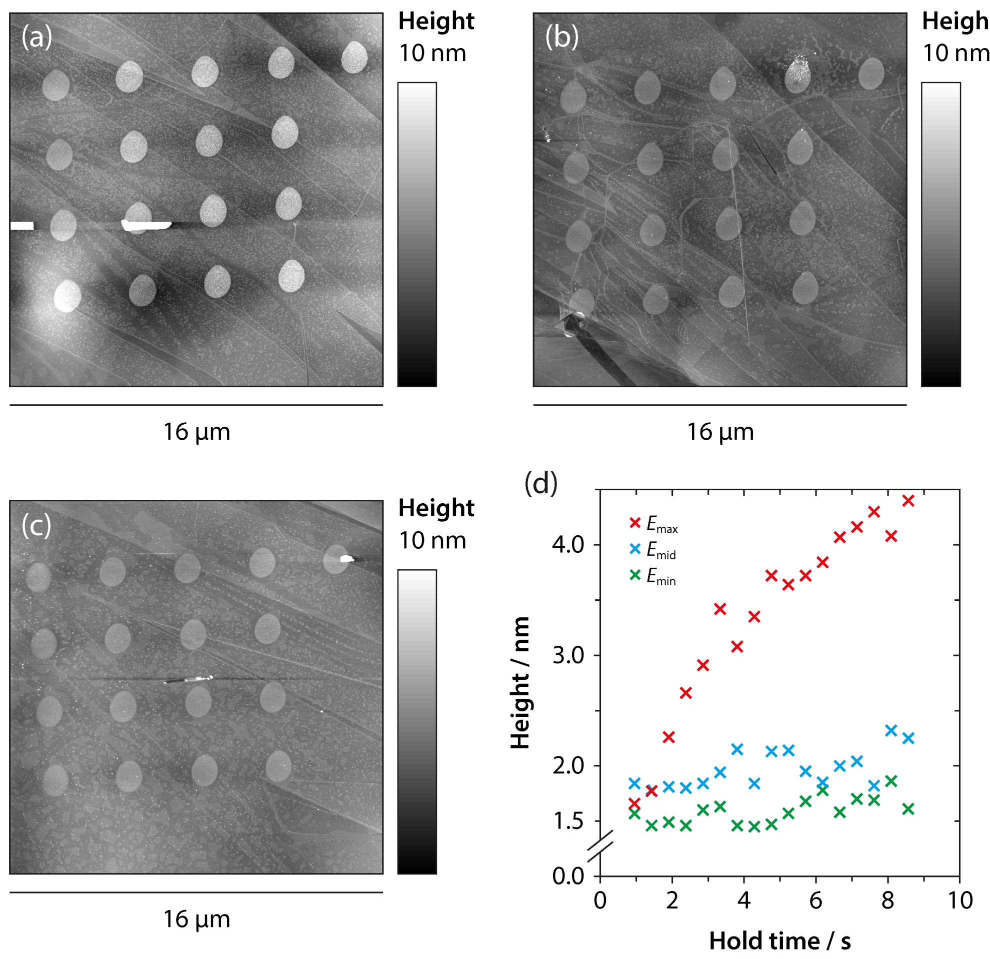

Figure 5.5 AFM topography images of typical deposition arrays created at potentials E_{max} (a), E_{mid} (b), and E_{min} (c), using various deposition times. (d) Heights of each deposit (determined by AFM) as a function of hold time, for the different potentials employed.

Clearly visible in each of the arrays are 17 well-defined discrete spots, each corresponding to a different hold time of the meniscus at the surface. The reproducible shape and dimensions of the diazonium pattern are determined purely by the SECCM pipet opening, ~ 1 µm in this case, a parameter that can, however, be easily varied from hundreds of nanometers to tens of microns, depending on the spatial resolution desired, another feature of the SECCM technique that makes it highly attractive for localized patterning. Just as noticeable throughout all three arrays is the homogeneity of the deposition within each spot, showing a consistent level of grafting within each individual modified area.

Additionally, AFM analysis provides information on the kinetics of film growth through the height of each deposition spot, measured for each potential deposition, plotted against time in Figure 5.5(d). Firstly, focusing on the array created at the most driving potential, E_{max}, it is evident that a multilayer growth process is dominant under these conditions. The film thickness increases with time (~ 4 nm after 8.5 seconds), attributed to electrogenerated aryl radicals reacting with the diazonium moieties already attached the surface. Contrastingly, AFM analysis for the two lower modification potentials shows that the spot height within each array remains more or less constant (~ 2 nm for E_{mid} and 1.5 nm for E_{min}) over the range of timescales investigated. This suggests a film growth regime where the film density (i.e. concentration of molecules in the film) increases with time, rather than the growth of multilayer structures. This is corroborated by the current-transient data, where the electrochemical charge associated with each of the deposition spots for E_{mid} and E_{min} increased monotonically, suggesting continued radical formation, despite the relatively constant microspot height.

Note, that for all timescales and potentials investigated, the thickness is still more than a monolayer (0.68 nm).[2] Importantly, the pipet used in SECCM provides high intrinsic diffusion rates to the surface, owing to non-linear diffusion from the tapered pipet design, and this rate is enhanced yet further via the applied potential between the QRCEs, leading to migration of the charged diazonium molecule to the surface.[53] Thus, compared to conventional macroscale measurements, film growth rates may be significantly enhanced, an effect also seen in recent diazonium modification on gold ultramicroelectrodes.[56]

5.2.5 Basal vs. Step Edge Modification

The use of such a small electrochemical cell, and high-quality AM grade HOPG with a very low step density, means that the basal surface of the HOPG is primarily targeted during deposition. Very similar modification spots can be seen on both the basal plane surface (without steps) and the basal surface with intersecting step edges, with no obvious material buildup around the step edges. This indicates clearly that the basal surface can easily support the electro-generation of the radical. It is also unlikely that this basal plane activity (electrochemistry) originates only at point defects. The average density of such defects on HOPG is reported to be between 10^6 and 10^{10} cm^{-2},[57,58] suggesting a maximum of ~ 100 point defects within each deposition area.

Additional macroscale modification experiments were performed on this high-quality AM HOPG, as well as SPI-3 HOPG, where the step edge density is known to be orders of magnitude higher.[59] Despite these large differences in sample quality, the resulting voltammograms and rate of blocking revealed by repetitive voltammetric cycling appear nearly identical (Figures 5.6(a) and (b)). These findings agree with other recent studies that the HOPG basal surface can easily support a wide range of electrochemical processes.[60,61]

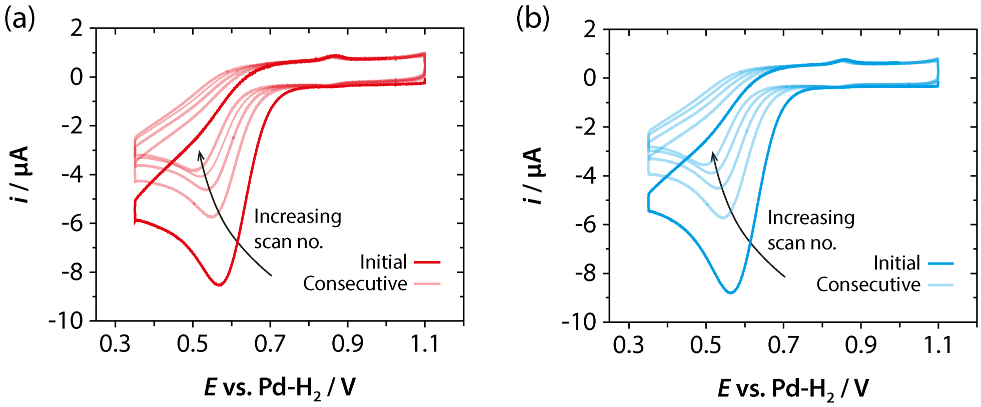

Figure 5.6 Macroscale CVs obtained for the diazonium reduction process at (a) high quality AM HOPG and (b) SPI-3 grade HOPG from 0.1 mM 4-CBD in 50 mM H_2SO_4. CVs were obtained at a scan rate of 100 mV s^{-1} with a working electrode area of 0.32 cm^2.

Furthermore, such findings shed additional light on the issue of radical attack at the pristine HOPG surface. Previous STM[15,62] and electrochemical-STM[63] studies have shown images consistent with the formation of well-ordered layers of perpendicularly oriented aryl groups coupled to the HOPG basal surface (as depicted in Figure 5.2(a)), however contrasting studies have suggested that film growth at the basal plane originates at atomic scale defects.[21] Indeed, further lateral film growth was shown to occur from these defects, via a proposed multilayer-like growth process, with the film only anchored to the surface at the original defect site. The data presented here clearly suggests radical attack at the pristine sp^2 basal surface is possible, and that surface atom rehybridization can be accommodated, as has been shown to be the case in graphene.[64]

5.2.6 Patterned Spot Raman Analysis

To further analyze the level of diazonium modification at the HOPG surface, Raman spectroscopy was employed. The Raman spectrum of bare HOPG shows a distinct peak at 1580 cm^{-1} (Figure 5.7(a)), due to the vibrational mode (G-band) of the sp^2 bonded network.[65] Full Raman details in section 2.7.4.

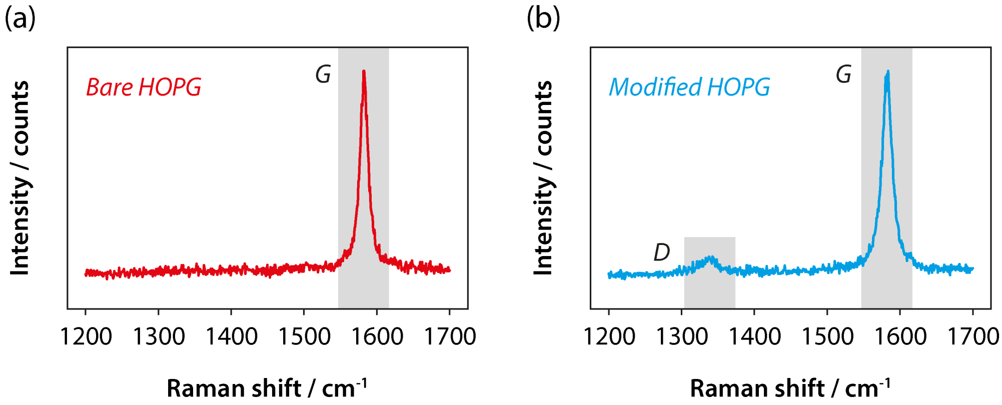

Figure 5.7 Representative Raman spectra for both bare HOPG (a) and diazonium modified HOPG (b), using the CV conditions also employed in Figure 5.6. Spectra were acquired using 633 nm laser, with ~ 1 μm laser spot size.

After diazonium modification, a second peak (D-band) develops at ~ 1350 cm^{-1} (Figure 5.7(b)), diagnostic of the local sp^3 carbon content of the HOPG surface, and hence, the level of diazonium modification.[64,66] Raman mapping of the diazonium patterned HOPG surfaces produced at E_{max} and E_{mid}, as representative of the two film growth regimes (multilayer vs. film density increase), was performed and plotted as D-band intensity, shown in Figures 5.8(a) and (b), respectively.

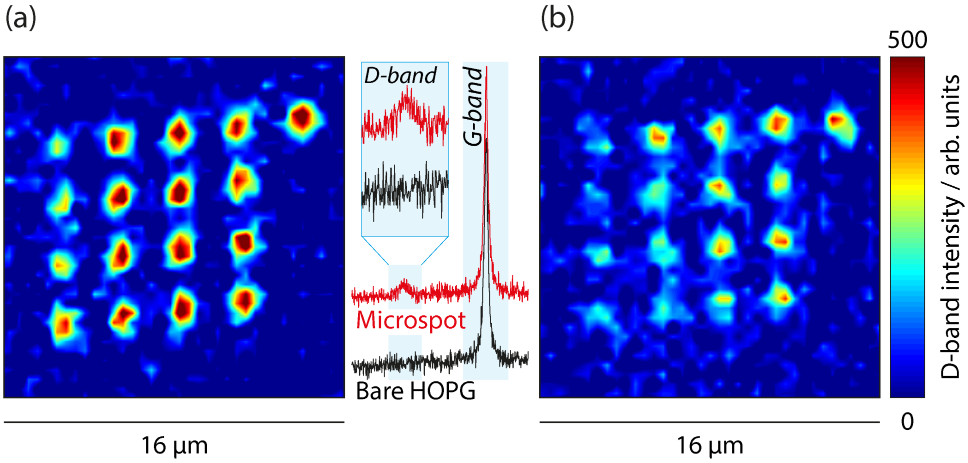

Figure 5.8 Typical Raman maps plotted as D-band intensity over the surface of the arrays created at E_{max} (a) and E_{mid} (b) along with representative spectra for both modified and unmodified areas of the surface.

Each map shows distinct features, in positions that correlate with the spots seen by AFM imaging, confirming the covalent attachment of aryl groups at both basal plane and step edge sites. Furthermore, Figure 5.9 plots normalized D-band intensity for each complete deposition spot, providing information on the level of sp^3 carbon over the range of hold times investigated. The two different growth regimes at E_{max} and E_{mid} are manifested as different trends in intensity vs. time. Firstly, the D-band at E_{max} shows a short, sharp increase over the first 2 seconds, attributed to increasing coverage of the HOPG surface, up to a maximum value, beyond which no major change in the Raman signal is seen.

Coupled with the AFM data, this points to a poly-aryl multilayer growth process[67] in which the film thickness increases with time, but the maximum surface coverage is obtained within a short (~ 2 seconds) period.

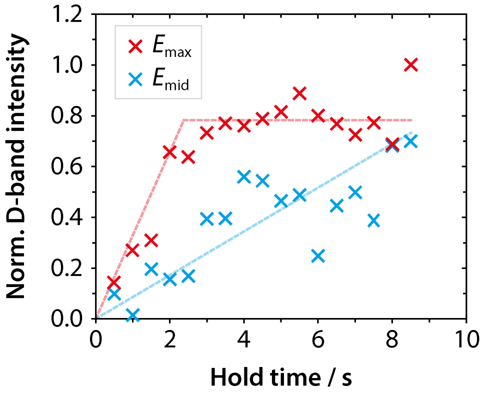

Figure 5.9 Normalized D-band intensity (with respect to maximum D-band intensity measured), plotted for each of the spots as a function of hold time, for the aforementioned maps at both E_{max} and E_{mid}.

In contrast, although the Raman data at E_{mid} shows some scatter (as a result of the laser spot and microspot being of similar size), an overall trend of increasing D-band intensity with time is evident, consistent with the interpretation of the AFM and current-time data that the major process at low driving force is the increase in concentration of a film of more or less constant thickness. Corresponding D/G ratio maps (Figure 5.10) showed the same trend, with typical D/G ratios in modified areas being 0.05, in very good agreement with values obtained previously for diazonium grafted HOPG electrodes.[68] However, it should be noted that analysis of the Raman data provides only a relative description of the levels of sp^3 carbon introduced, since the overwhelming G-band signal arises from both the surface and from the underlying graphite material.

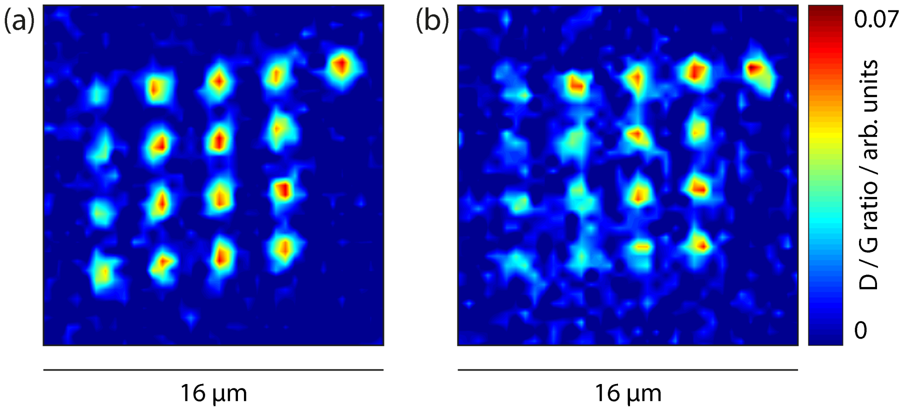

Figure 5.10 Corresponding Raman maps of D / G-band intensity to those presented in Figure 5.8, for modification at E_{max} (a) and E_{mid} (b).

The electrochemical charge associated with the grafting process can provide details as to the level of surface coverage, Γ, achieved, as it directly relates to the number of aryl radicals produced, providing a quantitative insight on the number of aryl moieties attached to the surface. However, it is well known that the grafting process is not wholly efficient and that a proportion of the radicals produced at the electrode surface can be lost to side reactions in solution. Thus, determining a level of surface coverage directly from the associated electrochemical charge is likely to introduce a degree of error. Methods do however exist for estimating such a grafting efficiency.

5.2.7 Modeling the Grafting Efficiency

Whilst the formation of a covalent bond to the surface during the diazonium grafting process may be the desirable outcome, diffusion of the radical back into solution, and side-reactions with solvent and/or diazonium molecules is known to occur. Such processes introduce a grafting efficiency term, which must thus be considered if one wishes to extract accurate quantitative data on the level of surface coverage. The simplified scheme in

Figure 5.11 summarizes the radical reaction possibilities, where all surface processes (binding to HOPG and binding to already grafted aryl moieties) are encapsulated in reaction R2, and all species that end up in solution are described by R3. The potential-dependent radical generation is defined by R1.

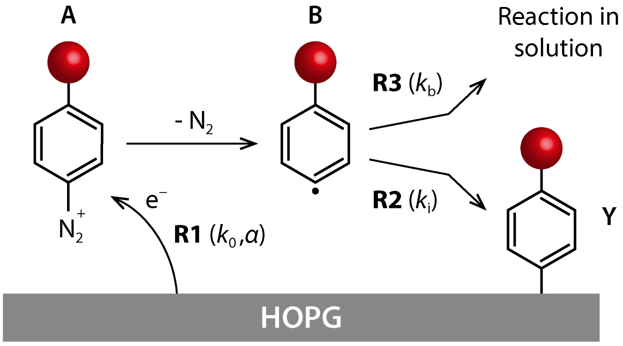

Figure 5.11 Schematic representation showing the generation of an aryl radical at an HOPG surface (R1), and possible radical reaction routes, with the surface (R2) and solution (R3).

A parameter characterizing the competition between surface and bulk reactions of the radical species (denoted hereon as '*s*') was originally introduced by Savéant *et al.*[69] and can be determined from detailed analysis of the diazonium grafting CV. It has been specifically applied to study electrode functionalization by diazonium compounds:[15]

$$s = \frac{k_\mathrm{i}}{k_\mathrm{i} + \sqrt{k_\mathrm{b} D}} \tag{5.1}$$

where *s* is the aforementioned sticking coefficient, *D* is the diffusion coefficient of the generated radical, and k_i and k_b are the rate constants associated with the respective reactions shown in the above scheme.

In order to aid the analysis process, simplifying assumptions are made, such that only the first cycle of the diazonium grafting CV is analyzed, thereby focusing on the formation of the initial layer. It is assumed that the rate constant of electron transfer on any unmodified part of the surface is unaffected by the blocking process on neighboring parts, as also assumed in reference 15. All possible solution processes that lead to escape of the radical are combined into one characteristic kinetic process, and it is also reasonably assumed that the kinetics of the electron transfer process with the diazonium molecule is fast on the CV timescale through the formal assignment of a standard rate constant, k_0 = 1 cm s^{-1}, typical for small rigid molecules of this type.[70]

A value of $D = 7.6 \text{ x } 10^{-6}$ cm^2 s^{-1} was determined for the 4-CBD molecule investigated using the Wilke-Chang method[71] and was assumed to be the same for both the diazonium cation and resulting aryl radical.

We may write a diffusion equation for species A (eq. 5.2) and for species B (eq. 5.3) taking into account net loss to bulk reaction:

$$\frac{\partial C_\mathrm{A}}{\partial t} = D\frac{\partial^2 C_\mathrm{A}}{\partial x^2} \qquad (5.2)$$

$$\frac{\partial C_\mathrm{B}}{\partial t} = D\frac{\partial^2 C_\mathrm{B}}{\partial x^2} - k_\mathrm{b} C_\mathrm{B} \qquad (5.3)$$

where C_A and C_B are the concentrations of species A and B, respectively, and all other terms take their predefined meaning. Species A is assumed to undergo irreversible electron transfer, essentially because of the rapid loss of N_2 to produce B, so that back electron transfer becomes negligible at the potentials of interest. In accordance with Butler-Volmer kinetics, this can be presented as a boundary condition at the electrode surface for A (eq. 5.4). Species B is derived from A, but can also react with the electrode, presenting a boundary condition for B (eq. 5.5) at the electrode surface.

At $x = 0$

$$j = -FD\left(\frac{\partial C_{\mathrm{A}}}{\partial x}\right) = -FC_{\mathrm{A}}k_0 exp\left[-\frac{\alpha F}{RT}(E - E^{0'})\right] \tag{5.4}$$

$$-D\frac{\partial C_{\mathrm{B}}}{\partial x} = D\frac{\partial C_{\mathrm{A}}}{\partial x} - k_{\mathrm{i}}C_{\mathrm{B}} \tag{5.5}$$

where j is the current density, $E^{0'}$ is the formal potential of the ET reaction, and other symbols have their usual meaning.

Crucially, as reaction R2 proceeds, the available surface area for reaction R1 diminishes, resulting in a decrease in the average current density, j_{av}, compared to the uninhibited process; thus, an expression for j_{av} was obtained (eq. 5.6)

$$j_{\mathrm{av}} = exp\left[-\frac{1}{\Gamma_0}\int_0^t k_{\mathrm{i}}(C_{\mathrm{B}})_{\mathrm{x=0}}dt\right]FD\left(\frac{\partial C_{\mathrm{A}}}{\partial x}\right)_{\mathrm{x=0}} \tag{5.6}$$

where Γ_0 is the maximum surface coverage obtainable (i.e. that of a fully packed layer).

The remaining boundary conditions are presented in eqs. 5.7 to 5.10.

At $x = \infty$

$$C_{\mathrm{A}} = C_{\mathrm{A,0}} \tag{5.7}$$

$$C_{\mathrm{B}} = 0 \tag{5.8}$$

and initial conditions are

$$C_{\mathrm{A}}(x, 0) = C_{\mathrm{A,0}} \tag{5.9}$$

$$C_{\mathrm{B}}(x,0) = 0 \tag{5.10}$$

where $C_{\mathrm{A},0}$ is the bulk concentration of A.

Differential equations 5.2 and 5.3, combined with 5.4, 5.5 and 5.7 – 5.10, were solved numerically and the average current density then determined from eq. 5.6. A value of 1.30 x 10^{-9} mol cm^{-2} was used for Γ_0 (within the literature range of 1.20 – 1.35 x 10^{-9} mol cm^{-2})[22,72] and a value of $\alpha = 0.5$ was set, based on a previously used value.[15]

Thus, values for $E^{0'}$, k_{i} and k_{b} were required based on an experimental LSV. To quantify the difference between the theoretical and experimental LSV, an objective function was employed, namely the square root of the sum of squares, referred to as $f((E^{0'})_{\mathrm{opt}}, k_{\mathrm{i}}, k_{\mathrm{b}})$.

A theoretical LSV computed with best-fit parameters is shown in Figure 5.12(a), along with corresponding experimental data. It is evident that the simple model employed provides a good fit to the experimental data presented. However, analysis of the chosen optimization procedure showed that reliable estimation was only achieved for the formal potential of the ET process, which we denote $(E^{0'})_{\mathrm{opt}} = 0.238$ V, and that the fit was equally good for a multitude of k_{i}, / k_{b} pairs. By fixing the formal potential at this optimal value, and plotting $f(k_{\mathrm{i}}, k_{\mathrm{b}})$ as a contour plot (Figure 5.12(b)), it was found that all k_{i} and k_{b} values associated with the 'best-fit' are located in a shallow canyon. However, a plot of k_{i} vs. k_{b} values located within the global canyon yielded a very close fit to eq. 5.11 (Figure 5.12(c)), a rearrangement of eq. 5.1.

$$k_{\mathrm{i}} = \frac{\sqrt{D}}{1-s}\sqrt{k_{\mathrm{b}}} \tag{5.11}$$

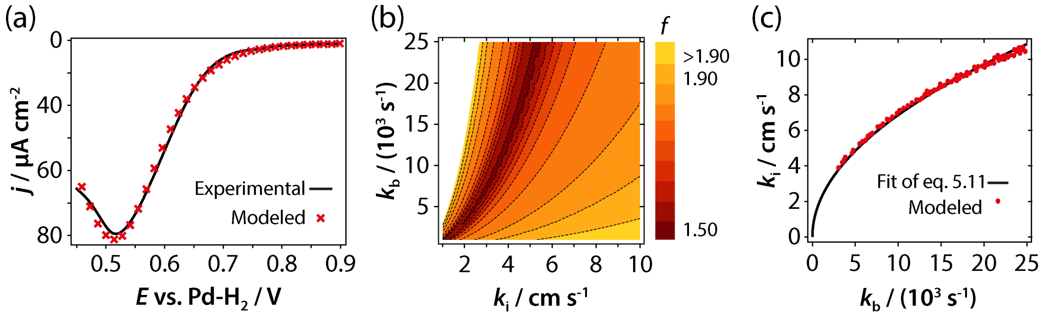

Figure 5.12 (a) LSV between 0.9 and 0.45 V vs. Pd-H$_2$ for the reduction of 1 mM 4-CBD at an HOPG electrode (line) and corresponding experimental fit to the data (crosses). (b) Plot of $f((E^{0'})_{\mathrm{opt}}, k_{\mathrm{i}}, k_{\mathrm{b}})$ values as a function of k_{i} and k_{b}. (c) k_{i} and k_{b} data for the global canyon visible in (b), and the fitted function according to eq. 5.11. The global minimum contour corresponds to $f_{\mathrm{min}} = 1.502$.

Such a fit yielded a value of s = 0.92, i.e. 92 % of the aryl radicals generated at the electrode go to the surface, and only a small fraction (8 %) are lost to solution.

5.2.8 Estimating Diazonium Film Density

With a value of s for the system investigated now known, levels of surface coverage were estimated. Figure 5.13(a) shows Γ (determined from the electrochemical charge) against hold time for all deposition experiments, considering an 8 % loss of radicals to solution, providing detail on the number of aryl moieties bound to the surface at each point. From such values, additional information can be extracted by also taking into account the individual spot deposition heights, Figure 5.13(b)

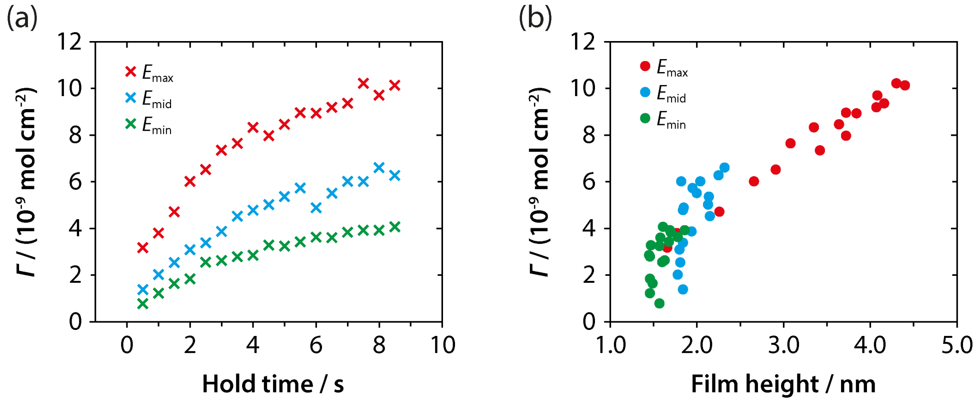

Figure 5.13 (a) Plots of surface coverage (determined from electrochemical charge with $s = 0.92$) against hold time for each of the three deposition potentials investigated. (b) Plots of surface coverage against deposition height for each of the three deposition potentials.

This plot informs on changes in film density with hold time, yielding film density values, and hence providing detail on the relative number of sp^3 carbon centers introduced at the sp^2 surface. Depositions performed at E_{max} show a distinct linear trend, suggesting film growth at a more or less constant density, with an estimate of the average film density of 1.7 x 10^{-9} mol cm^{-2} monolayer^{-1}, a reasonable match with the range expected if all layers were densely packed (1.20 – 1.35 x 10^{-9} mol cm^{-2} monolayer^{-1}),[22,72] and in very good agreement with previous literature.[15,49] Thus, films appear densely packed, with hold time controlling only the degree of multilayer extension. Only the density values for depositions < 2 seconds deviate below this average value, indicating the film has a lower density at these very short timescales. Interestingly, the Raman intensity data (Figure 5.8) for these short timescales also suggested films of lower density, since the values associated with the D-band had not plateaued at this point.

In contrast, the density values produced at E_{mid} and E_{min} appear to increase with longer deposition times, as depicted by increasing surface coverage values, despite relatively constant deposition heights (Figure 5.5), before beginning to plateau at 1.8 x 10^{-9} mol cm^{-2} $monolayer^{-1}$ and 1.7 x 10^{-9} mol cm^{-2} $monolayer^{-1}$ respectively, at the longest hold time investigated.

This analysis fully corroborates conclusions drawn from both AFM and Raman data, which suggested that small driving potentials accessed an initial film-filling regime. This highlights the whole range of film densities, and hence levels of sp^3 carbon, obtainable in the final film through the use of lower modification potentials, and suitable modification times.

5.3 Conclusions

The ability of SECCM to perform diazonium compound reactive patterning, with a high-degree of spatial resolution, at a pristine sp^2 carbon surface has been demonstrated. Such an approach provides a route to detailed surface patterning, whilst overcoming the numerous disadvantages associated with diazonium patterning techniques previously demonstrated in the literature.

Crucially, the resulting properties of the diazonium modification could be tuned purely via applied potential and meniscus contact time, as investigated through detailed AFM and Raman analysis of the resulting diazonium deposits. Regimes focused on the introduction of sp^3 carbon at the sp^2 surface could be preferentially selected and controlled through low modification potentials, whilst the extent of a predominantly multilayer growth regime could be selected through the application of more driving potentials, consistent with those commonly used in the literature. Such tight control over the diazonium reaction process paves the way for both electrochemistry, and SECCM, in tailored surface modification.

5.4 References

(1) Lehr, J.; Williamson, B. E.; Flavel, B. S.; Downard, A. J. *Langmuir* **2009**, *25*, 13503.

(2) Laforgue, A.; Addou, T.; Belanger, D. *Langmuir* **2005**, *21*, 6855.

(3) Ghilane, J.; Delamar, M.; Guilloux-Viry, M.; Lagrost, C.; Mangeney, C.; Hapiot, P. *Langmuir* **2005**, *21*, 6422.

(4) Bernard, M. C.; Chausse, A.; Cabet-Deliry, E.; Chehimi, M. M.; Pinson, J.; Podvorica, F.; Vautrin-Ul, C. *Chem. Mater.* **2003**, *15*, 3450.

(5) Hines, T.; Diez-Perez, I.; Nakamura, H.; Shimazaki, T.; Asai, Y.; Tao, N. *J. Am. Chem. Soc.* **2013**, *135*, 3319.

(6) Chamoulaud, G.; Belanger, D. *J. Phys. Chem. C* **2007**, *111*, 7501.

(7) Kullapere, M.; Matisen, L.; Saar, A.; Sammelselg, V.; Tammeveski, K. *Electrochem. Commun.* **2007**, *9*, 2412.

(8) Combellas, C.; Delamar, M.; Kanoufi, F.; Pinson, J.; Podvorica, F. I. *Chem. Mater.* **2005**, *17*, 3968.

(9) Allongue, P.; de Villeneuve, C. H.; Cherouvrier, G.; Cortes, R.; Bernard, M. C. *J. Electroanal. Chem.* **2003**, *550*, 161.

(10) deVilleneuve, C. H.; Pinson, J.; Bernard, M. C.; Allongue, P. *J. Phys. Chem. B* **1997**, *101*, 2415.

(11) Valenti, G.; Bardini, L.; Bonazzi, D.; Rapino, S.; Marcaccio, M.; Paolucci, F. *J. Phys. Chem. C* **2010**, *114*, 22165.

(12) Mangeney, C.; Qin, Z.; Dahoumane, S. A.; Adenier, A.; Herbst, F.; Boudou, J. P.; Pinson, J.; Chehimi, M. M. *Diam. Relat. Mater.* **2008**, *17*, 1881.

(13) Bahr, J. L.; Yang, J. P.; Kosynkin, D. V.; Bronikowski, M. J.; Smalley, R. E.; Tour, J. M. *J. Am. Chem. Soc.* **2001**, *123*, 6536.

(14) Strano, M. S.; Dyke, C. A.; Usrey, M. L.; Barone, P. W.; Allen, M. J.; Shan, H. W.; Kittrell, C.; Hauge, R. H.; Tour, J. M.; Smalley, R. E. *Science* **2003**, *301*, 1519.

(15) Allongue, P.; Delamar, M.; Desbat, B.; Fagebaume, O.; Hitmi, R.; Pinson, J.; Saveant, J. M. *J. Am. Chem. Soc.* **1997**, *119*, 201.

(16) Downard, A. J. *Langmuir* **2000**, *16*, 9680.

(17) Itoh, T.; McCreery, R. L. *J. Am. Chem. Soc.* **2002**, *124*, 10894.

(18) Kariuki, J. K.; McDermott, M. T. *Langmuir* **2001**, *17*, 5947.

(19) Saby, C.; Ortiz, B.; Champagne, G. Y.; Belanger, D. *Langmuir* **1997**, *13*, 6805.

(20) Bradbury, C. R.; Kuster, L.; Fermin, D. J. *J. Electroanal. Chem.* **2010**, *646*, 114.

(21) Kariuki, J. K.; McDermott, M. T. *Langmuir* **1999**, *15*, 6534.

(22) Liu, Y. C.; McCreery, R. L. *J. Am. Chem. Soc.* **1995**, *117*, 11254.

(23) Koehler, F. M.; Luechinger, N. A.; Ziegler, D.; Athanassiou, E. K.; Grass, R. N.; Rossi, A.; Hierold, C.; Stemmer, A.; Stark, W. J. *Angew. Chem. Int. Ed.* **2009**, *48*, 224.

(24) Novoselov, K. S.; Geim, A. K.; Morozov, S. V.; Jiang, D.; Zhang, Y.; Dubonos, S. V.; Grigorieva, I. V.; Firsov, A. A. *Science* **2004**, *306*, 666.

(25) Bekyarova, E.; Sarkar, S.; Wang, F.; Itkis, M. E.; Kalinina, I.; Tian, X.; Haddon, R. C. *Acc. Chem. Res.* **2013**, *46*, 65.

(26) Johns, J. E.; Hersam, M. C. *Acc. Chem. Res.* **2013**, *46*, 77.

(27) Paulus, G. L. C.; Wang, Q. H.; Strano, M. S. *Acc. Chem. Res.* **2013**, *46*, 160.

(28) Niyogi, S.; Bekyarova, E.; Itkis, M. E.; Zhang, H.; Shepperd, K.; Hicks, J.; Sprinkle, M.; Berger, C.; Lau, C. N.; deHeer, W. A.; Conrad, E. H.; Haddon, R. C. *Nano Lett.* **2010**, *10*, 4061.

(29) Zhang, H.; Bekyarova, E.; Huang, J.-W.; Zhao, Z.; Bao, W.; Wang, F.; Haddon, R. C.; Lau, C. N. *Nano Lett.* **2011**, *11*, 4047.

(30) Mesnage, A.; Esnouf, S.; Jegou, P.; Deniau, G.; Palacin, S. *Chem. Mater.* **2010**, *22*, 6229.

(31) Mirkhalaf, F.; Mason, T. J.; Morgan, D. J.; Saez, V. *Langmuir* **2011**, *27*, 1853.

(32) Bahr, J. L.; Tour, J. M. *Chem. Mater.* **2001**, *13*, 3823.

(33) Kosynkin, D.; Bockman, T. M.; Kochi, J. K. *J. Am. Chem. Soc.* **1997**, *119*, 4846.

(34) Delamar, M.; Hitmi, R.; Pinson, J.; Saveant, J. M. *J. Am. Chem. Soc.* **1992**, *114*, 5883.

(35) Adenier, A.; Bernard, M. C.; Chehimi, M. M.; Cabet-Deliry, E.; Desbat, B.; Fagebaume, O.; Pinson, J.; Podvorica, F. *J. Am. Chem. Soc.* **2001**, *123*, 4541.

(36) Adenier, A.; Cabet-Deliry, E.; Chausse, A.; Griveau, S.; Mercier, F.; Pinson, J.; Vautrin-Ul, C. *Chem. Mater.* **2005**, *17*, 491.

(37) Lim, H.; Lee, J. S.; Shin, H.-J.; Shin, H. S.; Choi, H. C. *Langmuir* **2010**, *26*, 12278.

(38) Brooksby, P. A.; Downard, A. J. *Langmuir* **2004**, *20*, 5038.

(39) Brooksby, P. A.; Downard, A. J. *J. Phys. Chem. B* **2005**, *109*, 8791.

(40) Wilbur, J. L.; Kumar, A.; Kim, E.; Whitesides, G. M. *Adv. Mater.* **1994**, *6*, 600.

(41) Herzer, N.; Hoeppener, S.; Schubert, U. S. *Chem. Commun.* **2010**, *46*, 5634.

(42) Brooksby, P. A.; Downard, A. J. *Langmuir* **2005**, *21*, 1672.

(43) Garrett, D. J.; Lehr, J.; Miskelly, G. M.; Downard, A. J. *J. Am. Chem. Soc.* **2007**, *129*, 15456.

(44) Torbensen, K.; Malmos, K.; Kanoufi, F.; Combellas, C.; Pedersen, S. U.; Daasbjerg, K. *ChemPhysChem* **2012**, *13*, 3303.

(45) Hossain, M. Z.; Walsh, M. A.; Hersam, M. C. *J. Am. Chem. Soc.* **2010**, *132*, 15399.

(46) Corgier, B. P.; Belanger, D. *Langmuir* **2010**, *26*, 5991.

(47) Flavel, B. S.; Gross, A. J.; Garrett, D. J.; Nock, V.; Downard, A. J. *ACS Appl. Mater. Interfaces* **2010**, *2*, 1184.

(48) Lehr, J.; Garrett, D. J.; Paulik, M. G.; Flavel, B. S.; Brooksby, P. A.; Williamson, B. E.; Downard, A. J. *Anal. Chem.* **2010**, *82*, 7027.

(49) Bekyarova, E.; Itkis, M. E.; Ramesh, P.; Berger, C.; Sprinkle, M.; de Heer, W. A.; Haddon, R. C. *J. Am. Chem. Soc.* **2009**, *131*, 1336.

(50) Cougnon, C.; Gohier, F.; Belanger, D.; Mauzeroll, J. *Angew. Chem. Int. Ed.* **2009**, *48*, 4006.

(51) Ritzert, N. L.; Rodriguez-Lopez, J.; Tan, C.; Abruna, H. D. *Langmuir* **2013**, *29*, 1683.

(52) Doppelt, P.; Hallais, G.; Pinson, J.; Podvorica, F.; Verneyre, S. *Chem. Mater.* **2007**, *19*, 4570.

(53) Snowden, M. E.; Güell, A. G.; Lai, S. C. S.; McKelvey, K.; Ebejer, N.; O'Connell, M. A.; Colburn, A. W.; Unwin, P. R. *Anal. Chem.* **2012**, *84*, 2483.

(54) Ebejer, N.; Schnippering, M.; Colburn, A. W.; Edwards, M. A.; Unwin, P. R. *Anal. Chem.* **2010**, *82*, 9141.

(55) Güell, A. G.; Ebejer, N.; Snowden, M. E.; Macpherson, J. V.; Unwin, P. R. *J. Am. Chem. Soc.* **2012**, *134*, 7258.

(56) Munteanu, S.; Garraud, N.; Roger, J. P.; Amiot, F.; Shi, J.; Chen, Y.; Combellas, C.; Kanoufi, F. *Anal. Chem.* **2013**, *85*, 1965.

(57) Zoval, J. V.; Stiger, R. M.; Biernacki, P. R.; Penner, R. M. *J. Phys. Chem.* **1996**, *100*, 837.

(58) Miranda-Hernandez, M.; Gonzalez, I.; Batina, N. *J. Phys. Chem. B* **2001**, *105*, 4214.

(59) Patel, A. N.; Tan, S.-Y.; Unwin, P. R. *Chem. Commun.* **2013**, *49*, 8776.

(60) Lai, S. C. S.; Patel, A. N.; McKelvey, K.; Unwin, P. R. *Angew. Chem. Int. Ed.* **2012**, *51*, 5405.

(61) Patel, A. N.; McKelvey, K.; Unwin, P. R. *J. Am. Chem. Soc.* **2012**, *134*, 20246.

(62) Liu, S. Q.; Tang, Z. Y.; Shi, Z.; Niu, L.; Wang, E. K.; Dong, S. J. *Langmuir* **1999**, *15*, 7268.

(63) Tanaka, M.; Sawaguchi, T.; Sato, Y.; Yoshioka, K.; Niwa, O. *Langmuir* **2011**, *27*, 170.

(64) Koehler, F. M.; Jacobsen, A.; Ensslin, K.; Stampfer, C.; Stark, W. J. *Small* **2010**, *6*, 1125.

(65) Malard, L. M.; Pimenta, M. A.; Dresselhaus, G.; Dresselhaus, M. S. *Phys. Rep.* **2009**, *473*, 51.

(66) Wang, Q. H.; Jin, Z.; Kim, K. K.; Hilmer, A. J.; Paulus, G. L. C.; Shih, C.-J.; Ham, M.-H.; Sanchez-Yamagishi, J. D.; Watanabe, K.; Taniguchi, T.; Kong, J.; Jarillo-Herrero, P.; Strano, M. S. *Nat. Chem.* **2012**, *4*, 724.

(67) Adenier, A.; Combellas, C.; Kanoufi, F.; Pinson, J.; Podvorica, F. I. *Chem. Mater.* **2006**, *18*, 2021.

(68) Zeb, G.; Gaskell, P.; Le, X. T.; Xiao, X.; Szkopek, T.; Cerruti, M. *Langmuir* **2012**, *28*, 13042.

(69) Bhugun, I.; Saveant, J. M. *J. Electroanal. Chem.* **1995**, *395*, 127.

(70) Bard, A. J.; Faulkner, L. R. *Electrochemical Methods: Fundamentals and Applications*; Wiley, 2001.

(71) Wilke, C. R.; Chan, P. *AIChE* **1955**, *1*, 264.

(72) Pinson, J.; Podvorica, F. *Chem. Soc. Rev.* **2005**, *34*, 429.

Chapter Six

The Direct Electrochemical Writing of Integrated Graphene Circuitry

In this chapter, the ability of SECCM to act as a lithographic writing tool is demonstrated. The patterning of graphene circuitry for applications in digital electronics is by no means straightforward, requiring both the production of defined graphene pathways or interconnects, as well regions that are SC in nature. Whilst numerous methodologies exist that target either one of these aspects, very few can successfully target both, thus requiring multi-step processes for the fabrication of a nanometer sized graphene circuit. Herein, SECCM is introduced as a potential tool for the production of circuits made entirely of graphene, in a single-step process. Making use of a confined meniscus probe, it is demonstrated that through the adjustment of applied potential, areas of either insulating, or diazonium modified graphene can be selectively introduced at a conducting graphene surface. Complementary Raman spectroscopy, electronic, and electrochemical data are used to highlight the extent of the modification procedures. This work paves the way for the production of digital electronic circuits made entirely of graphene, an important advance toward high-speed, low power processors of the future.

6.1 Introduction

The past 10 years have seen the worldwide scientific community captivated by the rise of graphene, with its discovery in 2004[1] sparking immense academic and industrial research efforts. Its key attractions of outstanding carrier mobility,[2,3] ultimate thinness,[4] and high stability,[5] combined with intense research efforts, are likely to ensure that the potential electronic applications for such a material will not go unmissed. In the public eye, it is the material of the future.[6]

Upon its discovery, initial research was heavily focused towards developing reliable production methods for graphene. Whilst the commonly used scotch-tape method may well suit fundamental studies in the academic community,[1] it is unfeasible when the potential demand for industrial applications is considered. Such research successfully highlighted growth via CVD methods on transition metals (Ni,[7] Pd,[8] Ru[9] and Cu[10]) as the most promising and readily accessible route to synthesis, and with large-scale production (> 30 inches)[11] now reported through this approach, the focus of graphene research has begun to change direction. Considering graphene integration into electronic circuits, for example, such large-scale continuous graphene films may be of little use on their own; applications are likely to require defined patterns of the highly conductive material. Indeed, numerous graphene patterning methods have been developed, using both top-down[12-17] and bottom-up approaches,[7,18] allowing for the production of defined areas of graphene, as recently discussed by *J. M. Tour*.[19]

However, the production of an entirely integrated circuit will also require more than one single patterned region, as with FETs, for example, where graphene has already shown promise.[20] Here, the inclusion of areas of a SC material will also be necessary for the basic function of FET devices, and this presents a hurdle for graphene. The presence of an electronic band-gap in traditional SC materials (e.g. silicon) creates the option of a barrier to electron flow, thus allowing for current passage to be completely switched off, as is required by digital technologies. The lack of such a band-gap in graphene means its extreme current carrying capabilities cannot be entirely halted,[21] making the production of integrated devices that consist entirely of graphene, challenging.

An appealing route to graphene modification is via chemical modification methods. The reaction of graphene's sp^2 carbon lattice with hydrogen to produce graphane,[22] for example, has been demonstrated as a method to create an insulating material.[23] The reaction of graphene with oxygen,[24] fluorine,[25] and more recently diazonium compounds,[26-29] has been highlighted as a way to introduce SC character to graphene by opening an electronic band-gap. As with GNRs, the size of the generated band-gap can be tuned, simply by controlling the extent of the sp^2 to sp^3 rehybridization process. Whilst attractive thanks to the possible level of control available, such treatments are often performed under bulk conditions, likely rendering the entire sample semiconducting, again making the realization of an entire graphene device somewhat difficult.

A limited number of patterning methods have been demonstrated as a means to localized modification, and could provide a route to device fabrication if combined with additional processing steps.[30] In terms of both time, and device quality, it is of course preferable for any device fabrication to occur in a single step, or at least the minimum number of steps realistic, given the somewhat complex nature of the end goal. Starting with a single graphene sheet, and focusing on FET devices, a single-step process would entail the production of areas of highly insulating material, defining a conductive graphene path, followed by modification at discrete sites, to introduce SC character. Although experimentally challenging at first, when one considers the insulating nature of GO,[31] the concept of producing defined conducting channels of graphene in a GO matrix seems feasible. Partially oxidized graphene has also been shown to be SC in nature, adding further viability to this route for entire device fabrication.[32] This graphene/GO combination has indeed been investigated through high-resolution SPM techniques, such as AFM, where local oxidation has been highlighted as a route to device fabrication (Figure 6.1(a)).[33,34] However, the somewhat limited scan size and reported scan rates sometimes required (5 nm s^{-1}), limit the practical use of the technique, as does the need for precise humidity control, ensuring a meniscus between the tip and substrate exists.[35]

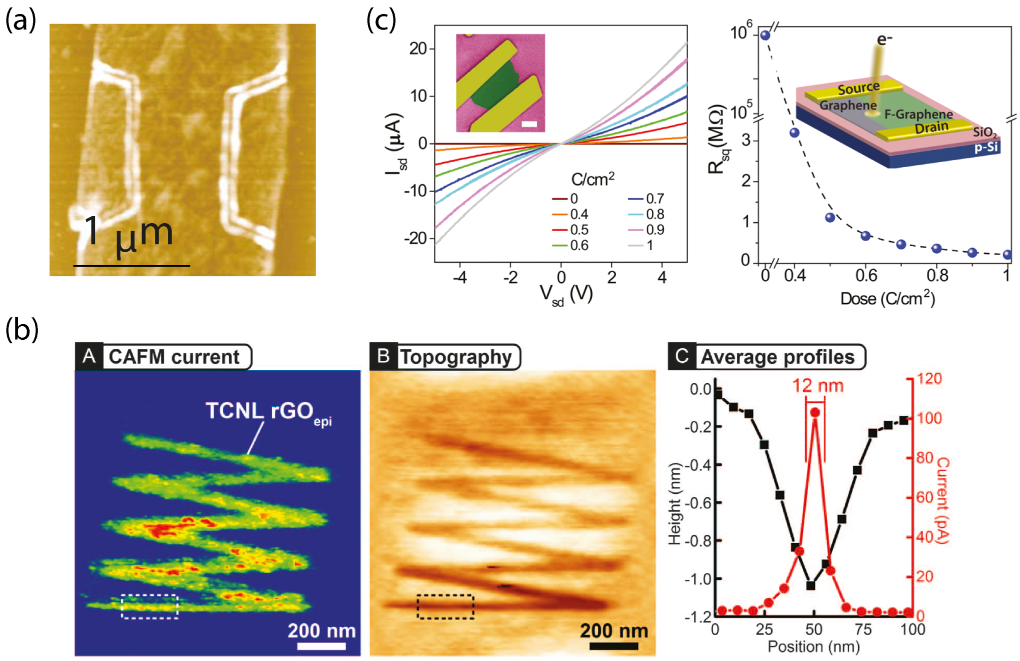

Figure 6.1 Examples of current methods for entire graphene device fabrication. (a) A single-layer graphene strip, narrowed by two oxidized regions, created with an AFM tip.[33] (b) A fluorinated graphene flake selectively reduced back to graphene using electron beam irradiation.[36] (c) A GO film with a zig-zag rGO ribbon fabricated using an AFM tip.[37]

The reverse approach to device fabrication has also been demonstrated, using GO as the host material, with subsequent patterning to create areas of rGO to form conductive channels. Here, AFM has also been demonstrated as a key patterning technique (Figure 6.1(b)),[37,38] but the use of extreme temperatures (> 1000 °C) and a reductive hydrogen atmosphere again limits the approach. Laser-based techniques have proven effective for the production of intricate rGO patterns,[39,40] as has electron beam exposure of fluorinated graphene (Figure 6.1(c)),[36] but the specialist equipment necessary may be restrictive. Furthermore, one must remember that although conductive, the electronic properties of rGO are incomparable to those of pristine graphene.[41]

In this work, SECCM is demonstrated as a realistic route to localized graphene patterning through its unique confined meniscus probe.[42] Firstly, high-quality CVD graphene is synthesized and subsequently fabricated into reproducible, individually addressable graphene microstrips, providing a suitable platform to investigate the effects SECCM modification, through both electrochemical and electronic measurements. Next, electrochemical oxidative patterning is demonstrated as a route for the production of isolated graphene regions or paths, the first requirement for graphene device fabrication (*vide supra*). The versatility of the SECCM technique is next highlighted through its ability to introduce diazonium surface chemistry, a previously identified route for the production of SC graphene,[26,27,43,44] and thus fulfilling the second requirement for device fabrication. Most importantly, the extreme potential control available with SECCM ensures that that oxidation of graphene, and the reduction process of diazonium compounds do not occur simultaneously at the graphene surface, allowing for either process to be selectively turned on or off through the potential applied to the SECCM probe. Such a unique approach could ultimately allow for pre-defined graphene circuits to be printed, a highly attractive prospect for the future of this material. This unique concept is illustrated in Figure 6.2.

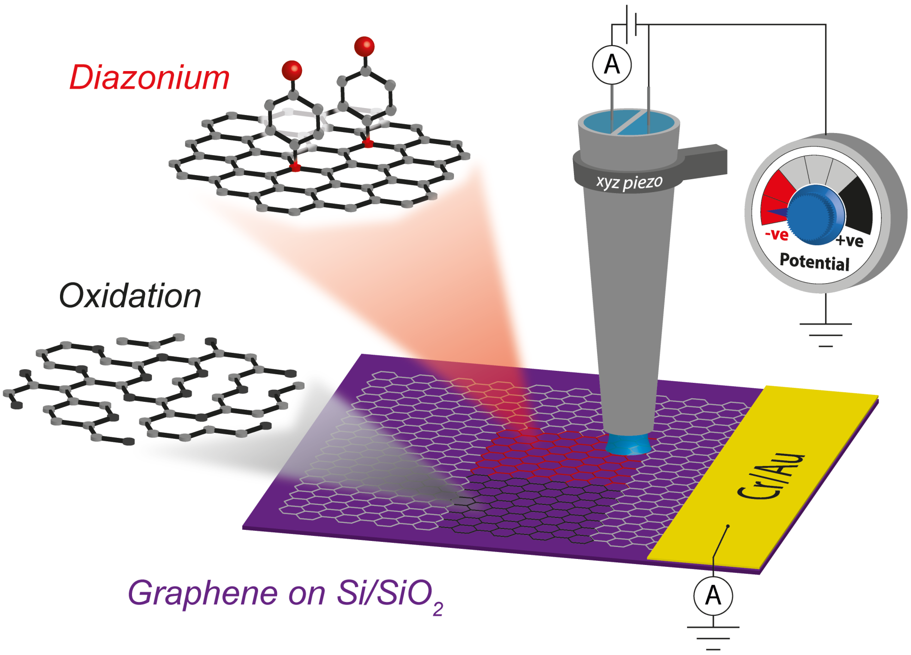

Figure 6.2 Schematic representation of the unique patterning concept introduced herein.

6.2 Results and Discussion

6.2.1 Graphene Characterization

Large-area graphene samples were synthesized on Cu foils using a CVD growth process, before being transferred to insulating Si/SiO_2 substrates using an established PMMA transfer method (experimental details in sections 2.2.3 and 2.2.4.).[45,46] Throughout the literature, it is generally accepted that samples transferred via this polymer-supported route are highly prone to contamination from PMMA residue, and, as such, additional cleaning steps are often employed. Annealing steps[47,48] have been reported as suitable for reducing PMMA contamination levels, however, it is worth noting that the likelihood of complete PMMA removal has been questioned.[49] Unfortunately, PMMA residue has been shown to affect the electronic properties of transferred graphene,[50,51] and furthermore, will likely hinder surface modification processes, such as those proposed herein, making its removal a necessity.

Figure 6.3(a) shows a typical 5 μm × 5 μm AFM image of an as-transferred graphene sample on Si/SiO_2, after PMMA dissolution in acetone. Somewhat striking is the extreme roughness of the surface, and seemingly large levels of PMMA particulate matter scattered throughout, to the extent that the underlying graphene structure is barely discernable. Similar images have been observed in other literature reports,[51] although discussion over the presence of such contamination is of course often avoided.

The effects of surface annealing were investigated by carefully dividing the same sample into quarters using a diamond pen, to produce 4 samples of identical quality. These were subsequently annealed under an Ar/H_2 atmosphere for 15 minutes (details in section 2.2.6), similar conditions to those reported as effective in the literature.[48] Figures 6.3(b), 6.3(c) and 6.3(d) show typical AFM images of the graphene samples post-annealing at 450 °C, 350 °C and 300 °C, respectively.

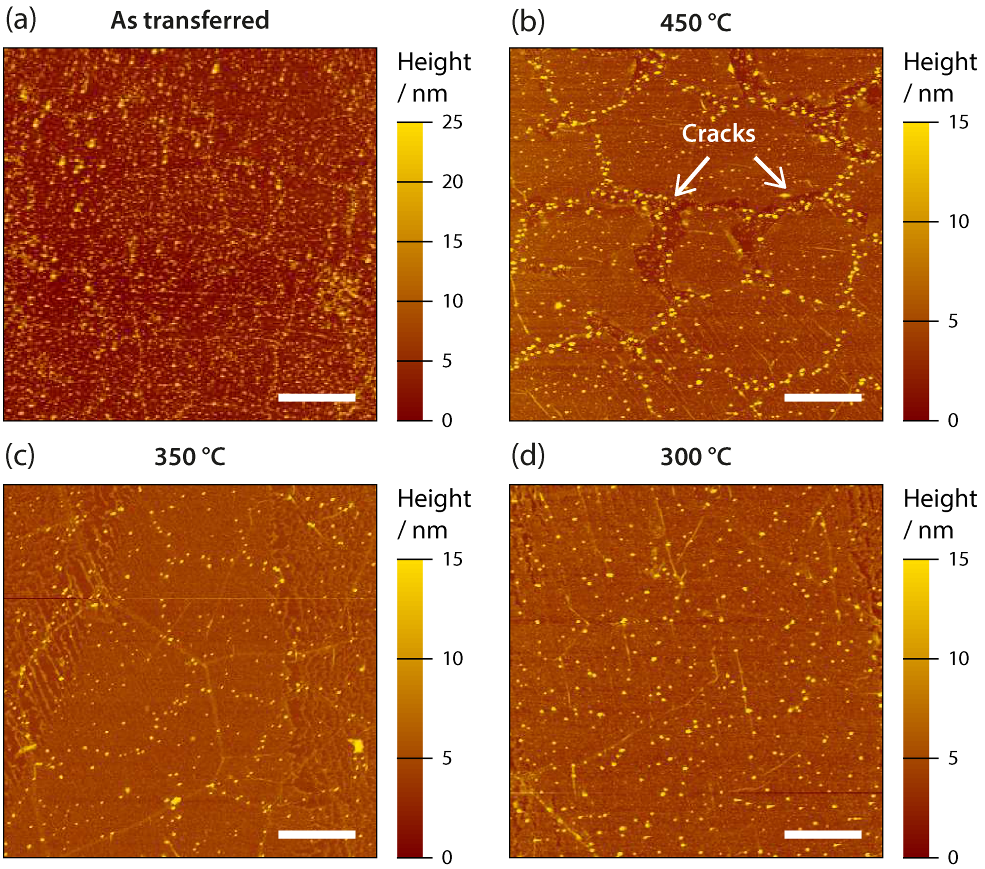

Figure 6.3 AFM images of (a) graphene on Si/SiO$_2$ post PMMA transfer with no additional treatment, and post annealing at (b) 450 °C (c) 350 °C and (d) 300 °C for 15 minutes in an Ar/H$_2$ atmosphere. Scale bars represent 1 μm.

Immediately apparent is the significant reduction in surface roughness and reduced levels of particulate matter yielded at all annealing temperatures (also note the reduced scale bars). Unfortunately, annealing at 450 °C also appears to introduce large cracks into the graphene sheet, with the underlying Si/SiO$_2$ substrate now visible. Indeed, the presence of individual graphene crystallites is likely to have a negative impact on the conducting properties of the graphene sheet, and, whilst such cracks may have always been present but masked by residue, there is no evidence of these features in samples annealed at 350 °C and 300 °C. Annealing at these lower temperatures does however reveal the underlying structure of the graphene, which displays the commonly observed graphene wrinkles associated with CVD growth.[52] In terms of PMMA contamination, the graphene surface annealed at 350 °C appears to show lower levels than at 300 °C, and this was thus selected as the most suitable annealing temperature.

Raman spectroscopy provides a more quantitative insight into the structural characteristics of graphene samples,[53] yielding information on the number of layers present, as well as their structural integrity (see section 1.1.1.3).[54-56] Figure 6.4 shows complementary Raman spectra for those samples investigated in Figure 6.3. Focusing on the as-transferred sample (Figure 6.4(a)), the measured 2D and G peak intensity ratio of 2.44 is in good agreement with that reported for SLG,[10] as is typical for graphene grown via CVD methods.[10,45] The presence of SLG is further supported by the 2D peak being positioned at 2680 cm^{-1}, and having an associated FWHM of 41 cm^{-1}.[55,56] Indeed, the presence of SLG is highly desirable for electronic devices (and hence this work), thus, grown samples were screened post-transfer/anneal and discarded if deemed to not be SLG.

The relative level of defectiveness within each sample was estimated through the ratio of the intensities of the D and G peaks, I_D and I_G, as is common practice in the literature.[57] Indeed, defect free graphene should display no D-peak at all, however the presence of a small contribution in CVD graphene is not unusual.[57,58] The typically low ratio of 0.12 exhibited here for the as-transferred sample suggests it to be of relatively high quality. Annealing at 450 °C (Figure 6.4(b)) resulted in an I_D/I_G increase to 0.30, suggesting a significantly higher level of defects within the sample, in agreement with the large cracks observed during AFM imaging, and suggestive of an overly harsh annealing process. The spot size of the Raman laser was ~ 2 μm in diameter, similar to the area interrogated by AFM, thus providing representative and comparable spectra.

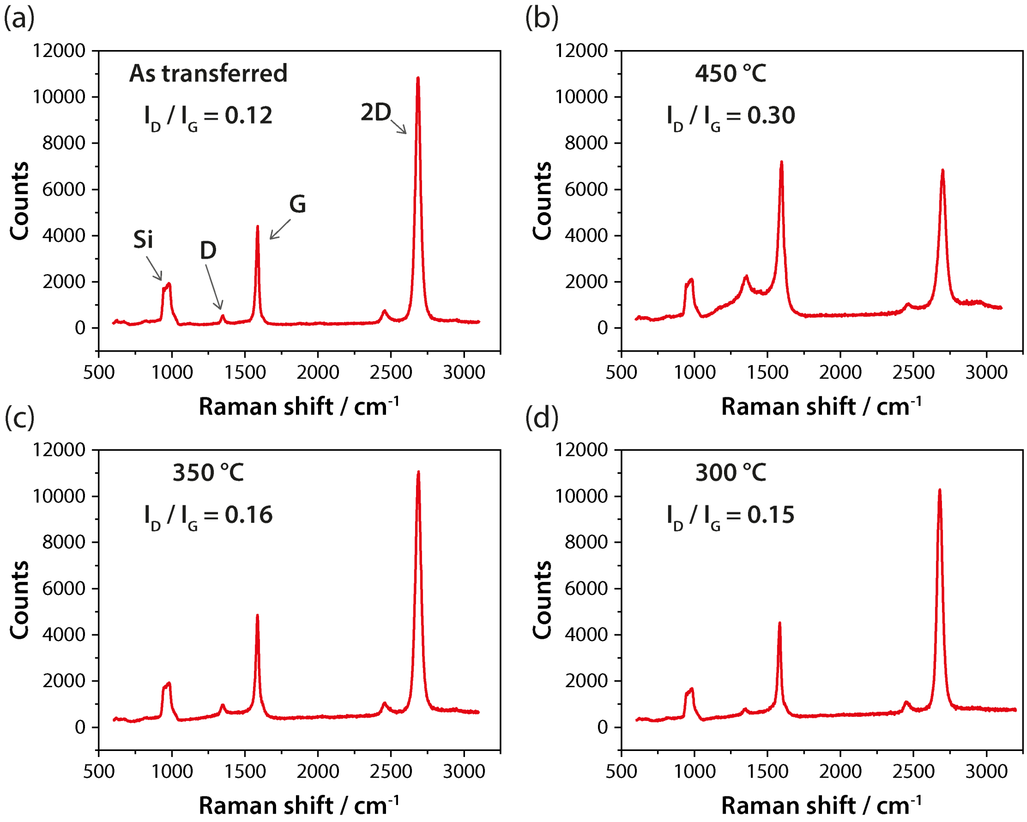

Figure 6.4 Representative Raman spectra of (a) graphene on Si/SiO_2 post PMMA transfer, and post-annealing at (b) 450 °C (c) 350 °C and (d) 300 °C for 15 minutes in an Ar/H_2 atmosphere. Shown on all spectra are the corresponding I_D/I_G values. Spectra were acquired using a 514 nm Ar^+ laser (20 s laser exposure time), with a spot diameter of ~ 2 μm.

Annealing at 350 °C (Figure 6.4(c)) and 300 °C (Figure 6.4(d)) yielded I_D/I_G ratios of 0.15 and 0.16 respectively, indicating little sample degradation with respect to that measured before annealing (Figure 6.4(a)).

Interestingly, the annealing process also introduced a small change in the position of the G peak, which shifted from 1587 cm^{-1} (as-transferred) to 1584 cm^{-1} post anneal. A similar small, yet significant shift has been previously reported in the literature, being ascribed to PMMA removal. PMMA contamination is known to p-dope graphene samples, causing a blue shift of the

G peak when present on the surface.[50] This finding corroborates with the AFM data (Figure 6.3), confirming reduced PMMA levels upon annealing.

Based on the above findings, subsequently transferred graphene samples determined to be single layer were annealed at 350 °C before further use. However, this demonstrates the lengths that must be taken during graphene preparation to ensure samples of adequate quality are obtained, at least when employing the PMMA transfer method.

6.2.2 Graphene Device Fabrication and Characterization

To effectively investigate the effects of SECCM patterning on graphene, a device platform was developed that contained numerous individually accessible graphene microstrips. Briefly, post-transfer and anneal, photolithography methods were employed to produce 24 graphene microstrips from a single graphene sample, with each microstrip measuring 20 μm × 100 μm in size, and still supported on Si/SiO_2. Au electrical contacts were established to each of the microstrips through a masked resistive evaporation method, before the substrate was mounted on, and connected to, a specially designed PCB that allowed for ease of handling/connection (full experimental procedure in section 2.2.6). Figure 6.5(a) is a schematic representation of an entire fabricated device, with a zoom of a single graphene strip. A photograph, photomicrograph, and SEM images (Figure 6.5(b)) show the fully fabricated device, including a contacted SLG strip and the wire bonding connections used between contacted strips and the PCB base.

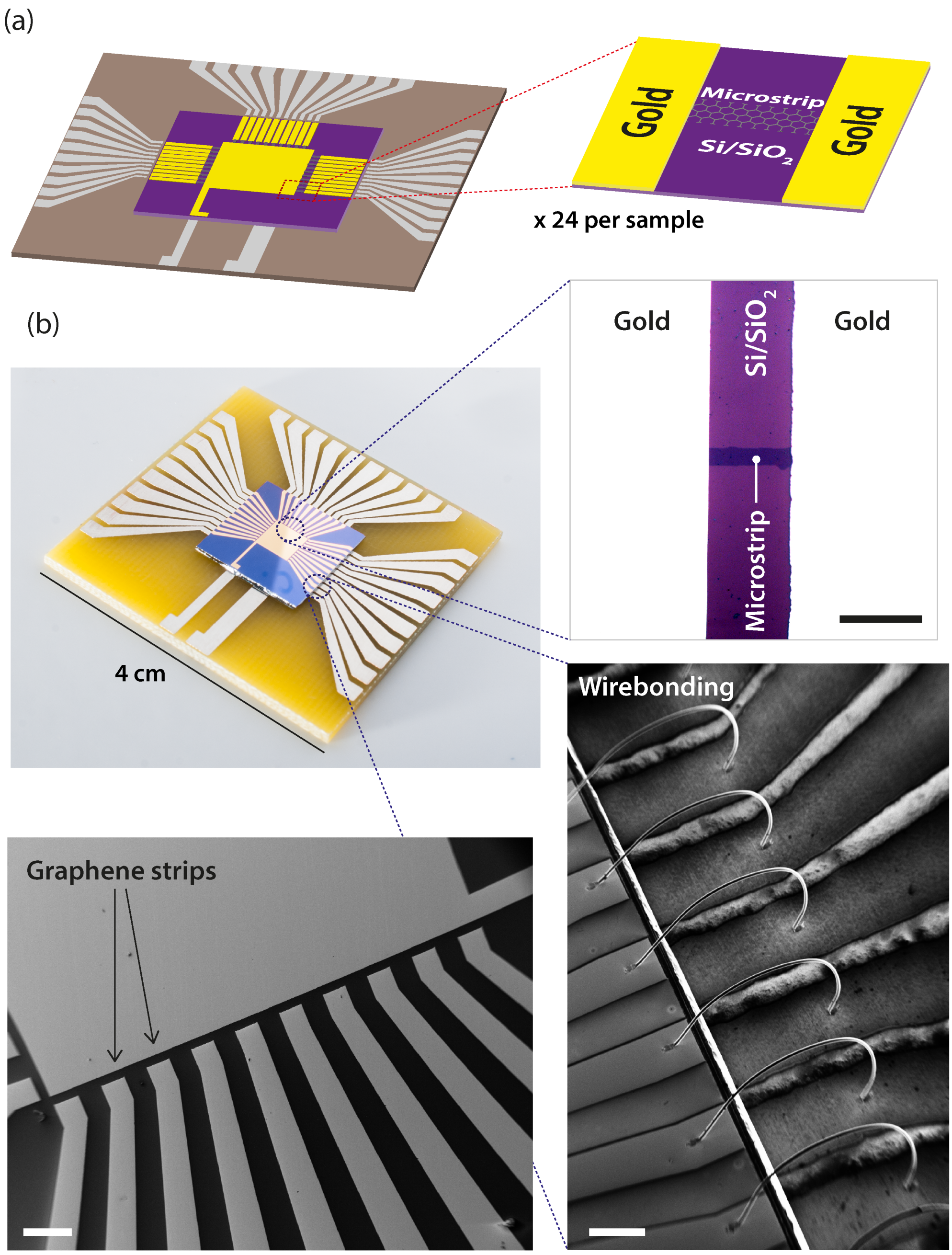
(a)
Gold
Microstrip
Si/SiO2
Gold
x 24 per sample
(b)
4 cm
Gold
Si/SiO2
Gold
Microstrip
Wirebonding
Graphene strips

Figure 6.5 (a) Schematic representation of a fully fabricated device. (b) Photograph, photomicrograph and SEM micrograph of various sections of a fabricated device. Scale bar represents 100 µm in photomicrograph, and 500 µm in SEM images.

Conductance current-voltage (*i*-*V*) curves were measured across each of the individual graphene microstrips for a typical fabricated device by contacting sharp metal pins to the PCB contact pads (in a 2-point measurement fashion), results shown in Figure 6.6(a) For comparison, identical measurements were also made on a device fabricated from graphene that did not undergo an annealing step (*vide supra*), Figure 6.6(b). The conductance curves appear linear, as would be expected, owing to graphene's semi-metal nature.

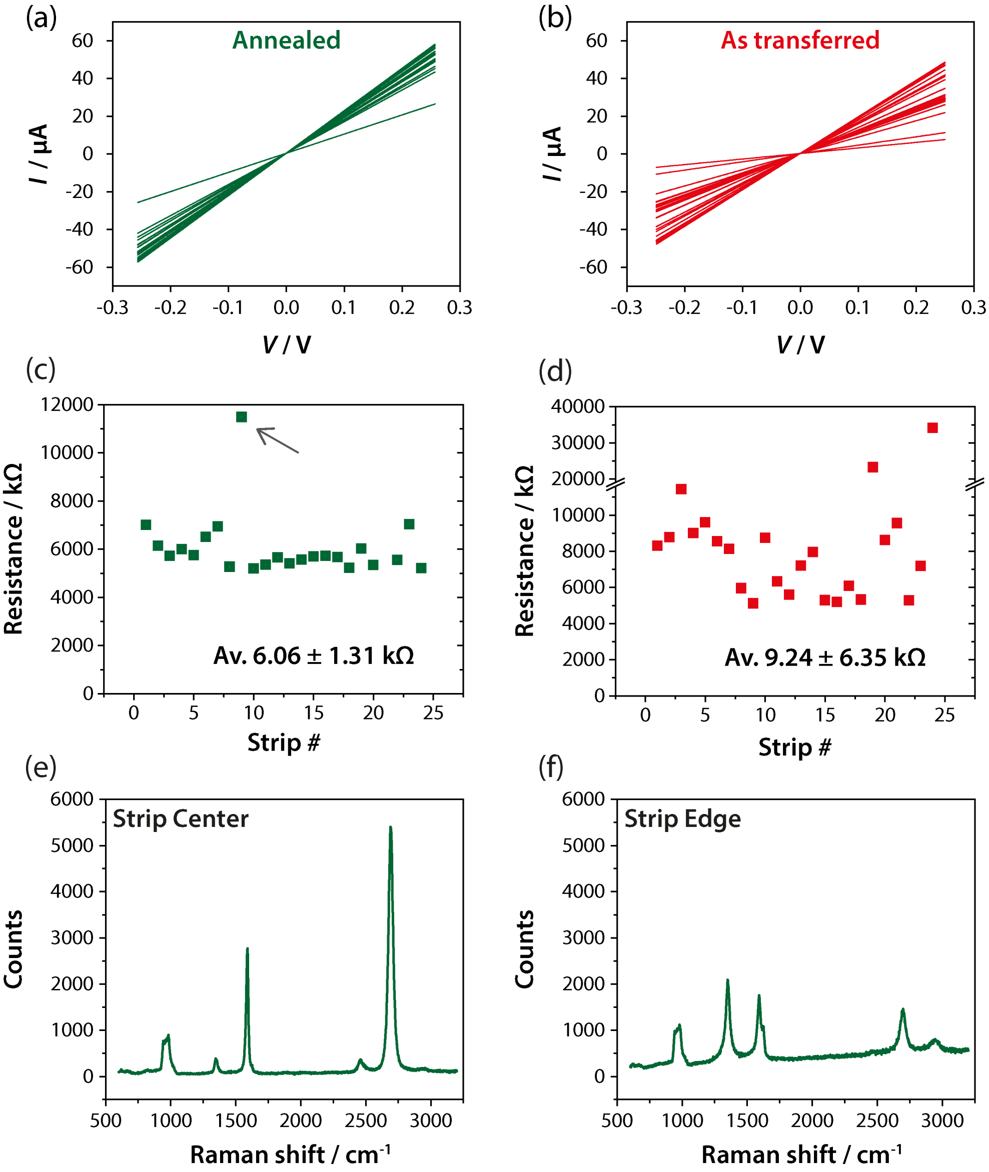

Figure 6.6 *i*-*V* curves for the 24 microstrips on a fabricated device formed from (a) annealed and (b) as-transferred graphene samples. Measured resistance values (determined from *i*-*V* curves) of individual graphene strips on a fabricated device, for (c) a sample that underwent 350 °C annealing, and (d) a device fabricated from as-transferred graphene. The arrow in (c) shows a strip having anomalously high resistivity, due to a tear in the strip, significantly reducing its width. Raman spectra acquired on (e) the center, and (f) the edge of a graphene fabricated microstrip, using identical conditions to those in Figure 6.4.

With respect to the annealed sample, determined resistance values appear very similar between strips, as shown in Figure 6.6(c), with the exception of a single outlier, marked by a black arrow. Optical inspection of this anomalous strip revealed a significant tear across it, reducing its width and hence increasing resistance. Analysis yielded an average strip resistance of 6.06 kΩ ± 1.31 kΩ (± 1 S.D.). For reference, resistance measurements from *i-V* curves in Figure 6.6(b) displayed > 50 % higher average resistance values (Figure 6.6(d)), with significantly more variation between strips also observed (9.24 kΩ ± 6.35 kΩ) (± 1 S.D.). With both samples prepared from graphene of matching quality, it is likely such differences arise from increased contact resistance in the un-annealed sample and decreased carrier mobility within the graphene strip, both resulting from surface PMMA residue,[50] again highlighting the need for such cleaning procedures.

Raman spectroscopy on the patterned strips confirmed no substantial damage was introduced during the photolithographic procedures employed. Figure 6.6(e) shows the Raman spectrum acquired on a fabricated microstrip, collected using the same acquisition parameters as those used in Figure 6.4. Figure 6.6(f) shows a spectrum collected at the very edge of the same fabricated strip, displaying a substantially higher D peak, as would be expected along the graphene edge, where the presence of sp^3 carbon is inevitable.

6.2.3 Graphene Oxidative Patterning

The effect of anodic oxidative treatment on graphene was next investigated using the SECCM setup, which in turn further served as means to visualize the strip post-treatment, through the inclusion of the electrochemical redox mediator ruthenium (III) hexamine, $Ru(NH_3)_6^{3+}$ in the tip solution. Figure 6.7(a) shows a summary schematic of the setup used for microstrip imaging and modification (complete experimental details in section 2.6), including an SEM image of a typical probe used throughout, measuring ~ 450 nm in diameter. It should be highlighted that SECCM probe dimensions can be easily adjusted during the pulling procedure, with probes between 300 nm and 1.5 μm demonstrated,[59,60] thus allowing the level of spatial resolution to be adjusted easily. This is a further advantage of the SECCM patterning approach.

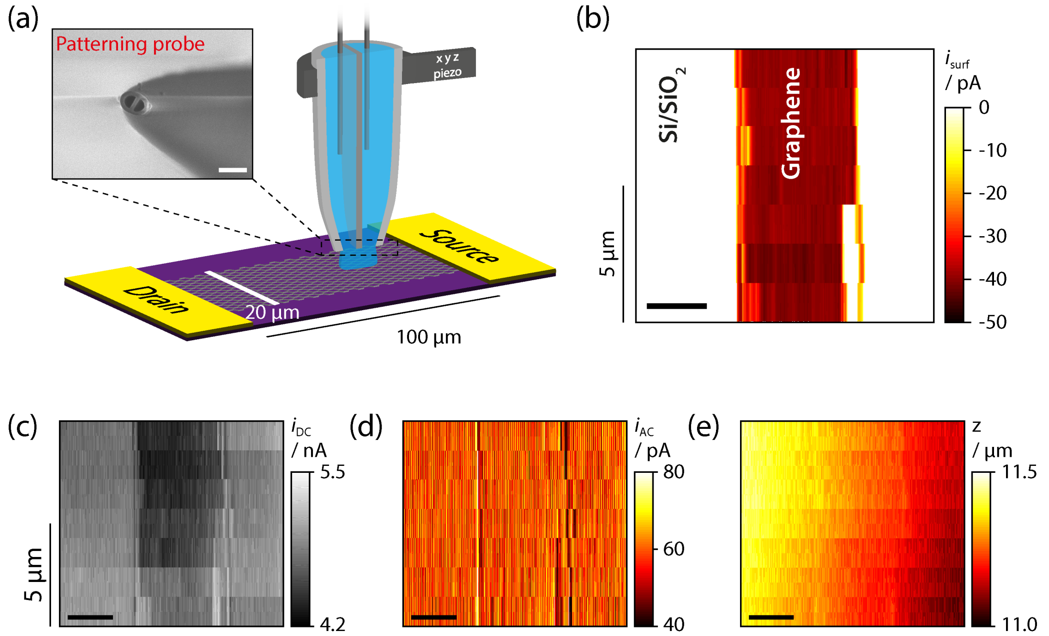

Figure 6.7 (a) Schematic representation of how the SECCM probe was employed in microstrip modification/mapping, with an SEM micrograph of a typical probe. Scale bar denotes 500 nm. (b) The electrochemical activity map of a pristine graphene microstrip towards 1 mM $[Ru(NH_3)_6]^{3+}$ reduction in 50 mM KCl at E_{surf} = -0.3 V vs. Ag/AgCl, acquired using the SECCM setup. Corresponding SECCM i_{DC} (c), i_{AC} (d) and topography (e), maps to (b). Horizontal scale bars denote 10 μm.

Figure 6.7(b) shows the electrochemical activity map of a pristine graphene microstrip towards the one-electron reduction process of $Ru(NH_3)_6^{3+}$, performed at E_{surf} = 0.3 V vs. Ag/AgCl, determined to be close to the value of $E_{1/2}$ for the system (*vide infra*). The pristine graphene strip, measuring ~ 20 μm in width, shows consistent electrochemical behavior along the entire imaged length, as would be expected for a conducting strip prior to any modification, and as previously reported in the literature for this redox mediator at graphene electrodes.[58] It should be noted that the reduction process was simply used to provide a means of visualizing the strip, rather than probing its intrinsic electrochemical properties. The strip position is also clearly visible in the corresponding map of i_{DC} barrel current, Figure 6.7(c), as a result of the graphene strip being significantly more hydrophobic than the surrounding Si/SiO_2,[61] leading to a reduction in size of the probe meniscus (increasing its resistance and lowering i_{DC}) when the meniscus is in contact with the graphene. Corresponding maps of i_{AC} (Figure 6.7(d)) and topography (Figure 6.7(e)) show the stability of the scanning droplet across both the graphene strip and surrounding Si/SiO_2 substrate, adding confidence that the glass probe never contacts the surface during scanning. Furthermore, this demonstrates the versatility of the system to scan areas of both conducting and non-conducting nature, as a consequence of the unique ion conductivity feedback mechanism employed.

The effect of applying oxidative potentials to graphene was next investigated using the same setup. A pristine strip was first visualized using the $Ru(NH_3)_6^{3+}$ reduction process (Figure 6.8(a)). The SECCM probe was subsequently used to apply a high anodic potential (E_{surf} = 3.3 V vs. Ag/AgCl) to the graphene strip, in an attempt to produce areas of oxidized material, potentially of an insulating nature. Once again, it should be noted that the unique nature of SECCM ensures no physical contact between the tapered glass pipet and the sample; ensuring measured effects are a result of an electrochemical reaction. The SECCM tip was approached to the Si/SiO_2 substrate with an i_{AC} set-point of 80 pA, before oxidative line scans were performed across the strip (marked by a grey box in Figure 6.8(a)), with 8 ‘cuts’ performed in total (4 x forward, 4 x reverse scans, with a displacement of 250 nm along the strip between each full line). A relatively slow scan speed of 0.25 μm s^{-1} provided a tip residence time of ~ 8 seconds to any point on the graphene strip, for the given tip size (~ 450 nm). Post oxidation, the strip was re-visualized using the $Ru(NH_3)_6^{3+}$ reduction process, using the same conditions to those employed initially, with the result shown in Figure 6.8(b). Strikingly, only half the strip now appears active towards the reduction process, suggesting the introduction of a highly-oxidized region through the strip center, effectively isolating the bottom-half of the strip (illustrated in Figure 6.8(c)) from the metal contact at which i_{surf} is measured. Crucially, in this bottom half, graphene still remains present and intact, after all, any probe contact with this half has only involved the reduction process of $Ru(NH_3)_6^{3+}$, a process also performed on the top half, where no deterioration in activity was observed whatsoever. The minute currents measured with SECCM[62] (on the order of pA for the above redox process) render it essentially immune to ohmic drop effects, further highlighting how very insulating the oxidized region must be.

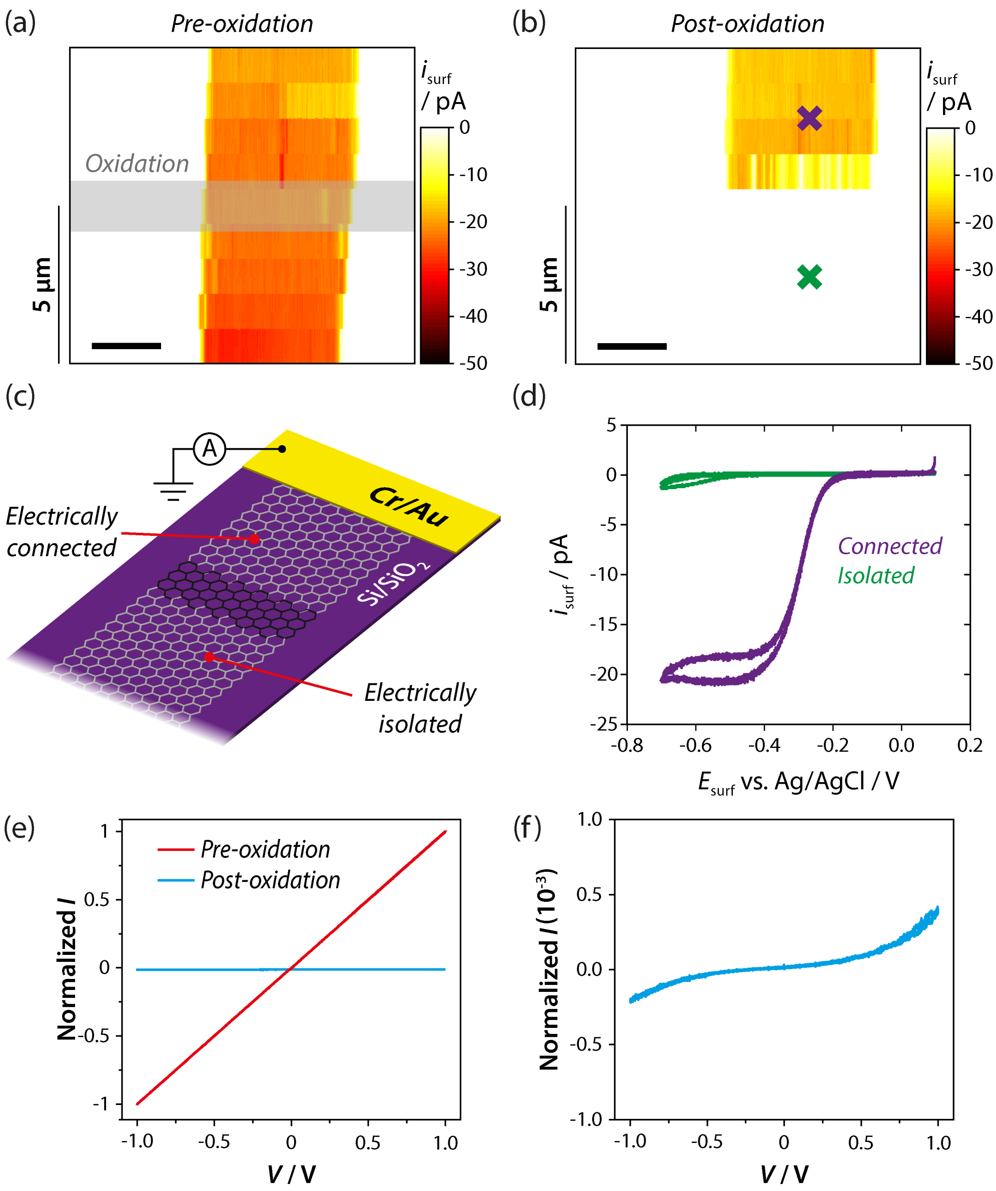

Figure 6.8 Electrochemical activity (i_{surf}) map of a graphene microstrip towards 1 mM $[Ru(NH_3)_6]^{3+}$ in 50 mM KCl at E_{surf} = -0.3 V vs. Ag/AgCl, before (a), and after (b), oxidative cutting along the region marked in grey on (a). Oxidative cutting was performed at E_{surf} = 3.3 V vs. Ag/AgCl and at a scan speed of 0.25 µm s^{-1}. (c) An illustration of the graphene microstrip post-oxidative cutting, resulting in part of the microstrip being electrically isolated from the rest. (d) CVs for the $[Ru(NH_3)_6]^{3+}$ reduction process acquired at the crosses marked in (b). Horizontal scale bars denote 10 µm. (e) Normalized (with respect to measured maximum) *i*-*V* curves of the graphene microstrip, prior to, and post, the oxidative cutting procedure. (f) A zoom of the post-oxidation *i*-*V* curve.

Figure 6.8(d) shows CVs for the $Ru(NH_3)_6^{3+}$ redox process using the SECCM tip at the corresponding colored crosses in Figure 6.8(b), which further show the lack of an electrical connection at the isolated portion of the strip.

Normalized strip *i-V* curves before and after oxidative cutting (Figure 6.8(e)) highlight the significant change in strip resistance resulting from the introduction of a highly oxidized region across the strip. Such a significant change in the strip conductance properties highlights the ability of SECCM to not only introduce areas of electrochemically oxidized graphene, but to introduce areas so heavily oxidized that parts of the initial graphene sample can be completely isolated, highly applicable for the production of graphene circuits, whereby the circuit outline could effectively be drawn using oxidized material. A zoom of the *i-V* curve post-oxidation (Figure 6.8(f)) reveals some asymmetrical behavior. Near identical *i-V* curves were obtained by Wu *et al.*[63] when investigating the properties of graphene-GO-graphene junctions, with the response ascribed to the formation of back-to-back Schottky diodes.

The ability of SECCM to introduce larger insulating patterns was next investigated by creating an oxidized ‘hole’ in the center of a graphene microstrip, through continuous line patterning. Figure 6.9(a) and 6.9(b) show the electrochemical activity of a graphene microstrip towards $Ru(NH_3)_6^{3+}$ reduction, before and after (respectively) patterning an oxidized region into the center of the strip. Oxidative conditions of E_{surf} = 3.3 V vs. Ag/AgCl and a scan rate of 0.25 $\mu m\ s^{-1}$ (determined above to be sufficient to oxidize graphene) were employed, and consecutive line scans (as used above) were performed in the center of the strip, rather than cutting entirely across it.

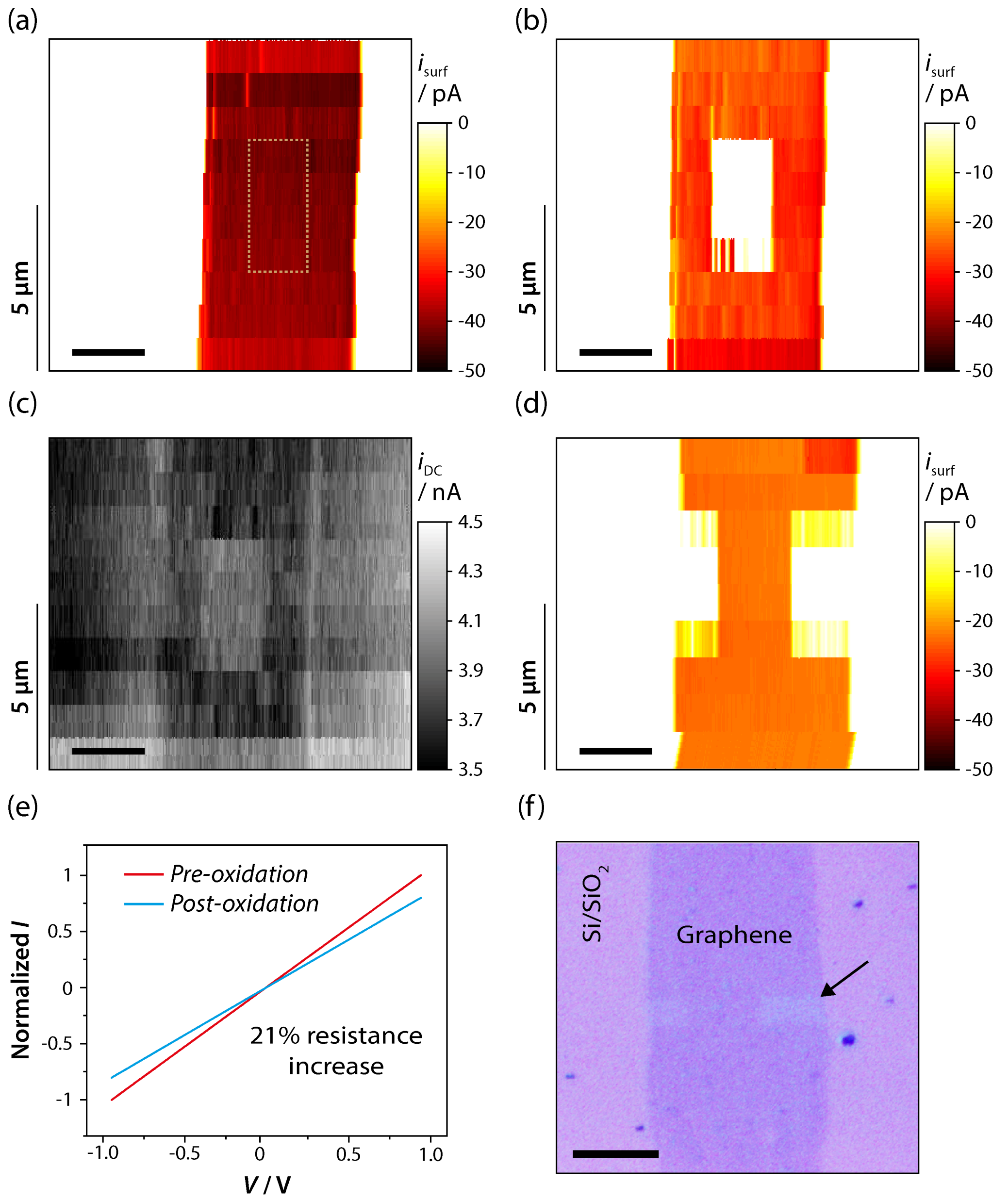

Figure 6.9 Electrochemical activity map of a graphene microstrip towards the reduction of 1 mM $Ru(NH_3)_6^{3+}$ in 50 mM KCl at E_{surf} = -0.3 V vs. Ag/AgCl, before (a), and after (b), oxidative patterning in the region marked on (a). (c) Corresponding i_{DC} map to (b), showing a more wetting region at the oxidized area, manifested as higher i_{DC} values in SECCM. (d) Electrochemical activity map of a graphene microstrip towards the reduction of 1 mM $Ru(NH_3)_6^{3+}$ in 50 mM KCl at E_{surf} = -0.3 V vs. Ag/AgCl after oxidative patterning to narrow the strip. Horizontal scale bars represent 10 µm. (e) *i*-*V* curves of the graphene microstrip, prior to, and post, the oxidative narrowing procedure. (f) High contrast optical micrograph of the narrowed microstrip, with an oxidized region marked with an arrow. Scale bar represents 10 µm.

The insulating nature of the patterned rectangular region is reflected by a complete lack of any detectable electrochemical current. Interestingly, the corresponding i_{DC} map (Figure 6.9(c)) provides additional information on the nature of the oxidized region, which highlights itself as being more hydrophilic (i.e. larger i_{DC} values) than its pristine graphene surroundings, in agreement with the introduction of oxygen containing functional groups.[64] This complementary data, unique to SECCM, provides a secondary route to visualizing the strip after oxidation, negating the need for the inclusion of a redox mediator (i.e. $Ru(NH_3)_6^{3+}$) in the probe solution, and instead allowing for other interesting electrochemically active compounds to be incorporated (*vide infra*). Figure 6.9(d) shows a microstrip that underwent an identical oxidation procedure, but with two individual scans focused on the graphene edges, effectively resulting in a portion of the strip being narrowed. *i-V* curves before and after narrowing (Figure 6.9 (e)) show an increase in measured resistance, in agreement with a narrowed region. Ultimately, this highlights the ability to produce areas of accurate width/size, with sharp, defined edges. Graphene regions that appear to display reduced electrochemical activity (with respect to the main strip) are likely an artifact of the imaging procedure, with the meniscus covering only some of the strip (and some SiO_2), effectively reducing the active electrode area. Figure 6.9(f) shows a high-contrast optical micrograph of the same narrowed strip, in which the patterned areas can be faintly seen (marked by an arrow). Their difference in appearance to the surrounding SiO_2 substrate also suggests the introduction of oxidized material during patterning, rather than the physical removal of graphene; after all, the glass probe never contacts the surface.

6.2.4 Diazonium Modification of Graphene using SECCM

The reaction of diazonium compounds at graphene surfaces has already been demonstrated as a route to band-gap generation,[26,43] and with SECCM already proven to be able to tune the degree of the reaction (Chapter 5), this process was next investigated at graphene surfaces. The solution contained within the SECCM probe was replaced with 0.1 mM 4-NBD in 25 mM H_2SO_4, conditions analogous to those previously used for diazonium grafting at sp^2 carbon surfaces.[30] Figure 6.10(a) shows 4 consecutive CVs recorded at the graphene surface using this SECCM setup.

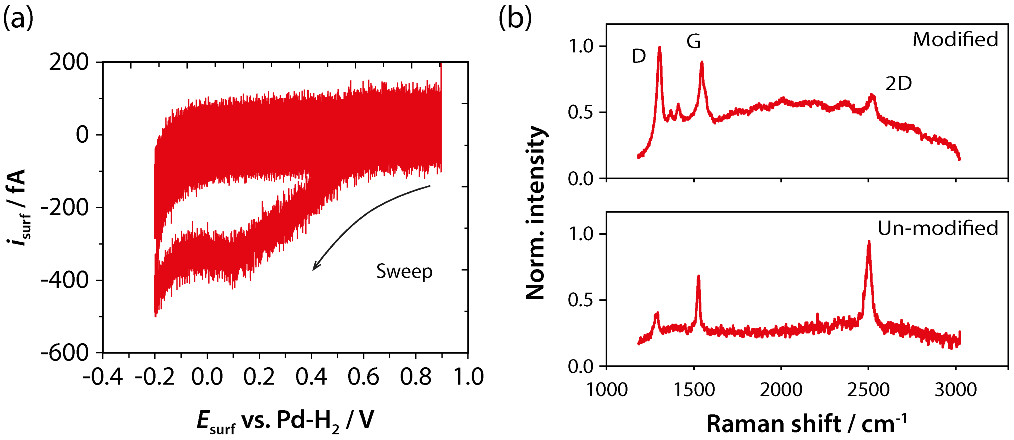

Figure 6.10 (a) CVs showing the reduction of 0.1 mM 4-NBD in 25 mM H_2SO_4 at a graphene surface using the SECCM setup, recorded at 100 mV s^{-1} with a tip 450 nm in diameter. (b) Raman spectra of a large graphene patch after CV modification using the parameters described in (a), and of the same area before modification. Spectra were acquired using a 633 nm laser, with ~ 1 µm laser spot size.

The resulting CV shows a broad, irreversible reduction wave (E_p = 0.10 V vs. Pd-H_2) on the initial sweep, assigned to the diazonium reduction process, with consecutive waves showing essentially zero current as a result of aryl moieties introduced at the surface blocking further ET. The apparently high noise levels are a result of minute currents now being measured (fA). Figure 6.10(b) shows Raman spectra recorded at a pristine, un-modified graphene surface, and at the same surface after diazonium modification using a large SECCM tip (~ 10 µm diameter to aid spectra recording), using the conditions described in 6.10(a). A significant increase in the size of the D-band at the modified surface corroborates the CV data, suggesting an increase in the number of sp^3 centers present, as a result of grafted aryl groups. Furthermore, a significant decrease in the size of the 2D is also apparent, along with increased background levels and the introduction of new peaks between the D and G-bands. Similar effects were also observed by Strano *et al.* when grafting 4-NBD at graphene surfaces.[57]

When this data is combined with that obtained for oxidative patterning measurements, the potential of SECCM as a tool for producing graphene circuitry becomes fully apparent. The application of harsh oxidative potentials (> 3.3 V vs. Ag/AgCl) results in the destruction of any graphene in contact with the meniscus, whilst potentials < 0.50 V vs. Pd-H_2 can introduce grafted aryl moieties, when diazonium compounds are present in solution. Crucially, at potentials between these reactions, no additional reactions occur, allowing for the meniscus to be in contact, but to leave pristine graphene completely intact. Thus, a single SECCM probe could act as a tool to define an entire graphene circuit, containing conductive pathways (defined by insulating regions) and areas with SC character, all in a single approach-scan-withdraw cycle.

6.3 Conclusions

In conclusion, the ability of SECCM to act as a lithographic writing tool for localized covalent surface modification with high spatial control has been demonstrated for the first time at well-characterized graphene surfaces. Through the application of harsh oxidizing potentials confined to the very tip of the probe, it was shown that areas of highly conductive pristine graphene can be converted to highly insulating material, allowing for the production of conducting graphene pathways of defined size in a single graphene sheet. This was demonstrated through a range of complementary techniques, including localized electrochemical mapping and resistance measurements. Furthermore, the ability of SECCM to introduce aryl diazonium functionality at graphene surfaces was demonstrated, a reaction that has been previously shown to generate an electronic band-gap within the intrinsic semi-metal.

Crucially, it was highlighted that either, or neither, reaction route could be selectively started whilst the probe is in contact with the surface, allowing for pristine graphene regions to be left completely intact. Overall, SECCM has been proven as a viable route for the production of integrated graphene circuitry, advancing not only versatility of SECCM, but also carrying enormous prospects for the future of digital electronics.

6.4 References

(1) Novoselov, K. S.; Geim, A. K.; Morozov, S. V.; Jiang, D.; Zhang, Y.; Dubonos, S. V.; Grigorieva, I. V.; Firsov, A. A. *Science* **2004**, *306*, 666.

(2) Bolotin, K. I.; Sikes, K. J.; Jiang, Z.; Klima, M.; Fudenberg, G.; Hone, J.; Kim, P.; Stormer, H. L. *Solid State Commun.* **2008**, *146*, 351.

(3) Chen, J.-H.; Jang, C.; Xiao, S.; Ishigami, M.; Fuhrer, M. S. *Nat. Nanotechnol.* **2008**, *3*, 206.

(4) Meyer, J. C.; Geim, A. K.; Katsnelson, M. I.; Novoselov, K. S.; Obergfell, D.; Roth, S.; Girit, C.; Zettl, A. *Solid State Commun.* **2007**, *143*, 101.

(5) Lee, C.; Wei, X.; Kysar, J. W.; Hone, J. *Science* **2008**, *321*, 385.

(6) Savage, N. *Nature* **2012**, *483*, S30.

(7) Reina, A.; Jia, X.; Ho, J.; Nezich, D.; Son, H.; Bulovic, V.; Dresselhaus, M. S.; Kong, J. *Nano Lett.* **2009**, *9*, 30.

(8) Kwon, S.-Y.; Ciobanu, C. V.; Petrova, V.; Shenoy, V. B.; Bareno, J.; Gambin, V.; Petrov, I.; Kodambaka, S. *Nano Lett.* **2009**, *9*, 3985.

(9) Sutter, P. W.; Flege, J.-I.; Sutter, E. A. *Nat. Mater.* **2008**, *7*, 406.

(10) Li, X.; Cai, W.; An, J.; Kim, S.; Nah, J.; Yang, D.; Piner, R.; Velamakanni, A.; Jung, I.; Tutuc, E.; Banerjee, S. K.; Colombo, L.; Ruoff, R. S. *Science* **2009**, *324*, 1312.

(11) Bae, S.; Kim, H.; Lee, Y.; Xu, X.; Park, J.-S.; Zheng, Y.; Balakrishnan, J.; Lei, T.; Kim, H. R.; Song, Y. I.; Kim, Y.-J.; Kim, K. S.; Ozyilmaz, B.; Ahn, J.-H.; Hong, B. H.; Iijima, S. *Nat. Nanotechnol.* **2010**, *5*, 574.

(12) Dimiev, A.; Kosynkin, D. V.; Sinitskii, A.; Slesarev, A.; Sun, Z.; Tour, J. M. *Science* **2011**, *331*, 1168.

(13) Kim, T.; Kirn, H.; Kwon, S. W.; Kim, Y.; Park, W. K.; Yoon, D. H.; Jang, A. R.; Shin, H. S.; Suh, K. S.; Yang, W. S. *Nano Lett.* **2012**, *12*, 743.

(14) Bai, J.; Duan, X.; Huang, Y. *Nano Letters* **2009**, *9*, 2083.

(15) Sinitskii, A.; Tour, J. M. *J. Am. Chem. Soc.* **2010**, *132*, 14730.

(16) George, A.; Mathew, S.; van Gastel, R.; Nijland, M.; Gopinadhan, K.; Brinks, P.; Venkatesan, T.; ten Elshof, J. E. *Small* **2013**, *9*, 711.

(17) Wang, W. M.; Stander, N.; Stoltenberg, R. M.; Goldhaber-Gordon, D.; Bao, Z. *ACS Nano* **2010**, *4*, 6409.

(18) Kim, K. S.; Zhao, Y.; Jang, H.; Lee, S. Y.; Kim, J. M.; Kim, K. S.; Ahn, J.-H.; Kim, P.; Choi, J.-Y.; Hong, B. H. *Nature* **2009**, *457*, 706.

(19) Tour, J. M. *Chem. Mater.* **2014**, *26*, 163.

(20) Lin, Y. M.; Jenkins, K. A.; Valdes-Garcia, A.; Small, J. P.; Farmer, D. B.; Avouris, P. *Nano Lett.* **2009**, *9*, 422.

(21) Avouris, P. *Nano Lett.* **2010**, *10*, 4285.

(22) Elias, D. C.; Nair, R. R.; Mohiuddin, T. M. G.; Morozov, S. V.; Blake, P.; Halsall, M. P.; Ferrari, A. C.; Boukhvalov, D. W.; Katsnelson, M. I.; Geim, A. K.; Novoselov, K. S. *Science* **2009**, *323*, 610.

(23) Gao, H.; Wang, L.; Zhao, J.; Ding, F.; Lu, J. *J. Phys. Chem. C* **2011**, *115*, 3236.

(24) Nourbakhsh, A.; Cantoro, M.; Klekachev, A. V.; Pourtois, G.; Vosch, T.; Hofkens, J.; van der Veen, M. H.; Heyns, M. M.; De Gendt, S.; Sels, B. F. *J. Phys. Chem. C* **2011**, *115*, 16619.

(25) Cheng, S. H.; Zou, K.; Okino, F.; Gutierrez, H. R.; Gupta, A.; Shen, N.; Eklund, P. C.; Sofo, J. O.; Zhu, J. *Phys. Rev. B* **2010**, *81*, 205435.

(26) Niyogi, S.; Bekyarova, E.; Itkis, M. E.; Zhang, H.; Shepperd, K.; Hicks, J.; Sprinkle, M.; Berger, C.; Lau, C. N.; deHeer, W. A.; Conrad, E. H.; Haddon, R. C. *Nano Lett.* **2010**, *10*, 4061.

(27) Bekyarova, E.; Sarkar, S.; Wang, F.; Itkis, M. E.; Kalinina, I.; Tian, X.; Haddon, R. C. *Acc. Chem. Res.* **2013**, *46*, 65.

(28) Johns, J. E.; Hersam, M. C. *Acc. Chem. Res.* **2013**, *46*, 77.

(29) Park, J.; Yan, M. *Acc. Chem. Res.* **2013**, *46*, 181.

(30) Kirkman, P. M.; Güell, A. G.; Cuharuc, A. S.; Unwin, P. R. *J. Am. Chem. Soc.* **2014**, *136*, 36.

(31) Eda, G.; Mattevi, C.; Yamaguchi, H.; Kim, H.; Chhowalla, M. *J. Phys. Chem. C* **2009**, *113*, 15768.

(32) Jung, I.; Dikin, D. A.; Piner, R. D.; Ruoff, R. S. *Nano Lett.* **2008**, *8*, 4283.

(33) Masubuchi, S.; Ono, M.; Yoshida, K.; Hirakawa, K.; Machida, T. *Appl. Phys. Lett.* **2009**, *94*, 082107.

(34) Masubuchi, S.; Arai, M.; Machida, T. *Nano Lett.* **2011**, *11*, 4542.

(35) Giesbers, A. J. M.; Zeitler, U.; Neubeck, S.; Freitag, F.; Novoselov, K. S.; Maan, J. C. *Solid State Commun.* **2008**, *147*, 366.

(36) Withers, F.; Bointon, T. H.; Dubois, M.; Russo, S.; Craciun, M. F. *Nano Lett.* **2011**, *11*, 3912.

(37) Wei, Z.; Wang, D.; Kim, S.; Kim, S.-Y.; Hu, Y.; Yakes, M. K.; Laracuente, A. R.; Dai, Z.; Marder, S. R.; Berger, C.; King, W. P.; de Heer, W. A.; Sheehan, P. E.; Riedo, E. *Science* **2010**, *328*, 1373.

(38) Zhang, K.; Fu, Q.; Pan, N.; Yu, X.; Liu, J.; Luo, Y.; Wang, X.; Yang, J.; Hou, J. *Nat. Commun.* **2012**, *3*, 1194.

(39) Guo, L.; Shao, R.-Q.; Zhang, Y.-L.; Jiang, H.-B.; Li, X.-B.; Xie, S.-Y.; Xu, B.-B.; Chen, Q.-D.; Song, J.-F.; Sun, H.-B. *J.Phys. Chem. C* **2012**, *116*, 3594.

(40) Strong, V.; Dubin, S.; El-Kady, M. F.; Lech, A.; Wang, Y.; Weiller, B. H.; Kaner, R. B. *ACS Nano* **2012**, *6*, 1395.

(41) Gomez-Navarro, C.; Weitz, R. T.; Bittner, A. M.; Scolari, M.; Mews, A.; Burghard, M.; Kern, K. *Nano Lett.* **2007**, *7*, 3499.

(42) Ebejer, N.; Gueell, A. G.; Lai, S. C. S.; McKelvey, K.; Snowden, M. E.; Unwin, P. R. *Annu. Rev. Anal. Chem.,* **2013**, *6*, 329.

(43) Paulus, G. L. C.; Wang, Q. H.; Strano, M. S. *Acc. Chem. Res.* **2013**, *46*, 160.

(44) Huang, P.; Jing, L.; Zhu, H.; Gao, X. *Acc. Chem. Res.* **2013**, *46*, 43.

(45) Li, X.; Zhu, Y.; Cai, W.; Borysiak, M.; Han, B.; Chen, D.; Piner, R. D.; Colombo, L.; Ruoff, R. S. *Nano Lett.* **2009**, *9*, 4359.

(46) Kang, J.; Shin, D.; Bae, S.; Hong, B. H. *Nanoscale* **2012**, *4*, 5527.

(47) Cheng, Z.; Zhou, Q.; Wang, C.; Li, Q.; Wang, C.; Fang, Y. *Nano Lett.* **2011**, *11*, 767.

(48) Ishigami, M.; Chen, J. H.; Cullen, W. G.; Fuhrer, M. S.; Williams, E. D. *Nano Lett.* **2007**, *7*, 1643.

(49) Lin, Y.-C.; Lu, C.-C.; Yeh, C.-H.; Jin, C.; Suenaga, K.; Chiu, P.-W. *Nano Lett.* **2012**, *12*, 414.

(50) Suk, J. W.; Lee, W. H.; Lee, J.; Chou, H.; Piner, R. D.; Hao, Y.; Akinwande, D.; Ruoff, R. S. *Nano Lett.* **2013**, *13*, 1462.

(51) Pirkle, A.; Chan, J.; Venugopal, A.; Hinojos, D.; Magnuson, C. W.; McDonnell, S.; Colombo, L.; Vogel, E. M.; Ruoff, R. S.; Wallace, R. M. *Appl. Phys. Lett.* **2011**, *99*, 112108.

(52) Zhu, W.; Low, T.; Perebeinos, V.; Bol, A. A.; Zhu, Y.; Yan, H.; Tersoff, J.; Avouris, P. *Nano Lett.* **2012**, *12*, 3431.

(53) Malard, L. M.; Pimenta, M. A.; Dresselhaus, G.; Dresselhaus, M. S. *Phys. Rep.* **2009**, *473*, 51.

(54) Dresselhaus, M. S.; Jorio, A.; Saito, R. *Annu. Rev. Condens. Matter Phys.* **2010**, *1*, 89.

(55) Ferrari, A. C.; Meyer, J. C.; Scardaci, V.; Casiraghi, C.; Lazzeri, M.; Mauri, F.; Piscanec, S.; Jiang, D.; Novoselov, K. S.; Roth, S.; Geim, A. K. *Phys. Rev. Lett.* **2006**, *97*, 187401.

(56) Ferrari, A. C.; Basko, D. M. *Nat. Nanotechnol.* **2013**, *8*, 235.

(57) Wang, Q. H.; Jin, Z.; Kim, K. K.; Hilmer, A. J.; Paulus, G. L. C.; Shih, C.-J.; Ham, M.-H.; Sanchez-Yamagishi, J. D.; Watanabe, K.; Taniguchi, T.; Kong, J.; Jarillo-Herrero, P.; Strano, M. S. *Nat. Chem.* **2012**, *4*, 724.

(58) Guell, A. G.; Ebejer, N.; Snowden, M. E.; Macpherson, J. V.; Unwin, P. R. *J. Am. Chem. Soc.* **2012**, *134*, 7258.

(59) Kinnear, S. L.; McKelvey, K.; Snowden, M. E.; Peruffo, M.; Colburn, A. W.; Unwin, P. R. *Langmuir* **2013**, *29*, 15565.

(60) Guell, A. G.; Meadows, K. E.; Dudin, P. V.; Ebejer, N.; Macpherson, J. V.; Unwin, P. R. *Nano Lett.* **2014**, *14*, 220.

(61) Ebejer, N.; Schnippering, M.; Colburn, A. W.; Edwards, M. A.; Unwin, P. R. *Anal. Chem.* **2010**, *82*, 9141.

(62) Snowden, M. E.; Guell, A. G.; Lai, S. C. S.; McKelvey, K.; Ebejer, N.; O'Connell, M. A.; Colburn, A. W.; Unwin, P. R. *Anal. Chem.* **2012**, *84*, 2483.

(63) Wu, X.; Sprinkle, M.; Li, X.; Ming, F.; Berger, C.; de Heer, W. A. *Phys. Rev. Lett.* **2008**, *101*, 026801.

(64) Wang, S.; Zhang, Y.; Abidi, N.; Cabrales, L. *Langmuir* **2009**, *25*, 11078.

Chapter Seven

A Biphasic Approach for the Polymer-Free Transfer of CVD Graphene

Recent advances in CVD graphene growth methods now allow for the production of high-quality graphene sheets on a large scale. Unfortunately, the subsequent transfer process of these graphene films from their growth substrate to a substrate of interest still proves problematic, with conventional polymer-assisted transfer routes often introducing undesirable surface contamination. In this short chapter, a polymer-free transfer method is demonstrated that allows for the transfer of graphene films from their growth substrate, directly to a substrate of interest, in a single step. By instead trapping the graphene at an immiscible interface during growth substrate etching, it is shown that films of almost identical structural quality to those transferred via conventional routes can be achieved, but crucially, films transferred via this biphasic method lack the stubborn polymer residue typically associated with more traditional methods.

7.1 Introduction

Mechanical exfoliation methods are currently the route of choice for the production of pristine graphene flakes, highly suitable for fundamental studies of the material. Through such studies, graphene's outstanding electrical,[1,2] mechanical[3,4] and chemical[5,6] properties have been exposed, highlighting it as the likely material of the future. Unfortunately, the simple scotch-tape based approach;[7] typically producing micron-sized flakes, is unrealistic when one considers the potential graphene demand for technological purposes, likely requiring graphene over a much larger area.[8] To solve this problem, CVD routes have been developed, showing enormous promise for the synthesis of large scale high-quality graphene,[9-11] producing continuous graphene films of single-layer nature, with sheets 30-inches in size already reported.[12] Depending on the desired application, the subsequent transfer of such films to substrates of interest (often Si/SiO_2) is likely necessary,[13] however this is far from easy given its atomically thin nature. Polymer-support routes have commonly been employed for such transfer, with PMMA,[14] PDMS[15] and polycarbonate[16] layers (amongst others) all reported as suitable supports for transfer to a wide range of substrates, before final dissolution of the polymer layer. Unfortunately, despite intense research into these methods, the resultant graphene surfaces commonly appear littered with stubborn polymer residue,[17] often despite claims otherwise, having detrimental effects on graphene's electronics performance[18,19] and ruling it out as a viable route to high-quality graphene production (see Chapter 6). Consequently, alternative routes to transfer are being sought, with polymer-free methods recently emerging as a fresh approach graphene transfer.[20]

In this short chapter, this trend is furthered, and a new biphasic approach for the polymer free transfer of single-layer CVD graphene to Si/SiO_2 substrates is introduced. Essentially, the approach makes use of a non-polar organic phase to stabilize the freestanding graphene sheet post Cu etching, a role played by the spin-coated polymer-support in the majority of reported graphene transfer processes (*vide supra*). This simple yet effective methodology results in polymer-free transferred graphene over a much shorter timescale, and uses only solution processing, also making it an appealing approach for industrial applications.

7.2 Results and Discussion

7.2.1 Biphasic Transfer Protocol

For these studies, monolayer graphene was grown on polycrystalline Cu foil substrates using a low-pressure commercial CVD system (full details in section 2.2.3). As-grown samples were initially floated (graphene side up) atop a 0.1 M ammonium persulphate ($(NH_4)_2S_2O_8$) Cu etchant solution, which has been shown to minimize residue compared to the more commonly used $FeCl_3$ and $Fe(NO_3)_3$ Cu etching solutions.[21] At this point, a crucial non-polar hexane layer is gently introduced to the etchant solution using a syringe, which, when done carefully, traps the graphene/Cu substrate at the formed organic/aqueous biphasic interface, with the hydrophobic graphene in contact only with the hexane, and the Cu foil contacting the etchant solution. After adequate etching time (i.e. complete Cu dissolution) the synthesized graphene sheet is left trapped in the same position at the interface, stabilized by the hexane layer, preventing the surface tension of the water pulling the sheet apart, as would be the case if the non-polar layer were not present.[22] To further minimize contamination, the used etchant solution is then replaced with pure water by syringe pumping, at which point it is crucial to minimize any disturbance to the delicate graphene layer. Finally, the solution-supported graphene is scooped from the interface using a pre-cleaned (rinsed with acetone and IPA) Si/SiO_2 substrate in a single swift motion, before being left to dry at room temperature, revealing polymer-free transferred graphene on the substrate. The biphasic transfer method introduced herein is summarized schematically in Figure 7.1, below.

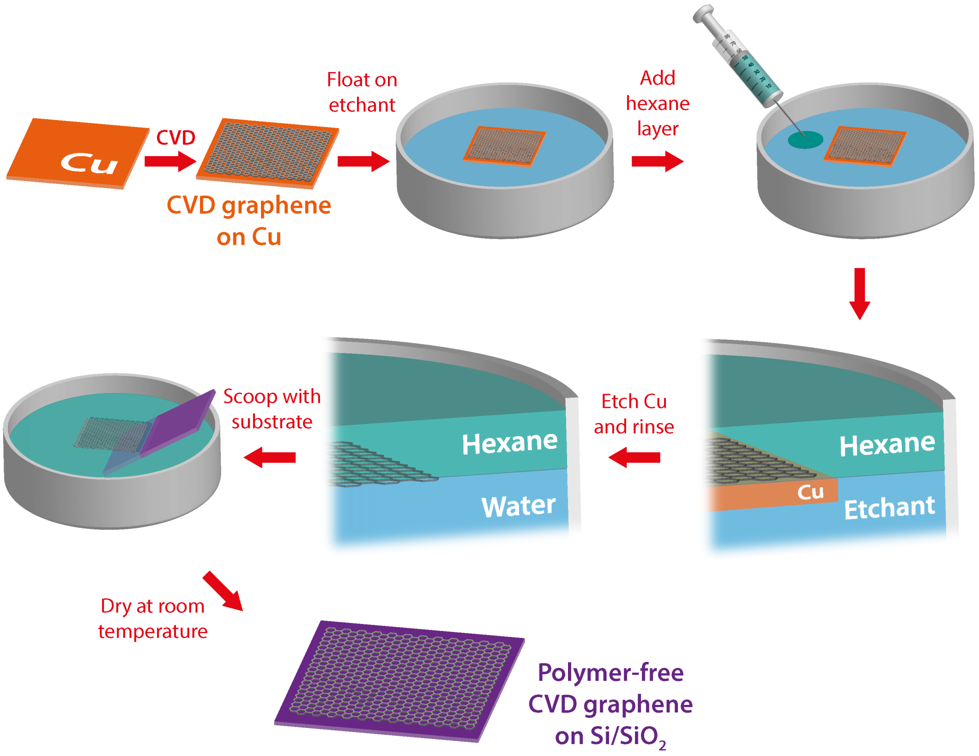
Cu
CVD
CVD graphene on Cu
Float on etchant
Add hexane layer
Hexane
Cu
Etchant
Etch Cu and rinse
Hexane
Water
Scoop with substrate
Dry at room temperature
Polymer-free CVD graphene on Si/SiO₂

Figure 7.1 A schematic representation of the biphasic polymer-free transfer method introduced herein.

7.2.2 Transferred Graphene Characterization

Optical microscopy of a resulting transferred sample showed areas of continuous monolayer graphene, ~ 100 – 200 μm in size, scattered across the sample, with occasional patches of bilayer graphene and some small tears, revealing the underlying Si/SiO_2 substrate.[23] Figure 7.2 shows optical microscopy images of a graphene sample transferred using the newly developed approach (Figure 7.2(a)) and a comparison to a sample transferred using the traditional PMMA route (Figure 7.22(b)), described in section 2.2.4. In the case of the latter, large levels of PMMA contamination are evident across the monolayer graphene surface, as well as patches of string-like graphitic contamination, likely as a result of the underside of the Cu substrate (on which graphene also grows) not being polished sufficiently before etching.

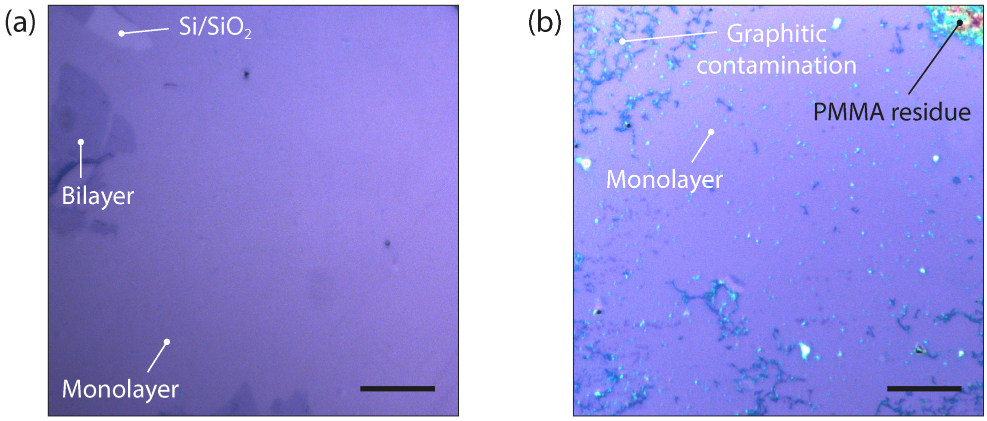

Figure 7.2 Optical micrographs of graphene on Si/SiO_2 transferred via (a) the biphasic method introduced herein and (b) the traditional PMMA supported route. Scale bars denote 10 μm.

AFM imaging of a monolayer area further revealed the cleanliness of the graphene surface (Figure 7.3(a)). Faintly visible in the background of the image are small folds and wrinkles, likely introduced during the growth process as a result of contraction of the Cu substrate upon cooling.[24] Also visible are small levels of particulate contamination, with close inspection of the image revealing they are likely sandwiched between the graphene layer and Si/SiO_2 substrate, creating small raised areas of graphene around the particles, appearing similar to small wrinkles. Such particulate matter is likely salt contamination (from $(NH_4)_2S_2O_8$ etchant solution), which could be reduced further through more extensive washing steps. Overall, the exposed graphene surface appears very clean, and crucially, is free from transfer residue, though direct comparisons with polymer-transferred graphene are difficult given the overall lack of such data in published literature. As such, it is likely that the sample presented herein is significantly cleaner than those achieved through the majority of polymer transfer routes (*vide infra*).

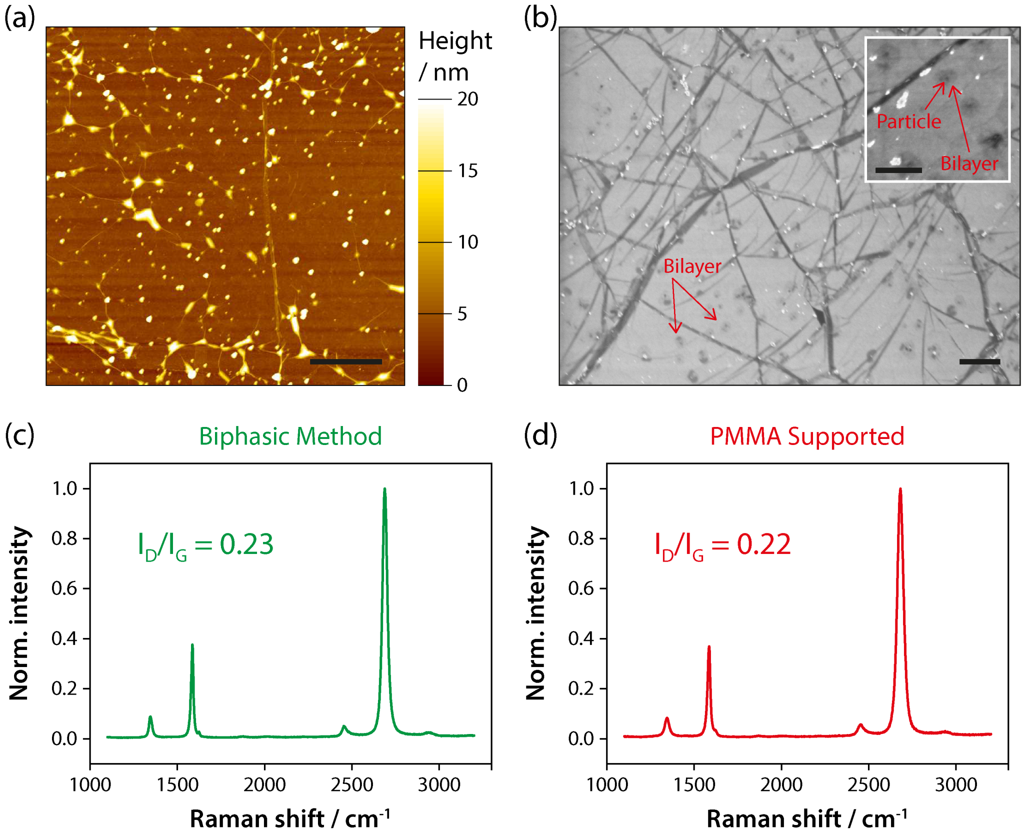

Figure 7.3 (a) AFM and (b) SEM images of graphene transferred via the biphasic approach to an Si/SiO$_2$ substrate. Scale bar denotes 1 μm in both cases. SEM inset further highlights bilayer patches, with a scale bar denoting 500 nm. Representative Raman spectra for graphene on Si/SiO$_2$ transferred using: (c) the biphasic method introduced herein, and (d) the common PMMA supported transfer route. Both samples were grown in the CVD chamber at the same time. Spectra are normalized to 2D band intensity.

SEM imaging of the same transferred graphene revealed similar surface features, but also highlighted small patches of bilayer graphene, as marked (Figure 7.3(b)). At the center of every bilayer patch, a small particle appeared to be present (Figure 7.3(b) inset), as was also highlighted by Kim *et al.* when investigating the effects of various pre-cleaning steps on Cu substrates, prior to graphene growth. They found such particles were often metallic, and acted as nucleation sites for graphene growth, but could also be removed prior to growth by cleaning in nitric acid.[25] These metallic particles may also be the observed particulate contamination in AFM imaging, again, highlighting the potential for their removal.

Finally, the effectiveness of this new approach is highlighted yet further by another direct comparison to a graphene sample transferred using a PMMA polymer-support route, using a sample synthesized in the CVD chamber at the same time as the one employed for the biphasic transfer approach, and thus of almost identical starting quality when on the Cu foil. The polymer-support route employed is likely the most well developed methodology in the literature,[14] and is probably considered the transfer standard by the graphene community, making it an ideal comparison to the new methodology introduced herein. Representative Raman spectra for both the biphasic method and a PMMA polymer-support route are presented in Figures 7.3(c) and 7.3(d), respectively, with no apparent differences. I_D/I_G ratios of 0.23 and 0.22 for the biphasic and polymer-support routes, respectively, further back this, suggesting the small D peak evident in both cases is a likely artifact of the CVD growth process, rather than graphene transfer, whilst respective full-width-half-maximum values of 33 cm^{-1} and 42 cm^{-1} further confirm the presence of monolayer graphene. As such, it is clear that the biphasic approach introduced herein is capable of producing transferred graphene samples on Si/SiO_2 of almost identical quality to those transferred using traditional polymer-supported routes, whilst being completely free from stubborn polymer residue, offering a significant step forward for the large scale production of transferred monolayer graphene.

7.3 Conclusions

To conclude, this chapter proves the suitability of a biphasic approach for the polymer-free transfer of high-quality monolayer CVD graphene to Si/SiO_2 substrates on a hundreds of microns scale. The quality of the resulting films match that of the most well-developed and commonly used PMMA transfer routes, highlighting the suitability of the biphasic methodology, with the added advantage that they are completely free from any PMMA contamination, often associated with such routes. Furthermore, the short timescales over which transfer can be achieved paves the way for industrially scalable polymer-free routes for the production of continuous graphene films on a much larger-scale.

7.4 References

(1) Geim, A. K.; Novoselov, K. S. *Nat. Mater.* **2007**, *6*, 183.

(2) Avouris, P. *Nano Lett.* **2010**, *10*, 4285.

(3) Lee, C.; Wei, X.; Kysar, J. W.; Hone, J. *Science* **2008**, *321*, 385.

(4) Bunch, J. S.; Verbridge, S. S.; Alden, J. S.; van der Zande, A. M.; Parpia, J. M.; Craighead, H. G.; McEuen, P. L. *Nano Lett.* **2008**, *8*, 2458.

(5) Paulus, G. L. C.; Wang, Q. H.; Strano, M. S. *Accounts Chem. Res.* **2013**, *46*, 160.

(6) Elias, D. C.; Nair, R. R.; Mohiuddin, T. M. G.; Morozov, S. V.; Blake, P.; Halsall, M. P.; Ferrari, A. C.; Boukhvalov, D. W.; Katsnelson, M. I.; Geim, A. K.; Novoselov, K. S. *Science* **2009**, *323*, 610.

(7) Novoselov, K. S.; Geim, A. K.; Morozov, S. V.; Jiang, D.; Zhang, Y.; Dubonos, S. V.; Grigorieva, I. V.; Firsov, A. A. *Science* **2004**, *306*, 666.

(8) Van Noorden, R. *Nature* **2012**, *483*, S32.

(9) Reina, A.; Jia, X.; Ho, J.; Nezich, D.; Son, H.; Bulovic, V.; Dresselhaus, M. S.; Kong, J. *Nano Lett.* **2009**, *9*, 30.

(10) Sutter, P. W.; Flege, J.-I.; Sutter, E. A. *Nat. Mater.* **2008**, *7*, 406.

(11) Li, X.; Cai, W.; An, J.; Kim, S.; Nah, J.; Yang, D.; Piner, R.; Velamakanni, A.; Jung, I.; Tutuc, E.; Banerjee, S. K.; Colombo, L.; Ruoff, R. S. *Science* **2009**, *324*, 1312.

(12) Bae, S.; Kim, H.; Lee, Y.; Xu, X.; Park, J.-S.; Zheng, Y.; Balakrishnan, J.; Lei, T.; Kim, H. R.; Song, Y. I.; Kim, Y.-J.; Kim, K. S.; Ozyilmaz, B.; Ahn, J.-H.; Hong, B. H.; Iijima, S. *Nat. Nanotechnol.* **2010**, *5*, 574.

(13) Kang, J.; Shin, D.; Bae, S.; Hong, B. H. *Nanoscale* **2012**, *4*, 5527.

(14) Li, X.; Zhu, Y.; Cai, W.; Borysiak, M.; Han, B.; Chen, D.; Piner, R. D.; Colombo, L.; Ruoff, R. S. *Nano Lett.* **2009**, *9*, 4359.

(15) Kim, K. S.; Zhao, Y.; Jang, H.; Lee, S. Y.; Kim, J. M.; Kim, K. S.; Ahn, J.-H.; Kim, P.; Choi, J.-Y.; Hong, B. H. *Nature* **2009**, *457*, 706.

(16) Park, H. J.; Meyer, J.; Roth, S.; Skakalova, V. *Carbon* **2010**, *48*, 1088.

(17) Lin, Y.-C.; Lu, C.-C.; Yeh, C.-H.; Jin, C.; Suenaga, K.; Chiu, P.-W. *Nano Lett.* **2012**, *12*, 414.

(18) Pirkle, A.; Chan, J.; Venugopal, A.; Hinojos, D.; Magnuson, C. W.; McDonnell, S.; Colombo, L.; Vogel, E. M.; Ruoff, R. S.; Wallace, R. M. *Appl. Phys. Lett.* **2011**, *99*, 112108.

(19) Suk, J. W.; Lee, W. H.; Lee, J.; Chou, H.; Piner, R. D.; Hao, Y.; Akinwande, D.; Ruoff, R. S. *Nano Lett.* **2013**, *13*, 1462.

(20) Regan, W.; Alem, N.; Aleman, B.; Geng, B.; Girit, C.; Maserati, L.; Wang, F.; Crommie, M.; Zettl, A. *Appl. Phys. Lett.* **2010**, *96*, 113102.

(21) Suk, J. W.; Kitt, A.; Magnuson, C. W.; Hao, Y.; Ahmed, S.; An, J.; Swan, A. K.; Goldberg, B. B.; Ruoff, R. S. *ACS Nano* **2011**, *5*, 6916.

(22) Lin, W.-H.; Chen, T.-H.; Chang, J.-K.; Taur, J.-I.; Lo, Y.-Y.; Lee, W.-L.; Chang, C.-S.; Su, W.-B.; Wu, C.-I. *ACS Nano* **2014**, *8*, 1784.

(23) Blake, P.; Hill, E. W.; Neto, A. H. C.; Novoselov, K. S.; Jiang, D.; Yang, R.; Booth, T. J.; Geim, A. K. *Appl. Phys. Lett.* **2007**, *91*, 063124.

(24) Zhu, W.; Low, T.; Perebeinos, V.; Bol, A. A.; Zhu, Y.; Yan, H.; Tersoff, J.; Avouris, P. *Nano Lett.* **2012**, *12*, 3431.

(25) Kim, S. M.; Hsu, A.; Lee, Y.-H.; Dresselhaus, M.; Palacios, T.; Kim, K. K.; Kong, J. *Nanotechnology* **2013**, *24*, 365602.

Chapter Eight

Conclusions

The aim of this thesis was to understand and exploit a number of surface modification processes, through approaches that combined results obtained from various complementary techniques, including electrochemistry, and that have implications at both the fundamental level and in real-life applications.

Chapter 3 highlighted the advantages of using well-defined model surfaces to understand the fundamental processes occurring in real-life systems, which in reality may be too complex to study directly. Colloidal particles are often stabilized by surfactant type molecules, with one example of such a system being the carbonaceous particles produced inside an automotive engine, which are typically kept oil soluble through the use of dispersant compounds. Using SAM chemistry, model surfaces representative of such carbonaceous soot were created and fully characterized. Through STM measurements it was shown that the formation of acid-terminated SAM assemblies is more complex than often described in the literature, and that modified preparation procedures are necessary for the creation of well-defined systems. The use of QCM-D was next explored as a method for evaluating the interactions between a range of synthesized model dispersant compounds and formed model soot surfaces, yielding detailed information on the relative affinities of different dispersant chemistries, without the need for costly engine testing or complex models.

Dispersants of a basic nature heavily favored interaction at acidic sites, where they exhibited multilayer type adsorption behavior, whilst those lacking basic character showed little interaction at all. Not only did the data obtained offer up details on the likely mechanisms of action of such dispersant compounds, but also highlighted QCM-D as a viable technique for future dispersant screening studies. In addition, CFM was investigated as a further means to study dispersant interactions, this time at a model sp^2 carbon surface. It was found that next-generation dispersants of an aromatic nature displayed significantly higher levels of interaction than dispersants that were polar in nature, likely explained by $\pi - \pi$ effects, suggesting this to be their primary mechanism of action in actual soot dispersions.

Chapter 4 introduced a new approach for profiling the local delivery and activity of molecular adsorbates at carbon electrode surfaces, ultimately allowing for the impact of electrode surface structure on observed activity to be elucidated unambiguously through the use of complementary techniques, such as AFM. Indeed, there has been a widely held belief that the basal surface of sp^2 carbon materials is highly inert toward electrochemical processes, suggesting ET to be confined to edges and defects. However, by focusing on quinones, as a widely studied and important class of molecules, it was shown that the electrochemical response at high-quality HOPG substrates is in fact dominated by the basal surface, with no influence of step edges. This result has implications for generally understanding the behavior of carbon electrodes, not least because quinone adsorption has been adopted widely as a measure of defect density on graphite, which itself also acts as a model for CNTs and graphene, where literature debate also exists.

Chapter 5 demonstrated the unique spatial and temporal control offered by SECCM as a methodology for localized surface modification, specifically through the use of diazonium compounds. The controlled modification of sp^2 carbon surfaces using diazonium chemistry is currently receiving renewed interest, particularly as a means of generating an electronic band-gap within graphene. Crucially, it has been previously demonstrated that the size of the band-gap can be controlled by the extent of diazonium modification (level of sp^3 carbon introduced), and localized modification methods that exhibit control over the extent of grafting could thus pave the way for entire graphene device fabrication. It was demonstrated that this is highly achievable through the use of SECCM. Using HOPG as a model sp^2 carbon surface, and complementing SECCM measurements with AFM and Raman mapping, it was shown clearly how localized electrochemistry can be used to tune the density of diazonium grafted films (and hence level of sp^3 carbon) at sp^2 carbon surfaces. The confined nature of this probe technique ensured that the surrounding surface remained free from contamination or unwanted diazonium modification, which are major issues associated with previously demonstrated patterning techniques.

Chapter 6 opened new avenues in the fabrication of graphene circuitry, demonstrating the potential of SECCM to one-day be the ultimate tool for the production of integrated graphene devices. Indeed, graphene needs little introduction, we're promised that it will one-day revolutionize digital electronics; however, at the moment, graphene's inclusion into even basic electronic devices (e.g. FETs) is hampered by both its semi-metal nature and a general lack of techniques that allow for the production of defined graphene pathways. It was shown that the unique meniscus-based probe associated with

SECCM can address both these issues. Starting with a single graphene sheet, the application of harsh anodic potentials at the confined, moveable, nanoscale SECCM droplet, allowed for patterned graphene areas that were completely insulating in nature to be introduced, effectively generating defined conductive pathways, proven through complementary resistance and electrochemical mapping measurements. Furthermore, the inclusion of diazonium chemistry in the meniscus reservoir allowed for diazonium grafted moieties to be selectively introduced at the graphene surface through a simple switch in applied potential, and with the grafting reaction shown to introduce an electronic band-gap into graphene, the power of this approach becomes apparent. Crucially, at potentials between those employed for modification, no reaction occurred, negating the need for the probe to be removed when moving between areas to be modified.

Chapter 7 introduced a novel, biphasic route for the effective transfer of CVD graphene from its growth substrate to a new substrate of interest. The production of graphene via CVD methods is now somewhat standard practice, to the extent that is has been demonstrated at the meter scale, making it a viable production route in both industry and academia. However, the full exploitation of graphene's unique properties may often be hampered by the significant levels of surface contamination introduced during its subsequent transfer to useful substrates - contamination widely attributed to the use of polymer-support layers, with even the most widely-used transfer protocols falling foul here. By trapping the graphene at an immiscible oil/water interface before subsequently removing its growth support, a route that completely avoids the use of polymer-support layers is introduced. AFM and SEM imaging demonstrate the resulting graphene surface to be devoid of polymer residue, whilst direct Raman spectroscopy comparisons with a polymer-transferred sample show that the structural integrity of the graphene is in no way compromised via this new approach, making it a highly attractive route for future applications, with industrial applicability.